

EFFECTIVE CONFINEMENT AND BOND STRENGTH OF GRADE 100 REINFORCEMENT

by

Eric T. Fleet

A Thesis

Submitted to the Faculty of Purdue University

In Partial Fulfillment of the Requirements for the degree of

Master of Science in Civil Engineering



Lyles School of Civil Engineering

West Lafayette, Indiana

May 2019

THE PURDUE UNIVERSITY GRADUATE SCHOOL
STATEMENT OF COMMITTEE APPROVAL

Dr. Robert J. Frosch, Chair

Lyles School of Civil Engineering

Dr. Christopher S. Williams

Lyles School of Civil Engineering

Dr. Sukru Guzey

Lyles School of Civil Engineering

Approved by:

Dr. Dulcy Abraham

Head of the Burke Graduate Program

*It is with great pride that I dedicate this thesis to my parents,
Robert and Lori Fleet, who instilled in me
The importance of living my truth,
Pursuing my passions, and
Seeking adventure
In all that
I do.*

ACKNOWLEDGMENTS

I would like to express my sincerest gratitude to my advisor, Dr. Robert J. Frosch, for his continual guidance, steadfast patience, inspiring work ethic, and unwavering support throughout the course of this project. It has been my pleasure having the privilege to work with him and explore the world of research in our profession. My appreciation must also be given to my advisory committee members, Dr. Christopher S. Williams and Dr. Sukru Guzey, for teaching me the importance of critical thinking, attention to detail, and for reminding me to never doubt my potential for success.

This project could not have been completed without the many people who contributed daily in the Bowen Laboratory for Large-Scale Civil Engineering Research and in the Civil Engineering Department. I want to thank Harry Tidrick and Kevin Brower for assisting me on the lab floor during the experimental testing portion of this research program. I would also like to thank Molly Stetler and Jenny Ricksy for their aptitude in helping students every day, aiding with all research project logistics, and readily responding to all inquiries about the graduate program.

A huge thank you goes to the many companies and establishments that lent a hand in making this research project possible. The financial support of the Charles Pankow Foundation was unmatched and beyond helpful in meeting project objectives. Thank you to Nucor Steel, Harris Rebar, Circle City Rebar, and MMFX Technologies (Commercial Metals Company) for providing the steel necessary to conduct required testing. Also, thank you to Dayton Superior for their generosity in providing steel cage construction materials.

I want to express gratitude toward my fellow research assistants for their help with test setup construction, specimen testing, and concrete casting labor. Without their strong devotion to

helping others and providing a fun work environment, my research would not have concluded. These numerous Bowen lab helpers include Ahmed Alimran, Morgan Broberg, David Derks, Robert Jacobs, Michael Phelan, William Pollalis, William Rich, Soheil Shafaei, Andi Vicksman, Hwa Ching Wang, Sijia Wang, and Ryan Whelchel. A special thank you belongs to Rebecca Glucksman, without whom this research would not be possible. Her guidance, resources, and instruction were invaluable to my experience here and the successful completion of this project.

My journey through graduate school would not have been possible without the support of my family. Thank you to my parents, Robert and Lori Fleet, for your continued support and encouragement over these last few years. My gratitude must also go to my many friends across this country who have lifted me up countless times and reminded me of what is most important throughout the graduate school process. In addition, I want to thank my Cowboy family at Oklahoma State University who pushed me to accomplish more than I ever thought I was capable. Carisa Ramming, Steve O'Hara, Suzanne Bilbeisi, Lanette Compton, Steven Blair - your teachings, mentorship, and wisdom will remain with me far beyond my time at Purdue University.

TABLE OF CONTENTS

LIST OF FIGURES	12
LIST OF TABLES	20
ABSTRACT	24
CHAPTER 1. INTRODUCTION	25
1.1 Background	25
1.2 Bond Design	25
1.3 Bond Mechanics	26
1.3.1 Force Transfer Mechanisms	26
1.3.2 Stress Formation	27
1.3.3 Bond Failure	30
1.3.3.1 <i>Splitting</i>	30
1.3.3.2 <i>Pullout</i>	31
1.4 Bond Variables	32
1.4.1 Splice Length	32
1.4.2 Concrete Compressive Strength	33
1.4.3 Bar Spacing and Cover	34
1.4.4 Transverse Reinforcement	37
1.5 High-Strength Steel	39
1.6 Research Objective and Scope	40
CHAPTER 2. EXPERIMENTAL PROGRAM: SLABS	41
2.1 Introduction	41
2.2 Specimen Selection	41
2.2.1 Slab Design	41
2.2.2 Slab Dimensions	42
2.2.3 Slab Testing Matrix	43
2.3 Materials	44
2.3.1 Concrete	44
2.3.1.1 <i>Concrete Testing</i>	45

2.3.1.2	<i>Compression Testing</i>	46
2.3.1.3	<i>Split Cylinder Testing</i>	49
2.3.1.4	<i>Elastic Modulus and Poisson's Ratio</i>	50
2.3.2	Reinforcing Steel	51
2.4	Specimen Construction	53
2.4.1	Formwork Assembly	53
2.4.2	Steel Cage Construction	55
2.5	Casting, Curing, and Storage.....	57
2.5.1	Cylinders.....	57
2.5.2	Casting	58
2.5.3	Curing and Storage	61
2.6	Test Setup.....	63
2.6.1	Schematic.....	63
2.6.2	Instrumentation and Equipment.....	67
2.6.2.1	<i>Deflection</i>	67
2.6.2.2	<i>Loading System</i>	68
2.6.2.3	<i>Concrete Cracking</i>	69
2.6.2.4	<i>Testing Documentation and Media</i>	70
2.6.3	General Testing Procedure	71
CHAPTER 3.	EXPERIMENTAL RESULTS: SLABS	72
3.1	Introduction	72
3.2	Experimental Results.....	72
3.2.1	Self-Weight.....	73
3.2.2	Specimen Observations	76
3.3	Load-Deflection Response	78
3.4	Concrete Cracking Behavior	79
3.5	Failure.....	84
3.5.1	Bond Failure	84
3.5.2	Flexural Failure.....	88
CHAPTER 4.	EXPERIMENTAL PROGRAM: BEAMS	91

4.1 Introduction	91
4.2 Specimen Selection	91
4.2.1 Beam Design.....	91
4.2.2 Beam Dimensions	95
4.2.3 Beam Testing Matrix	96
4.3 Materials.....	99
4.3.1 Concrete.....	99
4.3.1.1 Concrete Testing.....	101
4.3.1.2 Compression Testing	102
4.3.1.3 Split Cylinder Testing	105
4.3.1.4 Elastic Modulus and Poisson's Ratio	105
4.3.2 Reinforcing Steel	107
4.3.2.1 ASTM A615.....	108
4.3.2.2 MMFX.....	110
4.4 Specimen Construction	111
4.4.1 Formwork Assembly	112
4.4.2 Steel Cage Construction	115
4.5 Casting, Curing, and Storage.....	120
4.5.1 Cylinders.....	120
4.5.2 Casting	121
4.5.2.1 Series VI.....	121
4.5.2.2 Series VII	123
4.5.3 Curing and Storage	125
4.6 Test Setup.....	127
4.6.1 Schematic.....	127
4.6.2 Instrumentation and Equipment.....	130
4.6.3 General Testing Procedure	130
CHAPTER 5. EXPERIMENTAL RESULTS: BEAMS.....	132
5.1 Introduction	132
5.2 Experimental Results.....	132

5.2.1 Self-Weight.....	133
5.2.2 Specimen Observations	135
5.3 Load-Deflection Response	136
5.4 Concrete Crack Behavior	139
5.5 Failure.....	145
5.5.1 Unconfined Specimens	145
5.5.2 Confined Specimens	147
5.5.2.1 25 psi Specimen	150
5.5.2.2 50 psi Specimens.....	151
5.5.2.3 200 psi Specimen	153
CHAPTER 6. ANALYSIS OF TEST RESULTS	155
6.1 Analysis and Design Methods.....	155
6.1.1 ACI 318-14	155
6.1.2 Pay (2005).....	160
6.1.3 Sim (2014)	164
6.1.4 Glucksman (2018)	170
6.1.5 Summary of Strength Comparisons.....	175
6.2 Influence of Investigated Parameters	177
6.2.1 Phase I Experimental Test Results	177
6.2.2 Splice Length	179
6.2.2.1 Unconfined Specimens.....	179
6.2.2.2 Confined Specimens.....	182
6.2.3 Concrete Compressive Strength	183
6.2.3.1 Unconfined Specimens.....	183
6.2.3.2 Confined Specimens.....	186
6.2.4 Transverse Reinforcement	189
6.2.4.1 Distributed Transverse Reinforcement Ratio	189
6.2.4.2 Confinement Pressure.....	197
6.2.4.3 Average Transverse Reinforcement Ratio	200
6.2.4.4 Location of Transverse Reinforcement.....	203

CHAPTER 7. BOND STRENGTH MODELING	205
7.1 Introduction	205
7.2 Unconfined Database	205
7.2.1 Frequency Distribution of Database Parameters	206
7.3 Unconfined Model.....	210
7.3.1 Equation Components.....	211
7.3.2 Cover Investigation.....	211
7.3.3 Nonlinear Regression Analysis.....	214
7.4 Confined Database	221
7.4.1 Frequency Distribution of Database Parameters	222
7.5 Confinement Model.....	228
7.5.1 Model.....	228
7.5.2 Model Application.....	232
7.5.3 Steel Contribution Term, f_{bs}	240
7.6 Bond Model.....	244
7.7 Recommendations	250
CHAPTER 8. SUMMARY AND CONCLUSIONS	252
8.1 Summary	252
8.2 Slab Testing.....	252
8.3 Beam Testing.....	253
8.3.1 Unconfined	253
8.3.2 Confined	254
8.4 Bond Modeling.....	255
8.4.1 Unconfined	255
8.4.2 Confined	256
8.4.3 Design Recommendations	260
8.5 Further Research	261
REFERENCES	263
APPENDIX A. STEEL STRESS-STRAIN CURVES	270
APPENDIX B. SLAB CONSTRUCTION AS-BUILT DIMENSIONS	275

APPENDIX C. LOAD DEFLECTION CURVES	278
APPENDIX D. CRACK WIDTH PROPAGATION.....	295
APPENDIX E. BEAM CONSTRUCTION AS-BUILT DIMENSIONS	312
APPENDIX F. STEEL DATABASE	317
VITA.....	319

LIST OF FIGURES

Figure 1.1: Bond Force Transfer Mechanisms	26
Figure 1.2: Initial Stresses on a Typical Concrete Element.....	28
Figure 1.3: Concrete Stress Resolution.....	28
Figure 1.4: Internal Crack Formations.....	29
Figure 1.5: Radial Stress Distribution.....	29
Figure 1.6: Splitting Failures	30
Figure 1.7: B-PG2-5-24 Bar Pullout Failure (Pay 2005).....	31
Figure 1.8: Types of Splitting Failure Modes.....	36
Figure 2.1: Typical Slab Cross-Section	41
Figure 2.2: Slab Specimen Identification Label	42
Figure 2.3: Typical Slab Test Specimen	43
Figure 2.4: Cylinder Testing Identification	46
Figure 2.5: Typical Compression Cylinder Failure	48
Figure 2.6: Concrete Compressive Strength Variation Over Time.....	48
Figure 2.7: Series V Splitting Tensile Cylinder Failure	49
Figure 2.8: Series V Modulus Testing Setup	50
Figure 2.9: Typical Stress-Strain Response for A615 Gr. 100 No. 5 Bars	52
Figure 2.10: Series V Formwork Components	54
Figure 2.11: Series V Completed Formwork.....	55
Figure 2.12: Slab Construction – Shear Region.....	55
Figure 2.13: Slab Construction – Splice Region.....	56
Figure 2.14: Typical Concrete Cylinder Preparation Space	57
Figure 2.15: Series V Cylinder Casting	58
Figure 2.16: Series V Consolidation Process.....	59
Figure 2.17: Series V Casting Process.....	60
Figure 2.18: Series V Casting Complete.....	60
Figure 2.19: Series V Moist Curing.....	61
Figure 2.20: Series V Side Form Removal	62

Figure 2.21: Series V Member Stacking and Storage	62
Figure 2.22: Series V Test Setup	63
Figure 2.23: Series V Testing Details	64
Figure 2.24: Typical Crossbeam Setup	65
Figure 2.25: Series V Test Setup – East Elevation	66
Figure 2.26: Series V Test Setup Schematic Plans	66
Figure 2.27: String Potentiometer Connections	67
Figure 2.28: Typical Load Cell Configuration	68
Figure 2.29: Typical Pump System for Testing	69
Figure 2.30: Crack Width Microscope and Mapping Process	70
Figure 2.31: StrainSmart Data Acquisition	70
Figure 2.32: General Slab Test – Crack Mapping (S-80-5)	71
Figure 3.1: Shear and Moment Diagrams for Slabs from Loading	75
Figure 3.2: Shear and Moment Diagrams for Slab Self-Weight	75
Figure 3.3: Slab Deformation during Testing (S-100-5)	77
Figure 3.4: Typical Flexural Cracking – West Side and Tension Face (S-80-5)	77
Figure 3.5: General Load-Deflection Behavior (S-60-5)	78
Figure 3.6: Series V Load-Deflection Response	79
Figure 3.7: Series V Crack Width Measurements	80
Figure 3.8: Observed Crack Branching Near End of Splice (S-60-5)	81
Figure 3.9: Side Crack Propagation (S-100-5)	82
Figure 3.10: Post-Failure Shear Span Cracking (S-60-5)	82
Figure 3.11: Splice Region Crack Observations	83
Figure 3.12: Load-Deflection Response of Series V Bond Failures	85
Figure 3.13: S-40-5 Face- and Side-Splitting Failure	85
Figure 3.14: S-60-5 Partial Failure 1	86
Figure 3.15: S-60-5 Partial Failure 2	87
Figure 3.16: S-60-5 Final Failure	87
Figure 3.17: Load-Deflection Response of Series V Flexural Failures	88
Figure 3.18: Initiation of S-80-5 Failure – East Elevation	89

Figure 3.19: Final S-80-5 Failure – East Elevation	89
Figure 3.20: S-100-5 End of Testing	90
Figure 4.1: Typical Beam Cross-Sections	92
Figure 4.2: Unconfined Specimen Identification Label.....	93
Figure 4.3: Confined Specimen Identification Label.....	94
Figure 4.4: Typical Beam Test Specimen.....	95
Figure 4.5: Series VI Stirrup Configurations.....	98
Figure 4.6: Series VII Stirrup Configurations.....	98
Figure 4.7: Cylinder Testing Identification	101
Figure 4.8: Typical Compression Cylinder Failure	104
Figure 4.9: Concrete Compressive Strength Variation Over Time.....	104
Figure 4.10: Series VI Splitting Tensile Cylinder Failure	105
Figure 4.11: Typical Stress-Strain Response for A615 Gr. 100 No. 8 Bars	108
Figure 4.12: Comparison of Grade 100 Bar Surfaces.....	110
Figure 4.13: Typical Stress-Strain Response for A1035 Gr. 100 No. 8 Bars	111
Figure 4.14: Series VI and VII Formwork Components.....	113
Figure 4.15: Beam Specimen Formwork Space	114
Figure 4.16: Series VII Cage Support Blocks.....	115
Figure 4.17: Typical Beam Cage Construction Details	116
Figure 4.18: Beam Shear Region and Cage Lifting.....	117
Figure 4.19: Typical Beam Cage Configurations	118
Figure 4.20: Final Beam Construction Details	119
Figure 4.21: Series VI Cylinders	120
Figure 4.22: Series VI Casting Process.....	121
Figure 4.23: Series VI Form Bracing.....	122
Figure 4.24: Series VI Cast Complete	123
Figure 4.25: Series VII Casting Procedure	124
Figure 4.26: Series VII Cast In Progress	124
Figure 4.27: Series VII Cast Complete	125
Figure 4.28: Series VI Moist Curing – Burlap Cover.....	125

Figure 4.29: Series VI Moist Curing – Plastic Cover	126
Figure 4.30: Series VII Beam Flipping Process.....	126
Figure 4.31: Series VI and VII Test Setup.....	127
Figure 4.32: Series VI and VII Testing Details	128
Figure 4.33: Typical Crossbeam Setup	128
Figure 4.34: Series VI and VII Test Setup – East Elevation	129
Figure 4.35: Series VI and VII Test Setup Schematic Plans	129
Figure 4.36: General Beam Test – Crack Mapping (C3/60/2-40-10-50).....	131
Figure 5.1: Shear and Moment Diagrams for Beams from Loading	134
Figure 5.2: Shear and Moment Diagram for Beam Self-Weight	134
Figure 5.3: Typical Flexural Cracking within Unconfined Splice Region (U-60-10).....	135
Figure 5.4: Typical Flexural Cracking within Confined Splice Region (C3/60-40-5-200).....	136
Figure 5.5: General Load-Deflection Behavior (C3/60-50-5-200).....	137
Figure 5.6: Unconfined Load-Deflection Responses.....	138
Figure 5.7: Confined Load-Deflection Responses.....	138
Figure 5.8: Series VI and VII Crack Width Measurements.....	139
Figure 5.9: Transverse Flexural Cracking within Splice Region (C3/60/2-40-10-50)	140
Figure 5.10: Initiation of Flexural Side Cracking	141
Figure 5.11: Shear Span – Early Testing (C3/60-40-5-200).....	142
Figure 5.12: Shear Span – Late Testing (C3/60-40-5-200)	142
Figure 5.13: Flexural Cracking at Stirrup Locations	143
Figure 5.14: Longitudinal Crack Propagation in Splice Region Failure	144
Figure 5.15: Longitudinal and Branch Cracking Before Flexural Failure (C3/60-50-5-200)	144
Figure 5.16: Typical Splice Side Cracking at Failure.....	146
Figure 5.17: Typical Failure Side Crack Extensions	146
Figure 5.18: Specimen C3/60/3-40-10-50 Side Cracking.....	149
Figure 5.19: Reconstructed Confined Splice Planes.....	150
Figure 5.20: Bar Slip on Specimen C3/60/2-40-10-25	151
Figure 5.21: Bent Stirrup on Specimen C3/60/3-40-10-50.....	152
Figure 5.22: Ruptured Stirrup on Specimen C3/60/2-40-10-50	153

Figure 5.23: Longitudinal Crack Branching (C3/60-50-5-200).....	154
Figure 5.24: Flexural Failure of Specimen C3/60-50-5-200	154
Figure 6.1: Unconfined Strength Calculation Comparison by ACI 318-14 Eq. 6-3.....	159
Figure 6.2: Confined Strength Calculation Comparison by ACI 318-14 Eq. 6-3.....	160
Figure 6.3: Unconfined Strength Calculation Comparison by Pay (2005) Eq. 6-8	164
Figure 6.4: Unconfined Strength Calculation Comparison by Sim (2014) Eq. 6-16.....	169
Figure 6.5: Confined Strength Calculation Comparison by Sim (2014) Eq. 6-16.....	169
Figure 6.6: Unconfined Strength Calculation Comparison by Glucksman (2018) Eq. 6-21	174
Figure 6.7: Confined Strength Calculation Comparison by Glucksman (2018) Eq. 6-21	174
Figure 6.8: Effect of Splice Length on Bar Stress – Slabs.....	179
Figure 6.9: Effect of Splice Length on Bar Stress (Unconfined).....	181
Figure 6.10: Effect of Splice Length on Actual Bar Stress.....	182
Figure 6.11: Effect of Splice Length on Actual Bar Stress (Confined 50 psi Beams)	183
Figure 6.12: Effect of Concrete Strength on Actual Bar Stress (Unconfined)	184
Figure 6.13: Effect of Concrete Strength on Bar Stress by Splice Length (Unconfined).....	185
Figure 6.14: Effect of Concrete Strength on Bar Stress (Confined)	187
Figure 6.15: Effect of Concrete Strength on Bar Stress (Confined).....	188
Figure 6.16: Representation of ρ_t	190
Figure 6.17: Effect of Transverse Reinforcement Ratio on Actual Bar Stress.....	191
Figure 6.18: Effect of Transverse Reinforcement Ratio on Normalized Bar Stress.....	193
Figure 6.19: Effect of Transverse Reinforcement Ratio on Steel Contribution to Bar Stress	194
Figure 6.20: Effect of Transverse Reinforcement Ratio on Normalized Steel Contribution to Bar Stress	196
Figure 6.21: Effect of Confinement Pressure on Actual Bar Stress	198
Figure 6.22: Effect of Confinement Pressure on Normalized Bar Stress	199
Figure 6.23: Effect of Total Transverse Reinforcement Ratio on Bar Stress, Grouped by Splice Length	202
Figure 6.24: Series VI Stirrup Configurations	203
Figure 6.25: Effect of Stirrup Configuration on Bar Stress	204
Figure 7.1: Distribution of Concrete Compressive Strength for Unconfined Database	206

Figure 7.2: Distribution of Bar Size for Unconfined Database	207
Figure 7.3: Distribution of Splice Length for Unconfined Database.....	208
Figure 7.4: Distribution of Splice-Length-to-Bar-Diameter Ratio for Unconfined Database	209
Figure 7.5: Distribution of Side-Cover-to-Bar-Diameter Ratio for Unconfined Database	210
Figure 7.6: Comparison of Cover Modification Terms c_{mod}	213
Figure 7.7: Equation Comparison for Bar Stress at Failure (Unconfined)	217
Figure 7.8: Equation Comparison for Calculated Bar Stress (Unconfined)	218
Figure 7.9: Equation Comparison for Concrete Strength (Unconfined).....	219
Figure 7.10: Equation Comparison for Splice Length over Bar Diameter (Unconfined).....	219
Figure 7.11: Equation Comparison for Side Cover over Bar Diameter (Unconfined)	219
Figure 7.12: Equation Comparison for Half Bar Spacing over Bar Diameter (Unconfined)	220
Figure 7.13: Equation Comparison for Bottom Cover over Bar Diameter (Unconfined)	220
Figure 7.14: Equation Comparison for Bar Diameter (Unconfined)	220
Figure 7.15: Distribution of Concrete Compressive Strength for Confined Database	222
Figure 7.16: Distribution of Bar Size for Confined Database	223
Figure 7.17: Distribution of Splice Length for Confined Database.....	224
Figure 7.18: Distribution of Splice-Length-to-Bar-Diameter Ratio for Confined Database	225
Figure 7.19: Distribution of Side-Cover-to-Bar-Diameter Ratio for Confined Database	226
Figure 7.20: Distribution of Total Transverse Reinforcement Area for Confined Database.....	227
Figure 7.21: Distribution of ρ_t for Confined Database	228
Figure 7.22: Nonlinear Bond Stress Distribution (Canbay and Frosch, 2005).....	229
Figure 7.23: Typical Model Regions	230
Figure 7.24: Potential Effective Confinement Models	231
Figure 7.25: Potential Ranges of k_{calc}	235
Figure 7.26: Trial 1 k_{test} vs. k_{calc}	237
Figure 7.27: Trial 2 k_{test} vs. k_{calc}	239
Figure 7.28: Normalized Steel Contribution to Bar Stress vs. Proposed Equation	242
Figure 7.29: Equation Comparison for Bar Stress at Failure (Confined)	246
Figure 7.30: Equation Comparison for Calculated Bar Stress (Confined)	247
Figure 7.31: Equation Comparison for Concrete Strength (Confined).....	248

Figure 7.32: Equation Comparison for Splice Length over Bar Diameter (Confined).....	248
Figure 7.33: Equation Comparison for Side Cover over Bar Diameter (Confined)	248
Figure 7.34: Equation Comparison for Half Bar Spacing over Bar Diameter (Confined)	249
Figure 7.35: Equation Comparison for Bottom Cover over Bar Diameter (Confined)	249
Figure 7.36: Equation Comparison for Bar Diameter (Confined)	249
Figure 7.37: Equation Comparison for Transverse Reinforcement Ratio (Confined).....	250
Figure 8.1: Proposed Effective Confinement Model	257
Figure 8.2: Total Effective Force from Transverse Reinforcement.....	258
Figure A.1: A1035 Gr. 100 No. 8 Longitudinal Bar (MMFX) Stress Strain Curve.....	270
Figure A.2: A615 Gr. 100 No. 8 Longitudinal Bar - Stress Strain Curve	271
Figure A.3: A615 Gr. 100 No. 5 Longitudinal Bar - Stress Strain Curve	272
Figure A.4: A615 Gr. 60 No. 3 Transverse Bar (Series VI) - Stress Strain Curve.....	273
Figure A.5: A615 Gr. 60 No. 3 Transverse Bar (Series VII) - Stress Strain Curve.....	274
Figure B.1: Slab Splice Region Layout for As-Built Dimensions.....	275
Figure C.1: S-40-5	279
Figure C.2: S-60-5	280
Figure C.3: S-80-5	281
Figure C.4: S-100-5	282
Figure C.5: U-40-5-X.....	283
Figure C.6: U-60-5-X.....	284
Figure C.7: U-50-5.....	285
Figure C.8: U-40-10.....	286
Figure C.9: U-60-10.....	287
Figure C.10: C3/60/2-40-10-25	288
Figure C.11: C3/60/2-40-10-50	289
Figure C.12: C3/60/3-40-10-50	290
Figure C.13: C3/60-40-5-150.....	291

Figure C.14: C3/60-40-5-200.....	292
Figure C.15: C3/60-50-5-150.....	293
Figure C.16: C3/60-50-5-200.....	294
Figure C.17: C3/60-50-5-200.....	311
Figure D.1: Typical Specimen Crack Monitoring Diagram	295
Figure D.2: S-40-5	296
Figure D.3: S-60-5	297
Figure D.4: S-80-5	298
Figure D.5: S-100-5	299
Figure D.6: U-40-5-X	300
Figure D.7: U-60-5-X	301
Figure D.8: U-50-5.....	302
Figure D.9: U-40-10.....	303
Figure D.10: U-60-10.....	304
Figure D.11: C3/60/2-40-10-25	305
Figure D.12: C3/60/2-40-10-50	306
Figure D.13: C3/60/3-40-10-50	307
Figure D.14: C3/60-40-5-150	308
Figure D.15: C3/60-40-5-200	309
Figure D.16: C3/60-50-5-150	310
Figure E.1: Beam Splice Region Layout for As-Built Dimensions.....	312

LIST OF TABLES

Table 2.1: Slab Testing Matrix	44
Table 2.2: General Slab Casting Information	45
Table 2.3: Normal-Strength Concrete – Mix Design Summary (Series V)	45
Table 2.4: Series V Compression and Tension Properties.....	47
Table 2.5: Series V Stress-Strain Properties	51
Table 2.6: Reinforcing Steel Bar Information	51
Table 2.7: Material Properties of Series V Steel.....	52
Table 3.1: Slab Test Results.....	73
Table 3.2: Test Results for Series V Bond Failures.....	84
Table 3.3: Test Results for Series V Flexural Failures	88
Table 4.1: Nominal Confinement Pressure and Spacing	94
Table 4.2: Unconfined Beam Testing Matrix	96
Table 4.3: Confined Beam Testing Matrix	97
Table 4.4: General Beam Casting Information	99
Table 4.5: Normal-Strength Concrete – Mix Design Summary (Series VI and VII)	100
Table 4.6: High-Strength Concrete – Mix Design Summary (Series VI).....	101
Table 4.7: Series VI Truck 1 Compression and Tension Properties.....	102
Table 4.8: Series VI Truck 2 Compression and Tension Properties.....	103
Table 4.9: Series VI Truck 3 Compression and Tension Properties.....	103
Table 4.10: Series VII Compression and Tension Properties	103
Table 4.11: Series VI Truck 1 Stress-Strain Properties	106
Table 4.12: Series VI Truck 2 Stress-Strain Properties	106
Table 4.13: Series VI Truck 3 Stress-Strain Properties	106
Table 4.14: Series VII Stress-Strain Properties	106
Table 4.15: Reinforcing Steel Bar Information	107
Table 4.16: ASTM A615 Material Properties.....	109
Table 4.17: ASTM A1035 Material Properties.....	111
Table 5.1: Beam Test Results	133

Table 5.2: Test Results for Unconfined Beams	145
Table 5.3: Test Results for Confined Beams	148
Table 6.1: f_{calc} Stress Comparison with Various Analytical Methods	175
Table 6.2: Statistical Analysis of f_{test}/f_{calc} for Various Analytical Methods	176
Table 6.3: Experimental Results from Glucksman (2018) and Fleet (2019)	178
Table 6.4: Effect of High-Strength Concrete for $40d_b$ and $60d_b$ Specimens	186
Table 7.1: Cover Modification Terms	212
Table 7.2: Statistical Analysis of f_{test}/f_{trial} in Cover Modifier Equations	214
Table 7.3: Statistical Analysis Comparison of f_{test}/f_{calc} for Unconfined Beams	216
Table 7.4: Trial Model Region Dimensions	230
Table 7.5: Model Boundaries	234
Table 7.6: Effective Confinement Test Specimens	236
Table 7.7: Statistical Analysis Comparison of f_{test}/f_{calc} for Confined Beams	245
 Table B.1: Slab Design Dimensions	 275
Table B.2: S-40-5	276
Table B.3: S-60-5	276
Table B.4: S-80-5	276
Table B.5: S-100-5	277
 Table C.1: S-40-5 Maximum Testing Values	 279
Table C.2: S-60-5 Maximum Testing Values	280
Table C.3: S-80-5 Maximum Testing Values	281
Table C.4: S-100-5 Maximum Testing Values	282
Table C.5: U-40-5-X Maximum Testing Values	283
Table C.6: U-60-5-X Maximum Testing Values	284
Table C.7: U-50-5 Maximum Testing Values	285
Table C.8: U-40-10 Maximum Testing Values	286
Table C.9: U-60-10 Maximum Testing Values	287
Table C.10: C3/60/2-40-10-25 Maximum Testing Values	288

Table C.11: C3/60/2-40-10-50 Maximum Testing Values	289
Table C.12: C3/60/3-40-10-50 Maximum Testing Values	290
Table C.13: C3/60-40-5-150 Maximum Testing Values	291
Table C.14: C3/60-40-5-200 Maximum Testing Values	292
Table C.15: C3/60-50-5-150 Maximum Testing Values	293
Table C.16: C3/60-50-5-200 Maximum Testing Values	294
Table D.1: S-40-5 Crack Width Summary	296
Table D.2: S-60-5 Crack Width Summary	297
Table D.3: S-80-5 Crack Width Summary	298
Table D.4: S-100-5 Crack Width Summary	299
Table D.5: U-40-5-X Crack Width Summary.....	300
Table D.6: U-60-5-X Crack Width Summary.....	301
Table D.7: U-50-5 Crack Width Summary.....	302
Table D.8: U-40-10 Crack Width Summary.....	303
Table D.9: U-60-10 Crack Width Summary.....	304
Table D.10: C3/60/2-40-10-25 Crack Width Summary	305
Table D.11: C3/60/2-40-10-50 Crack Width Summary	306
Table D.12: C3/60/3-40-10-50 Crack Width Summary	307
Table D.13: C3/60-40-5-150 Crack Width Summary.....	308
Table D.14: C3/60-40-5-200 Crack Width Summary.....	309
Table D.15: C3/60-50-5-150 Crack Width Summary.....	310
Table D.16: C3/60-50-5-200 Crack Width Summary.....	311
Table E.1: Beam Design Dimensions	312
Table E.2: U-40-5-X	313
Table E.3: U-60-5-X	313
Table E.4: U-50-5	313
Table E.5: U-40-10	314
Table E.6: U-60-10	314

Table E.7: C3/60/2-40-10-25	314
Table E.8: C3/60/2-40-10-50	315
Table E.9: C3/60/3-40-10-50	315
Table E.10: C3/60-40-5-150	315
Table E.11: C3/60-40-5-200	316
Table E.12: C3/60-50-5-150	316
Table E.13: C3/60-50-5-200	316
Table F.1: Summary of Unconfined Lap-Splice Specimen Database	317
Table F.2: Summary of Confined Lap-Splice Specimen Database	318

ABSTRACT

Author: Fleet, Eric, T. MSCE

Institution: Purdue University

Degree Received: May 2019

Title: Effective Confinement and Bond Strength of Grade 100 Reinforcement

Committee Chair: Robert J. Frosch

The primary reinforcement used for construction of structural concrete members has a yield strength of 60 ksi. This reinforcement grade was incorporated into construction over 50 years ago and remains the standard. Recent advances in material technology have led to the development of commercially available reinforcing steel with yield strengths of 100 ksi. While greater yield strengths can be utilized in design, it is essential that the bars can be properly anchored and spliced to fully develop their strength. Although design expressions are available for this purpose, they were established considering 60 ksi reinforcement. Therefore, the objective of this research program is to evaluate the development of high-strength reinforcing steel and establish a design expression for the development and splicing of this steel. Two phases of experimental tests were conducted. Phase I was performed by Glucksman (2018) and investigated the influence of splice length and transverse reinforcement on bond strength over four series of beam tests. This study (Phase II) was conducted following Phase I and consisted of reinforced concrete slab and beam testing over three series. An investigation was conducted on reinforcement development with a focus on the effect of splice length, concrete compressive strength, stress-strain relationships of the steel (ASTM A615 vs. ASTM A1035), and transverse reinforcement. Based on the results, the influences of test variables were identified, and a new confinement model was developed that estimates the transverse reinforcement contribution to bond strength. Finally, a design expression is provided for calculating the development and splice lengths of high-strength reinforcement.

CHAPTER 1. INTRODUCTION

1.1 Background

The primary reinforcement used in structural concrete members in construction has maintained a standard yield strength of 60 ksi for over 50 years. Advances in material technology have led to the development of commercially available reinforcing steel with yield strengths of 100 ksi. While greater yield strengths can be utilized in design, it is essential that the bars can be properly anchored and spliced to fully develop their strength. Although design expressions are available for this purpose, they were established considering 60 ksi reinforcement. To ensure safety and reliability in the use of high-strength reinforcement, bond development to achieve the higher stresses required by this reinforcement must be evaluated. In fact, the Applied Technology Council (ATC 115) provided a roadmap for the adoption of high-strength reinforcement indicating investigation of bar development as a vital need.

1.2 Bond Design

The bond strength equation that was adopted by ACI Building Code (ACI 318) has origins in nonlinear regression analysis research of Orangun, Jirsa, and Breen (1977). Over 100 splice beam tests were analyzed to isolate the effect of numerous factors on bond strength, resulting in an expression for the average bond stress accumulated across the splice. At the time of development, the primary reinforcing steel included in the test results was Grade 60. Furthermore, limited tests with high-strength concrete were available. Based on these limitations, the ACI building code limits the yield strength to 80 ksi and the compressive strength to 10,000 psi. While these limits are in the code, use beyond Grade 60 has not been widespread as only Grade 60 steel is in common use.

1.3 Bond Mechanics

1.3.1 Force Transfer Mechanisms

Bond forces at the interface between reinforcing bars and the surrounding concrete are transferred primarily through three (3) physical mechanisms during tensile loading: chemical adhesion, friction forces, and anchorage bearing. The three mechanisms are illustrated in Figure 1.1 for a typical section along the length of a deformed reinforcing bar embedded in concrete.

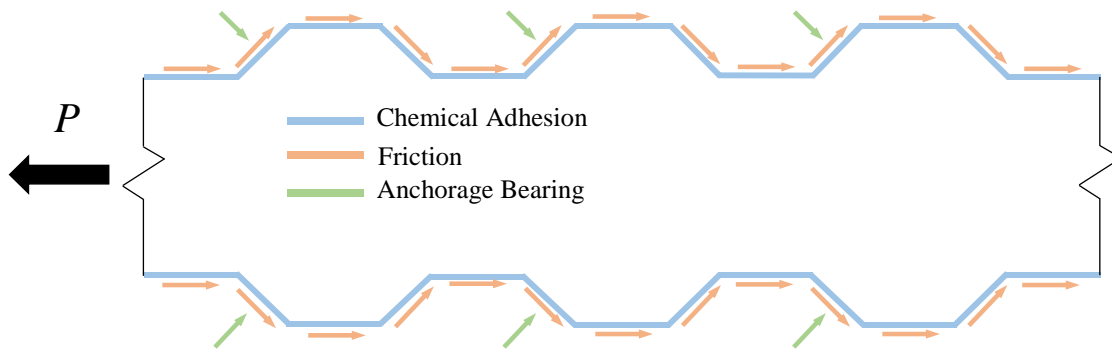


Figure 1.1: Bond Force Transfer Mechanisms

Chemical adhesion forms at the molecular level when the concrete begins curing around the embedded reinforcing bars. This mechanism exists under low stress levels, and the composite action created by adhesion contributes to the initial stiffness of the member (Lutz and Gergely 1967).

Once adhesion is lost due to initial slip of the reinforcing bar in the concrete, the other two mechanisms are responsible for transferring bond forces. Friction forces exist in the direction of the longitudinal bar axis on its surface and become activated once the bar has slipped. Because the surface has a nonzero coefficient of friction, the force increases with an increase in bar

roughness. Typical mill scale or light rust on the reinforcing bars, for example, will produce a higher bond resistance than clean bars (Abrams 1913).

As the reinforcing bar continues to slip within the concrete, the interstitial space between the concrete and the bar slowly widens. Friction forces along the bar surface decrease, leaving bearing between the bar deformations and the concrete as the primary bond transfer mechanism. Bar deformations provide surface area transverse to the axis of the bar that allows stresses to develop in a different plane than the friction stresses. In addition to the effects of surface friction, this mechanical interlock between the deformations and the concrete engages both materials and effectively transfers bond forces through wedging action (Eligehausen et al. 1983).

Concrete near the front of each rib can crush, resulting in small internal cracks near the bar surface. Due to bearing and compressive stresses that accumulate on the front faces of the bar deformations, splitting cracks propagate through the concrete (Eligehausen et al. 1983).

1.3.2 Stress Formation

As a reinforced concrete member is loaded, stresses are developed along the interface between the bar and concrete. Cracking planes are formed longitudinal to the bar axis and radially to its surface, resulting in internal cracking that propagates through the concrete as stresses increase.

To understand the formation of tensile cracking, a plane stress transformation may be implemented using Mohr's Circle. For simplicity, the angle of all lugs on a typical reinforcing bar is assumed to be 45° . As the reinforcing bar resists tension, concrete between the ribs experiences a resultant compressive stress from bearing in addition to shear stress from friction along the interface. A typical concrete element near the deformed bar surface is shown in Figure 1.2.

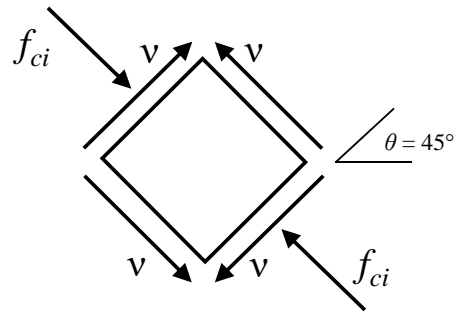
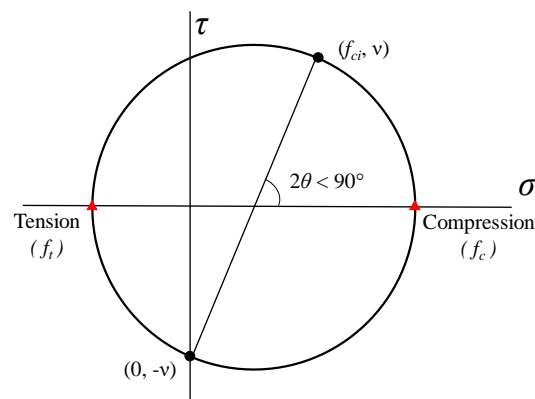
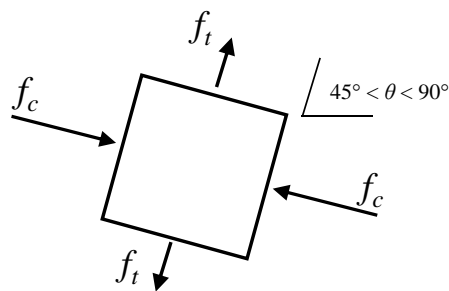


Figure 1.2: Initial Stresses on a Typical Concrete Element

A plane stress transformation on a typical element using Mohr's circle is shown in Figure 1.3(a). The transformation results in a principal tensile stress that is smaller than the principal compressive stress developed as shown in Figure 1.3(b).



(a) Stress Transformation using Mohr's Circle



(b) Resolved Stresses

Figure 1.3: Concrete Stress Resolution

Internal cracking results from the principal tensile stresses near the deformations around the bar. Subsequently, regions of crushed concrete can form between the bar deformations from the principal compressive stress. The general propagation of internal cracks is shown in Figure 1.4 for the longitudinal direction. Additionally, stresses propagate radially outward from the bars and allow tensile splitting cracks to form across both planes transverse to the bars (Figure 1.5). As the tensile splitting cracks travel through the member width and depth, a splitting plane forms and can initiate a splitting failure.

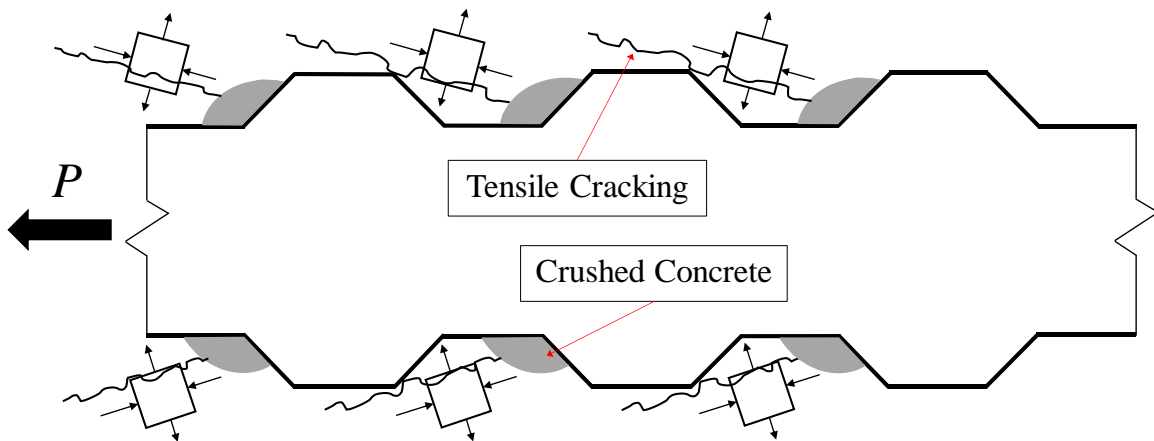


Figure 1.4: Internal Crack Formations

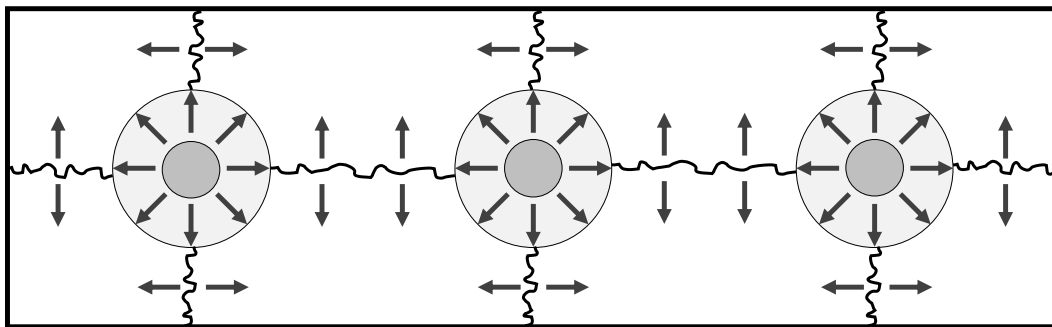


Figure 1.5: Radial Stress Distribution

1.3.3 Bond Failure

Bond failures occur through one of two possible modes: splitting of the concrete cover along the splice length, or bar pullout.

1.3.3.1 *Splitting*

The most common type of bond failure in splice specimens is a splitting failure. Figure 1.6 provides examples of splitting failures in different test specimens. In this failure mode, either sufficient cover or confinement is not provided such that the cover around the splice splits off.



(a) Unconfined Specimen



(b) Slab Specimen



(c) Confined Specimen

Figure 1.6: Splitting Failures

1.3.3.2 Pullout

Tests conducted by Abrams (1913) showed that bond is affected by bar surface. A pullout failure is more likely to occur under the presence of smooth longitudinal bars due to the absence of the anchorage bearing mechanism found when deformed bars are used. For smooth bars, only chemical adhesion and friction resist the tension force. Furthermore, due to Poisson's effect, the bar surface area available for resisting forces by friction decreases with increasing load.

The presence of a bar pullout failure can be readily identified. Splitting cracks do not propagate in members that experience a pullout failure (Pay 2005). In this mode, the bars simply pull out of the concrete, developing one large crack when the bars slide out as shown in Figure 1.7. Pullout failures can also occur with deformed bars. If sufficient confinement or cover is provided to preclude a splitting failure, the bar deformations can shear the concrete between the lugs resulting in a pullout of the bar.

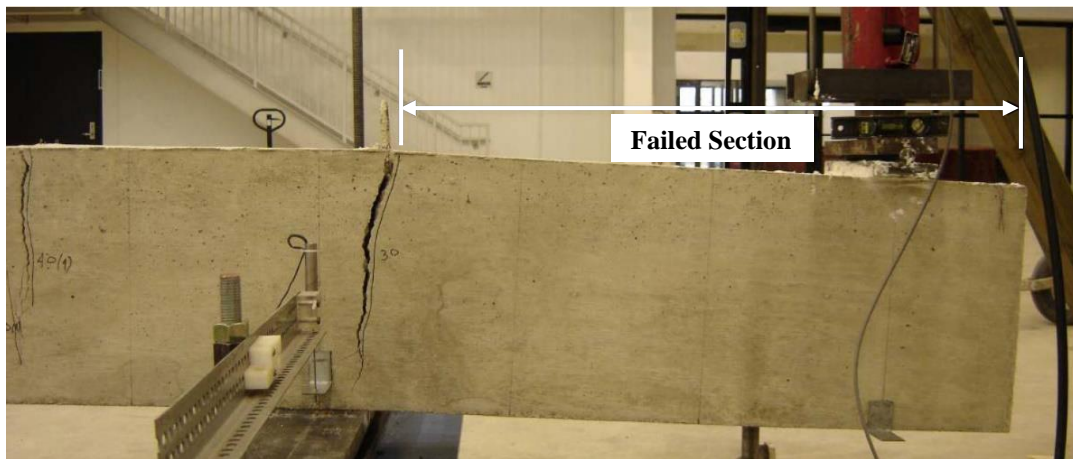


Figure 1.7: B-PG2-5-24 Bar Pullout Failure (Pay 2005)

1.4 Bond Variables

A number of parameters are considered to have a significant influence on bond strength including splice length, concrete compressive strength, bar spacing, cover, and transverse reinforcement. The type, size, casting position, surface properties, and rigidity of the spliced bars have also been found to influence bond strength.

1.4.1 Splice Length

Several studies have been conducted that investigate the effect of splice length on bond strength in reinforced concrete. The origins of the development length equation in ACI 318 are based on research conducted to investigate the influence of this variable. It has been found that there is a strong correlation between splice length and developed bar stress. As the splice length increases, bond strength and therefore bar stress increase.

Mathey and Watstein (1961) found the relationship between splice length and bar stress to be nonlinear. As splice length increased, the unit strength gain decreased. This finding was based on experimental testing with relatively short splice lengths up to $40d_b$. Results from Glucksman (2018) support these findings and expand them to splice lengths of $120d_b$; therefore, for longer splice lengths, the effectiveness of the increase in anchorage length is lower when compared to shorter splices. Chinn, Ferguson, and Thompson (1955) also supported the notion that an increase in bond strength is not directly proportional to an increase in splice length. Azizinamini et al. (1993) found that the nonlinear relationship between splice length and bond strength also holds true regardless of concrete strength. Recent testing has also shown that this trend is independent of bar type. Nonlinearity in splice length and bond strength was observed when using fiber reinforced polymer (FRP) reinforcing bars (Pay 2005).

The relationship between splice length and bond strength was found to be proportional to the square root of the splice length to bar diameter ratio ($\sqrt{l_s/d_b}$) by Canbay and Frosch (2005). Findings from Seliem, Hosny, and Rizkalla (2009) support the notion that bond strength is proportional to the square root of the splice-length-to-bar-diameter ratio. Additionally, tests conducted by Richter (2012) support that achieving a higher bond strength by increasing splice length is inefficient because bond stress distribution across long splice regions causes the additional contribution from larger embedment to be less effective in increasing bond strength.

1.4.2 Concrete Compressive Strength

The contribution of concrete compressive strength on bond strength has commonly been represented by the square root, $\sqrt{f'_c}$. This has been supported by experimental testing in a number of research programs (Ferguson and Thompson 1962, Tepfers 1973, Orangun et al. 1977, Darwin et al. 1992, Esfahani and Rangan 1998).

Later testing has shown that this representation is less accurate for concrete with higher compressive strengths. The square root has been shown to provide a reasonable representation for values of f'_c below 8000 psi, but tests conducted by Azizinamini et al. (1993) and Zuo and Darwin (1998) show that this trend deviates for concrete with higher compressive strengths. Azizinamini et al. (1993) noted that higher-strength concrete behaves differently than normal-strength concrete. Less crushing occurs at the bar deformations. It was observed that a reduction in bar slip causes less stress to be transferred between the steel bars and the concrete, ultimately increasing tensile stresses around the bars and increasing the likelihood of causing a splitting failure. Continued testing of high-strength concrete was conducted by Esfahani and Rangan (1998) where it was observed that no crushing was present in tests with concrete strengths greater than 11,000 psi.

Recent studies have investigated a different representation of concrete compressive strength. The quarter root, $\sqrt[4]{f'_c}$, has been shown to provide a more accurate representation of the relationship between concrete strength and developed reinforcement strength (Darwin et al. 1996, Zuo and Darwin 2000). Canbay and Frosch (2005) analyzed a total of 203 unconfined beams with f'_c ranging from 2600 psi to 15,600 psi and concluded that the use of the quarter root provided a better prediction of spliced bar strength as compared to the use of the square root.

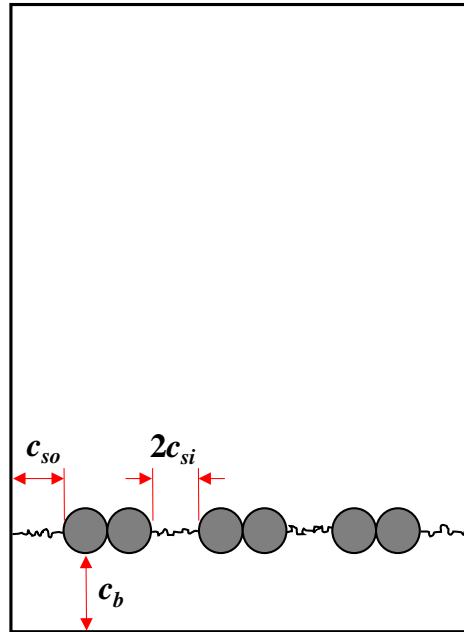
When transverse reinforcement is present, Zuo and Darwin (1998, 2000) found that a power of 0.75 is more appropriate for representing the effect of concrete strength on bond capacity. In their analytical investigation, a trend was nearly nonexistent when comparing test-to-prediction ratios. Canbay and Frosch (2005) analyzed a total of 278 confined beams and found that the use of the quarter root provides a better prediction of confined spliced bar strength when compared to other powers.

1.4.3 Bar Spacing and Cover

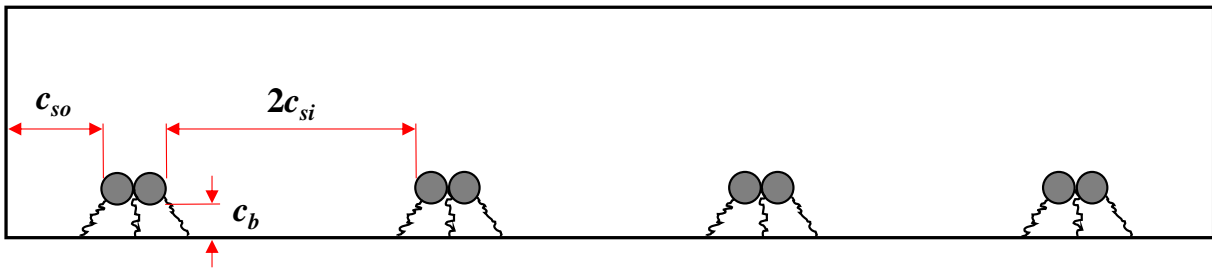
When investigating the effects of surrounding concrete on lap splices, three (3) dimensions are typically considered: the concrete side cover (c_{so}), the bottom cover (c_b), and half the inner clear distance between spliced bars (c_{si}), which is based on bar spacing. These represent the concrete directly surrounding the spliced bars in all critical directions and are shown in Figure 1.8. From previous testing by Chamberlin (1958) and Chinn et al. (1955), it was determined that an increase in longitudinal bar spacing results in higher bar stresses. When splices are confined with transverse reinforcing steel, Zuo and Darwin (1998) found that the influence of bar spacing on bond capacity was smaller based on tests of 245 confined specimens. The presence of the transverse reinforcement increased bond strength more than increasing the bar clear spacing.

Chinn et al. (1955) found that bond strength of spliced bars increases as the bottom cover increases. Ferguson and Thompson (1962) observed that as the diameter of spliced bars increases for a constant cover, the rate of increase in bond capacity decreases. This finding was confirmed by Sim (2014) after testing various covers in specimens with No. 5 and No. 6 spliced bars. Orangun, Jirsa, and Breen (1977) initially found that although the minimum of bottom cover, side cover, and bar spacing is important in determining the type of failure mode, the value of c_{so}/d_b or c_{si}/d_b has a stronger correlation to the stress achieved in the longitudinal reinforcement, as long as this ratio is less than three or four. Orangun et al. (1977) also observed that as side cover or inner bar spacing increased, bond capacity increased. Thompson et al. (1975) found that bond strength can be improved by increasing the ratio of side cover to bar spacing. Tests showed that a 10% increase in bond strength could be achieved by increasing the ratio of side cover to bar spacing.

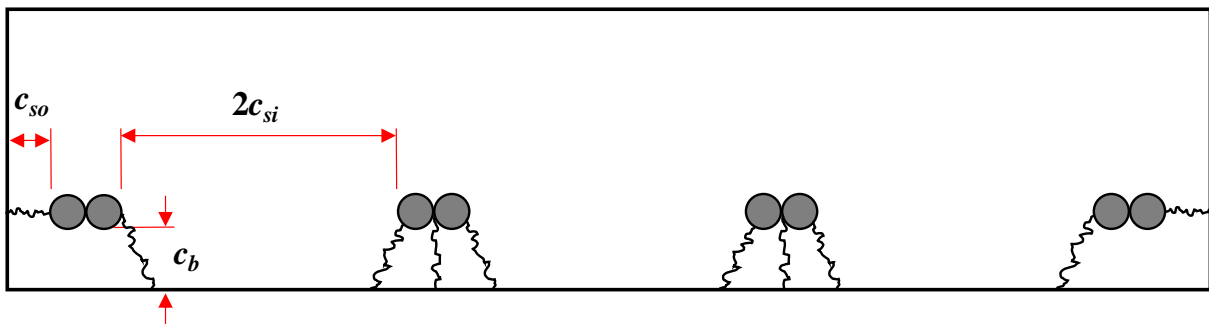
Studies by Tepfers (1973) indicated that the type of splitting failure depends on the concrete surrounding the spliced bars. If c_{so} or c_{si} is smaller than c_b for a given member, splitting cracks will form across the splice plane as indicated in Figure 1.8(a). If c_b is smaller than c_{so} and c_{si} , face-splitting will control along the tension face directly above the spliced bars as shown in Figure 1.8(b). Results by Sim (2014) found that the initiation of side-splitting is primarily dependent on bar spacing, while face-splitting is a function of face cover. A face- and side-splitting combination mechanism can occur if the bar spacing is large while the bottom and side covers are small (similar to the face-splitting conditions). In this case, the interior splices will experience a face-splitting failure while the outside two splices experience face-splitting and side-splitting as shown in Figure 1.8(c).



(a) Side-Splitting



(b) Face-Splitting



(c) Face- and Side-Splitting

Figure 1.8: Types of Splitting Failure Modes

1.4.4 Transverse Reinforcement

The use of transverse reinforcement to confine the splice region is known to improve bond strength. Chinn, Ferguson, and Thompson (1955) observed that the use of ties around the splice region increased bond strength by almost 50%. Ferguson and Breen (1965) observed a similar outcome when conducting tests with varying amounts of confinement steel within the splice region. Bond capacities were increased by 20% when the minimum number of stirrups was present ($\rho_t = 0.15\%$) and up to 50% when ρ_t was increased to 1.23%.

Stirrups have been shown to slow the progression of splitting cracks and increase the force required to initiate failure of the splice (Orangun, Jirsa, and Breen 1977, Seliem et al. 2009). Transverse steel crosses the plane of side-splitting, allowing the steel to resist these splitting stresses and delay bond failure. This effect of transverse reinforcement was discussed by Thompson et al. (1975) who observed that tension was resisted by the transverse steel after cracking and up until failure. Rezansoff, Konkankar, and Fu (1992) showed that the contribution to bond strength provided by confining stirrups is greater than the contribution of increasing concrete cover on an unconfined section. Additionally, Seliem et al. (2009) found that when confining steel was included in the splice region, high bond stresses were developed in specimens spliced with MMFX (ASTM A1035) high-strength reinforcing steel.

Another benefit of including transverse reinforcement in the splice region is added ductility. Morita and Fujii (1982) concluded that the primary purpose of confining stirrups is to maintain and ultimately increase ductility after cracking. Seliem et al. (2009) witnessed greater deformations before reaching failure in confined specimens. Thompson et al. (1975) found that the presence of transverse steel increases bond strength, and the number of splitting cracks on all faces decreases with increasing quantities of transverse reinforcement.

Orangun, Jirsa, and Breen (1977) determined that if the moment and bond capacity of the section is adequate, the failure mode switches from splitting to bar pullout when the amount of transverse reinforcement is increased. Once this failure mode is reached, any additional reinforcement becomes ineffective. Tests by Glucksman (2018) also indicate that increasing the amount of confinement within the splice region can create sufficient bond strength such that a flexural failure can develop (inadequate moment capacity).

The effectiveness of stirrups along the splice has also been analyzed. Thompson et al. (1975) found that the highest strains in the transverse steel across the confined splice region were observed in the stirrups closest to the splice ends. This supports the finding that bond stress is nonlinear across the embedded length and reaches a maximum at the ends (Canbay and Frosch 2005). Azizinamini et al. (1999) found that higher strains in the end stirrups of high-strength concrete beams can cause the transverse reinforcement to yield and potentially rupture. Stirrup configuration testing conducted by Sim (2014) explored the effect of the layout of stirrups across the splice region on bond strength when the total area of transverse reinforcement in the splitting plane remains constant. Sim (2014) found that stirrups placed in the middle of the splice region resulted in essentially no increase in bond strength; however, when stirrups were placed at the ends of the splice, bond strength was increased by either 20% or 30%, depending on splice length.

Glucksman (2018) found that specimens constructed with Grade 100 transverse reinforcement did not perform better than identical specimens constructed with Grade 60 transverse reinforcement, indicating that yield strength of transverse reinforcement greater than 60 ksi is not effective in providing additional bond strength.

1.5 High-Strength Steel

ASTM A615 “Standard Specification for Deformed and Plain Carbon-Steel Bars for Concrete Reinforcement” provides available steel grades of 40 ksi, 60 ksi, 75 ksi, 80 ksi, and 100 ksi. The two highest grades available, 80 ksi and 100 ksi, were recently added to the material standard in 2009 and 2015, respectively (ASTM A615). ASTM A1035 “Standard Specification for Deformed and Plain, Low-Carbon, Chromium, Steel Bars for Concrete Reinforcement” also provides for high-strength steel reinforcement. Commonly called MMFX (Martensitic Microcomposite Formable Steel), this high-strength steel is available in two designations that were added in 2004 and 2007, respectively: Grade 100 bars and Grade 120 bars (ASTM A1035).

The stress-strain responses between conventional A615 bars and A1035 MMFX bars differ outside of the linear-elastic region. The yield point is not well-defined for MMFX steel and does not plateau like traditional mild reinforcing steel. El-Hacha et al. (2006) conducted experimental tests on concrete specimens spliced with A1035 MMFX reinforcing bars and A615 Grade 60 reinforcing bars. It was observed that the response of these two types of beams was nearly identical within the linear-elastic range of the steel; however, once the proportional limit was reached, behaviors diverged. An observable change in the failure behavior of spliced concrete specimens with MMFX longitudinal reinforcement was described as exhibiting more ductile, gradual failures compared to the sudden brittle failures observed in the A615 specimens. Additional testing by Seliem et al. (2009) showed that the behavior of concrete members with spliced MMFX bars within the linear-elastic region is comparable to the behavior observed with conventional black bars.

Testing by El-Hacha et al. (2006) observed a nonlinear correlation to splice length when high-strength reinforcement was used, similar to previous studies with A615 bars (Chinn et al. 1955, Mathey and Watstein 1961, Canbay and Frosch 2005, Glucksman 2018). Seliem et al. (2009)

conducted testing that resulted in high stresses of up to 120 ksi in No. 5 A1035 MMFX bars for unconfined concrete specimens. Additionally, stresses of up to 150 ksi for No. 8 and No. 11 MMFX bars were achieved when transverse steel was present along the splice region.

Experimental tests with A1035 MMFX steel in bond have been more prevalent than A615 high-strength steel bars in the last two decades due to its availability. Test results of A615 high-strength reinforcement are not widely available in the literature as it has only recently become available.

1.6 Research Objective and Scope

The objective of this research program is to evaluate the development of high-strength reinforcing steel and establish a design expression for the development and splicing of this steel. Two phases of experimental tests were conducted. Phase I of this research program was conducted by Glucksman (2018) which investigated the influence of splice length and transverse reinforcement on bond strength, as well as the effectiveness of high-strength transverse reinforcement over four series of beam tests. Phase II of the research program is the focus of this study. Testing in Phase II complements the testing conducted in the first four series. Of specific interest in Phase II of research are the following:

1. Bar development in slabs. Slabs are of specific concern as they are unconfined and are constructed with small covers (0.75 in.)
2. Effect of high-strength concrete (10,000 psi)
3. Effect of different stress-strain relationships of the high-strength steel (ASTM A615 vs. ASTM A1035)
4. Effect of transverse reinforcement location

CHAPTER 2. EXPERIMENTAL PROGRAM: SLABS

2.1 Introduction

The objective of this series in Phase II was to investigate the development of high-strength reinforcement in slabs. Slabs are considered separately from beams due to several factors: (a) no transverse reinforcement is typically provided, (b) small covers ($3/4$ in.) are present, and (c) larger bar spacings are typical. This series of testing was named Series V as part of a larger testing program. Series V contained four reinforced concrete slab specimens. The program for planning, preparing, and conducting these tests is discussed in this chapter.

2.2 Specimen Selection

2.2.1 Slab Design

Series V was implemented to investigate the effect of splice length considering typical slab bar spacings and concrete cover. The rectangular cross-section consisted of a 6 in. thickness typical of building slabs. No. 5 longitudinal reinforcing bars were selected as they are typical in slabs. A minimum bottom cover of $3/4$ in. allowed for No. 5 bars in ACI 318-14 (Table 20.6.1.3.1) was selected for all slab specimens. Figure 2.1 shows the cross-section for all slabs in Series V.

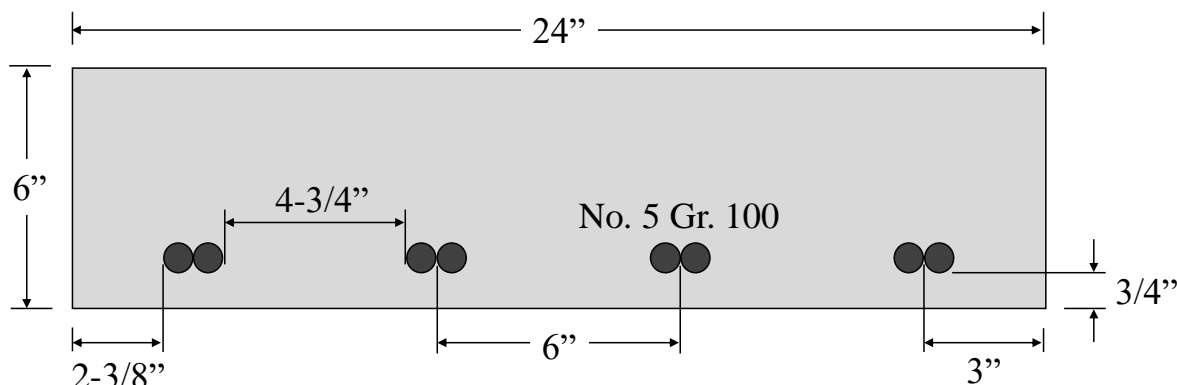


Figure 2.1: Typical Slab Cross-Section

In Series V, four No. 5 Grade 100 longitudinal bars were spliced over a variable distance, with the bar spacing set to 6 in. on-center. With this spacing, the clear bar spacing is 4-3/4 in. The side cover was set equal to half the clear bar spacing (2-3/8 in.). Based on the bar spacings, bar diameters, and cover, the overall slab width totaled 24 in. The primary labeling convention used for this test series indicates the specimen type, splice length, and target concrete strength. The identification convention implemented in Series V is provided in Figure 2.2.

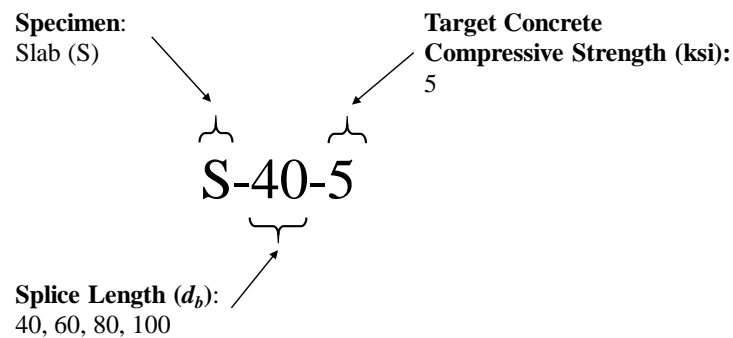


Figure 2.2: Slab Specimen Identification Label

2.2.2 Slab Dimensions

Splice test specimens from previous research programs have been tested in four-point bending to create a tension region at the location of the spliced bars. This four-point bending test setup requires two points of applied loading near the ends of the specimens and two points of support located a distance away from the applied loads (shear span). Due to the 24 in. spacing of the Bowen Laboratory strong floor grid and the need for a symmetric test setup, even dimensions were selected for the spacings between components of the test setup.

A maximum splice length of $100d_b$ (62.5 in.) was selected for Series V slab testing, which directly influenced the size of the constant moment region. A constant moment length of 10 ft

(L_M) was maintained between supports for all slabs to accommodate this length. The length of the shear region was selected to be 4 ft (L_V) away from the supports. No transverse reinforcement was required in the shear span considering the shear required to produce a flexural failure. An additional 2 ft overhang (L_O) was included to ensure anchorage of the reinforcement. Overall, the selected dimensions led to a total length of 22 ft (L_T) for all specimens. The slab test configuration is shown in Figure 2.3.

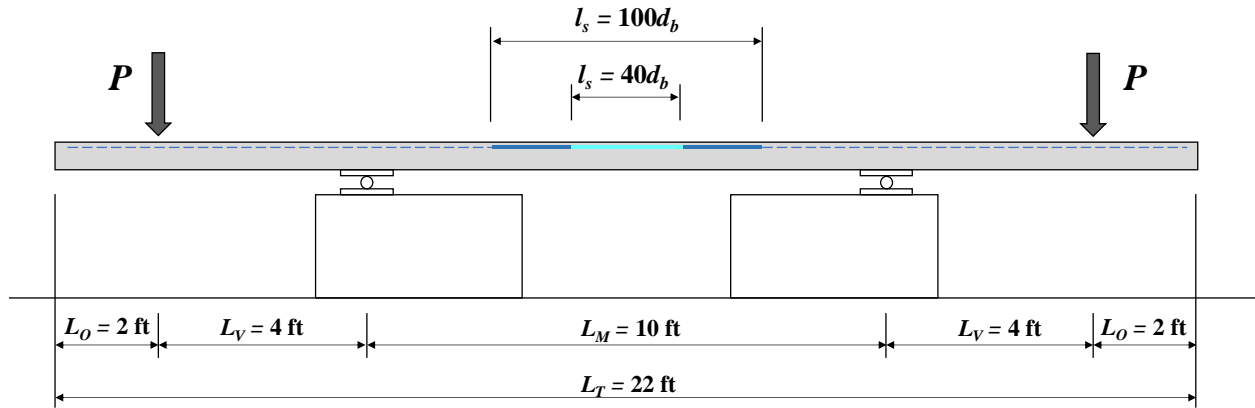


Figure 2.3: Typical Slab Test Specimen

2.2.3 Slab Testing Matrix

Table 2.1 provides the testing matrix for all slab specimens. The splice length is the primary variable, while the cover and bar spacing are fixed. A target concrete compressive strength of 5 ksi was selected based on typical slab design.

Table 2.1: Slab Testing Matrix

Series	Specimen ID	Splice Length (l_s)		Longitudinal Bar Size (No.)	Target Concrete Strength (f'_c)	$\frac{1}{2}$ Bar Clear Spacing (c_{si})	Side Cover (c_{so})	Bottom Cover (c_b)
		d_b	in.		ksi	in.	in.	in.
V	S-40-5	40	25	5	5	2.375	2.375	0.75
	S-60-5	60	37.5	5	5	2.375	2.375	0.75
	S-80-5	80	50	5	5	2.375	2.375	0.75
	S-100-5	100	62.5	5	5	2.375	2.375	0.75

2.3 Materials

2.3.1 Concrete

Concrete for Series V was provided by Irving Materials, Inc. (IMI), a local ready-mix concrete supplier with a distribution plant less than one mile away from the casting location. All test specimens were constructed and cast in the Bowen Laboratory for Large-Scale Civil Engineering Research in West Lafayette, Indiana.

The concrete mixture design selected for Series V was consistent with testing conducted in Phase I of this project. The concrete had a target compressive strength of 5000 psi and a target slump of 6 in. A breakdown of general casting information for Series V is provided in Table 2.2, and the mix design is provided in Table 2.3 with the batched quantities.

Table 2.2: General Slab Casting Information

Casting Quantities	Series V
Cast Date	4/16/2018
Truck No.	1
Load Size (yd ³)	4
Specimens	S-40-5 S-60-5 S-80-5 S-100-5

Table 2.3: Normal-Strength Concrete – Mix Design Summary (Series V)

Material	Type	Mix Design 4101CC	Batched
Cement	ASTM C150 - Type I (lb/yd ³)	517	519
Course Aggregate	#8 Limestone (lb/yd ³)	1875	1875
Fine Aggregate	#23 Natural Sand (lb/yd ³)	1475	1540
Water-Reducing Admixture	MasterGlenium 7511 (oz/yd ³)	20.7	20.3
Water (lb/yd ³)		250	246
Water/Cement Ratio		0.483	0.475
Slump (in.)		6.0	6.0

2.3.1.1 Concrete Testing

In Series V of this testing program, mechanical properties of the concrete were determined using an ASTM C193 standard cylinder size of 6 x 12 in. Before cylinder testing began, each cylinder was marked with a label indicating series, truck number, designated test, and cylinder number for that test. Figure 2.4 shows an example of the identification label and explains the designations used in this testing program.

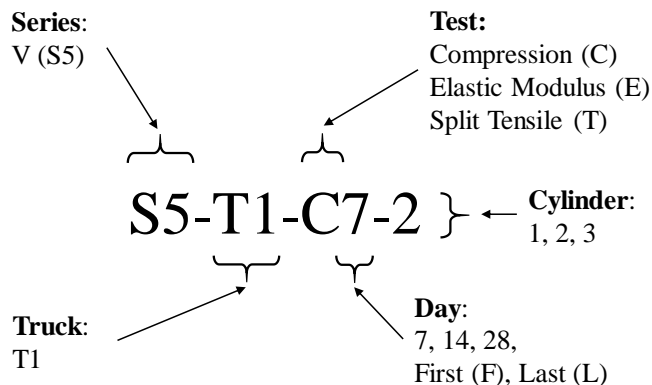


Figure 2.4: Cylinder Testing Identification

2.3.1.2 Compression Testing

To determine the increase in concrete compressive strength as curing took place, several cylinders were tested to failure. This required three (3) cylinders to be tested on days 7, 14, and 28, in addition to the first and last day of specimen testing. The cylinders were placed in a 600-kip Forney compression testing machine with a CA-0396 automatic control system interface. Nominal cylinder diameter and height dimensions were measured with a Fowler 12 in. Dial Caliper and recorded based on the “Standard Test Method for Compressive Strength of Cylindrical Concrete Specimens” in ASTM C39 (2018).

Steel caps lined with a neoprene elastomeric pad were installed on the top and bottom faces of the cylinder to ensure uniform distribution of the compression load and to reduce the chances of edge spalling. Two (2) standard 60-durometer pads were selected for all cylinder testing in Series V consistent with the target compressive strength of the concrete mix. The outer surfaces of the neoprene pads were lined with a polysaccharide powder to prevent frictional forces. With the loading platen installed, the capped cylinder was placed in the machine. The control system was set to a loading rate of 35 psi/s in accordance with ASTM C39 (2018). Once the loading cycle

was completed, compressive strength values were recorded and averaged in Table 2.4. A typical compression cylinder test setup before and after failure is shown in Figure 2.5(a) and Figure 2.5(b), respectively. Average concrete compressive strength, f_c , over time is plotted in Figure 2.6 for Series V. It should be noted that Specimen S-100-5 was tested at 102 days. Concrete cylinders were not available for this test; therefore, results are not available and can only be estimated based on previous strength gains for this mix design.

Table 2.4: Series V Compression and Tension Properties

Time (days)	Compressive Strength, f_c (psi)				Fracture Pattern (ASTM C39)			Split Tensile Strength, f_t (psi)			
	Cylinders			Avg.	Cylinders			Cylinders			Avg.
	1	2	3		1	2	3	1	2	3	
7	4680	4870	4690	4780	4	3	3	-	-	-	-
14	5960	5950	5830	5910	4	2	5	-	-	-	-
28	6260	6030	6230	6170	4	2	5	540	525	525	530
38 ^[1]	6170	5960	6400	6180	1	4	4	510	450	570	510
44 ^[2]	6130	6290	6290	6240	2	4	4	470	565	435	490
102 ^[3]	-	-	-	(6490)	-	-	-	-	-	-	-

[1] First Day of Testing

[2] Last Day of Testing

[3] Day 102 average strength was estimated by linear interpolation of strengths on Day 28 and Day 44

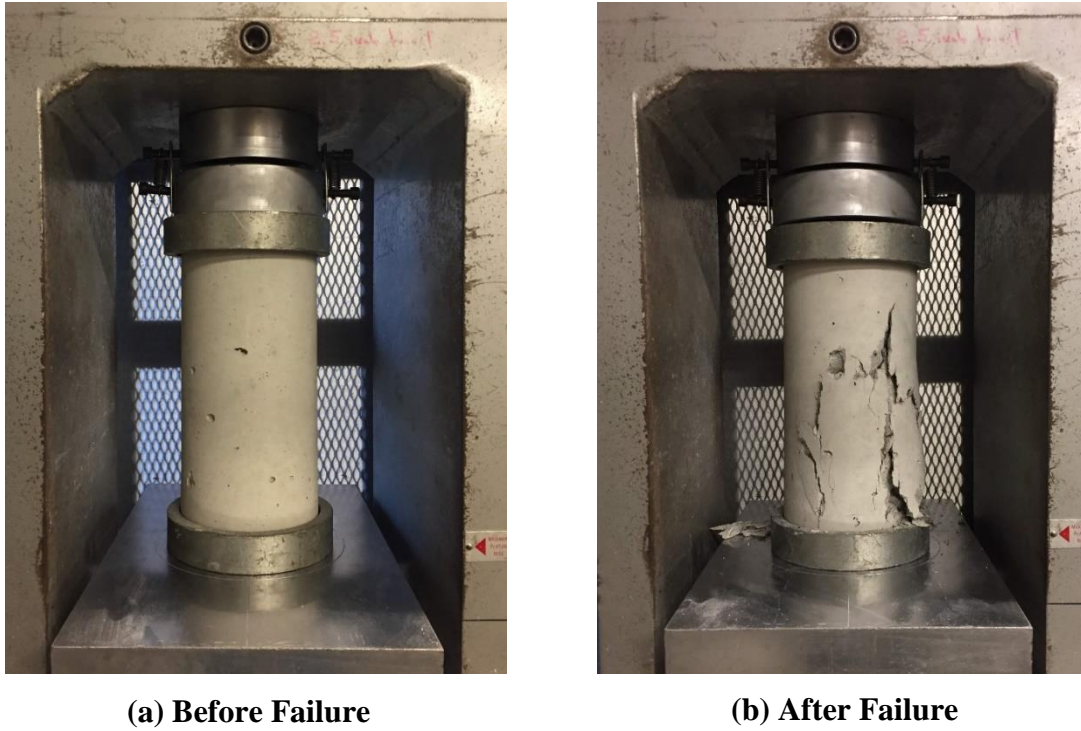


Figure 2.5: Typical Compression Cylinder Failure

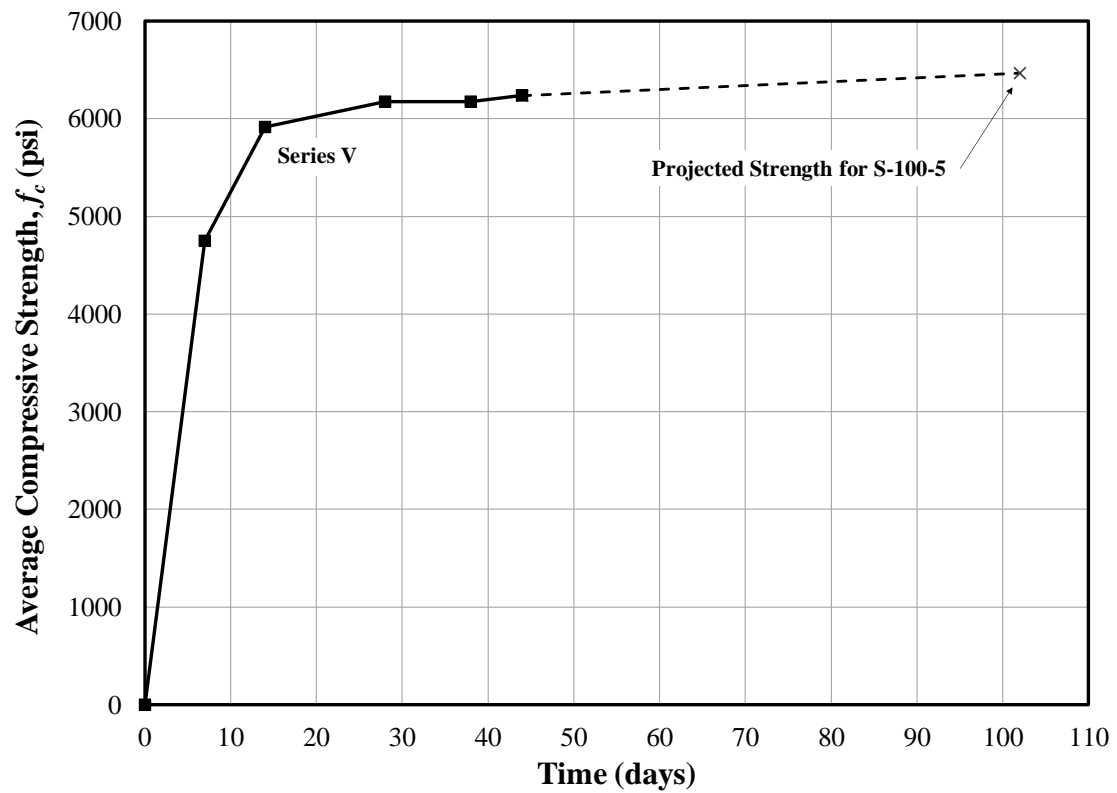


Figure 2.6: Concrete Compressive Strength Variation Over Time

2.3.1.3 Split Cylinder Testing

Split cylinder testing was conducted in accordance with ASTM C496 (2017). Diametrical lines were drawn and measured on each face of the 6 x 12 in. cylinder to assist in test alignment. A split cylinder loading jig was installed before placing the cylinder in the Forney testing machine between two 1/8 x 1 in. plywood bearing strips each approximately 13 in. long. Testing commenced at a loading rate of 2.5 psi/s in accordance with the range permitted by ASTM C496 (2017). Tensile strengths were recorded and averaged in Table 2.4. A typical splitting tensile test setup before and after failure is shown in Figure 2.7(a) and Figure 2.7(b), respectively.



(a) Before Failure



(b) After Failure

Figure 2.7: Series V Splitting Tensile Cylinder Failure

2.3.1.4 Elastic Modulus and Poisson's Ratio

Young's modulus and Poisson's ratio were also determined. These properties were tested by mounting a compressometer built with two linear variable differential transformers (LVDT) to the concrete cylinder. Both direct-current LVDT high-sensitivity sensors were installed orthogonally, allowing the change in length to be measured in two directions. As a result, the stress-strain relationships in each direction could be determined, resulting in measurement of the modulus of elasticity and Poisson's ratio.

The concrete cylinder was assembled with steel caps, pads, and polysaccharide powder, similar to the compression test procedure. The compressometer model had an elastic modulus gauge length of 8 in. and a Poisson's gauge length of 6 in. Once the compressometer was secured to the cylinder, the setup was placed in the Forney machine and centered. LVDT sensors were aligned, and the mechanism brackets were removed before testing (Figure 2.8)



Figure 2.8: Series V Modulus Testing Setup

The control system was set to a loading rate of 35 psi/s according to ASTM C469 (2014). Average compressive load from previous testing was used to specify a 40% upper bound for modulus testing (ASTM C469) conducted over three loading cycles. Average values for Young's Modulus and Poisson's Ratio were calculated and provided in Table 2.5.

Table 2.5: Series V Stress-Strain Properties

Time (days)	Young's Modulus, E (ksi)			Poisson's Ratio, ν		
	Cylinders		Avg.	Cylinders		Avg.
	1	2		1	2	
38 ^[1]	4600	5060	4830	0.26	0.24	0.25
44 ^[2]	5210	4960	5090	0.24	0.26	0.25
102 ^[3]	-	-	-	-	-	-

[1] *First Day of Testing*

[2] *Last Day of Testing*

[3] *Day 102 data was unavailable due to lack of cast concrete test cylinders*

2.3.2 Reinforcing Steel

ASTM A615 reinforcing steel used in Series V was supplied by Nucor Steel, Kankakee, Illinois and fabricated by Harris Rebar. Only longitudinal reinforcing bars were used in this series. Table 2.6 provides general information for the reinforcing steel used in Series V. All bars were rolled from the same heat.

Table 2.6: Reinforcing Steel Bar Information

Series	Material	Type	Supplier	Fabricator	Grade	Size (No.)	Purpose
V	ASTM A615	Black	Nucor ^[1]	Harris Rebar ^[2]	100	5	Longitudinal

[1] *Nucor Steel-Kankakee, IL*

[2] *Harris Rebar-Mooresville, IN*

Bar strength testing was conducted on four bars in a 220-kip MTS universal testing machine. Stress was calculated by dividing applied load by the nominal bar area. A 2 in. extensometer was installed on the bar to measure strain during testing. The stress-strain response of the steel in Series V is provided in Figure 2.9 and Appendix A. From the linear-elastic region of the response, the linear-elastic limit was estimated by determining the point where the linear slope begins to decrease. The 0.2% offset method as specified in ASTM E8-04 (2016) was selected to determine the yield strength of the steel in Series V. The ultimate strength of the steel occurred just before fracture. Material properties are documented in Table 2.7.

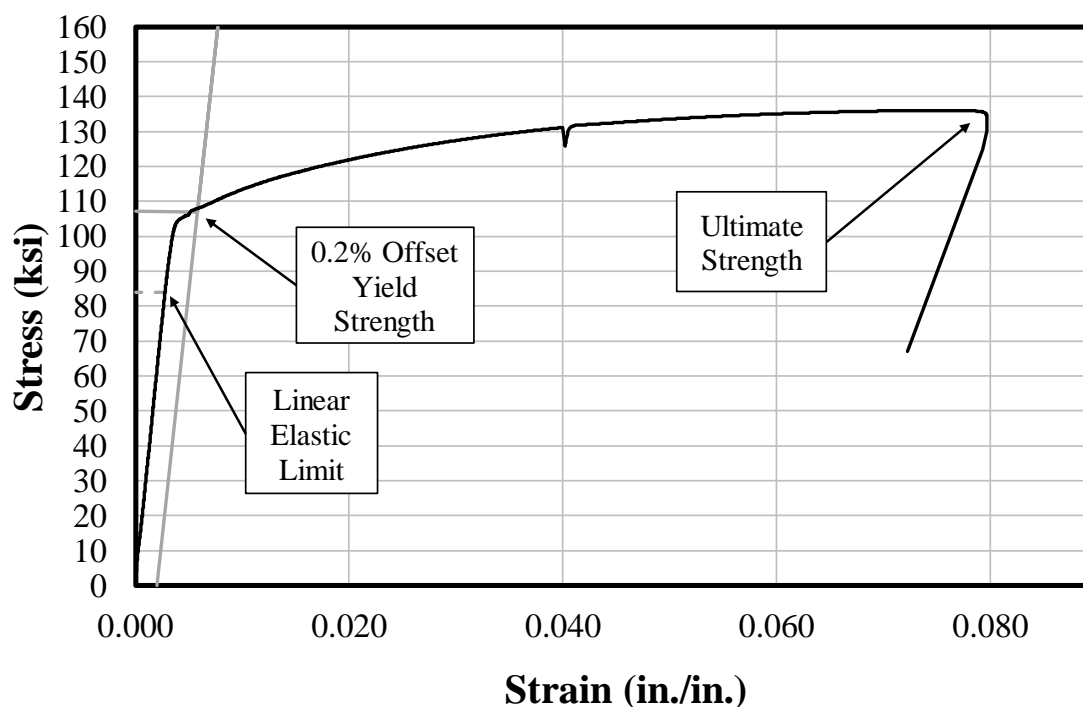


Figure 2.9: Typical Stress-Strain Response for A615 Gr. 100 No. 5 Bars

Table 2.7: Material Properties of Series V Steel

Series	Bar Size (No.)	Grade (ksi)	Linear-Elastic Limit Stress (ksi)	Yield Stress 0.2% Offset (ksi)	Ultimate Strength (ksi)
V	5	100	84	107	137

2.4 Specimen Construction

Four slab specimens were cast by first assembling and securing the appropriate formwork. Once formwork construction was completed, the necessary steel was placed and tied within the forms before casting.

2.4.1 Formwork Assembly

All formwork materials for this series were provided by a local lumber retailer. To accommodate the size of the test specimens in Phase I and Phase II, base platforms were constructed at a width of 4 ft and a total length of 27 ft - 6 in. The 3/4 in. top plywood was finished with a high density overlay (HDO) to provide a smooth finish. The HDO plyform was mounted on a series of 4 ft long 2 x 4 in. lumber spaced at 8 in. on-center running in the short direction. This allowed the platforms to be moved and configured into various arrangements for each series while also limiting warping in the plyform. The platforms were used for all seven series in the testing program.

For slab casting, a center form was bolted between two platforms, effectively allowing the two platforms to work as one uniform base. The center form was constructed on a piece of 2 x 4 in. lumber spanning the full slab length of 22 ft, plus an additional 5 in. on each side to accommodate the width of the end forms. Typical 2 x 4 in. wood bracing studs were installed vertically at a 16 in. spacing along the entire length. With the structure of the center form completed, a 6 in. sheet of HDO plyform with a thickness of 3/4 in. was secured to each side by screws. The center form and other main formwork components are shown in Figure 2.10.

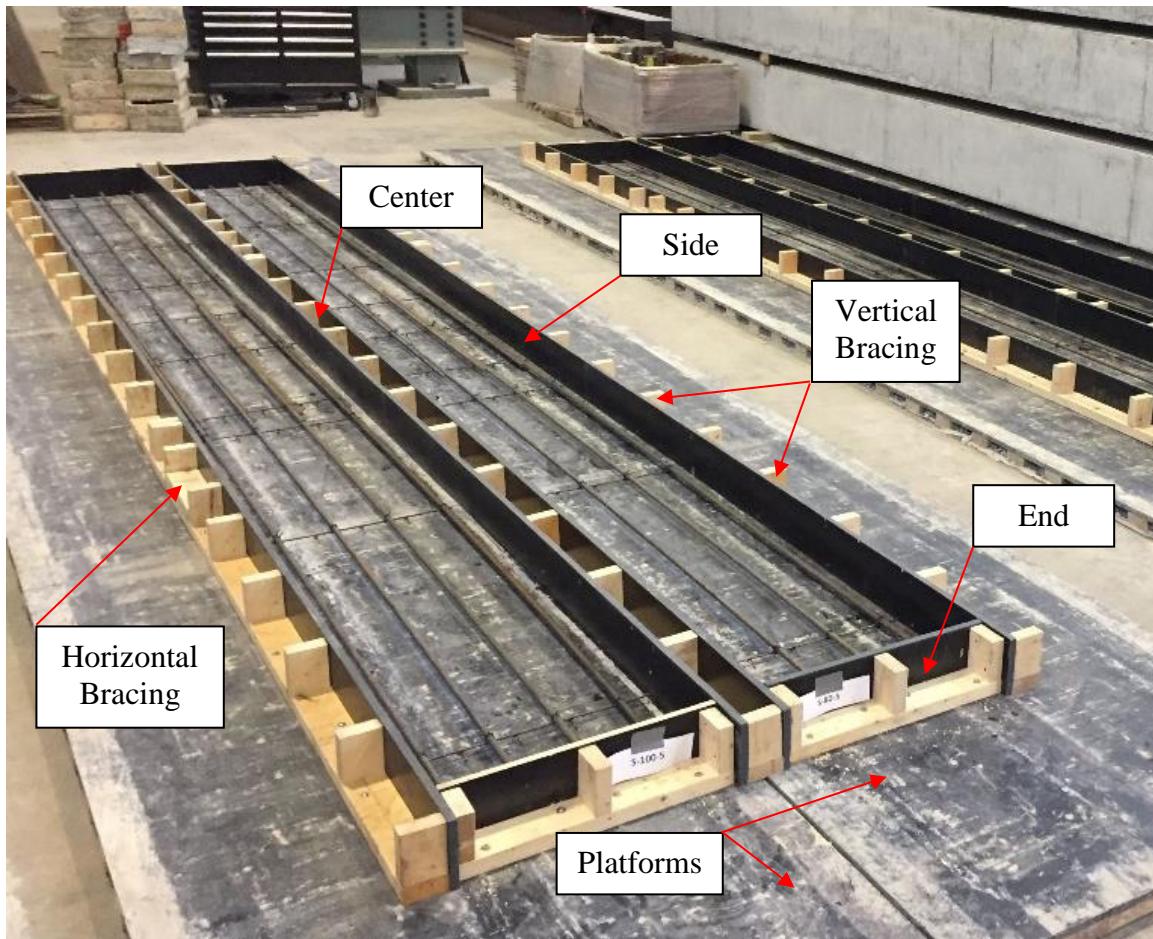


Figure 2.10: Series V Formwork Components

The two side forms were constructed in the same manner as the center form, but only one side sheet of HDO plyform was required for each. Similarly, the end forms were constructed identically to the side forms but with an overall length of 24 in. and a wood brace spacing of approximately 12 in. The locations of all formwork components were first marked with chalk lines before being secured with 1/4 in. lag screws and washers. The completed formwork construction for Series V is shown in Figure 2.11.



Figure 2.11: Series V Completed Formwork

2.4.2 Steel Cage Construction

Once the formwork was secured, the interior surfaces of the plywood were cleaned before cage construction began. The layout of steel for the slabs required eight No. 5 Grade 100 bars to be measured and cut to the appropriate length for each specimen. As shown in Figure 2.12, a 2 in. gap was provided between the end of each bar and the end plyform surface in the shear region.

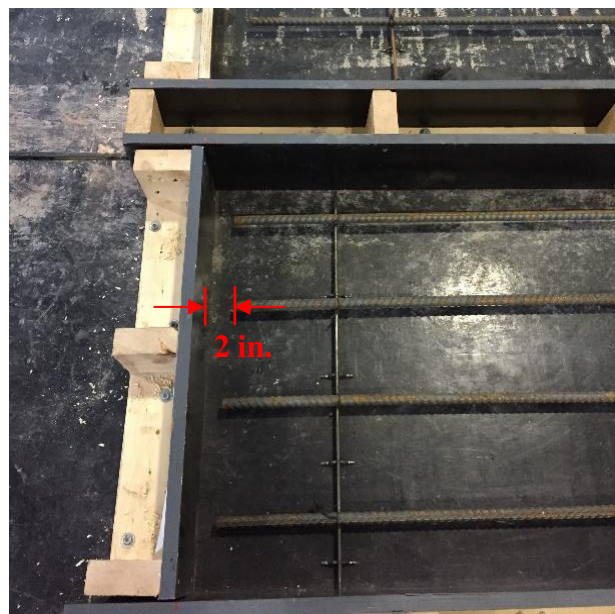


Figure 2.12: Slab Construction – Shear Region

All longitudinal bars were placed on 3/4 in. steel chairs at various points along the length of the slab to ensure a consistent cover across the bottom surface. Annealed steel wire ties were used to secure the bars to the chairs in all locations to prevent any movement or slip during casting.

The intended location of each lap splice termination was marked on the bars. Steel ties were secured to the longitudinal reinforcing steel in the lap splice to prevent a noncontact lap splice from forming during casting. Bar spacing and cover were critical for the splice zone; therefore, care was taken in securing the bars to the steel chairs in this region (Figure 2.13). All four slab specimens were constructed in this manner with the steel reinforcing on the bottom (bottom cast). Immediately after concrete was cast in each specimen, 3 in. plain steel coil loop lifting-inserts were placed 5 ft from the ends of each slab to allow for transporting.



Figure 2.13: Slab Construction – Splice Region

2.5 Casting, Curing, and Storage

2.5.1 Cylinders

Concrete was used to cast cylinder sets (Figure 2.14) for all series in this testing program in accordance with the “Standard for Making and Curing Concrete Test Specimens in the Laboratory” in ASTM C192 (2016).



Figure 2.14: Typical Concrete Cylinder Preparation Space

The molds were filled halfway with a metal scoop before using a low frequency internal vibrator to consolidate the lower layer of concrete. The mold was then filled to the top and vibrated a second time, ensuring that the steel-head vibrator penetrated into the bottom layer of concrete approximately 1 in. to consolidate the concrete. The top surface was finished as shown in Figure 2.15 before sealing the cylinder mold with a flexible, domed plastic lid to prevent loss of moisture and maintain shape during curing.



Figure 2.15: Series V Cylinder Casting

All cylinders in Phase II cured in the same location as the specimens to prevent differences in humidity and temperature. Each cylinder was moist cured for seven (7) days in capped plastic containers that sealed moisture. On Day 7, molds were removed and all cylinders were relocated for storage. Cylinders were labeled before being stored until testing.

2.5.2 Casting

All specimens in Series V were cast at the same time from the same delivery of concrete. Series V required one truck of concrete due to the low volume of desired specimens. Concrete was delivered to the specimens using a concrete bucket. Care was taken to ensure that the steel cages in the forms stayed in place while concrete was placed from above. Two external mechanical vibrators operating at 3600 cycles per minute (60 Hz) were inserted following concrete shoveling

to ensure proper consolidation. The casting process for Series V was conducted using one lift along the length of each slab specimen. Once concrete had been cast and vibrated within each test specimen (Figure 2.16), the top surface was screeded with a 2 x 4 in. magnesium straight-edge.



Figure 2.16: Series V Consolidation Process

The top surface was evened out through screeding and finished with hand floats. Lifting-inserts were placed by hand within the concrete 5 ft from each end to assist in moving the slab and flipping it over 180 degrees about its longitudinal axis before being placed in the test setup. The lifting-insert location and screeding steel tube used after consolidation are shown in Figure 2.17. The Series V specimens after finishing are shown in Figure 2.18.



Figure 2.17: Series V Casting Process

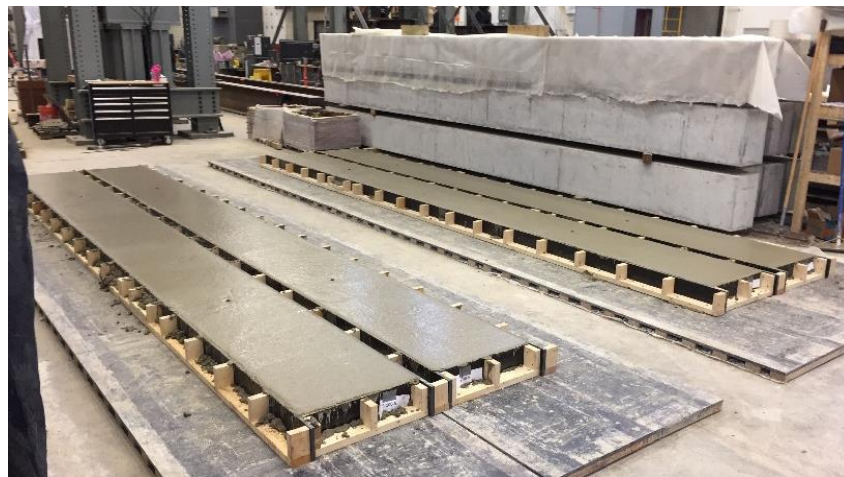


Figure 2.18: Series V Casting Complete

2.5.3 Curing and Storage

Once all test specimens were finished and cured for approximately one hour, a final finish was conducted with a magnesium float to smooth out any noticeable irregularities in specimen height. To initiate moist curing, all specimens were covered with burlap sheets and watered evenly. Plastic sheathing was placed over the cast specimens to maintain moisture and promote hydration (Figure 2.19). The burlap was watered each day for the following five days, with the final watering period occurring on Day 6.

On Day 7, three (3) compression cylinder tests were performed to evaluate strength gain of the series before removing all side formwork (Figure 2.20). The slabs were then flipped 180° about their longitudinal axis using the crane and lifting-inserts to orient the lap splice on the top face of each member before storing the specimens (Figure 2.21).



Figure 2.19: Series V Moist Curing



Figure 2.20: Series V Side Form Removal



Figure 2.21: Series V Member Stacking and Storage

2.6 Test Setup

2.6.1 Schematic

All specimens in Series V were tested in four-point bending with the load being applied to the top face at the ends of the member and supports provided by rollers on the bottom face. Initially, a pin-roller support condition was selected for specimens in Phase I of testing, but unequal north-south lateral translation introduced a loading eccentricity in the test setup. By employing a roller-roller condition, all specimens were allowed to deform equally in the longitudinal direction.

The supports under all slabs were constructed on two 4 x 4 x 2-1/2 ft concrete bearing blocks (Figure 2.22). Roller supports were assembled using a 2 in. diameter steel rod placed between two 1/2 in. thick steel plates measuring 6 x 36 in. The 2 in. rod was selected to allow the Series V slabs to deform at the ends without interfering with the concrete bearing block (Figure 2.23(a)). Hydrostone was used to secure these components to the concrete bearing blocks and the specimens. Wood cribbing was placed below the test specimens in the middle and near the ends to protect string potentiometers (Figure 2.23(b)) and provide a safer testing environment when the concrete member reached failure.



Figure 2.22: Series V Test Setup



(a) Roller Support



(b) End Cribbing

Figure 2.23: Series V Testing Details

Once the test specimens were placed and secured with hydrostone to the roller supports, two bearing plates were positioned on the top face to align with the loading rams. Two (2) 100-ton double-acting hydraulic rams with a maximum stroke of 9.8 in. were secured to the bottom face of a crossbeam built-up from a double channel steel section (Figure 2.24). A 1 in. steel plate and 3/8 in. bolts were used to secure the ram to the crossbeam bottom flange. The crossbeam was threaded through two 1-1/4 in. diameter DYWIDAG force transfer bars that were secured to the strong floor. Center-hole load cells were installed and secured around the DYWIDAG bars above the crossbeam. Once the hydraulic rams were lowered and centered on the bearing plates, the crossbeams were leveled. Figure 2.25 shows an elevation of the test setup for Series V, and Figure 2.26 shows various plan sections of the Series V test setup.



Figure 2.24: Typical Crossbeam Setup

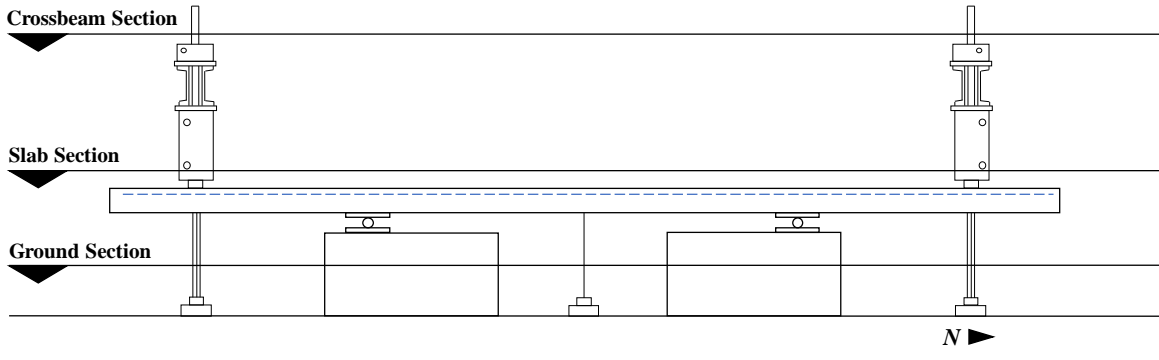
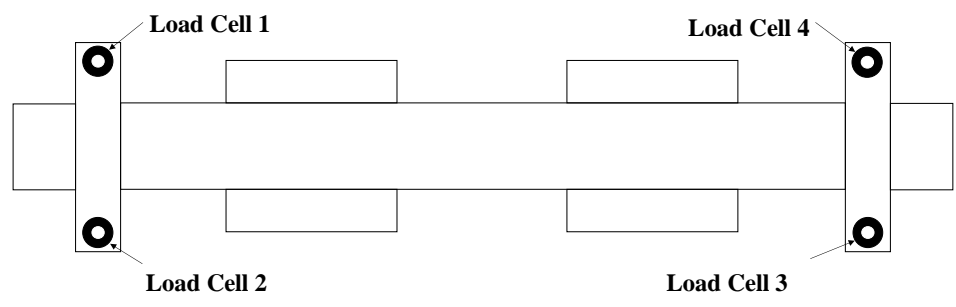
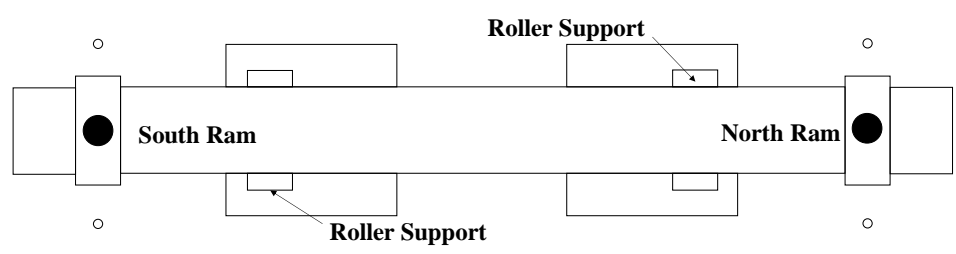


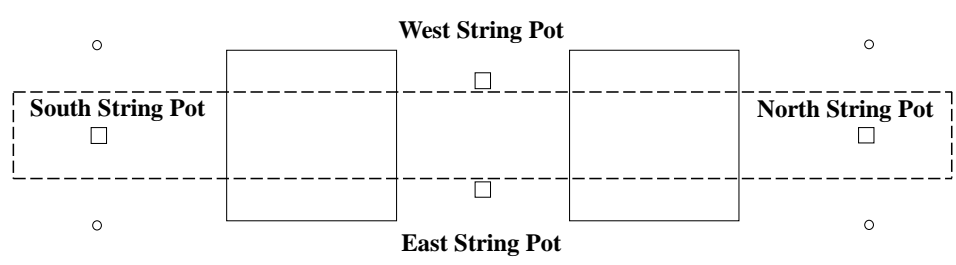
Figure 2.25: Series V Test Setup – East Elevation



(a) Crossbeam Section



(b) Slab Section



(c) Ground Section

Figure 2.26: Series V Test Setup Schematic Plans

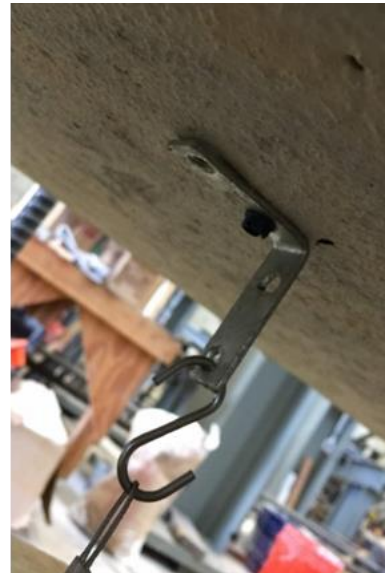
2.6.2 Instrumentation and Equipment

2.6.2.1 Deflection

Four 10 in. UniMeasure digital encoder string potentiometers were secured to the strong floor to measure vertical deflections. Two were located at midspan, aligning with the east and west faces of the slab, while the other two were placed directly below the hydraulic loading rams on the north and south ends of the slab. The two midspan string potentiometers were connected to the test specimen through epoxied steel brackets as shown in Figure 2.27(a), while the north and south brackets were secured with concrete screws (Figure 2.27(b)). The use of concrete screws provided a stronger, more reliable bracket connection as opposed to the epoxied brackets; however, the screws were not installed at midspan to avoid potentially interfering with the stress distribution within the splice region during testing. Calibration was performed using a Fowler Trimos electronic height gauge for all four units.



(a) Midspan



(b) End of Member

Figure 2.27: String Potentiometer Connections

2.6.2.2 Loading System

Two 50-kip center-hole load cells were secured above each crossbeam, requiring a total of four load cells for the test setup. A 1-1/2 in. steel plate and 1-1/4 in. threaded steel nut were used as a reaction point against the loading rams (Figure 2.28). The four load cells were calibrated on a 120-kip Baldwin universal testing machine using an Instron data acquisition system.

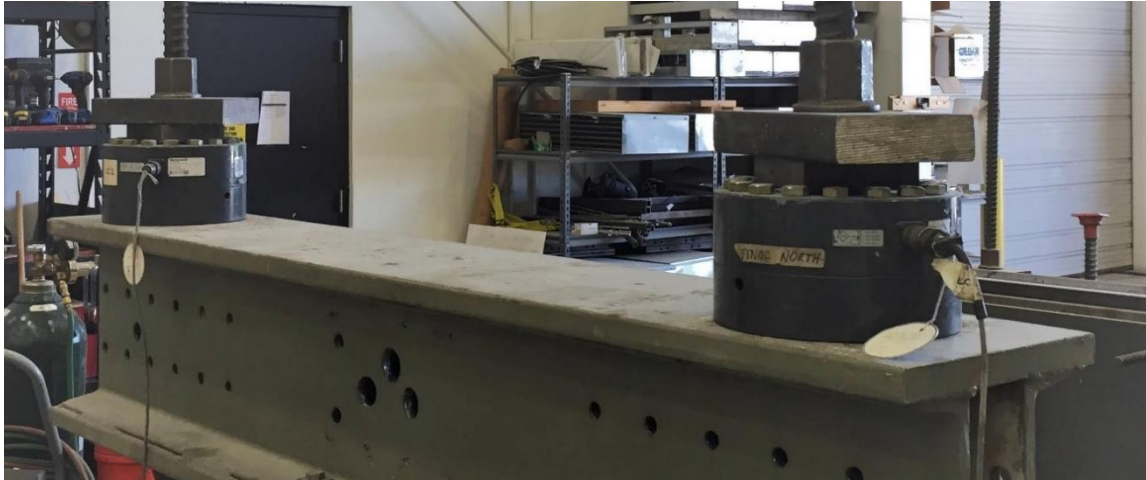
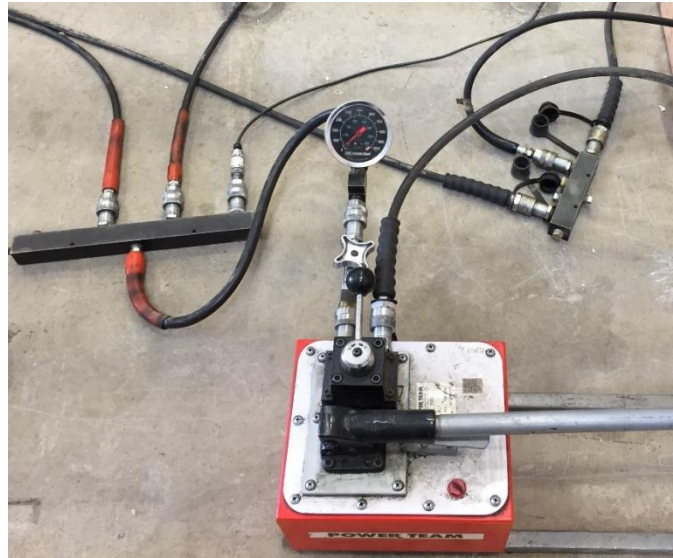


Figure 2.28: Typical Load Cell Configuration

A manual hand pump was selected to pump hydraulic fluid into a three-outlet manifold. Two of the outlets fed hydraulic fluid to each of the double-acting hydraulic rams (Figure 2.29(a)) while a stainless steel pressure transducer was attached to the third outlet. For three specimens in Series V, the same 10,000 psi pressure transducer was used from Phase I testing. Because the pressures required for the slab tests to reach failure were generally lower, it was difficult to obtain accurate data with this high capacity transducer; therefore, a 2000 psi pressure transducer was selected for the S-100-5 slab specimen to provide better resolution at lower pressures. Hydraulic fluid was returned from the loading rams to the hand pump reservoir through a two-outlet manifold. All hoses used in this test setup were rated for 10,000 psi. Figure 2.29(b) shows the layout of the supply and return system.



(a) Ram Supply and Return



(b) Manifolds and Pump

Figure 2.29: Typical Pump System for Testing

2.6.2.3 Concrete Cracking

Cracks along the sides and tension face of each specimen were mapped and measured using an Edmund Industrial Optics Crack Width Direct Measuring Microscope with a 50x magnification, allowing concrete crack widths to be identified and measured to 1/1000 in. (Figure 2.30). Four cracks were selected for each specimen outside of the splice region but between the supports. These locations ensured that the measured cracks were in the constant moment region and were not influenced by the splice. The four cracks were observed at each loading interval, and widths were manually recorded.

For some test specimens, a crack was selected early in the testing procedure and over time, another crack formed adjacent to this original crack. It was observed that this close proximity of cracks caused the original crack to reduce in size from shifting of the surrounding concrete.



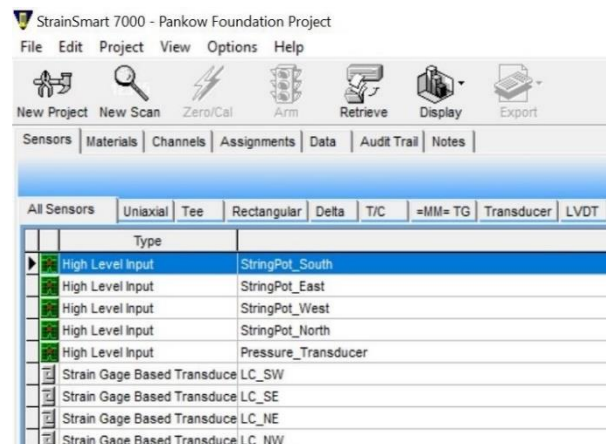
Figure 2.30: Crack Width Microscope and Mapping Process

2.6.2.4 Testing Documentation and Media

A Vishay Precision Group, Inc. System 7000 Digital Data System was selected to collect data from the testing equipment using StrainSmart Version 5.3 (Figure 2.31). The data acquisition software recorded test data at a time interval of 0.1 seconds for all specimens in Series V.



(a) System 7000



(b) StrainSmart Version 5.3 Layout

Figure 2.31: StrainSmart Data Acquisition

A GoPro, Inc. Hero 5 video recording camera was mounted to a nearby steel column and used to capture all load steps during testing, as well as final failure of each specimen. By using a wide lens, most of the specimen was captured; however, a focus was placed on the splice region. Photographs were taken of each specimen before, during, and after failure. During testing, photos were taken to document changes in the splice region, propagation of established cracks, formation of new cracks, and deflections along the member.

2.6.3 General Testing Procedure

Before applying load to each of the specimens, the top surface was inspected for any minor cracks caused by flipping or transporting the specimen to the test setup. No perceptible cracks were found on any of the four specimens. The initial pressure reading was recorded at the beginning of each test. Load was applied to the slabs in 1-kip intervals up to failure of the specimen.

Cracks were mapped (Figure 2.32) and measured in 1-kip increments across the tension face and sides of each specimen. This process was repeated throughout testing until failure was reached. As-built dimensions were measured after failure within the splice region to document cover and bar spacing and are provided for all slabs in Appendix B.



Figure 2.32: General Slab Test – Crack Mapping (S-80-5)

CHAPTER 3. EXPERIMENTAL RESULTS: SLABS

3.1 Introduction

The experimental results of each test in Series V are presented to evaluate the effect of splice length on bond strength. Series V consisted of four slab specimens, each tested in four-point bending. The test results are summarized in Table 3.1. Two specimens experienced failure of the splice while two specimens failed in flexure at a support.

3.2 Experimental Results

The applied load at failure, P_{ult} , was determined by doubling the most accurate of the four load cell readings for each slab. Prior to loading, approximately 1 kip was applied to each end of Specimens S-40-5, S-60-5, and S-80-5 from direct bearing of the crosshead assembly. This initial loading is believed to have caused increased readings for various load cells, with some specimens exhibiting a difference between the north and south end loads of up to 20%. The difference in recorded end load may also be attributed to excessive concrete cracking and rotation of the test frame. The ultimate moment at failure, M_{ult} , was calculated by multiplying the failure load, P_{ult} , by the shear span for each slab. The increased moment due to self-weight was neglected.

The stress achieved in the longitudinal reinforcing bars, f_b , was calculated using moment-curvature analysis and the failure load reached for each slab. All cross-sectional dimensions in this calculation were design values. The tensile capacity of the concrete was neglected. The stress-strain relationship for the longitudinal steel was determined from experimental lab testing of the material, while the stress-strain relationship for concrete was represented using the Hognestad (1951) model.

Table 3.1: Slab Test Results

Series	Specimen	Test Age (days)	f_c (psi)	l_s (in.)	P_{ult} (kip)	M_{ult} (ft-kip)	f_b (ksi)	Failure Mode
V	S-40-5	44	6240	25	11.1	44.6	97.9 ^[1]	Splitting
	S-60-5	40	6200	37.5	13.6	54.4	121.0 ^[2]	Splitting
	S-80-5	38	6180	50	13.4	53.6	119.2 ^[2]	Flexure
	S-100-5	102	6490	62.5	13.2	52.8	117.0 ^[2]	Flexure

[1] Beyond linear-elastic limit (84 ksi)

[2] Beyond yield strength (107 ksi)

As included in Table 3.1, the test age was recorded for all specimens with test dates ranging from 38 days to 102 days. The variation in concrete strength, f_c , between Day 28 and Day 44 of testing was negligible for this test series. Compressive strength data after Day 44 was not obtained; therefore, the S-100-5 slab specimen compressive strength was conservatively approximated. The strength of this specimen, however, was not considered vital to the analysis as the failure mode was flexure.

3.2.1 Self-Weight

Although the slab specimens are subjected to a loading configuration that creates constant moment between supports, self-weight provides for moment variation. When self-weight is acknowledged, moment across the splice increases slightly in the slab specimens. The moment diagrams for loading and self-weight are shown in Figure 3.1 and Figure 3.2, respectively. In general, the maximum moment which occurs at the support is calculated by Equation 3-1:

$$M_{ult (slab)} = M_{load} + M_{Self-Weight (slab)} \quad (3-1)$$

where:

$$L_V = 4 \text{ ft}$$

$$M_{load} = (L_V)(P_{ult})$$

$$P_{ult} = \text{applied load at failure (kip)}$$

For all slab specimens, the maximum moment at the support due to self-weight is calculated by Equation 3-2:

$$M_{Self-Weight (slab)} = \frac{L_s^2 w_s}{2} \quad (3-2)$$

where:

$$L_s = \text{length of slab from support to closest end, 6 ft}$$

$$w_s = \text{slab self-weight}$$

$$= \left(\frac{0.150 \text{ kips}}{\text{ft}^3} \right) (24 \text{ in.}) (6 \text{ in.}) \left(\frac{1 \text{ ft}^2}{144 \text{ in.}^2} \right) = 0.15 \frac{k}{\text{ft}}$$

Therefore:

$$M_{ult (slab)} = (4 \text{ ft})(P_{ult}) + \frac{(6 \text{ ft})^2 \left(0.15 \frac{k}{\text{ft}} \right)}{2}$$

$$M_{ult (slab)} = (4 \text{ ft})(P_{ult}) + 2.7 \text{ ft-k}$$

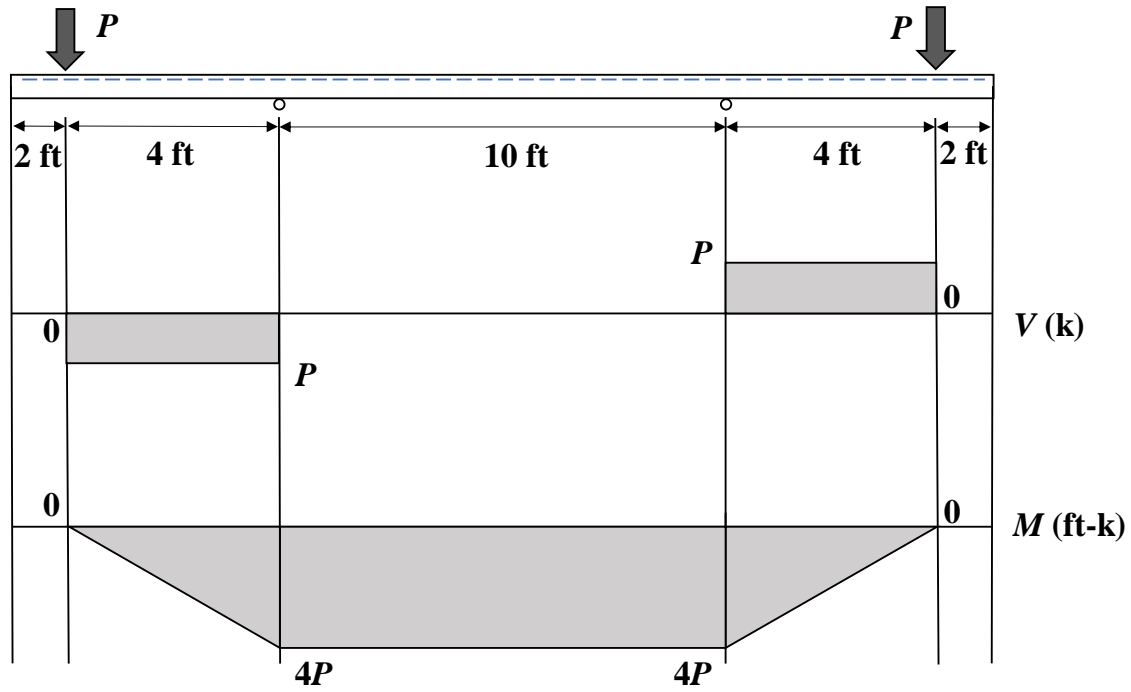


Figure 3.1: Shear and Moment Diagrams for Slabs from Loading

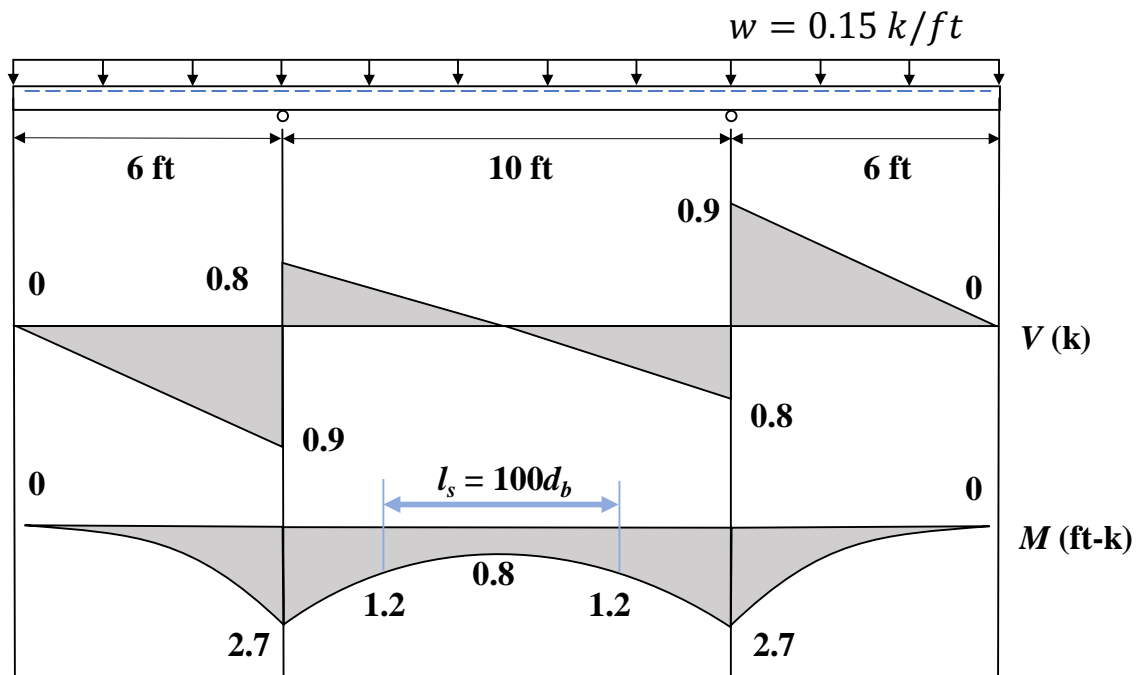


Figure 3.2: Shear and Moment Diagrams for Slab Self-Weight

Because the constant negative moment from the applied load occurs between the supports while the negative moment due to the slab's self-weight peaks at each support, the ultimate moment occurs near the supports. The largest variation in moment across the splice is 0.4 ft-k for the 100 d_b specimen resulting from an additional negative moment of 0.8 ft-k in the center and 1.2 ft-k at the ends of the splice.

Considering the applied loads, the self-weight acts as a small percentage of the resisted moment. The greatest influence occurs in the S-40-5 slab, where a 6% increase in ultimate moment occurs due to self-weight. This difference is considered negligible; therefore, the self-weight contribution is conservatively ignored.

3.2.2 Specimen Observations

Cracking moment occurred at approximately 1.8 kips of applied load for all slabs. Large deflections and an abundance of cracking were observed in all slab specimens as shown in Figure 3.3 and Figure 3.4, respectively. The hydraulic ram for Specimens S-80-5 and S-100-5 reached the maximum stroke while loading. To continue testing for the S-80-5 specimen, load was entirely removed from the slab, and the crossbeam was lowered before applying load again until failure was reached. For the S-100-5 specimen, the test was concluded early based on the load reached and considering the results of S-80-5.



Figure 3.3: Slab Deformation during Testing (S-100-5)



Figure 3.4: Typical Flexural Cracking – West Side and Tension Face (S-80-5)

3.3 Load-Deflection Response

Load-deflection behavior was monitored for all slab specimens. Although each curve was unique, the underlying mechanics and regions within the responses were similar. Before reaching the cracking moment for each slab, the stiffness of the specimen was primarily governed by the concrete as shown in Region 1 of Figure 3.5. Once cracking occurred, the stiffness of the member immediately decreased as evidenced in Region 2. The overall response in this region is approximately linear due to the elastic response of the steel. The final region (Region 3) demonstrates yielding of the longitudinal bars. Region 3 only occurred in specimens where the splice strength exceeded the yield strength of the steel. This region provides the lowest member stiffness observed during testing.

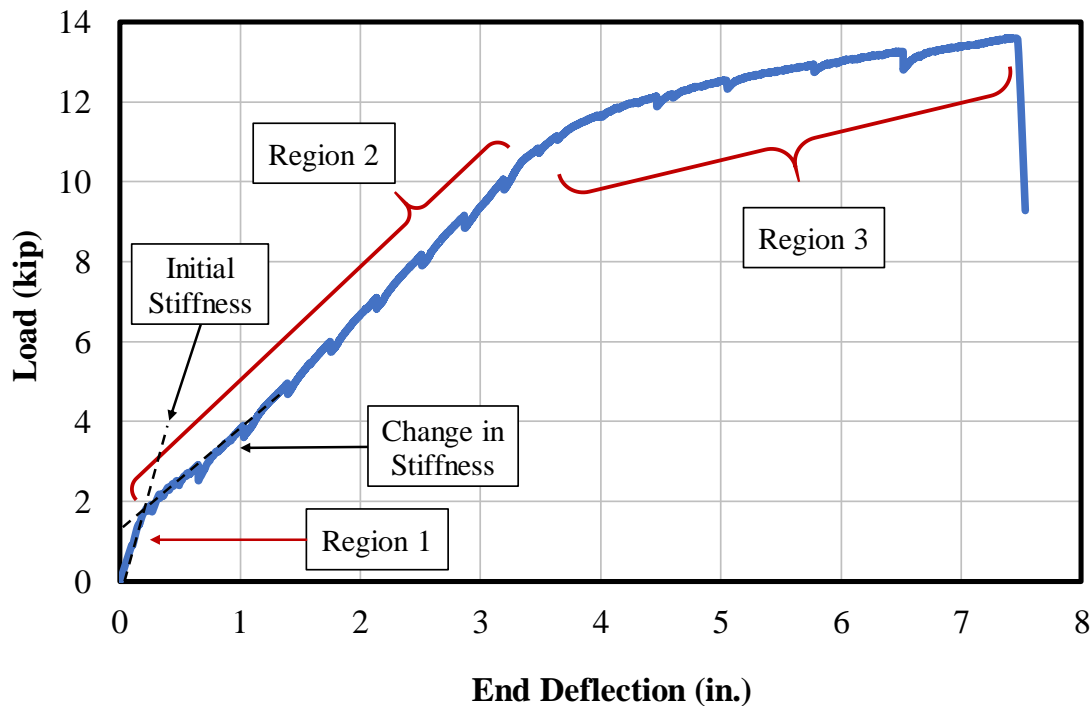


Figure 3.5: General Load-Deflection Behavior (S-60-5)

As shown in Figure 3.6, Specimen S-40-5 did not yield but did begin to exhibit inelastic behavior. Yielding occurred for all other slabs. While S-60-5 provided significant inelastic response, it ultimately failed in splitting. Specimen S-80-5 and S-100-5 failed in flexure initiated by crushing of the concrete. The load-deflection response for all specimens is provided in Appendix C. Note that the slight increase in cracked stiffness of the specimens (Region 2) may be attributed to the increase in steel within the cross-section as the splice length increased.

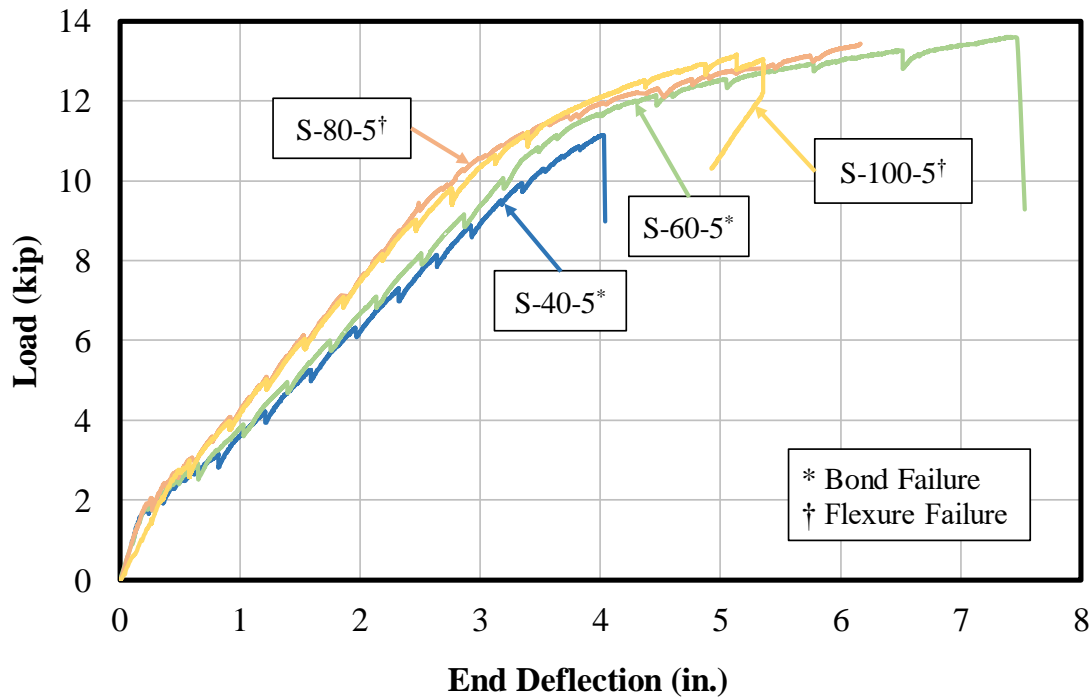
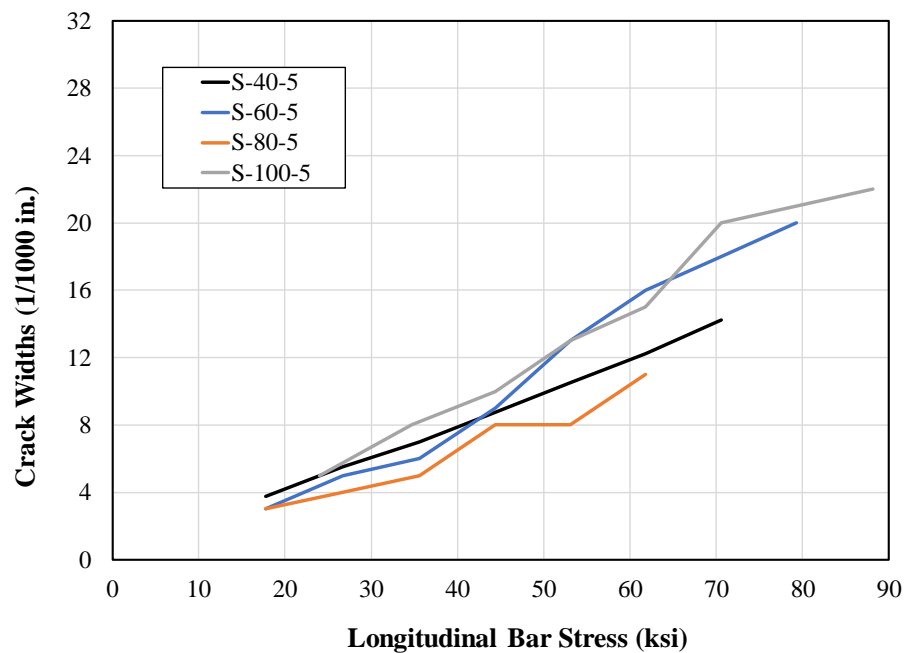


Figure 3.6: Series V Load-Deflection Response

3.4 Concrete Cracking Behavior

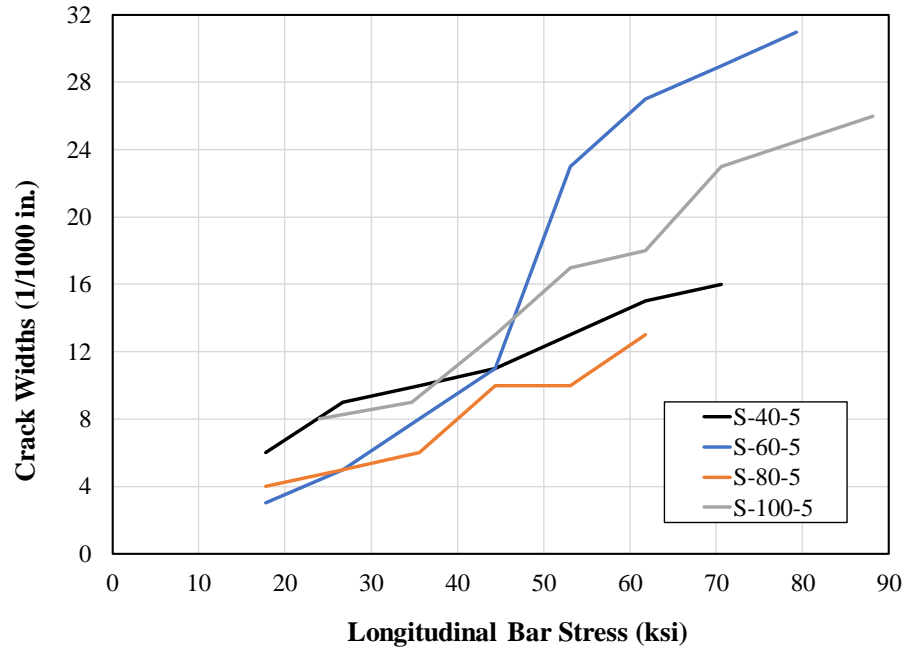
Four cracks were selected in the constant moment region, two past the north end of the splice region and two past the south end. Crack widths were monitored at each load step and recorded. Throughout testing within the linear range of the reinforcing steel, crack widths consistently increased linearly. Average and maximum crack width measurements for all slabs in

Series V are provided in Figure 3.7. All transverse cracks initiated at a spacing of approximately 1 in. to 4 in. along the entire length of the slab, including throughout the splice region. Fewer new cracks formed across the full width of the slab at each additional load step after cracking moment was reached; however, any established cracks experienced large amounts of branching in all directions (Figure 3.8). Transverse flexural cracking tended to initiate in the middle of the slab at multiple locations outside of the splice region and spread toward the edges as load increased. The region above both supports appeared to have a slightly smaller spacing of cracks along the tension face. The growth pattern of flexural crack widths as bar stress increased is provided in Appendix D for all specimens.



(a) Average Crack Widths

Figure 3.7: Series V Crack Width Measurements



(b) Maximum Crack Widths

Figure 3.7: Series V Crack Width Measurements (Continued)

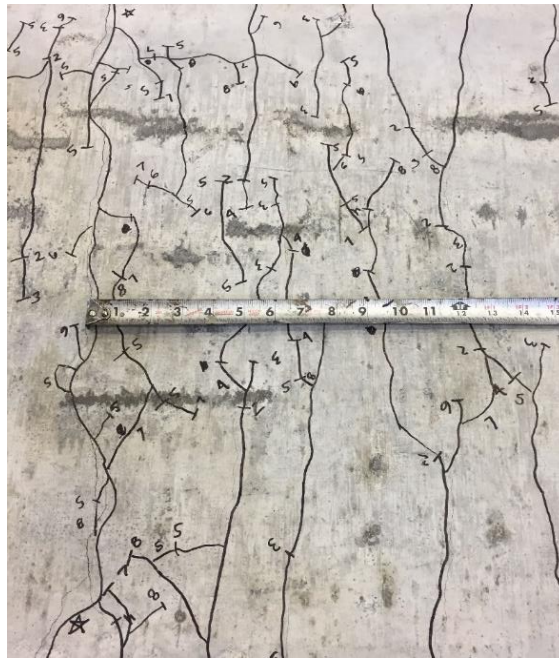


Figure 3.8: Observed Crack Branching Near End of Splice (S-60-5)

Side cracking propagated down along the depth of the slabs at a slow rate, often starting at a depth of 2 in. from the tension face and reaching a maximum depth of approximately 4 in. from the tension face before failure. This depth was indicative of the neutral axis of the cross-section. An example of the propagation of this side cracking at approximately half the full load capacity is shown in Figure 3.9 for Specimen S-100-5.



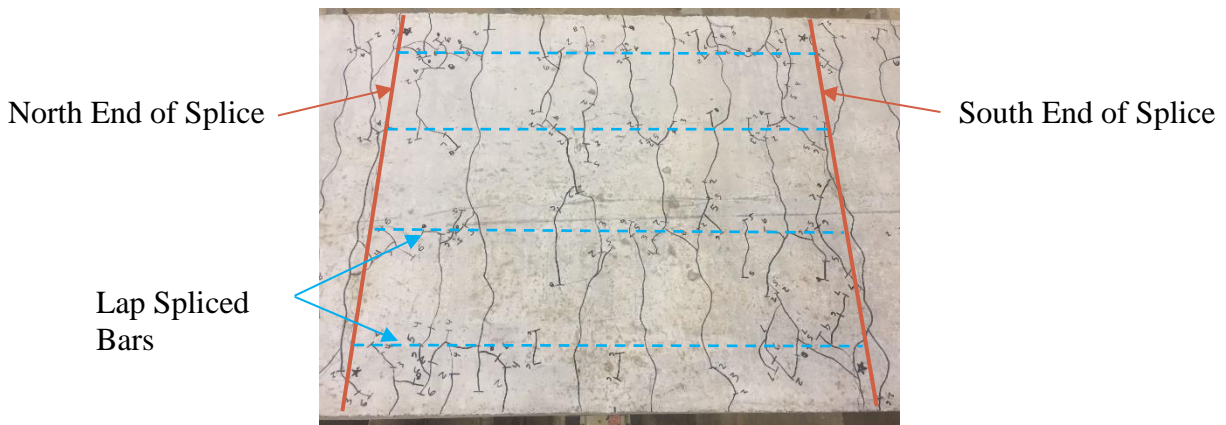
Figure 3.9: Side Crack Propagation (S-100-5)

Branching cracks were less present within the shear spans of each slab. Spacing between transverse flexural cracks in this region was noticeably larger than in the constant moment region and is shown in Figure 3.10. The presence of diagonal cracking across the member depth in this region was minimal due to the small overall depth of the slab specimens.

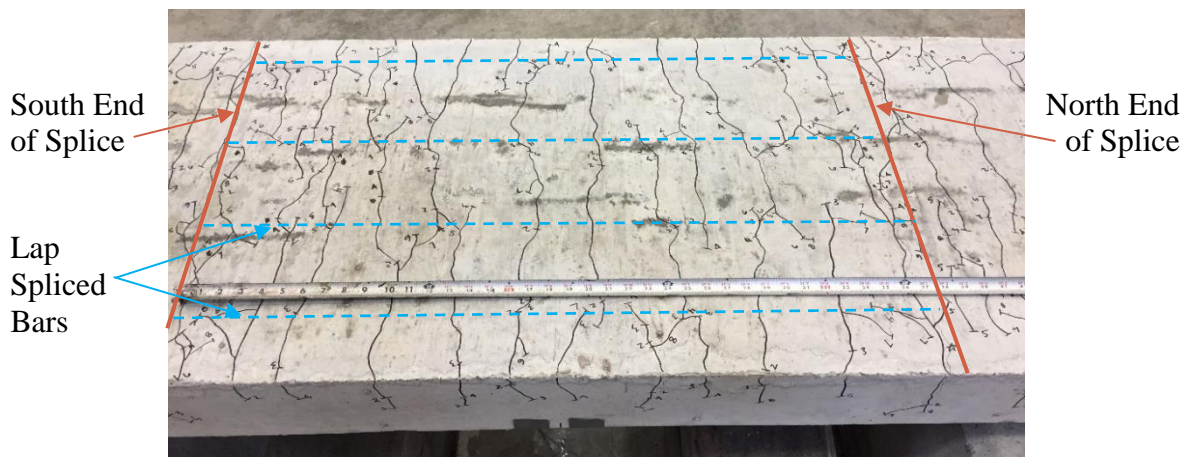


Figure 3.10: Post-Failure Shear Span Cracking (S-60-5)

Longitudinal cracking occurred above each of the four lap splices in all specimens as shown in Figure 3.11 and was present in all slab specimens, independent of the failure mode. Longitudinal cracking initiated near the ends of the splice on the tension face after approximately 3 kips were applied to each slab specimen. As load increased, longitudinal cracks slowly propagated toward the middle of the specimen. In the specimens with shorter splices, crack branching occurred near the ends of the splice and seemed to be localized closer to the sides of the slabs. It was observed that slabs experiencing a side-splitting failure had a greater concentration of longitudinal cracking near the edges and sides before failure.



(a) S-40-5



(b) S-60-5

Figure 3.11: Splice Region Crack Observations

3.5 Failure

As splice length was increased from $40d_b$ to $100d_b$ in Series V, the failure mode changed. Specimens S-40-5 and S-60-5 failed in splitting of the bottom and side cover in the splice region. Specimens S-80-5 and S-100-5 developed sufficient bond strength along the splice to transition the failure from bond to flexure.

3.5.1 Bond Failure

Longitudinal cracking was present above all four splices. In both slabs (S-40-5 and S-60-5), longitudinal cracking was present along the east, west, and top faces of the specimens, initiating at the ends of the splice and propagating toward the middle. Upon failure, the bottom cover remained relatively intact over the inner two splices while the side cover spalled off entirely. Due to the small bottom cover, concrete spalling was not extensive.

Based on analysis of the maximum longitudinal bar stress achieved, Specimen S-40-5 did not reach yielding of the bars before splice failure. The yield strength of the longitudinal reinforcement, however, was exceeded for the S-60-5 slab. A decrease in slope in the load-deflection plot confirms this behavior with a larger increase in deformation occurring as the applied load increases. Table 3.2 provides the maximum results for each specimen that failed in bond at the conclusion of testing. The load-deflection response for these specimens is provided in Figure 3.12. Load-deflection plots for all slabs are provided in Appendix C.

Table 3.2: Test Results for Series V Bond Failures

Specimen	Load (kip)	Avg. End Deflection (in.)	Avg. Midspan Deflection (in.)	Bar Stress (ksi)
S-40-5	11.1	4.1	2.2	97.9
S-60-5	13.6	7.5	3.7	121.0

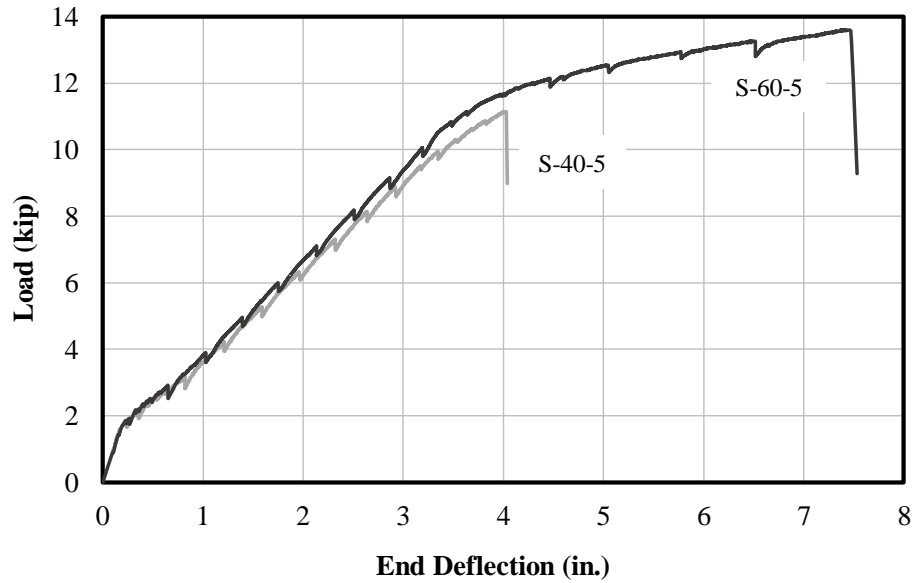


Figure 3.12: Load-Deflection Response of Series V Bond Failures

Failure of S-40-5 occurred in a single event where all splices failed simultaneously while the side cover completely spalled. The bottom cover remained slightly intact for the two inner splices but heavy longitudinal cracking occurred on the tension face as shown in Figure 3.13.

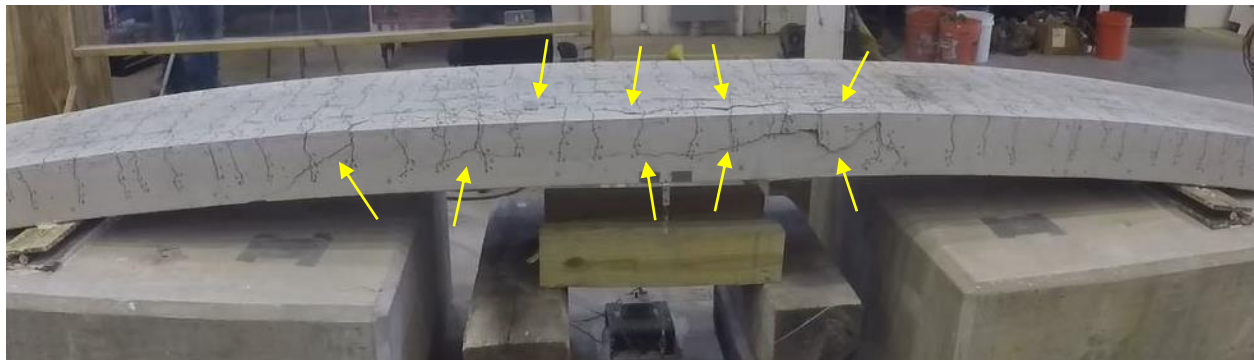


Figure 3.13: S-40-5 Face- and Side-Splitting Failure

Failure of S-60-5 was not a single event. Failures of individual splices occurred twice while loading the slab. The west splice failed first, exhibiting large amounts of cracking while load continued to be carried (Figure 3.14). As more load was applied, the east splice failed and large amounts of cracking were present (Figure 3.15). In both cases, load was maintained and no spalling was observed. Final failure occurred when both inner splices failed and the side cover spalled off entirely (Figure 3.16). It should be noted that a similar failure progression was observed by Seliem et al. (2009) while conducting bond strength testing on MMFX steel in splice specimens.



(a) Before



(b) After

Figure 3.14: S-60-5 Partial Failure 1



(a) Before



(b) After

Figure 3.15: S-60-5 Partial Failure 2



Figure 3.16: S-60-5 Final Failure

3.5.2 Flexural Failure

When splice length was sufficient in developing the reinforcement, a flexural failure was observed. Longitudinal and transverse cracking was observed along the tension face and sides, but a splitting failure was precluded. Final bar stresses indicate that the reinforcing steel exceeded the yield capacity for Specimens S-80-5 and S-100-5.

Table 3.3 provides the maximum results for each specimen that failed in flexure. Load-deflection response for these specimens is provided in Figure 3.17. Note that for Specimen S-100-5, the initial high stiffness region is slightly lower than that of Specimen S-80-5. This may be attributed to possible minor cracking of the concrete prior to testing from flipping and transporting.

Table 3.3: Test Results for Series V Flexural Failures

Specimen	Load (kip)	Avg. End Deflection (in.)	Avg. Midspan Deflection (in.)	Bar Stress (ksi)
S-80-5	13.4	6.2	2.9	119.2
S-100-5	13.2	5.4	2.2	117.0

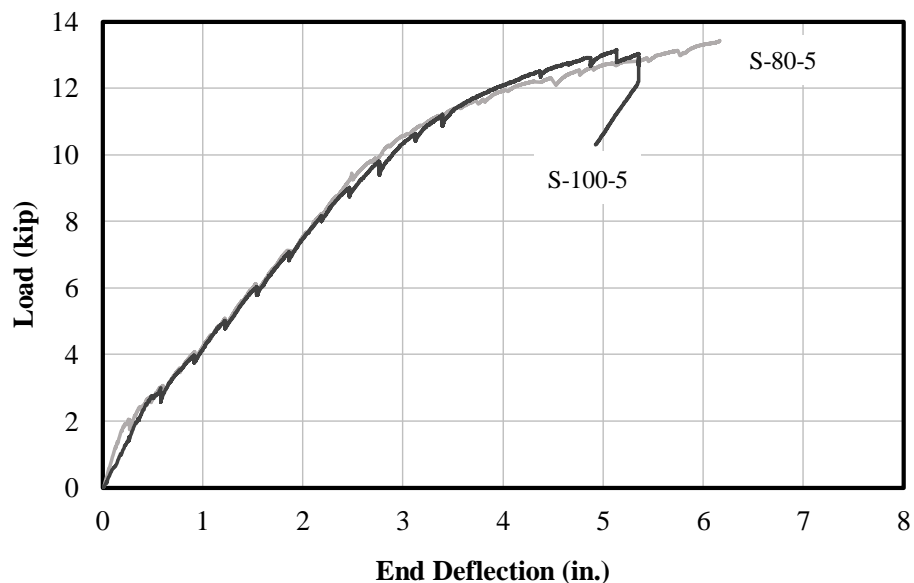


Figure 3.17: Load-Deflection Response of Series V Flexural Failures

Specimen S-80-5 experienced a flexural failure near the north support as evidenced by crushing of the concrete along the compression face of the member (Figure 3.18). As the applied load increased, crushing became more apparent (Figure 3.19).

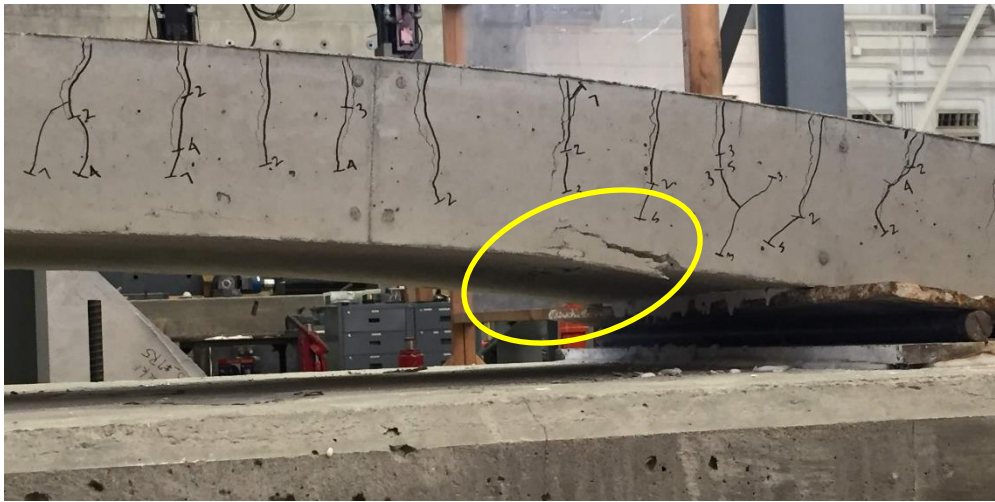


Figure 3.18: Initiation of S-80-5 Failure – East Elevation



Figure 3.19: Final S-80-5 Failure – East Elevation

Load was applied to Specimen S-100-5 until it nearly matched the failure load of Specimen S-80-5. The bar stress achieved in Specimen S-100-5 was nearly equal to the bar stress achieved in Specimen S-80-5, however, failure did not occur. Because the maximum stroke of the loading rams was reached (Figure 3.20), testing was concluded before a flexural failure was observed at the supports. While a flexural failure had not initiated at the supports, it was previously observed in the 50 in. lap splice specimen (S-80-5) that sufficient development length had been provided to prevent a splitting failure.



Figure 3.20: S-100-5 End of Testing

CHAPTER 4. EXPERIMENTAL PROGRAM: BEAMS

4.1 Introduction

The objective of Series VI and VII in Phase II was to investigate the bond strength of high-strength steel reinforcement. Selected variables included splice length, concrete compressive strength, high-strength steels, and transverse reinforcement location. All four parameters were investigated in Series VI by testing eight (8) beams, while the influence of splice length and transverse reinforcement location on bond strength was further investigated in Series VII by testing four (4) additional beams. The program for planning, preparing, and conducting these tests is discussed in this chapter.

4.2 Specimen Selection

4.2.1 Beam Design

For consistency, all specimens tested in Series VI and VII were selected primarily based on specimens designed by Glucksman (2018). Beams with splices confined by transverse reinforcing stirrups are called confined specimens, while beams without transverse reinforcement are called unconfined specimens. Series VI consisted of three confined beams and five unconfined beams, while Series VII contained four confined beams.

Cross-section dimensions are the same for all confined (Figure 4.1(a)) and unconfined (Figure 4.1(b)) beams. Specimen height was selected to be 20 in. No. 8 bars were selected to be the primary longitudinal reinforcement. The confined specimen was designed first using the minimum bottom cover of 1-1/2 in. allowed for No. 8 bars in ACI 318-14 (Table 20.6.1.3.1). For confinement, No. 3 Grade 60 stirrups were selected. The effective depth from the compression

face was therefore calculated to be $17\frac{5}{8}$ in. To maintain this effective depth parameter throughout the unconfined beam specimens and maintain the same cover to the longitudinal reinforcement, a bottom cover of $1\frac{7}{8}$ in. was required for the unconfined cross-section. No. 3 longitudinal bars were included at a distance of $1\frac{7}{8}$ in. from the compression face to aid in steel cage construction, stirrup alignment, and failure containment after testing.

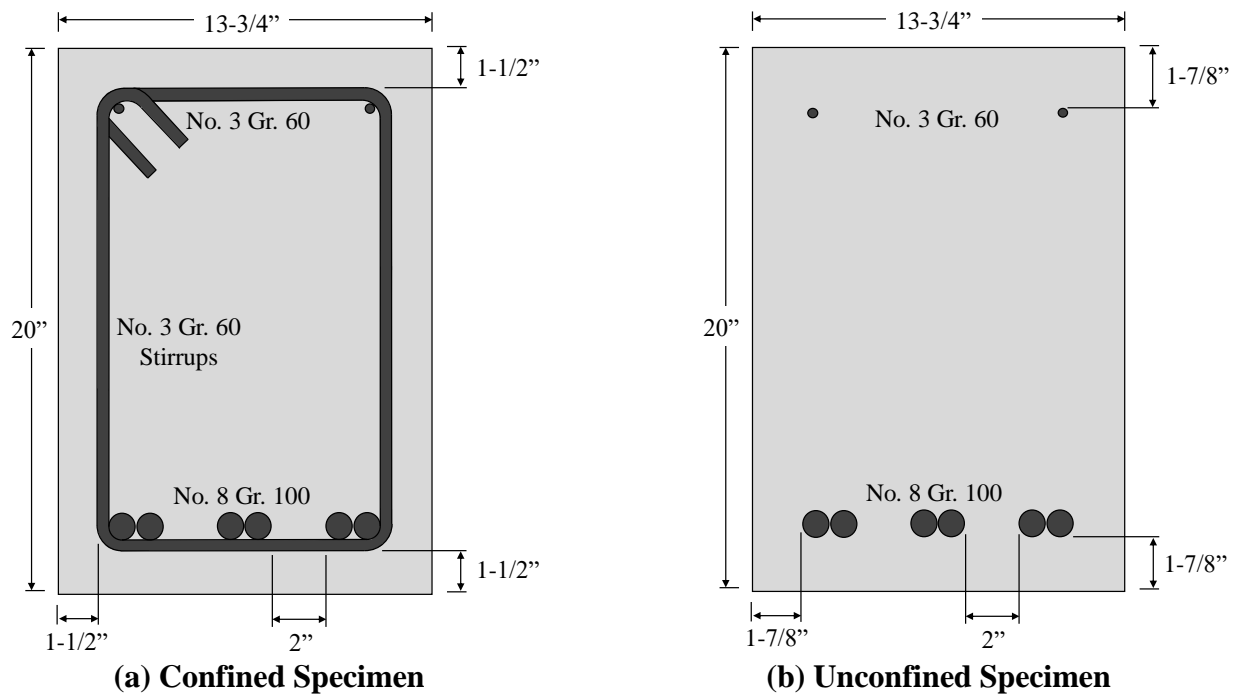


Figure 4.1: Typical Beam Cross-Sections

Three (3) No. 8 Grade 100 longitudinal bars were spliced over a variable length with the clear bar spacing between splices fixed at 2 in. Because of the presence of transverse steel in confined beams, the clear side cover was selected to be $1\frac{1}{2}$ in. to achieve the same side cover of $1\frac{7}{8}$ in. over the longitudinal bars. The resulting overall width was $13\frac{3}{4}$ in. for the confined and unconfined specimens. A total beam length of 26 ft was selected by Glucksman (2018) and implemented in Phase II for specimen consistency.

The unconfined beam specimens were designed with various splice lengths, concrete strengths, and types of high-strength steel. Figure 4.2 discusses the general labeling convention for the unconfined specimens in Series VI.

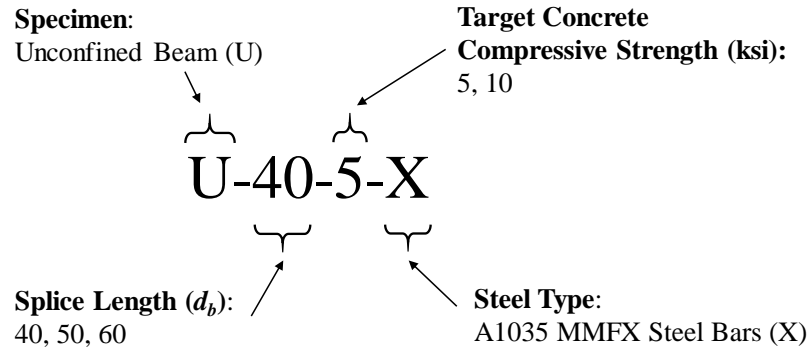


Figure 4.2: Unconfined Specimen Identification Label

For confined beams, a nominal confinement pressure was assigned to give an indication of stirrup spacing based on ACI 318-14:

$$A_{v,min} = 50 \frac{b_w s}{f_{yt}} \quad (4-1)$$

where:

50 = coefficient; represents pressure developed by transverse reinforcement (psi)

$A_{v,min}$ = minimum area of shear reinforcement within spacing s (in.²)

b_w = beam width (in.)

f_{yt} = specified yield strength of transverse reinforcement (psi)

s = center-to-center spacing of transverse reinforcement (in.)

The coefficient 50 represents the tensile-resisting pressure produced by the presence of transverse reinforcement. By rearranging Equation 4-1 to solve for the transverse reinforcement

spacing s , various nominal pressures (p_c) can be substituted into Equation 4-1. For example, a nominal pressure of 50 psi (No. 3 stirrups, Grade 60) results in a stirrup spacing of 19.2 in. for a beam with a width of 13.75 in. Table 4.1 provides a summary of the nominal pressures and stirrup spacings selected in Phase II. The identification label for confined beams is expanded to include this information in Figure 4.3.

Table 4.1: Nominal Confinement Pressure and Spacing

Nominal Pressure, p_c (psi)	Bar Size (No.)	$A_{v,min} = A_t N_l$ (in. ²)	f_{yt} (psi)	b_w (in.)	$s = \frac{A_{v,min} f_{yt}}{p_c b_w}$ (in.)	Spacing used (in.)
25	3	0.22	60,000	13.75	38.4	38
50	3	0.22	60,000	13.75	19.2	19
150	3	0.22	60,000	13.75	6.4	6.375
200	3	0.22	60,000	13.75	4.8	4.75

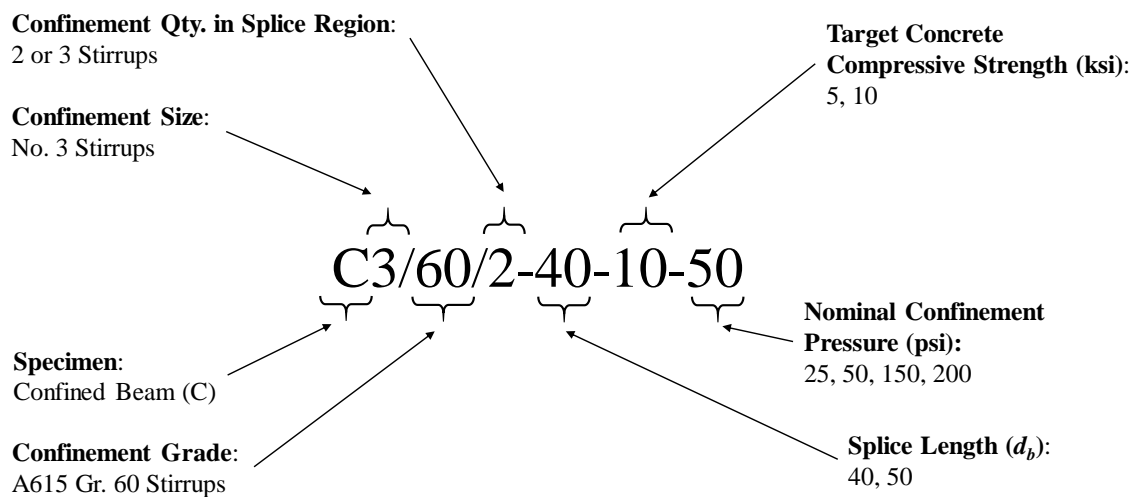


Figure 4.3: Confined Specimen Identification Label

4.2.2 Beam Dimensions

Splice test specimens from previous research programs have been tested in four-point bending to create a tension region at the location of the spliced bars. The four-point bending test setup requires two points of applied loading near the ends of the specimen and two points of support located a distance away from the applied loads (shear span). Due to the 24 in. spacing of the Bowen Laboratory strong floor grid and the need for a symmetric test setup, even dimensions were selected for all spacings between components of the test setup.

Splice length testing requirements of $120d_b$ from Phase I directly influenced the specimen length for Series VI and VII of Phase II. A constant moment region of 16 ft (L_M) was maintained between supports for all beams. This allowed all lap splices (L_S) to be located entirely within this region. The length of the shear region was selected to be 4 ft (L_V) away from the supports. To prevent the possibility of a shear failure during testing, twelve No. 4 Grade 60 stirrups were spaced at 4-1/4 in. between the support and the ends of the beam. A 1 ft overhang (L_O) was included to ensure anchorage of the reinforcement. Overall, the selected dimensions produced a total length of 26 ft (L_T) for all confined and unconfined beam specimens. The beam test configuration is shown in Figure 4.4.

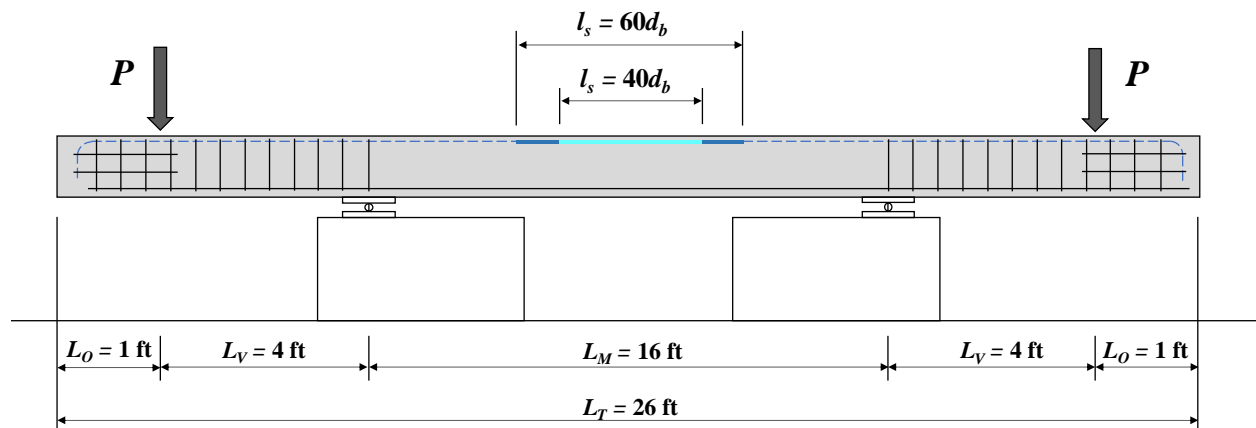


Figure 4.4: Typical Beam Test Specimen

4.2.3 Beam Testing Matrix

Table 4.2 and Table 4.3 provide the testing matrix for the unconfined and confined specimens, respectively. The splice length, concrete strength, and amount of confinement were investigated while the bar size, bar spacing, and concrete cover remained constant for each matrix. All stirrups placed within the constant moment region of the confined specimens were centered at midspan of the beam. Therefore, all beams with an even number of stirrups within the constant moment region did not have a stirrup at midspan. The full stirrup configurations for all confined beams in Series VI and VII can be found in Figure 4.5 and Figure 4.6, respectively.

Table 4.2: Unconfined Beam Testing Matrix

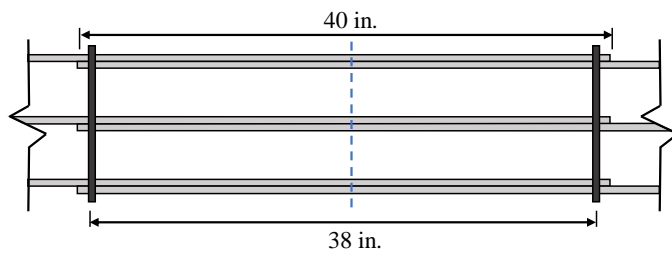
Series	Specimen ID	Splice Length (l_s)		Longitudinal Bar Size (No.)	Target Concrete Strength (f'_c)	c_{si}	c_{so}	c_b
		d_b	in.		ksi	in.	in.	in.
VI	U-40-10	40	40	8	10	1	1.875	1.875
	U-60-10	60	60	8	10	1	1.875	1.875
	U-40-5-X	40	40	8	5	1	1.875	1.875
	U-60-5-X	60	60	8	5	1	1.875	1.875
	U-50-5	50	50	8	5	1	1.875	1.875

Table 4.3: Confined Beam Testing Matrix

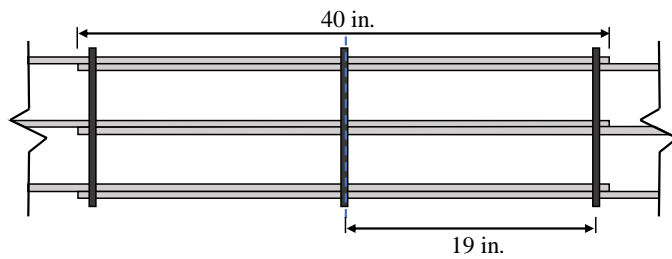
Series	Specimen ID	Splice Length (l_s)		Long. Bar Size (No.)	Target Concrete Strength (f'_c)	c_{si}	c_{so}	c_b	Nominal Pressure (p_c)	Stirrup Spacing ^[1] (s)	Total No. Stirrups		
		d_b	in.		ksi	in.	in.	in.	psi	in.	Splice Region	Constant Moment Region ^[2]	Shear Regions
VI	C3/60/2-40-10-50	40	40	8	10	1	1.5	1.5	50	19	2	10	24
	C3/60/3-40-10-50	40	40	8	10	1	1.5	1.5	50	19	3	9	24
	C3/60/2-40-10-25	40	40	8	10	1	1.5	1.5	25	38	2	4	24
VII	C3/60-40-5-150	40	40	8	5	1	1.5	1.5	150	6.375	6	12	24
	C3/60-40-5-200	40	40	8	5	1	1.5	1.5	200	4.75	8	14	24
	C3/60-50-5-150	50	50	8	5	1	1.5	1.5	150	6.375	8	14	24
	C3/60-50-5-200	50	50	8	5	1	1.5	1.5	200	4.75	10	16	24

[1] Spacing for stirrups within constant moment region.

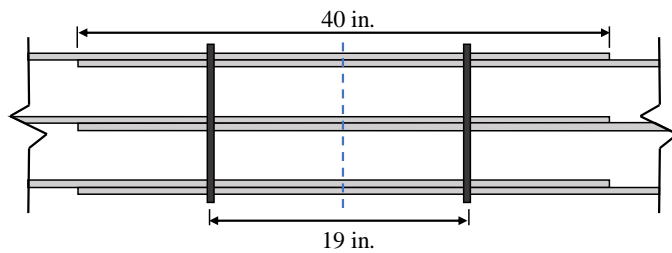
[2] Stirrups within the splice region.



(a) C3/60/2-40-10-25

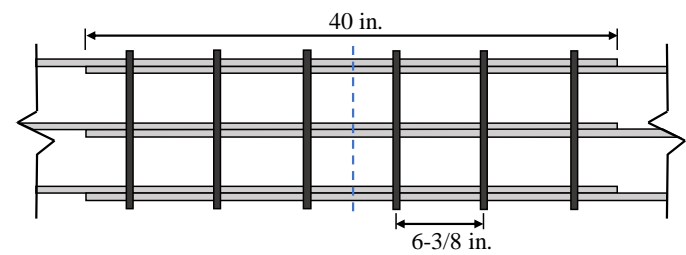


(b) C3/60/3-40-10-50

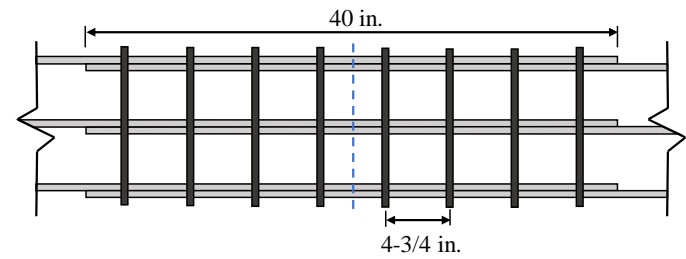


(c) C3/60/2-40-10-50

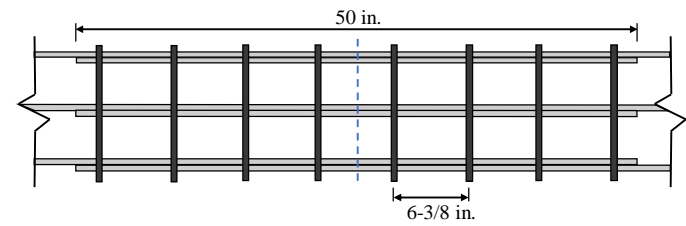
Figure 4.5: Series VI Stirrup Configurations



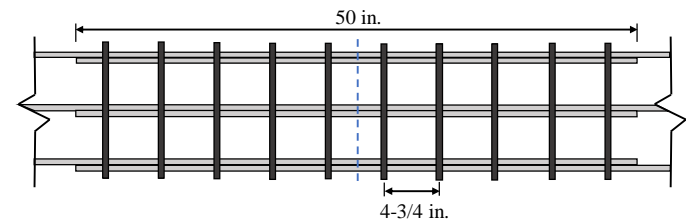
(a) C3/60-40-5-150



(b) C3/60-40-5-200



(c) C3/60-50-5-150



(d) C3/60-50-5-200

Figure 4.6: Series VII Stirrup Configurations

4.3 Materials

4.3.1 Concrete

Concrete for Series VI and VII was provided by Irving Materials, Inc. (IMI). All test specimens were constructed and cast in the Bowen Laboratory for Large-Scale Civil Engineering Research in West Lafayette, Indiana.

The concrete mixture design selected for three specimens in Series VI and all of Series VII was consistent with Phase I of this project. The concrete had a target compressive strength of 5000 psi and a target slump of 6 in. A breakdown of general casting information for both series, indicating the division of specimens by truck, is given in Table 4.4. The mix design for the normal-strength mix is provided in Table 4.5 with the batched quantities in Series VI and VII.

Table 4.4: General Beam Casting Information

Casting Quantities	Series VI			Series VII
Cast Date	9/18/2018			12/18/2018
Truck No.	1	2	3	1
Load Size (yd ³)	7	5	7	8.5
Specimens	U-60-10	U-40-10	U-40-5-X	C3/60-40-5-150
	C3/60/3-40-10-50	C3/60/2-40-10-25	U-60-5-X	C3/60-40-5-200
	C3/60/2-40-10-50	-	U-50-5	C3/60-50-5-150
	-	-	-	C3/60-50-5-200

Table 4.5: Normal-Strength Concrete – Mix Design Summary (Series VI and VII)

Material	Type	Mix Design 4101CC	Batched	
			Series VI Truck 3	Series VII
Cement	ASTM C150 - Type I (lb/yd ³)	517	512	514
Course Aggregate	#8 Limestone (lb/yd ³)	1875	1866	1875
Fine Aggregate	#23 Natural Sand (lb/yd ³)	1475	1523	1522
Water-Reducing Admixture (oz/yd ³)	MasterGlenium 7511 (oz/yd ³)	20.7	20.2	20.6
Water (lb/yd ³)		250	248	251
Water/Cement Ratio		0.483	0.485	0.471
Slump (in.)		6.0	6.0	5.5

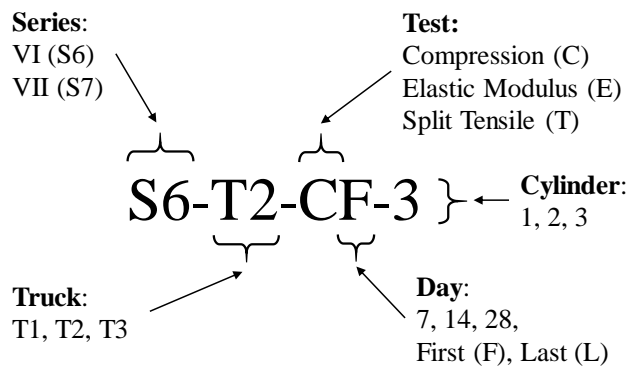
For Series VI, five of the eight beams required a mix design to achieve a target compressive strength of 10,000 psi. The selection of cementitious material, coarse aggregate, and fine aggregate was consistent with the previous mix design selected for normal-strength concrete; however, slag and silica fume were also included. The mix design for the high-strength concrete beams in Series VI is provided in Table 4.6 along with the batched quantities.

Table 4.6: High-Strength Concrete – Mix Design Summary (Series VI)

Material	Type	Mix Design 7820CM	Batched	
			Series VI Truck 1	Series VI Truck 2
Cement	ASTM C150 - Type I (lb/yd ³)	705	703	702
	ASTM C989 - Slag (lb/yd ³)	200	202	198
	ASTM C1240 - Silica Fume (lb/yd ³)	25	25	25
Course Aggregate	#8 Limestone (lb/yd ³)	1700	1691	1692
Fine Aggregate	#23 Natural Sand (lb/yd ³)	1203	1243	1244
Water- Reducing Admixture	MasterGlenium 7511 (oz/yd ³)	65.1	62.9	63.2
Water (lb/yd ³)		275	269	268
Water/Cement Ratio		0.304	0.297	0.298
Slump (in.)		6.0	5.0	5.5

4.3.1.1 Concrete Testing

In Series VI and VII, mechanical properties of the concrete were determined using an ASTM C193 standard cylinder size of 6 x 12 in. for each truck. Before cylinder testing began, each cylinder was marked with a label indicating series, truck number, designated test, and cylinder number for that test. Figure 4.7 shows an example of the identification label.

**Figure 4.7: Cylinder Testing Identification**

4.3.1.2 Compression Testing

To determine the increase in compressive strength of the concrete as it cured, several cylinders were tested to failure following the “Standard Test Method for Compressive Strength of Cylindrical Concrete Specimens” in ASTM C39 (2018).

Steel caps lined with a neoprene elastomeric pad were installed on the top and bottom faces of the cylinder to ensure uniform distribution of the compression load and to reduce the chances of edge spalling. Two standard 60-durometer pads were selected for Truck 3 of Series VI and all cylinders in Series VII consistent with the target compressive strength of the concrete mix. Two 70-durometer pads were selected for Truck 1 and Truck 2 in Series VI because of the use of high-strength concrete. Compressive strengths were recorded and averaged in Table 4.7 through Table 4.10. A typical compression cylinder test setup before and after failure is shown in Figure 4.8(a) and Figure 4.8(b), respectively. Average concrete compressive strength, f_c , over time is also plotted in Figure 4.9. The compressive strength gain for Series V is included for comparison.

Table 4.7: Series VI Truck 1 Compression and Tension Properties

Time (days)	Compressive Strength, f_c (psi)				Fracture Pattern (ASTM C39)			Split Tensile Strength, f_t (psi)			
	Cylinders			Avg.	Cylinders			Cylinders			Avg.
	1	2	3		1	2	3	1	2	3	
7	8630	8490	8430	8520	6	4	6	-	-	-	-
14	9190	9140	8990	9110	3	5	6	-	-	-	-
28 ^[1]	8960	9820	10,000	9590	6	5	5	680	660	525	622
35 ^[2]	10,200	10,300	9790	10,100	4	5	6	580	665	755	667

[1] First Day of Testing

[2] Last Day of Testing

Table 4.8: Series VI Truck 2 Compression and Tension Properties

Time (days)	Compressive Strength, f_c (psi)				Fracture Pattern (ASTM C39)			Split Tensile Strength, f_t (psi)			
	Cylinders			Avg.	Cylinders			Cylinders			Avg.
	1	2	3		1	2	3	1	2	3	
28	9680	10,100	9480	9750	4	5	5	505	755	815	692
37 ^[1]	10,400	10,000	9780	10,100	3	2	6	625	685	725	678
58 ^[2]	10,100	9000	10,500	9870	6	6	3	-	-	-	-

[1] First Day of Testing

[2] Last Day of Testing

Table 4.9: Series VI Truck 3 Compression and Tension Properties

Time (days)	Compressive Strength, f_c (psi)				Fracture Pattern (ASTM C39)			Split Tensile Strength, f_t (psi)			
	Cylinders			Avg.	Cylinders			Cylinders			Avg.
	1	2	3		1	2	3	1	2	3	
7	4340	4210	4180	4240	6	5	2	-	-	-	-
14	4620	4870	4800	4760	2	2	5	-	-	-	-
28	5180	5120	5320	5210	5	6	3	395	560	485	480
43 ^[1]	5320	5260	5350	5310	5	6	5	495	560	595	550
69 ^[2]	5680	5840	5500	5670	2	2	2	465	555	580	533

[1] First Day of Testing

[2] Last Day of Testing

Table 4.10: Series VII Compression and Tension Properties

Time (days)	Compressive Strength, f_c (psi)				Fracture Pattern (ASTM C39)			Split Tensile Strength, f_t (psi)			
	Cylinders			Avg.	Cylinders			Cylinders			Avg.
	1	2	3		1	2	3	1	2	3	
21	5700	6090	-	5900	2	2	-	-	-	-	-
28 ^[1]	6160	6320	6160	6210	5	6	5	520	620	540	560
42 ^[2]	6540	6670	6710	6640	5	6	5	545	510	495	517

[1] First Day of Testing

[2] Last Day of Testing

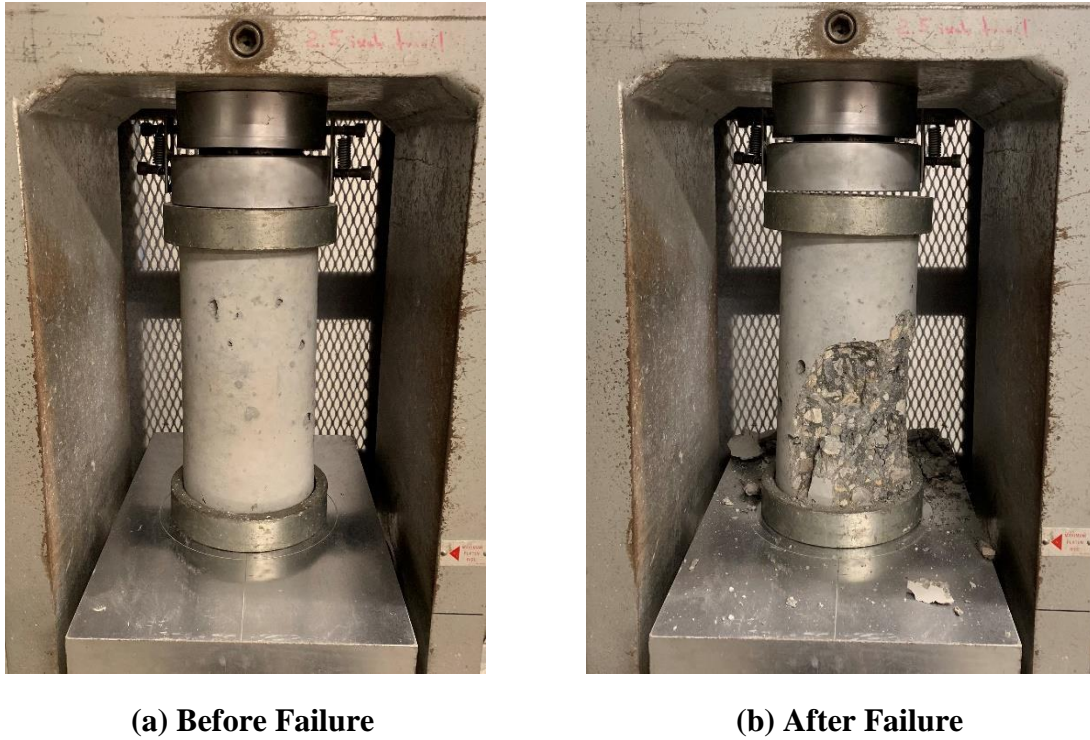


Figure 4.8: Typical Compression Cylinder Failure

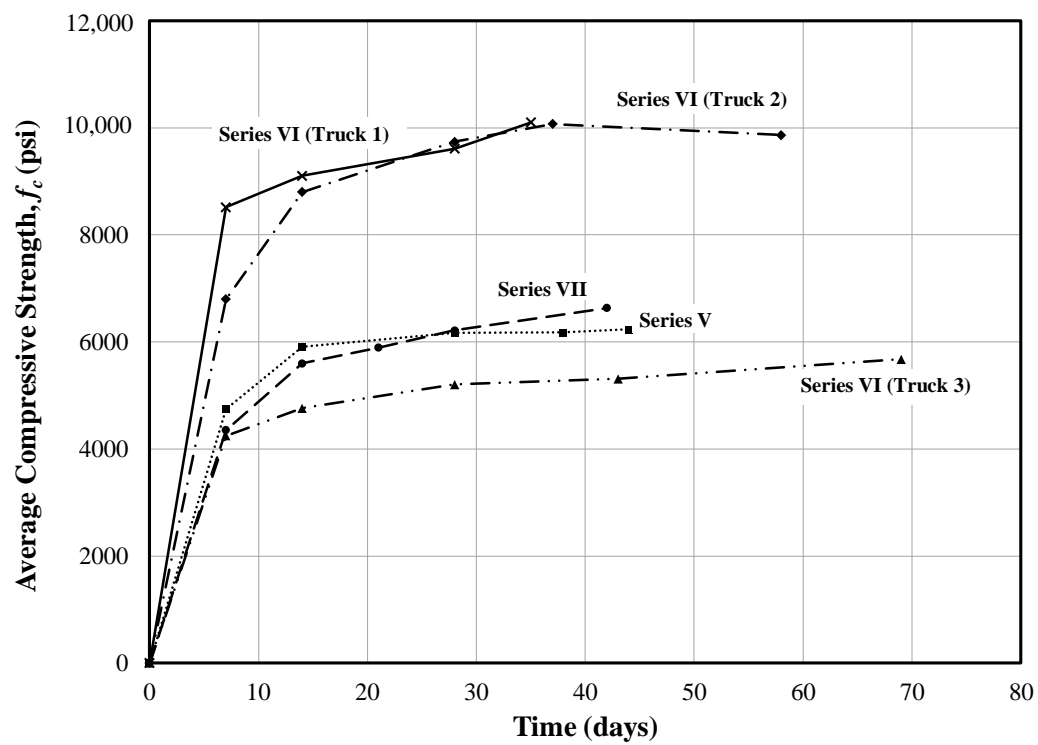


Figure 4.9: Concrete Compressive Strength Variation Over Time

4.3.1.3 Split Cylinder Testing

Split cylinder testing was conducted in accordance with ASTM C496 (2017). Tensile strengths were recorded and averaged in Table 4.6 through Table 4.9. A typical splitting tensile test setup before and after failure is shown in Figure 4.10(a) and Figure 4.10(b), respectively.



(a) Before Failure



(b) After Failure

Figure 4.10: Series VI Splitting Tensile Cylinder Failure

4.3.1.4 Elastic Modulus and Poisson's Ratio

The method for determining Young's modulus and Poisson's ratio followed the same procedure as Series V and was in accordance with ASTM C469 (2014). Average compressive load from previous testing was used to specify a 40% upper bound for modulus testing (ASTM C469) conducted over three loading cycles. Average values for Young's Modulus and Poisson's Ratio were calculated and provided in Table 4.11 through Table 4.14.

Table 4.11: Series VI Truck 1 Stress-Strain Properties

Time (days)	Young's Modulus, E (ksi)			Poisson's Ratio, ν		
	Cylinders		Avg.	Cylinders		Avg.
	1	2		1	2	
28 ^[1]	5470	5570	5520	0.27	0.27	0.27
35 ^[2]	5620	5910	5770	0.27	0.27	0.27

[1] *First Day of Testing*[2] *Last Day of Testing***Table 4.12: Series VI Truck 2 Stress-Strain Properties**

Time (days)	Young's Modulus, E (ksi)			Poisson's Ratio, ν		
	Cylinders		Avg.	Cylinders		Avg.
	1	2		1	2	
37 ^[1]	5540	5530	5540	0.28	0.26	0.27

[1] *First Day of Testing***Table 4.13: Series VI Truck 3 Stress-Strain Properties**

Time (days)	Young's Modulus, E (ksi)			Poisson's Ratio, ν		
	Cylinders		Avg.	Cylinders		Avg.
	1	2		1	2	
43 ^[1]	5150	5010	5080	0.48	0.24	0.36
69 ^[2]	5130	4910	5020	0.29	0.22	0.26

[1] *First Day of Testing*[2] *Last Day of Testing***Table 4.14: Series VII Stress-Strain Properties**

Time (days)	Young's Modulus, E (ksi)			Poisson's Ratio, ν		
	Cylinders		Avg.	Cylinders		Avg.
	1	2		1	2	
28 ^[1]	5800	5570	5690	0.24	0.20	0.22
42 ^[2]	5620	5620	5620	0.25	0.26	0.26

[1] *First Day of Testing*[2] *Last Day of Testing*

4.3.2 Reinforcing Steel

Reinforcing steel in Series VI and VII was supplied by Nucor Steel, Kankakee, Illinois, and fabricated by Harris Rebar (Series VI) and Circle City Rebar (Series VII). Longitudinal and transverse reinforcing bars were used in Series VI and VII. Table 4.15 provides information for the reinforcing steel used in these two series. All bars designated as Grade 100 were rolled from the same heat while Grade 60 bars of different sizes were rolled from different heats.

Table 4.15: Reinforcing Steel Bar Information

Series	Material	Type	Supplier	Fabricator	Grade	Size (No.)	Purpose
VI	ASTM A615	Black	Nucor ^[1]	Harris Rebar ^[2]	60	3	Vertical Stirrups
							Longitudinal Compression
						4	Vertical Stirrups
							Horizontal Stirrups
					100	8	Longitudinal
	ASTM A1035	MMFX ^[3]	Cascade ^[4]	Harris Rebar	100	8	Longitudinal
VII	ASTM A615	Black	Nucor	Circle City Rebar ^[5]	60	3	Vertical Stirrups
							Longitudinal Compression
						4	Vertical Stirrups
							Horizontal Stirrups
				Harris Rebar	100	8	Longitudinal

[1] Nucor Steel-Kankakee, IL

[2] Harris Rebar-Mooresville, IN

[3] MMFX, a Commercial Metals Company-Irving, TX

[4] Cascade Steel Rolling Mills, Inc.-McMinnville, OR

[5] Circle City Rebar, LLC-Indianapolis, IN

4.3.2.1 ASTM A615

Bar strength testing was conducted in a 220-kip MTS universal testing machine for all longitudinal bars and a 120-kip Baldwin universal testing machine for smaller transverse reinforcement. Stress was calculated by dividing applied load by the nominal bar area. A 2 in. extensometer was installed on each bar to measure strain during testing. A typical stress-strain response for the A615 No. 8 bars is provided in Figure 4.11, while the stress-strain responses for all steel used in Series VI and VII is provided in Appendix A. From the linear-elastic region of the response, the linear-elastic limit was estimated by determining the point where the linear slope begins to decrease. The 0.2% offset method, as specified in ASTM E8-04 (2016), was selected to determine the yield strength of the steel in Series VI and VII. The ultimate strength of the steel occurred just before fracture. Material properties are documented in Table 4.16.

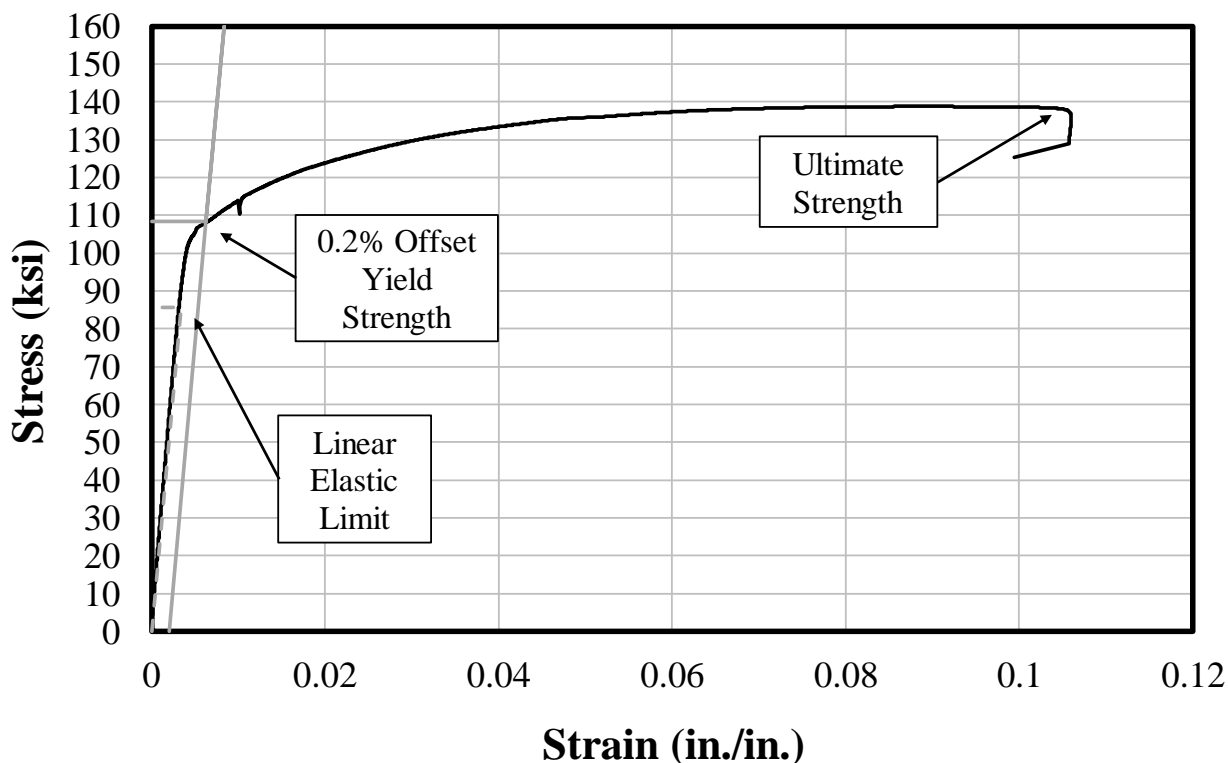


Figure 4.11: Typical Stress-Strain Response for A615 Gr. 100 No. 8 Bars

Table 4.16: ASTM A615 Material Properties

Series	ASTM	Bar Size (No.)	Grade	Elastic Limit Stress (ksi)	Yield Stress 0.2% Offset (ksi)	Ultimate Strength (ksi)
VI	A615	3	60	62	79	101
VII				58	64	98
VI, VII	A615	4 ^[1]	60	-	-	-
VI, VII		8	100	87	108	140

[1] No. 4 bars in Series VI and VII were not included in the test region

For Series VI and VII beam construction, an additional shipment of high-strength steel was required. This shipment was from the same heat and rolled at the same time as the initial steel shipment from Phase I of this testing program; however, these bars were stored outside and accumulated rust along the surface. Abrams (1913) suggested that the formation of rust on the bar surface helps to increase bond strength. To prevent the iron oxide from significantly affecting bond strength, the bars were wire-brushed within the splice region and approximately 12 in. outside of the splice region for all beams constructed with this steel is Series VI and VII. A comparison between the original bar shipment, the new shipment before wire brushing, and the new shipment after wire brushing is provided in Figure 4.12. Wire brushing was conducted in accordance with ACI 318-14 (Section 26.6.1.2).

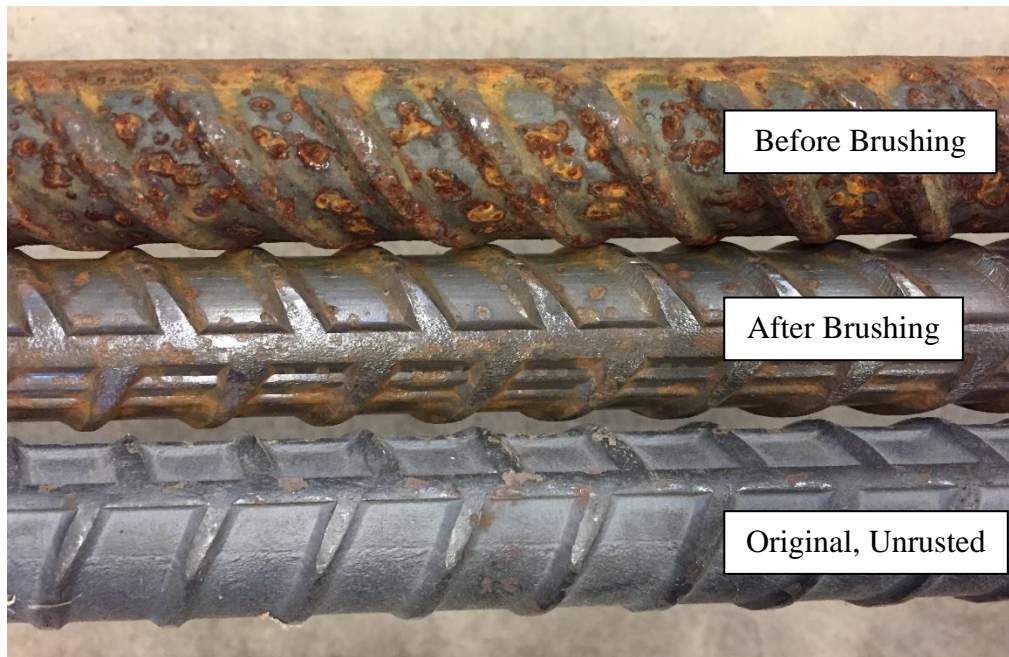


Figure 4.12: Comparison of Grade 100 Bar Surfaces

4.3.2.2 MMFX

Conforming to ASTM A1035, MMFX steel (Martensitic Microcomposite Formable Steel) is a low-carbon, high chromium alloy, high-strength steel. Tests were conducted in Series VI of this research program to investigate bond capacity in members constructed using MMFX longitudinal reinforcement.

This steel was used in two specimens in Series VI and was supplied by Cascade Steel Rolling Mills, Inc. in McMinnville, Oregon. In this program, the ChromX 9000 series of steel bars with a minimum specified yield strength of 100 ksi were tested, formerly known as MMFX II. A typical stress-strain response for the A1035 No. 8 bars is provided in Figure 4.13, while material properties are documented in Table 4.17.

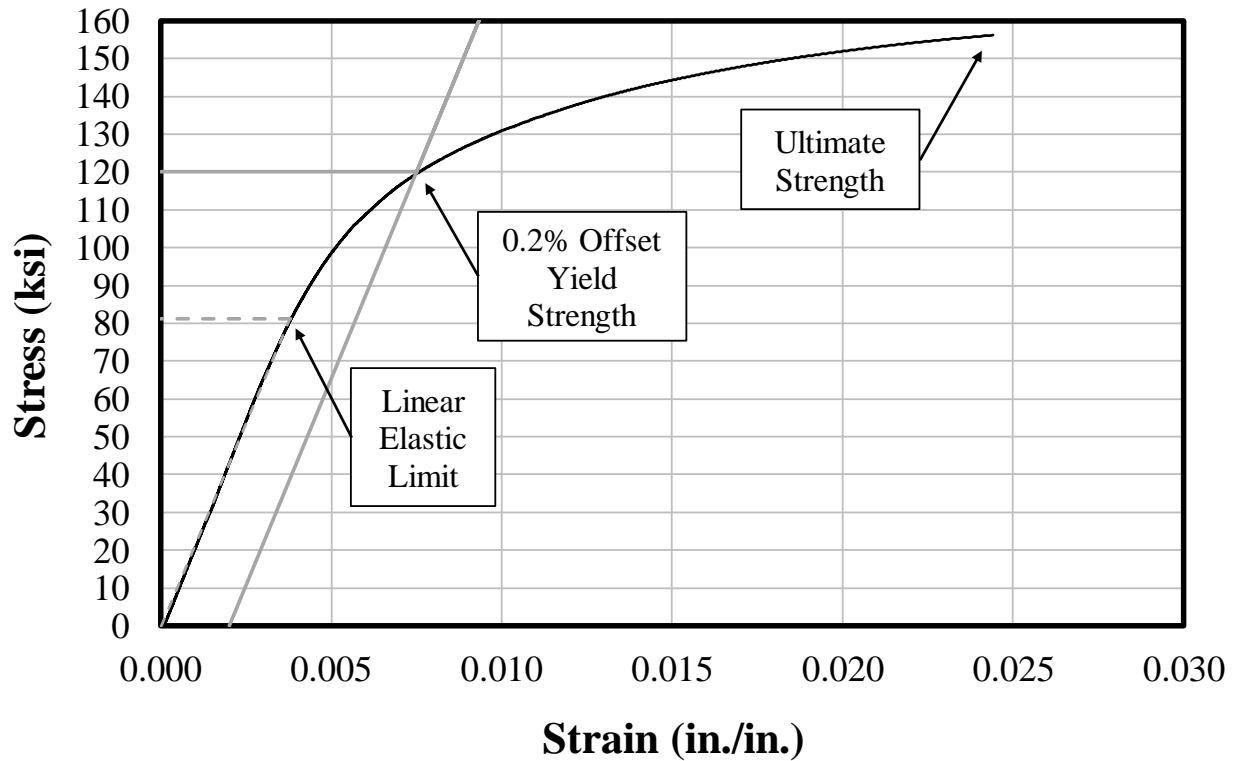


Figure 4.13: Typical Stress-Strain Response for A1035 Gr. 100 No. 8 Bars

Table 4.17: ASTM A1035 Material Properties

Series	ASTM	Bar Size (No.)	Grade	Elastic Limit Stress (ksi)	Yield Stress 0.2% Offset (ksi)	Ultimate Strength (ksi)
VI	A1035	8	100	81	120	156

4.4 Specimen Construction

Twelve (12) beam specimens were constructed by first arranging and securing the appropriate formwork. Once formwork construction was completed, the necessary steel was placed and tied within the forms before casting.

4.4.1 Formwork Assembly

For specimens cast in Series VI and VII, the same four platforms from Series V were used. A 20 in. vertical center form was secured along the bottom face with lag screws to divide each of the four platforms into 2 halves. This center form was constructed on 2 x 4 in. lumber. Typical 2 x 4 in. wood bracing studs were installed vertically at a 16 in. spacing along the length. With the center form complete, a 20 in. wide sheet of HDO plyform with a thickness of 3/4 in. was attached on one side using 3/8 in. diameter wood screws. Finally, another plyform sheet was attached to the other side, enclosing and completing the center form. The components of the formwork are shown in Figure 4.14.

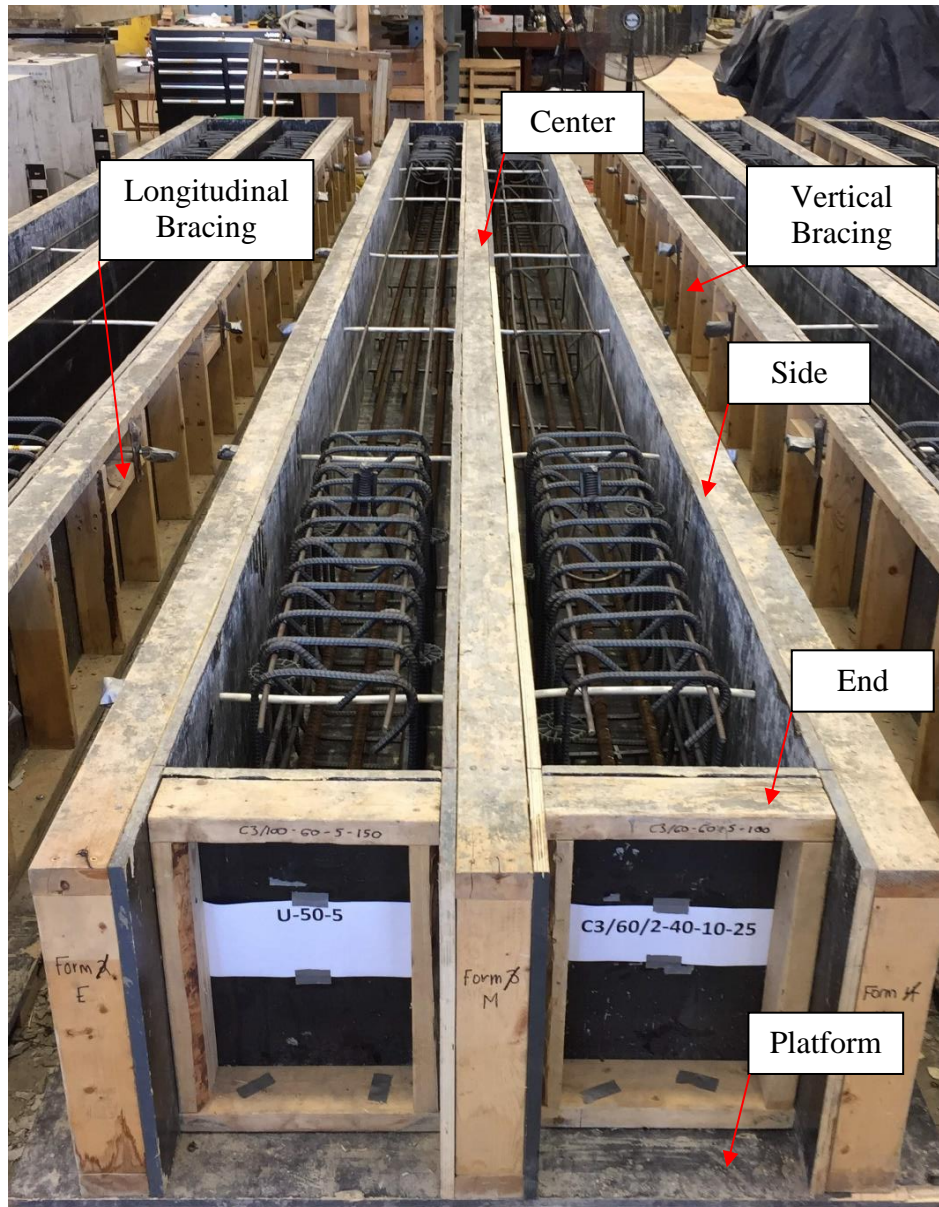


Figure 4.14: Series VI and VII Formwork Components

The side forms for each platform were constructed in the same manner as the center form, but only one side sheet of HDO plyform was required for each. Supplemental stability was provided by adding longitudinal bracing throughout the side forms (Figure 4.14). This also provided a bracing point for the end plates of the form tie installations.

The end forms were constructed identically to the side forms but with an overall length of 13-3/4 in. to match the specified width of the beam specimens. The locations of all formwork components were first marked on the platforms with chalk lines before being secured with 1/4 in. lag screws and washers. The completed formwork construction for Series VI is shown in Figure 4.15(a), while the completed formwork construction for Series VII is shown in Figure 4.15(b).



(a) Series VI



(b) Series VII

Figure 4.15: Beam Specimen Formwork Space

Any remaining concrete from previous casts was removed from all plyform surfaces to ensure a flat and clean surface for Series VI casting. Any seams, joints, or noticeable damage on the plyform surfaces were repaired with silicone caulk and smoothed. All end forms were labeled with the appropriate beam identification label in Series VI and VII before cage construction began. Series VII required the construction of new end and side forms as a result of poor formwork surface conditions. Center forms and platforms were repaired as needed and oiled before casting.

4.4.2 Steel Cage Construction

The longitudinal steel for all cages was placed near the bottom of the forms so that the reinforcement was in the bottom cast position. Seven blocks of 4 x 6 in. lumber were placed above each beam's formwork to support the hanging steel cage during construction (Figure 4.16). Two No. 3 mild steel bars were marked with the location of stirrups and the midpoint for each beam, extending from the shear region on one end of the beam to the shear region on the other. The No. 3 mild steel bars were mounted on the 4 x 6 in. wood blocks above each form void to be cast in the compression zone of the beams.



Figure 4.16: Series VII Cage Support Blocks

Because Series VI contained confined and unconfined specimens, different stirrup layouts were used. For unconfined beams, stirrups were necessary in both end shear regions (Figure 4.17(a)). For those beams with confining steel, stirrups were placed along the length of the member in the constant moment region (Figure 4.17(b)) and both shear regions. For confined beams in Series VI, stirrups were included along the entire length of the constant moment region. For confined beams in Series VII with transverse steel in the constant moment region, stirrups were included over the entire splice and three stirrups were included past both ends of the splice. This had no effect on experimental results and allowed the construction process to be expedited. All stirrups were attached to the No. 3 mild steel bars using 9 in. annealed steel ties.



(a) Shear Region



(b) Splice Region

Figure 4.17: Typical Beam Cage Construction Details

Longitudinal reinforcement was laid out, marked, and cut to the appropriate length for the splice lengths selected. By leaving the end forms unsecured from each beam, longitudinal steel was placed within the beam from the end, bearing directly on the hanging stirrups. The six bars in each beam were aligned with a plumb bob to achieve the correct lap splice configuration and bar spacing within the splice region. For confined specimens, the lap splice was configured within the constant moment region using 9 in. steel ties to engage the longitudinal reinforcing and the stirrups (Figure 4.17(b)); however, because the unconfined splice had no stirrups for support in the constant moment region, wood cribbing was placed in the middle of the beam beneath the splice region to keep the center of the longitudinal bars level with the ends while tying. Two horizontal stirrups were placed at the ends of each beam and tied to the vertical stirrups (Figure 4.18) to provide confinement and prevent splitting at the ends of the hooks.



Figure 4.18: Beam Shear Region and Cage Lifting

Once tying was complete, an overhead crane was used to lift the cages up, allowing the 4 x 6 in. support blocks to be removed and the form bases to be cleaned. Plastic chairs (2 in.) were cut and grinded to a specified height of 1-7/8 in. before being spaced within the form at regular intervals of 3 ft. To avoid altering the propagation of stresses that develop within the splice region, a single chair was placed at the middle of the region where bond stress was considered to be the smallest to provide stability in cage construction and to maintain the bar spacing, top cover, and side cover. Care was taken to prevent chairs from being placed at the ends of the splice region where bond stress is maximum. Chairs were instead placed just outside the splice region to avoid altering the distribution of tensile stresses along the length of the splice. Cages were lowered back into the forms onto the chairs and adjusted to align the center of the splice with the center of the form for all confined (Figure 4.19(a)) and unconfined (Figure 4.19(b)) beams.



(a) Confined Specimen



(b) Unconfined Specimen

Figure 4.19: Typical Beam Cage Configurations

Steel coil loop lifting-inserts were greased and attached to the end stirrups 42 in. from each end of the beam using 9 in. steel ties. Threaded bars (1/4 in. diameter) were guided through the formwork and secured at the ends using wheeler plates and nuts to prevent the formwork sides from bowing out when the concrete was later cast. Polyvinyl chloride tubing surrounded the threaded bars within the steel cage to prevent bonding with the concrete and to permit easy removal during moist curing. Plastic spacer wheels were placed at the ends of each beam along the sides of the stirrups to achieve proper alignment of the steel cage with respect to the formwork. Figure 4.20 shows the final construction details. All end forms were secured, and all cages were straightened and cleaned before casting.



Figure 4.20: Final Beam Construction Details

4.5 Casting, Curing, and Storage

4.5.1 Cylinders

The interior face of all plastic 6 x 12 in. cylinder molds was lined with a thin layer of form oil to aid in the demolding process after curing. Slump tests were performed before casting cylinders (Figure 4.21(a)). Molds were filled halfway before using a low frequency internal vibrator to consolidate the concrete. The mold was then filled to the top and vibrated a second time, ensuring that the steel-head vibrator penetrated the bottom layer of concrete approximately 1 in. to consolidate the concrete (Figure 4.21(b)). The top surface was finished before sealing the mold with a domed plastic lid to prevent moisture loss and maintain shape during curing.

All concrete cylinders were cured in the same location as the specimens to prevent any differences in humidity or temperature. Each cylinder was moist cured for seven days. On Day 7, all cylinders were relocated for storage, and all plastic molds were removed. The cylinders were labeled with the appropriate series, truck, and test number (Figure 4.7) before being stored.



(a) Slump Test



(b) Cylinder Casting Space

Figure 4.21: Series VI Cylinders

4.5.2 Casting

4.5.2.1 Series VI

All specimens in Series VI were cast at the same time from the same delivery of concrete. Series VI required the use of three trucks of concrete due to the number of specimens tested and the requirement of two different target compressive strengths. All three slump tests achieved an appropriate measure of slump on the first test. The beams in Series VI were filled using two equal lifts along the beam length due to the increased member depth required for consolidation. Because each platform housed formwork for two beams, half of one beam was filled followed by filling the neighboring beam halfway to prevent bowing of the formwork (Figure 4.22(a)). Concrete was then placed to the top of each beam.



(a) Half-Beam Casting



(b) Casting In Progress

Figure 4.22: Series VI Casting Process

Concrete was delivered to the specimens using a concrete bucket. Care was taken to ensure that the steel cages stayed in place while concrete was placed. Two external mechanical vibrators operating at 3600 cycles per minute (60 Hz) were inserted following concrete shoveling to maximize consolidation. Concrete from a given truck was maintained in one specimen; therefore, it was not possible to balance side-by-side beams in all cases (Figure 4.22(b)). To prevent the neighboring voided form from bowing out during the wait for the following truck of concrete, metal rods were used to brace the formwork to the correct nominal width of 13-3/4 in. (Figure 4.23). This resulted in Specimens U-60-10 and C3/60/2-40-10-25 needing bracing. Because the high-strength concrete mix set very fast due to the warm temperature of the day, the top compression surface of these two beams was not finished perfectly level. This variation was not considered a problem as this was the compression face of the member during testing.



Figure 4.23: Series VI Form Bracing

Once all the concrete had been cast and vibrated within each test specimen, the top surface was screeded with 2 x 4 in. lumber and finished by hand with a float. Figure 4.24 shows the final state of all eight beams after casting was completed.



Figure 4.24: Series VI Cast Complete

4.5.2.2 Series VII

The concrete casting process for Series VII was conducted similar to Series VI. Because only one truck was required with one target compressive strength, no center form bracing with external steel bars was required. The half-beam cast method from Series VI was implemented when placing concrete to maintain stability. Once all the concrete had been cast, consolidation was provided by vibrating each test specimen along the entire length (Figure 4.25(a)). All beams were screeded with 2 x 4 in. lumber (Figure 4.25(b)) and finished by hand with a float. The casting process and completed specimens are shown in Figure 4.26 and Figure 4.27, respectively.



(a) Consolidation Process



(b) Screeding Process

Figure 4.25: Series VII Casting Procedure



Figure 4.26: Series VII Cast In Progress



Figure 4.27: Series VII Cast Complete

4.5.3 Curing and Storage

Once all test specimens were finished and cured for approximately one hour, a final finish was performed with a magnesium float to smooth out any noticeable irregularities in specimen height. To initiate moist curing, all specimens were covered with burlap sheets and watered evenly (Figure 4.28). Plastic sheathing was then placed over the specimens to maintain moisture and promote hydration (Figure 4.29). The burlap was watered each day for the following five days, with the final watering period occurring on Day 6. On Day 7, the burlap was not watered and three compression cylinder tests were performed to evaluate strength gain of the concrete.



Figure 4.28: Series VI Moist Curing – Burlap Cover



Figure 4.29: Series VI Moist Curing – Plastic Cover

Once the concrete had adequate strength on Day 7, the side formwork and threaded bars were completely removed from all beams. The beams were then flipped (Figure 4.30) about their longitudinal axis using the crane to orient the lap splice on the top face of each member. All beams were stacked in a staging area before being moved to the test setup.

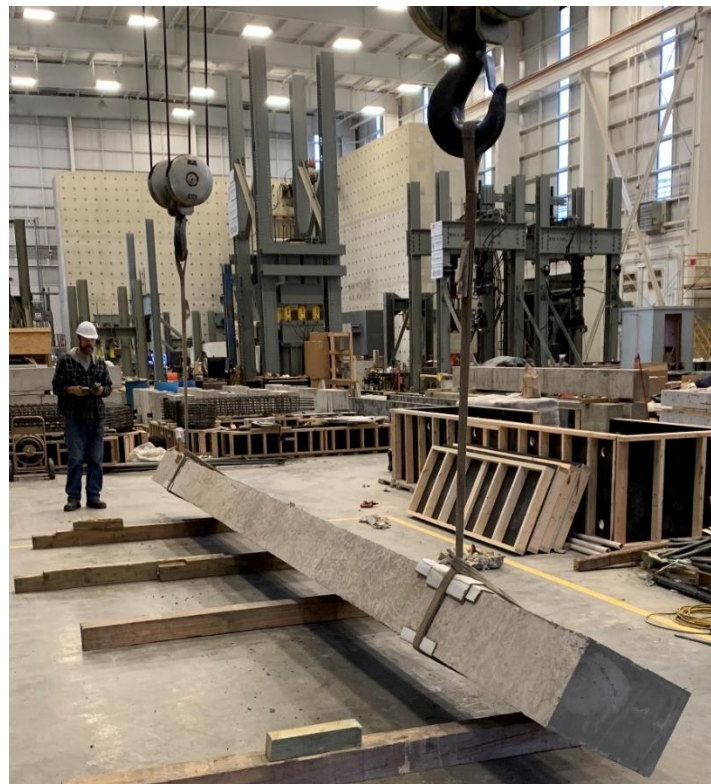


Figure 4.30: Series VII Beam Flipping Process

4.6 Test Setup

4.6.1 Schematic

All specimens in Series VI and VII were tested in four-point bending using an identical test setup shown in Figure 4.31. Roller supports were selected to support the specimens during testing. Due to the larger moment of inertia compared to the slab specimens and lower expected deflections, a 1 in. steel rod was selected for the roller supports. The rod was placed between two 1/2 in. thick steel plates measuring 6 x 24 in. to distribute bearing stresses uniformly (Figure 4.32(a)). The supports under all beams were constructed on two 4 x 4 x 2-1/2 ft concrete bearing blocks. Hydrostone was used to secure these components to the bearing blocks and the specimens. Wood cribbing was placed below the test specimens in the middle and near the ends to protect string potentiometers (Figure 4.32(b)) and provide a safer testing environment when failure was reached.

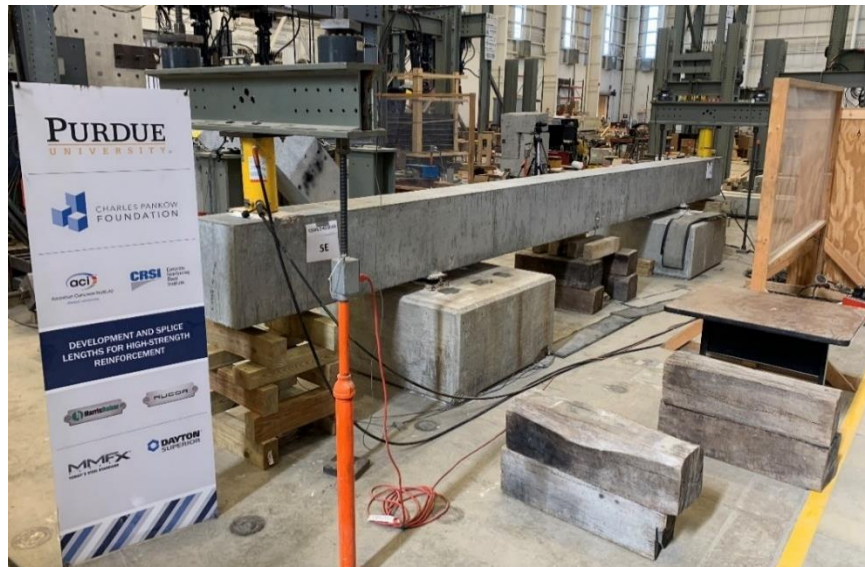


Figure 4.31: Series VI and VII Test Setup



(a) Roller Support



(b) Middle Cribbing

Figure 4.32: Series VI and VII Testing Details

Once the beams were placed and secured with hydrostone to the roller supports, two bearing plates were positioned on the top face to align with the loading rams. Two (2) 100-ton double-acting hydraulic rams, each with a maximum stroke of 9.8 in. were secured to the bottom face of a crossbeam built-up from a double channel steel section using 3/8 in. bolts (Figure 4.33). The crossbeam was threaded through two 1-1/4 in. diameter DYWIDAG bars that were secured to the strong floor. Center-hole load cells were secured above the crossbeam before being threaded through the supporting DYWIDAG bars. Once the hydraulic rams were lowered and centered on the bearing plates, the crossbeam was leveled. Figure 4.34 shows an elevation of the test setup implemented for Series VI and VII while Figure 4.35 shows various plan sections of the test setup.



Figure 4.33: Typical Crossbeam Setup

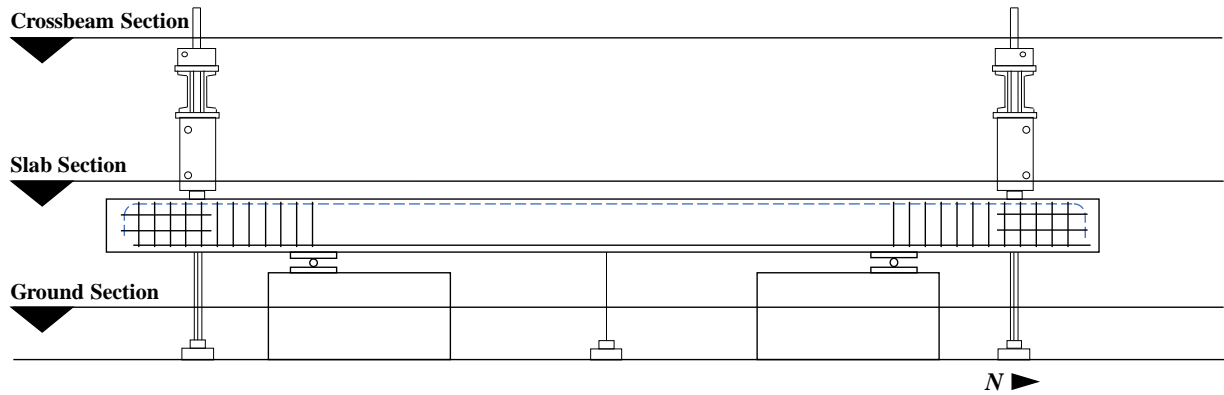
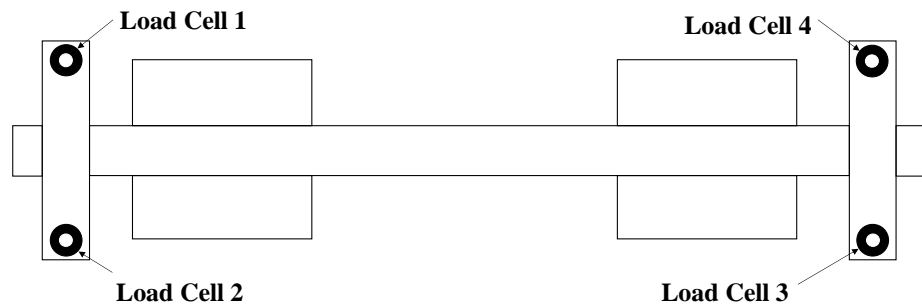
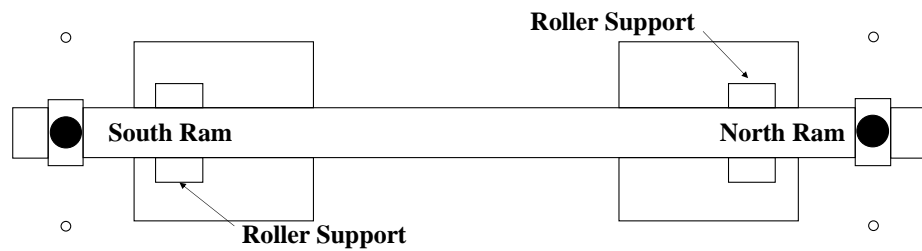


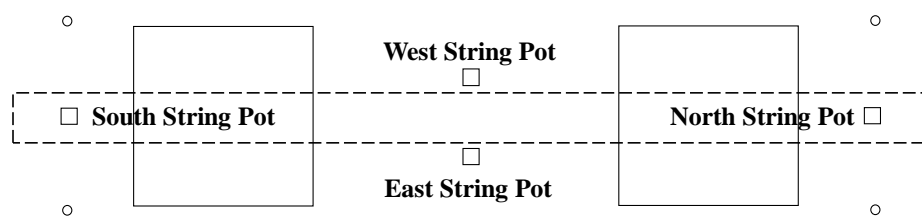
Figure 4.34: Series VI and VII Test Setup – East Elevation



(a) Crossbeam Section



(b) Beam Section



(c) Ground Section

Figure 4.35: Series VI and VII Test Setup Schematic Plans

4.6.2 Instrumentation and Equipment

Details of the test setup used in Series VI and VII follow in accordance with the test setup used in Series V. A 10,000 psi pressure transducer was selected for all tests in these two series.

4.6.3 General Testing Procedure

The testing procedure was nearly identical for all beams, regardless of confinement. The top surface of all beams was first inspected for any minor cracks caused by flipping or transporting the specimen to the test setup space. No perceptible cracks were present on the five unconfined specimens or the seven confined specimens in Series VI and VII before testing began. The pressure reading was recorded at the beginning of each test. Load was applied to the beams until cracking moment was reached between 11 and 15 kips, depending on the concrete strength.

Cracks were then mapped across the tension face and sides of each specimen (Figure 4.36). Load was applied throughout testing in 5-kip intervals and cracks widths were measured up until failure of the specimen. For unconfined specimens, flexural cracking was mapped on the specimens in 10-kip intervals up to failure, starting at 15 kips. For confined specimens, flexural cracks were mapped on the beams in 15-kip intervals up to failure, starting at 15 kips. This larger mapping interval was selected to maintain a consistent testing timeframe due to the higher loads required to fail all confined specimens. Video footage was captured for each load step and any notable specimen deformations were documented. This process was repeated throughout testing until failure was reached. As-built dimensions were measured after failure within the splice region to document cover and bar spacing dimensions from constructed. These measurements are provided for all beams in Appendix E.



Figure 4.36: General Beam Test – Crack Mapping (C3/60/2-40-10-50)

CHAPTER 5. EXPERIMENTAL RESULTS: BEAMS

5.1 Introduction

The experimental results of each test in Series VI and VII are presented to evaluate the effects of splice length, concrete strength, high-strength steel type, and confinement on bond strength. Series VI and VII consisted of twelve beams total. The test results are summarized in Table 5.1. Eleven (11) beams reached failure of the splice while one beam failed in flexure over the support.

5.2 Experimental Results

The applied load at failure, P_{ult} , was determined by averaging the load applied to the north and south end of each beam. This load was measured through the use of two load cells at each end. Load cell measurements varied for all test specimens with an average approximate difference of 1% between load cells. The ultimate moment at failure, M_{ult} , was calculated by multiplying the failure load, P_{ult} , by the shear span for each beam. The increased moment due to self-weight was neglected.

The stress achieved in the longitudinal reinforcing bars, f_b , was calculated using moment-curvature analysis and the failure load reached for each beam. All cross-sectional dimensions used in this calculation were design values. The tensile capacity of the concrete was neglected. Any influence from the compression steel was also neglected. The stress-strain relationship for the longitudinal steel was determined from experimental lab testing of the material, while the stress-strain relationship for the concrete was represented using the Hognestad (1951) model.

As included in Table 5.1, the test age was recorded for all specimens, with test dates ranging from 28 days to 69 days. Concrete compressive strength, f_c , was calculated by linear interpolation of the first and last day of testing.

Table 5.1: Beam Test Results

Series	Specimen	Test Age (days)	f_c (psi)	l_s (in.)	P_{ult} (kip)	M_{ult} (ft-kip)	f_b (ksi)	Failure Mode
VI	U-40-5-X	69	5600	40	55.0	220	71.0 ^[1]	Bond
	U-60-5-X	43	5300	60	61.4	245.6	80.8 ^[1]	Bond
	U-50-5	49	5400	50	55.5	222	73.2	Bond
	U-40-10	58	9800	40	65.0	260	83.6	Bond
	U-60-10	30	9700	60	73.2	292.8	94.2 ^[2]	Bond
	C3/60/2-40-10-25	37	10,000	40	69.5	278	89.4 ^[2]	Bond
	C3/60/2-40-10-50	28	9600	40	68.8	275.2	88.4 ^[2]	Bond
	C3/60/3-40-10-50	35	10,100	40	68.7	274.8	88.2	Bond
VII	C3/60-40-5-150	28	6200	40	69.9	279.6	90.4 ^[2]	Bond
	C3/60-40-5-200	30	6300	40	74.5	298	96.8 ^[2]	Bond
	C3/60-50-5-150	40	6600	50	80.1	320.4	104.6 ^[2]	Bond
	C3/60-50-5-200	42	6600	50	85.2	340.8	111.3 ^[3]	Flexure

[1] Within the linear-elastic limit of the A1035 response (81 ksi)

[2] Beyond linear-elastic limit of A615 response (87 ksi)

[3] Beyond yield strength of A615 response (108 ksi)

5.2.1 Self-Weight

As previously discussed for the slab specimens, self-weight is a small percentage of the applied loading. The moment diagrams for the beam loading configuration are shown in Figure 5.1 and Figure 5.2.

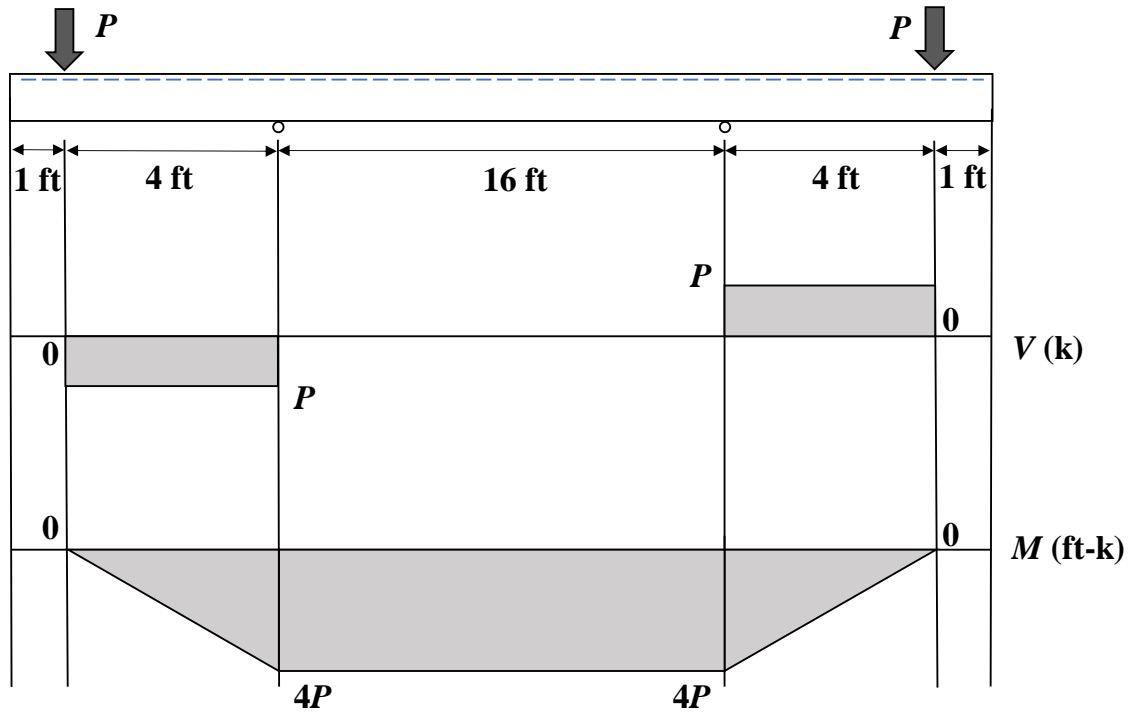


Figure 5.1: Shear and Moment Diagrams for Beams from Loading

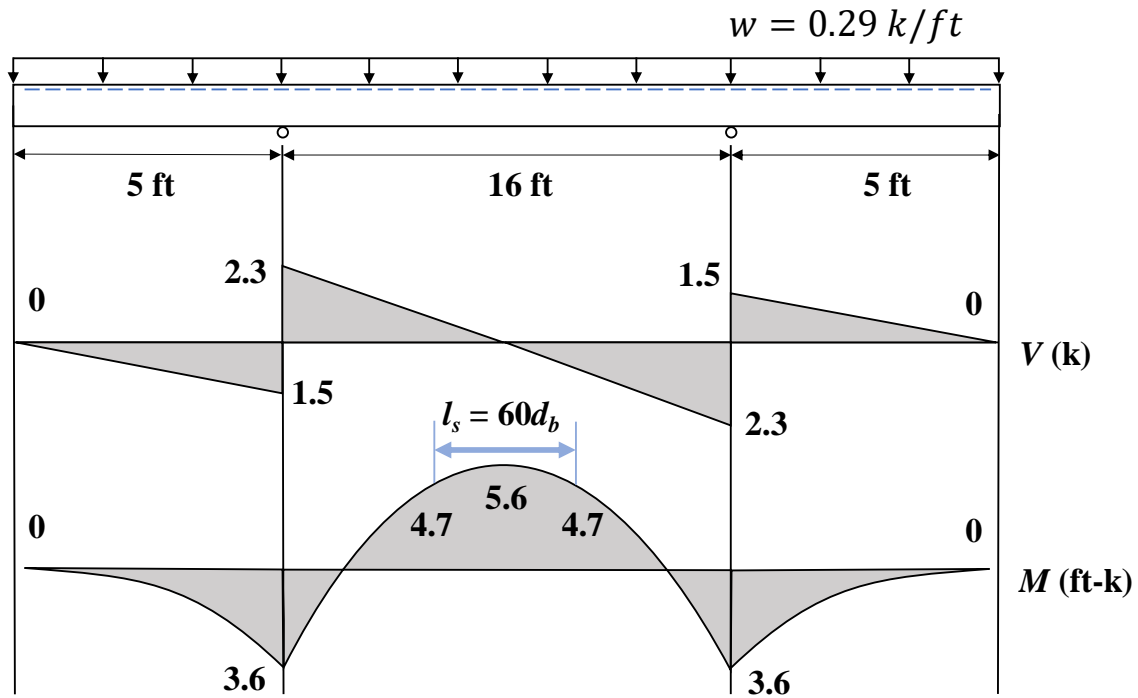


Figure 5.2: Shear and Moment Diagram for Beam Self-Weight

Because a maximum constant negative moment from the applied load occurs between the supports while the maximum negative moment due to the beam's self-weight peaks at each support, the overall ultimate moment occurs at the supports. The largest variation in moment across the splice is 0.9 ft-k for the 60 d_b specimens resulting from the self-weight positive moment in the center of 5.6 ft-k and 4.7 ft-k at the end of the splice.

Considering the applied loads, the greatest influence on self-weight is for Specimen U-40-5-X for which the self-weight provides a 1.6% increase in the ultimate moment. This difference is considered negligible; therefore, the self-weight is ignored for all beams.

5.2.2 Specimen Observations

The unconfined beams experienced minimal amounts of end and middle deflection compared to the slab specimens; therefore, more wood cribbing was required at the ends to support the end of the beam after failure and to decrease the severity of concrete spalling around the splice. General spacing of cracking patterns varied slightly within the splice region between the unconfined (Figure 5.3) and the confined (Figure 5.4) beam specimens.



Figure 5.3: Typical Flexural Cracking within Unconfined Splice Region (U-60-10)



Figure 5.4: Typical Flexural Cracking within Confined Splice Region (C3/60-40-5-200)

5.3 Load-Deflection Response

Load-deflection behavior was monitored for all beam specimens. Although each curve was unique to a specific test, the underlying mechanics and regions within the responses were similar in Series VI and VII. Before reaching the cracking moment for each beam, the stiffness of the specimen was primarily governed by the concrete as shown in Region 1 of Figure 5.5. Once cracking occurred, the stiffness of the member immediately decreased as evident in Region 2 where the overall response is linear due to the elastic response of the steel. The final region (Region 3) demonstrates yielding of the longitudinal bars. Region 3 only occurred in specimens where the splice strength exceeded the yield strength of the steel. This region provides the lowest member stiffness observed during testing.

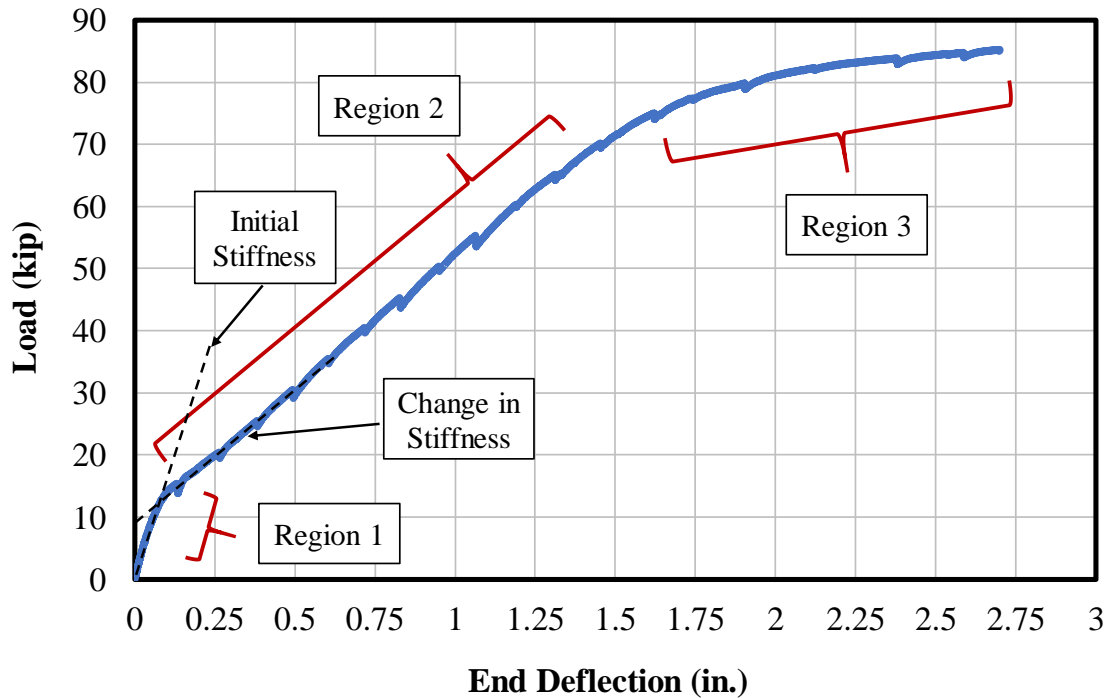


Figure 5.5: General Load-Deflection Behavior (C3/60-50-5-200)

In Series VI, five of the eight beams remained within the linear-elastic region of the response while three exceeded this limit but remained below the yield strength of the bars. In Series VII, all four beams achieved a bar stress above the linear-elastic limit. One beam surpassed the yield strength (greater than 0.2% offset) of the longitudinal reinforcement by approximately 3 ksi. This specimen (C3/60-50-5-200) developed sufficient bond strength and ultimately failed in flexure initiated by crushing of the concrete in the compression zone.

A comparison of all unconfined beams is provided in Figure 5.6 while a comparison of all confined beams is shown in Figure 5.7. Beams cast with high-strength concrete are represented by blue dashed lines and beams with MMFX spliced bars are represented by solid green lines. Load-deflection response for all specimens is provided in Appendix C.

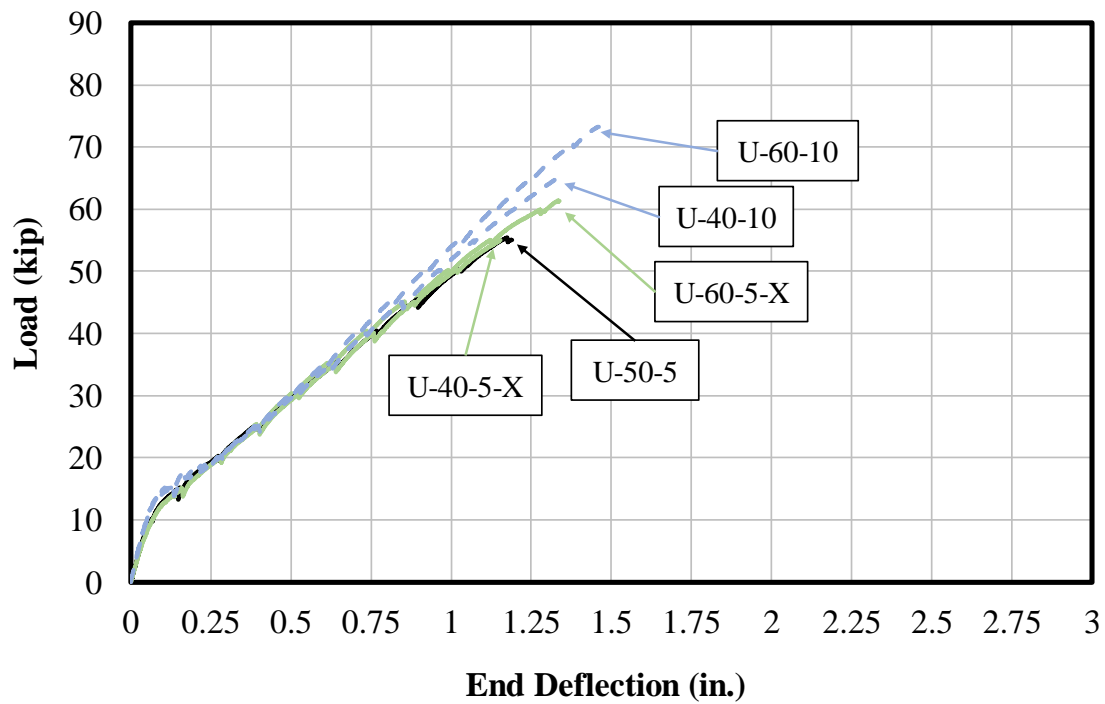


Figure 5.6: Unconfined Load-Deflection Responses

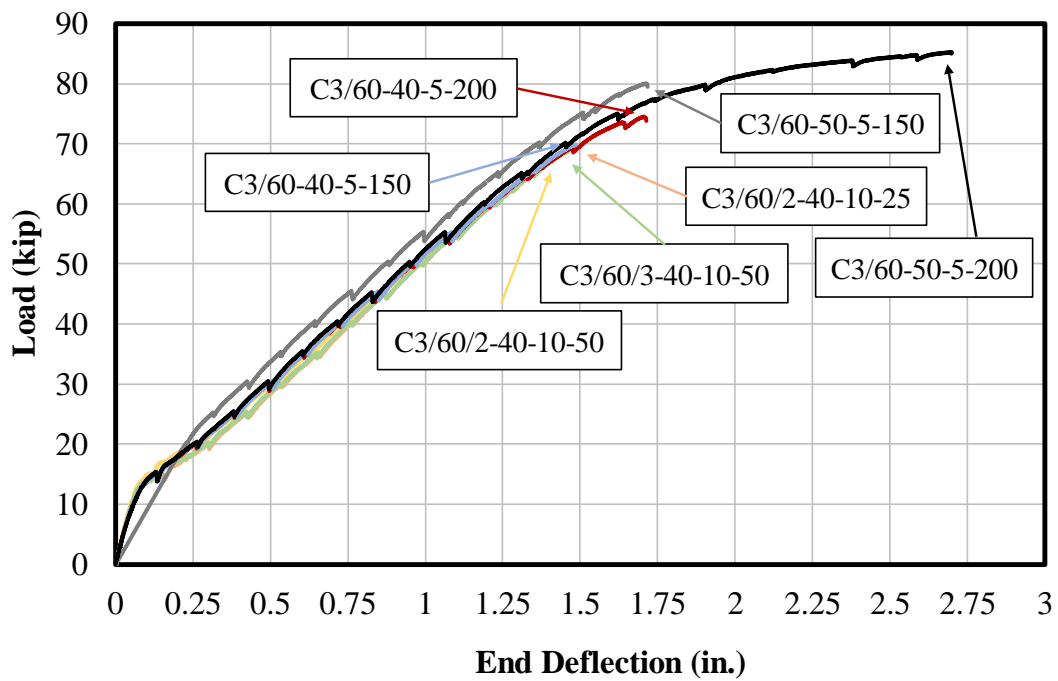
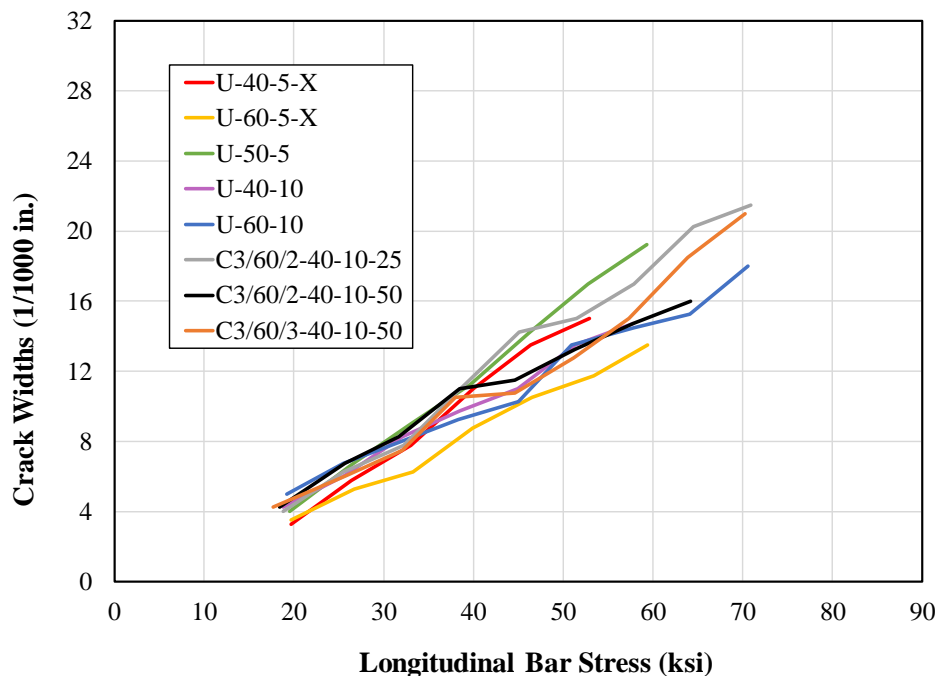


Figure 5.7: Confined Load-Deflection Responses

5.4 Concrete Crack Behavior

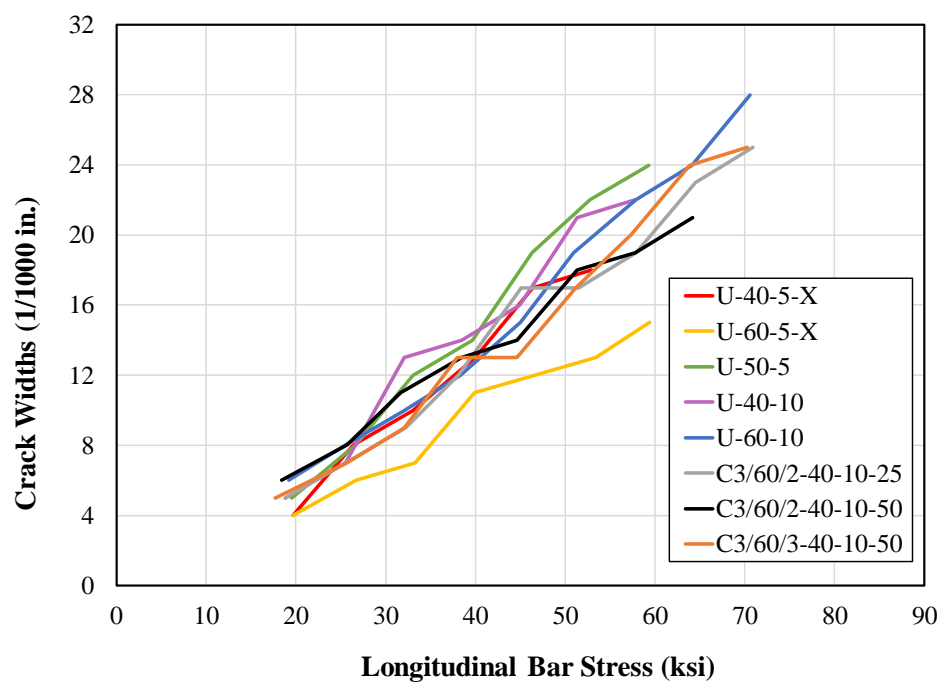
Four cracks were selected in the constant moment region, two past the north end of the splice region and two past the south end. Crack widths were monitored at each load step and recorded. The growth of these flexural crack widths as bar stress increased is provided in Appendix D for all specimens.

Throughout testing within the linear range of the reinforcing steel, crack widths consistently increased linearly as applied load increased for the unconfined and the confined beam specimens. Average and maximum crack width measurements for all beams are provided in Figure 5.8. Cracking initiated early during testing at a spacing between 4 in. and 15 in. with most cracks occurring in intervals of 10 in. (Figure 5.9) and continuing throughout the constant moment region but not the shear span. Transverse flexural cracking propagated at a wider spacing in the splice region with concentrated regions of flexural cracking developing near the ends of the splice.



(a) Average Crack Widths

Figure 5.8: Series VI and VII Crack Width Measurements



(b) Maximum Crack Widths

Figure 5.8: Series VI and VII Crack Width Measurements (Continued)



Figure 5.9: Transverse Flexural Cracking within Splice Region (C3/60/2-40-10-50)

After the cracking moment was exceeded, side cracking propagated down toward the compression region by approximately half the depth of the beams and is shown in Figure 5.10, regardless of confinement and concrete strength. This depth was indicative of the neutral axis location of the cross-section as load was applied.



(a) West Elevation (U-40-5-X)



(b) West Elevation (C3/60/2-40-10-25)

Figure 5.10: Initiation of Flexural Side Cracking

Flexural cracking was not initially present in the shear span of the beam specimens (Figure 5.11). Most cracks along the tension face and the beam sides were only present between supports immediately after surpassing the cracking moment. As the applied load increased, transverse flexural cracks began to develop in the shear span and slowly progressed from above the support toward the point of applied load. Crack spacing was noticeably larger in this region than in the constant moment region. Diagonal cracking was observed across the member depth in the shear span for all specimens in Series VI and VII as the applied load increased (Figure 5.12).



Figure 5.11: Shear Span – Early Testing (C3/60-40-5-200)

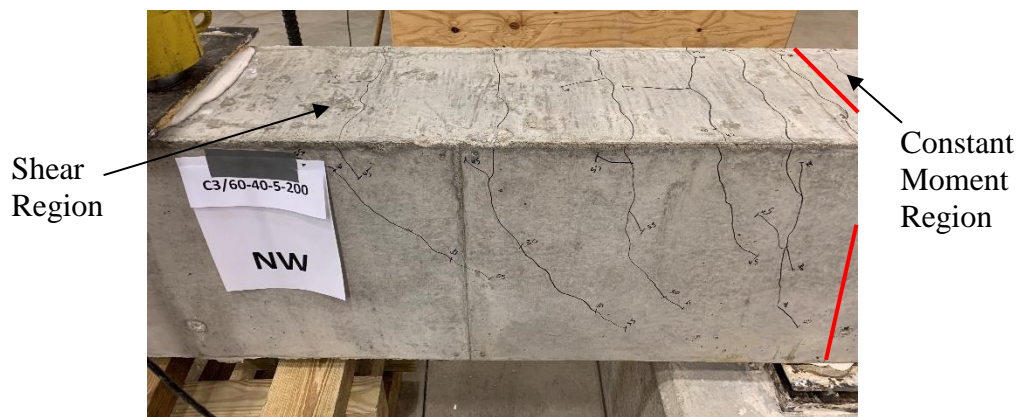


Figure 5.12: Shear Span – Late Testing (C3/60-40-5-200)

Longitudinal cracking initiated near the ends of the splice on the tension face for all beam specimens. For most beams, longitudinal cracking was not observed until approximately 30 kips, regardless of confinement. For confined beams, testing conducted by Glucksman (2018) found that primary transverse flexural cracks within the splice region typically formed at or near the underlying stirrups. This finding was also present during confined beam testing, as evidenced by Figure 5.13(a). Cracks formed above most stirrups in the splice region, however, cracking also occurred where stirrups were not present depending on stirrup spacing. Furthermore, cracking

typically formed at the end of the splice due to the cross-section discontinuity (blue in Figure 5.13(b)).



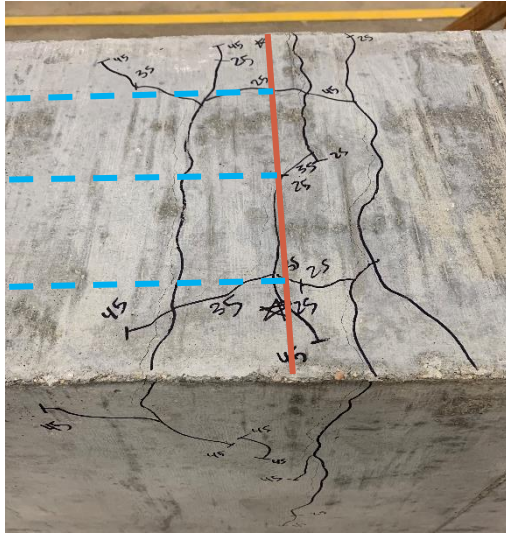
(a) C3/60/2-40-10-50



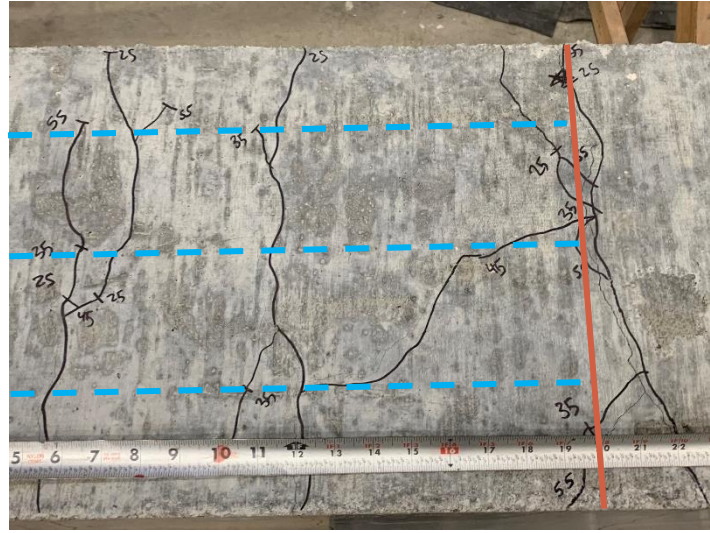
(b) C3/60-50-5-150

Figure 5.13: Flexural Cracking at Stirrup Locations

Longitudinal cracking was present in all beam specimens, regardless of confinement and failure mode. As load increased, longitudinal cracks slowly propagated toward the middle of the specimen from the ends of the splice and did not necessarily occur over all three bar splices. Many beam specimens experienced longitudinal cracking along the outer two splices as shown in Figure 5.14(a). Some specimens exhibited longitudinal cracking that branched from one lap splice to another as load increased (Figure 5.14(b)). Although Specimen C3/60-50-5-200 failed in flexure at the north support, longitudinal cracking was present over the splice (Figure 5.15).



(a) Edge Splitting Cracks (U-40-10)



(b) Branching Crack (C3/60/2-40-10-25)

Figure 5.14: Longitudinal Crack Propagation in Splice Region Failure



Figure 5.15: Longitudinal and Branch Cracking Before Flexural Failure (C3/60-50-5-200)

5.5 Failure

5.5.1 Unconfined Specimens

All five unconfined beams failed in splitting. Table 5.2 provides the results for each unconfined specimen at the end of testing.

Table 5.2: Test Results for Unconfined Beams

Specimen	Load (kip)	Avg. End Deflection (in.)	Avg. Midspan Deflection (in.)	Bar Stress (ksi)	Failure Mode
U-40-5-X	55.0	1.2	0.9	71.0	Splitting
U-60-5-X	61.4	1.3	1.1	79.6	Splitting
U-50-5	55.5	1.2	1.0	71.8	Splitting
U-40-10	65.0	1.3	1.0	82.3	Splitting
U-60-10	73.2	1.5	0.9	92.9	Splitting

Failure was brittle and explosive. Instead of releasing energy gradually, release occurred suddenly and without warning. The propagation of crack branching and longitudinal cracking along the sides and tension face, however, provided evidence that failure was imminent. Longitudinal cracks began at the ends of the splice and slowly extended toward the middle.

It was observed upon reaching failure that a full-depth crack opened at the ends of the splice and propagated entirely to the compression face of all unconfined beams. Typically, these larger cracks extended down part of the depth before extending out longitudinally approximately a distance d away from the end of the splice as shown in Figure 5.16 and Figure 5.17.



(a) U-40-10



(b) U-60-5-X

Figure 5.16: Typical Splice Side Cracking at Failure



(a) U-40-10

Figure 5.17: Typical Failure Side Crack Extensions



(b) U-60-5-X

Figure 5.17: Typical Failure Side Crack Extensions (Continued)

Upon reaching failure, the beam remained intact only due to the No. 3 mild steel bars within the compression region. Two unconfined beams in Series VI were cast with a target concrete compressive strength of 10,000 psi. The failures of these beams appeared to be more brittle, louder, and more explosive than the normal-strength concrete beams. All other observations at failure remained consistent with beams cast with a target concrete compressive strength of 5000 psi.

5.5.2 Confined Specimens

Table 5.3 provides the results for each confined specimen at the end of testing. Three of the seven confined beam specimens were cast using a high-strength concrete mix with a target compressive strength of 10,000 psi. No difference in specimen behavior during testing and at failure relative to normal-strength concrete specimens was observed.

Table 5.3: Test Results for Confined Beams

Specimen	Load (kip)	Avg. End Deflection (in.)	Avg. Midspan Deflection (in.)	Bar Stress (ksi)
C3/60/2-40-10-25	69.5	1.5	1.1	88.1
C3/60/2-40-10-50	68.8	1.5	1.1	87.1
C3/60/3-40-10-50	68.7	1.5	1.1	86.8
C3/60-40-5-150	69.9	1.5	1.1	90.4
C3/60-40-5-200	74.5	1.7	1.4	96.8
C3/60-50-5-150	80.1	1.7	1.3	104.6
C3/60-50-5-200	85.2	2.7	2.0	111.3

Due to the presence of transverse reinforcement, the ductility of the confined beams was higher than the unconfined specimens. In addition, greater tensile strains were achieved in the longitudinal reinforcement, allowing for more curvature and vertical deformation at the ends of the beam and at midspan. The greater ductility and vertical deflection also allowed splitting failure of the specimens to be slightly more predictable. Longitudinal cracking throughout the splice region also provided indication that failure was approaching, similar to the unconfined specimens.

Confined beams that failed in splitting behaved similarly to the unconfined beams. Concrete immediately spalled from the splice region; however, confining stirrups prevented the longitudinal bars from moving vertically. This mechanism helped contain the failure more than the unconfined beams and decreased the amount and distance of concrete blowout upon failure of the splice.

The final crack pattern at the ends of the splice after failure was slightly less severe than the unconfined beams as shown in Figure 5.18 for Specimen C3/60/3-40-10-50. The presence of transverse steel did not prevent the longitudinal crack in the compression zone from propagating

along the beam length, but crack widths were noticeably smaller. The concrete in this region was held together and confined by the stirrups and the No. 3 bars in the compression zone.



(a) Full Splice at Failure



(b) Side Crack Extension and Attenuation

Figure 5.18: Specimen C3/60/3-40-10-50 Side Cracking

After failure, the spalled concrete was collected to verify that cracks occurred at stirrup locations. These pieces were reconstructed to assemble the splice planes of the C3/60/2-40-10-50 and C3/60/3-40-10-50 specimens. These specimens had identical design parameters with the

exception of the stirrup locations (Figure 4.5). It was observed that some of the cracks that developed along the splice formed directly above or next to the specified stirrup locations (Figure 5.19), indicating that the stirrup locations clearly influence crack locations.

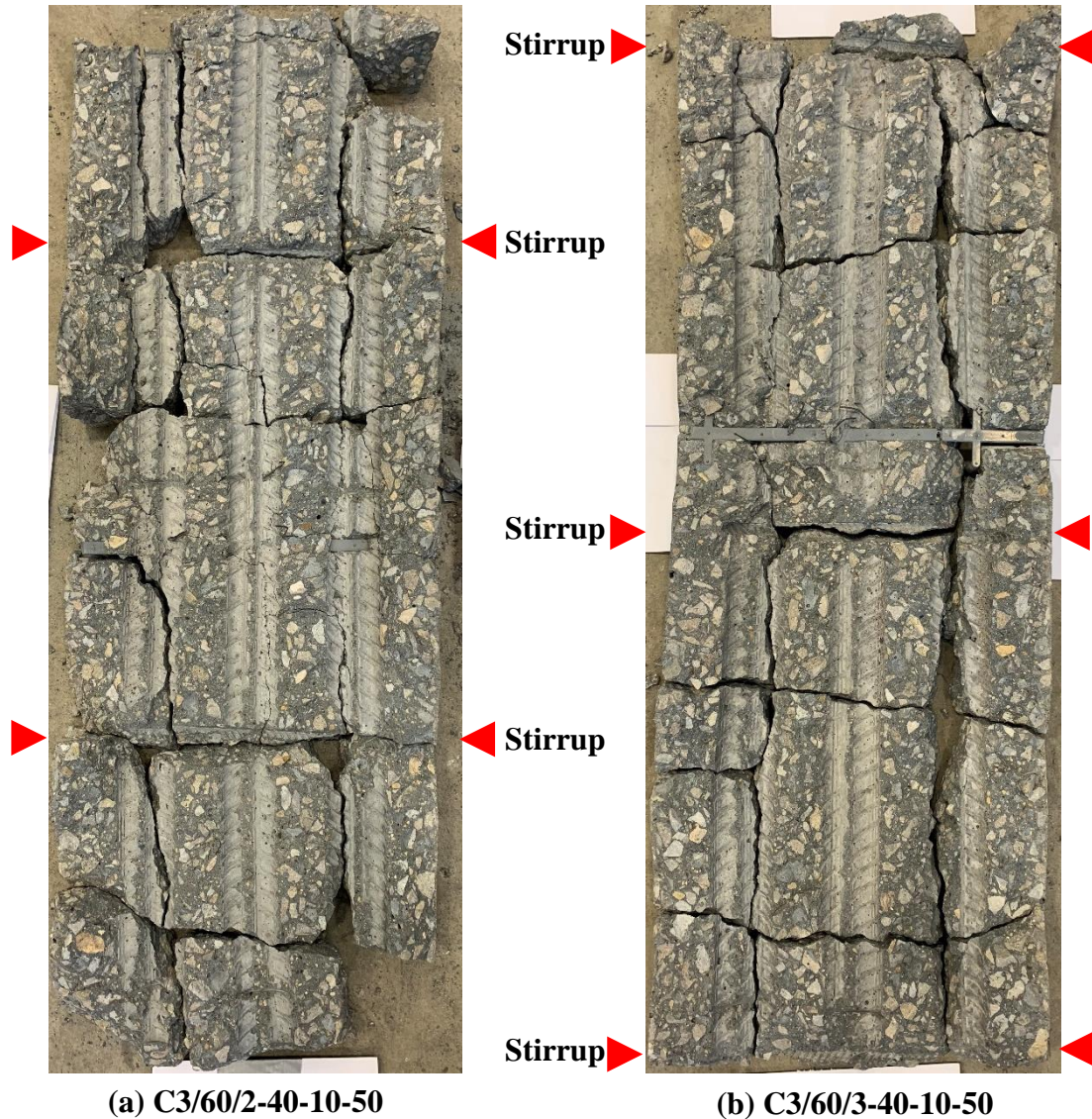


Figure 5.19: Reconstructed Confined Splice Planes

5.5.2.1 25 psi Specimen

The C3/60/2-40-10-25 specimen contained two stirrups, each located at the ends of the splice. It was observed after failure that all three of the longitudinal reinforcing bars had slipped

out from under the confining stirrups (Figure 5.20). It is unclear whether the bars slipped out of the confining steel before failure was achieved when deformations were large or immediately after failure occurred when the longitudinal bars were pulled outward. It is assumed due to the lack of a singular large crack at this location that the slip followed failure. The correct spacing and placement of these two stirrups within the beam was verified after failure.

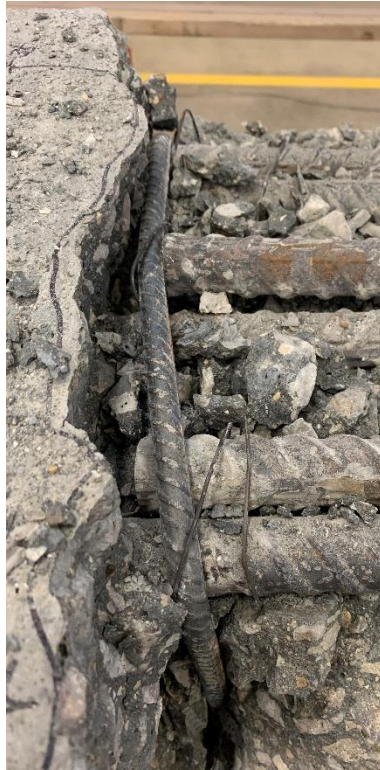


Figure 5.20: Bar Slip on Specimen C3/60/2-40-10-25

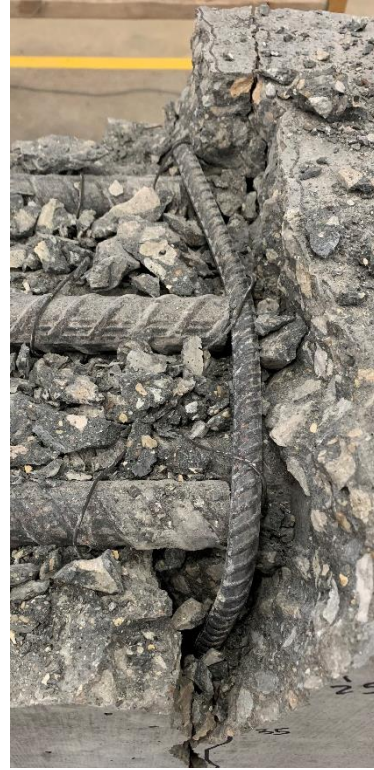
5.5.2.2 50 psi Specimens

Upon inspection of the C3/60/3-40-10-50 specimen after failure, the outer two splices remained well-confined; however, the inner splice was pulled out from under the confining stirrup (Figure 5.21). At both ends of the splice, it was observed that the stirrup was pushed away from its original location, indicating that the inner splice was confined for the entirety of testing up until

failure. When failure occurred and the beam reacted upward, the bars slipped and bent the stirrup upon reaching a rest position.



(a) South End of Splice



(b) North End of Splice

Figure 5.21: Bent Stirrup on Specimen C3/60/3-40-10-50

For the C3/60/2-40-10-50 specimen, one of the two stirrups in the splice region exceeded its yield strength and ruptured at failure as shown in Figure 5.22. The failure of this stirrup may have initiated the failure of the entire splice itself. Similar failure results were observed by Azizinamini et al. (1999) when it was observed that confining stirrups near the ends of the splice could experience very high strains and exceed the yield strength of the material.



Figure 5.22: Ruptured Stirrup on Specimen C3/60/2-40-10-50

5.5.2.3 200 psi Specimen

Specimen C3/60-50-5-200 experienced a flexural failure at both supports. Longitudinal branch cracking was present at the ends of the splice in this specimen (Figure 5.23). Longitudinal bars reached yield and experienced large axial strains resulting in increased member deformations at the ends of the beam and at midspan. A flexural failure ultimately occurred at the north and south supports (Figure 5.24) evidenced by the initiation of concrete crushing within the compression zone.



Figure 5.23: Longitudinal Crack Branching (C3/60-50-5-200)



(a) North Support



(b) South Support

Figure 5.24: Flexural Failure of Specimen C3/60-50-5-200

CHAPTER 6. ANALYSIS OF TEST RESULTS

6.1 Analysis and Design Methods

The results from this testing program were compared with the bond strengths calculated from four different bar development expressions. These development expressions considered are ACI 318-14, Pay (2005), Sim (2014), and Glucksman (2018).

6.1.1 ACI 318-14

The bond strength equation that was adopted by the American Concrete Institute has origins in the nonlinear regression analysis research of Orangun, Jirsa, and Breen (1977). Over 100 splice beam tests were analyzed to isolate the effect of numerous factors on bond strength, resulting in an expression for the average bond stress accumulated across the splice. This expression was designed to solve for an average bond stress given a number of parameters, including embedment length (Equation 6-1).

$$\frac{u}{\sqrt{f'_c}} = 1.2 + \frac{3C}{d_b} + \frac{50d_b}{l_d} + \frac{A_{tr}f_{yt}}{500sd_b} \quad (6-1)$$

where:

A_{tr} = total cross-sectional area of transverse reinforcement within the spacing s that crosses the plane of splitting through the developed reinforcement (in.²)

C = minimum of the clear bottom concrete cover and half the clear spacing of the bars or splices (in.)

d_b = bar diameter of lap-spliced longitudinal bar (in.)

f'_c = compressive strength of concrete (psi)

f_{yt} = yield strength of transverse reinforcement (psi)

l_d = development length in tension of deformed bar (in.)

s = spacing of transverse reinforcement, center-to-center (in.)

u = average bond stress (psi)

The expression was rearranged, modified, and simplified, leading to the current development length equation in the concrete building code. Equation 25.4.2.3a from ACI 318-14 provides an expression for the required development length of a reinforcing bar in terms of bar diameter (Equation 6-2).

$$\frac{l_d}{d_b} = \frac{3}{40} \frac{f_y}{\lambda \sqrt{f'_c}} \frac{\psi_t \psi_e \psi_s}{\left(\frac{c_b + K_{tr}}{d_b} \right)} \quad (6-2)$$

where:

A_{tr} = total cross-sectional area of transverse reinforcement within the spacing s that crosses the plane of splitting through the developed reinforcement (in.²)

c_b = minimum of (a) the concrete side cover measured to the center of the bar, (b) the bottom concrete cover measured to the center of the bar, and (c) half the center-to-center spacing of the bars (in.)

d_b = bar diameter of lap-spliced longitudinal bar (in.)

f'_c = compressive strength of concrete (psi)

f_y = specified yield strength of lap-spliced longitudinal bar steel (psi)

K_{tr} = transverse reinforcement index (in.)

$$= \frac{40A_{tr}}{sn}$$

l_d = development length in tension of deformed bar (in.)

n = number of bars or wires being developed or lap spliced

s = spacing of transverse reinforcement, center-to-center (in.)

λ = lightweight modification factor (ranging from 0.75 to 1.0)

ψ_t = casting position modification factor (ranging from 1.0 to 1.3)

ψ_e = epoxy coating modification factor (ranging from 1.0 to 1.5)

ψ_s = reinforcement size modification factor (ranging from 0.8 to 1.0)

In Equation 6-2, the K_{tr} term is permitted to be conservatively taken as zero even if transverse reinforcement is present. In addition, the confinement term $(c_b + K_{tr})/d_b$ is limited to 2.5. This constraint increases the likelihood of the failure mode being splitting within the splice region instead of bar pullout. When the confinement term is greater than 2.5, any additional confinement or increase in cover is unlikely to provide additional bond strength because a splice failure will likely be prevented, resulting in a pullout failure (ACI 318-14).

When written in terms of bar stress, f_y is replaced with f_b . After rearranging Equation 6-2 to solve for bar stress, the resulting Equation 6-3 takes the following form:

$$f_b = \frac{40\lambda\sqrt{f'_c}}{3\psi_t\psi_e\psi_s} \left(\frac{l_d}{d_b} \right) \left(\frac{c_b + K_{tr}}{d_b} \right) \quad (6-3)$$

This equation accounts for instances where transverse reinforcement is present and instances where transverse reinforcement is absent. The K_{tr} term accounts for this confining steel, but the yield strength of the transverse reinforcement is not directly included. The coefficient 40

is based on the expression $f_{yt}/1500$ when $f_{yt} = 60,000$ psi. Therefore, yield strength of the transverse reinforcement is indirectly accounted for in the ACI 318-14 equation for bar stress.

Figure 6.1 and Figure 6.2 provide a strength comparison for the unconfined and confined beams, respectively. This comparison is provided by calculating the ratio of measured bar stress to the bar stress calculated by Equation 6-3. The f_{test}/f_{calc} ratio reflects how well the proposed equation compares to the actual failure stress achieved by the longitudinal bars. When the ratio of f_{test}/f_{calc} exceeds one, the test performed better than the predicted failure stress, signifying a conservative calculation. If the proposed equation yields a f_{test}/f_{calc} value less than one, the result is unconservative. The division between regions is represented by a horizontal red line.

Specimens constructed with ASTM A1035 MMFX longitudinal steel are noted in the comparison and specimens cast with high-strength concrete (HSC) are also identified. Furthermore, slabs and beams are also identified. It should be noted that Specimens S-80-5, S-100-5, and C3/60-50-5-200 specimens had adequate bond strength and ultimately failed in flexure. Comparisons can be drawn between beams containing A615 and A1035 steels because it has been seen in Phase II of this testing program that behavior is similar within the linear-elastic region of the stress-strain response for these two steel types.

For Figure 6.1, it should be noted that the equation performs well for specimens with a splice length of $40d_b$ to $50d_b$; however, as splice length increases, the calculated bar stress becomes more unconservative. In addition, the two unconfined HSC beam results show that as concrete compressive strength increases, Equation 6-3 yields less conservative results. A similar trend is shown in the confined HSC specimens in Figure 6.2 when the K_{tr} equation is implemented compared to the normal-strength concrete specimens.

Figure 6.2 provides results using K_{tr} as calculated (orange) and K_{tr} conservatively calculated as zero (blue). In Figure 6.2, all specimens have splice lengths of $40d_b$ and $50d_b$. Equation 6-3 appears to yield conservative results for all specimens when K_{tr} is taken to be zero (confinement not considered). As confinement increases, the amount of conservatism increases as expected. When K_{tr} is considered, however, the results from Equation 6-3 produce less conservative values as the confinement is increased both for normal-strength and high-strength concrete.

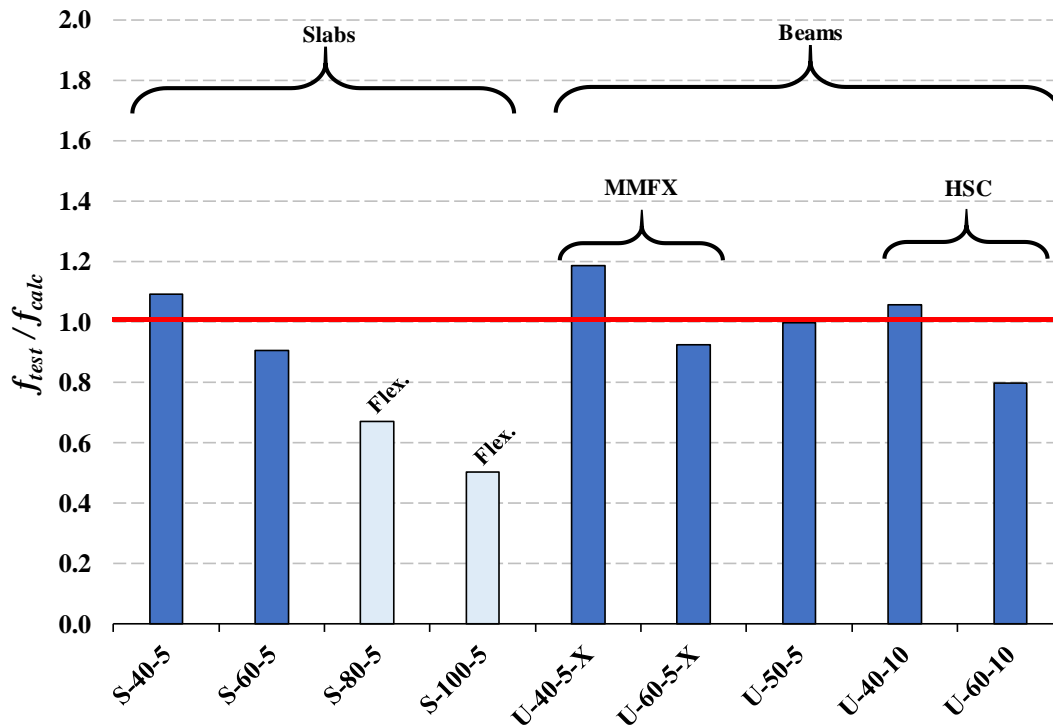


Figure 6.1: Unconfined Strength Calculation Comparison by ACI 318-14 Eq. 6-3

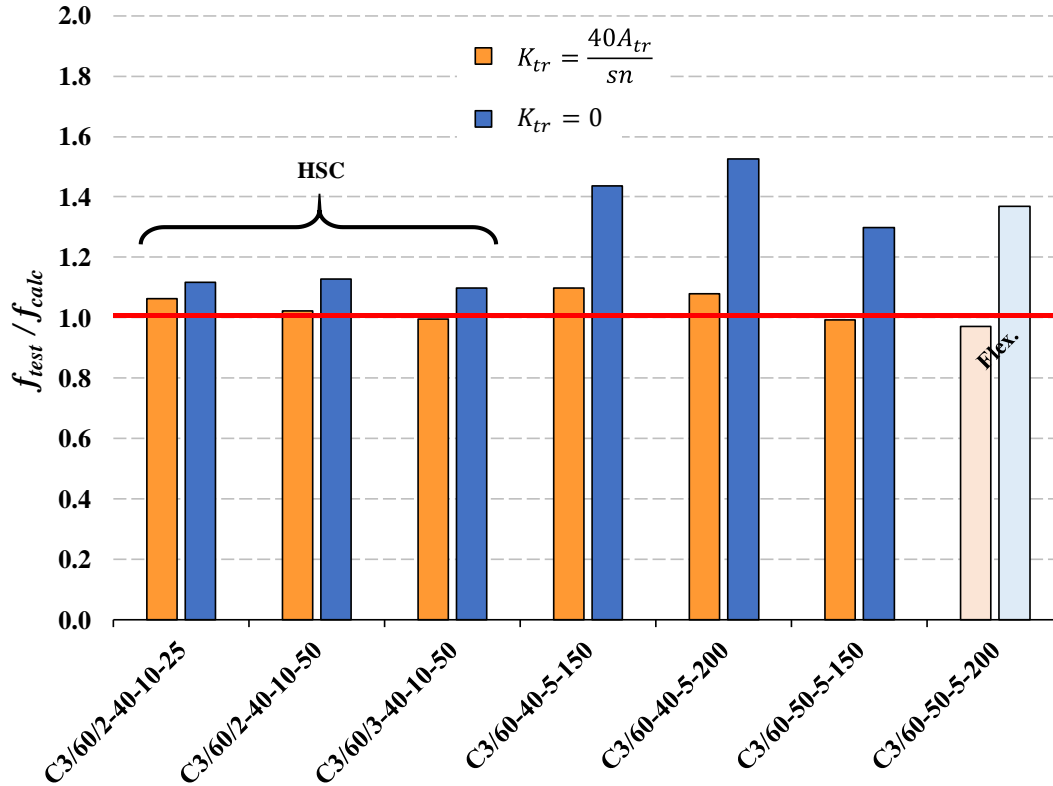


Figure 6.2: Confined Strength Calculation Comparison by ACI 318-14 Eq. 6-3

6.1.2 Pay (2005)

A research program conducted at Purdue University in 2005 sought to evaluate the effect of axial stiffness on bond behavior of concrete beams reinforced with various types of bars, among other parameters. These bar types included glass FRP, carbon FRP, and black steel, each with various surface properties. The conclusion was made that axial rigidity is a parameter that influences bond strength. As axial stiffness increases in the longitudinal reinforcement, bar stress achieved during testing increases as well.

This relationship was quantified with an expression that relates the spliced bar stiffness to a reference value. The expression defines an equivalent splice length to be the product of splice

length and a ratio of the present axial stiffness to a reference axial stiffness. This equivalent splice length is shown in Equation 6-4.

$$L_{eq} = l_s \frac{E_b A_b}{E_{ref} A_{ref}} \quad (6-4)$$

where:

A_b = area of spliced reinforcement (in.²)

A_{ref} = area of reference reinforcement (in.²)

E_b = elastic modulus of spliced reinforcement (ksi)

E_{ref} = elastic modulus of reference reinforcement (ksi)

L_{eq} = equivalent splice length (in.)

l_s = splice length (in.)

In addition to the influence of axial stiffness, Pay analyzed the effect of cover and bar spacing on bond strength. He found that a modification factor M was dependent on spliced bar diameter and the minimum of clear cover and half the inner bar spacing. Equation 6-5 quantifies this general modification factor for use in face-splitting or side-splitting failures.

$$M = 0.2 \left(\frac{c}{d_b} \right) + 0.75 \quad (6-5)$$

where:

c = minimum of the bottom concrete cover, or half the clear spacing of the spliced bars (in.)

d_b = bar diameter of lap-spliced longitudinal bar (in.)

M = cover modification term

The effects from axial stiffness, cover, and bar spacing were incorporated in an equation of best fit after analyzing numerous FRP and steel reinforced concrete beams in a database. Regression analysis was performed on each specimen after normalizing the bar force to a concrete strength of 4000 psi to find a curve of best fit. The resulting Equation 6-6 takes the following form:

$$f_b A_b \sqrt[4]{\frac{4000}{f'_c}} = 2.1 L_{eq}^{0.5} \left(0.2 \left(\frac{c}{d_b} \right) + 0.75 \right) \quad (6-6)$$

where:

A_b = area of spliced reinforcement (in.²)

c = minimum of the bottom concrete cover, or half the clear spacing of the spliced bars (in.)

d_b = bar diameter of lap-spliced longitudinal bar (in.)

f_b = stress in lap-spliced longitudinal bar (ksi)

f'_c = compressive strength of concrete (psi)

L_{eq} = equivalent splice length (in.)

By substituting for the area of the spliced bar and the equivalent splice length, the equation can be simplified. Rearranging for the splice length in terms of bar diameter yields the following equation:

$$\frac{l_s}{d_b} = \frac{20,280}{E_b} \frac{f_b^2 d_b}{\sqrt{f'_c}} \left(\frac{1}{M} \right)^2 \quad (6-7)$$

When Equation 6-7 is rearranged to solve for bar stress, the following analytical expression is derived to determine the expected bar stress achieved in a reinforced concrete beam without transverse confinement steel:

$$f_b = \left(\frac{l_s E_b M^2 \sqrt{f'_c}}{20,280 d_b^2} \right)^{0.5} \quad (6-8)$$

This analytical expression indicates that bar stress is proportional to the quarter-root of the concrete compressive strength. Bar stress is also proportional to the square-root of the ratio of splice length to bar diameter. In addition, the bar stress is directly proportional to a linear cover modification term.

Figure 6.3 provides a strength comparison for all unconfined splice specimens in this testing program. Confined specimens are not included as this expression is for unconfined behavior only. The measured bar stress achieved at failure is compared with Equation 6-8 using the cover modification factor M (orange) or by simplifying this term to 1.0 (blue) as also recommended by Pay.

From Figure 6.3, the stress equation developed by Pay (2005) provides slightly conservative results for all specimens that did not fail in flexure. When the cover modification term is included, the results become more conservative; however, the difference between when cover is considered and when it is not is minimal.

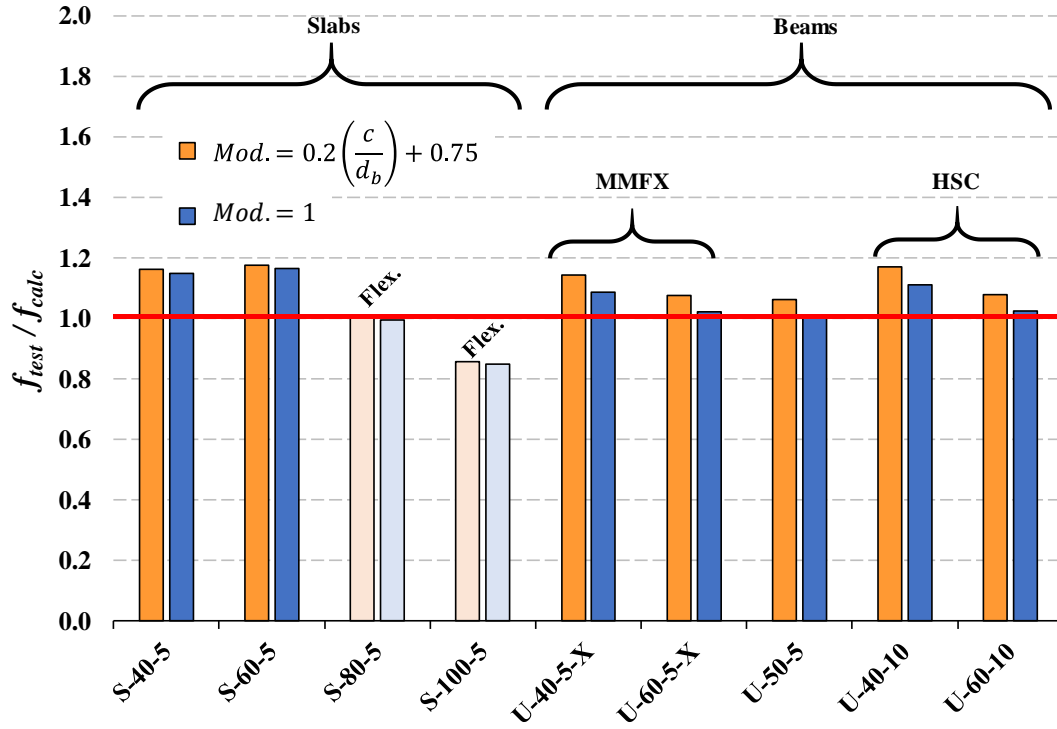


Figure 6.3: Unconfined Strength Calculation Comparison by Pay (2005) Eq. 6-8

6.1.3 Sim (2014)

In 2014, a different approach was taken toward establishing a model for determining the failure stress of unconfined splice beam tests. By evaluating the relationship between several base variables that influence bond strength using the Buckingham Π theorem, Sim (2014) developed Equation 6-9 to relate bar stress, bar diameter, concrete compressive strength, and cover. Expressions that were influenced by the presence of confinement were neglected for this investigation.

$$\frac{F_b}{\pi d_b l_s} = k(f'_c)^{b_1} \left(\frac{l_s}{d_b}\right)^{b_2} \left(\frac{c_{min}}{d_b}\right)^{b_3} \quad (6-9)$$

where:

- b_1, b_2, b_3 = constants found by regression analysis
 c_b = bottom clear cover of spliced bars (in.)
 c_{min} = minimum of c_{so} , c_{si} , and c_b (in.)
 c_{si} = half the clear spacing between spliced bars (in.)
 c_{so} = side clear cover of spliced bars (in.)
 d_b = nominal bar diameter (in.)
 F_b = bond force (kip)
 f'_c = specified compressive concrete strength (psi)
 k = constant found by regression analysis
 l_s = splice length (in.)

Initial values were determined for the four constants in Equation 6-9; however, it was observed that the side clear cover c_{so} had a greater influence on bond strength than c_{min} . After running the regression analysis once more, these constants were determined to be:

$$b_1 = 0.25 \quad b_2 = -0.50 \quad b_3 = 0.25 \quad k = 0.25$$

The following equation was produced by substituting these values into Equation 6-9 and replacing the cover term to reflect the influence of the side cover. The force developed in the spliced bar is also isolated on one side of Equation 6-10 as shown:

$$F_b = 0.25(\pi d_b l_s)^4 \sqrt{f'_c} \sqrt{\frac{d_b}{l_s}}^4 \sqrt{\frac{c_{so}}{d_b}} \quad (6-10)$$

By dividing both sides by the area of the spliced bar, the bar force can be converted into a stress. In addition, after rearranging the terms to solve for splice length in terms of bar diameter, Equation 6-10 takes the following form:

$$\frac{l_s}{d_b} = \frac{f_b^2}{\sqrt{f'_c}} \frac{1}{\sqrt{\frac{c_{so}}{d_b}}} \quad (6-11)$$

When Equation 6-11 is rearranged to solve for bar stress, the following analytical expression is derived to determine the expected bar stress achieved in a reinforced concrete beam without transverse confinement steel:

$$f_b = \left[\frac{l_s \sqrt{f'_c} \sqrt{\frac{c_{so}}{d_b}}}{d_b} \right]^{0.5} \quad (6-12)$$

This analytical expression indicates that bar stress is proportional to the quarter-root of the concrete compressive strength. Bar stress is also proportional to the square-root of splice length in terms of bar diameter. Finally, the influence of cover is best represented by the quarter-root of c_{so}/d_b in the cover modification term.

The influence of transverse reinforcement within the splice was also investigated. Various confining stirrup configurations along the splice length were constructed using the same total area of transverse reinforcement, and it was found that the location of these stirrups along the splice affected the added contribution of these stirrups. Ultimately, the additional force contribution from the confining steel was related to the stress in the transverse steel. The stress developed in the stirrups is transferred to the longitudinal reinforcement, and this relationship is modeled by the following equation:

$$F_{tr} = k \frac{A_{tr} f_{yt}}{N_b} N_s \quad (6-13)$$

where:

A_t = area of one leg of transverse reinforcement crossing the splitting plane (in.²)

A_{tr} = area of one unit of transverse reinforcement crossing splitting plane (in.²)

= $A_t N_l$ (in.²)

F_{tr} = contribution of transverse reinforcement in splice region (kip)

f_{yt} = yield strength of transverse reinforcement (psi)

k = confinement contribution factor

N_b = number of spliced or developed bars

N_l = number of legs of transverse reinforcement crossing the splitting plane

N_s = number of stirrups within the splice region

The value of the confinement contribution factor was explored by investigating the correlation between the measured F_{tr} and $A_{tr} f_{yt} N_s / N_b$ for 338 confined specimens in a steel database. The slope of this correlation varied for beams of different l_s / d_b , but an average value of 0.5 was observed and selected for the final equation.

$$F_{tr} = \frac{1}{2} \frac{A_{tr} f_{yt}}{N_b} N_s \quad (6-14)$$

The bar force achieved at failure for a confined specimen was then taken as a sum of Equations 6-12 and 6-14.

$$F_s = F_b + F_{tr} \quad (6-15)$$

The two components of Equation 6-15, F_b and F_{tr} , can be divided by the longitudinal bar area to convert the expression into one resulting in the bar stress achieved at failure. Equation 6-16 shows the full bar stress expression for reinforced concrete members with or without confining steel within the splice region.

$$f_s = \left[\frac{l_s \sqrt{f'_c} \sqrt{\frac{c_{so}}{d_b}}}{d_b} \right]^{0.5} + \frac{1}{2} \frac{A_{tr} f_{yt}}{A_b N_b} N_s \quad (6-16)$$

Figure 6.4 and Figure 6.5 provide a strength comparison for unconfined and confined splice beams, respectively. Bar plots for each unconfined and confined specimen are constructed by comparing Equation 6-16 to the measured bar stress achieved at failure. The cover modification term $\sqrt[4]{c_{so}/d_b}$ (orange), was considered as well as using the factor simplified to 1.0 (blue).

In Figure 6.4, the unconfined specimens show conservative results for all tests except the S-100-5 slab which failed in flexure. When the proposed quarter-root cover modification term is taken to conservatively be one, the results are very conservative with some f_{calc} values yielding only 57% of the actual bar failure stress in the slab specimens. However, when the proposed cover modification term is included, results still remain slightly conservative but close to the actual bar failure stress. When the cover term is included, the low f_{calc} value of 57% increases to nearly 80% of the bar failure stress in the S-60-5 specimen. In general, as the splice length increases, Equation 6-16 yields less conservative results for most slabs and unconfined beams. Additionally, the use of high-strength concrete in two unconfined beams did not produce significantly different results from Equation 6-16 when compared to specimens with similar splice lengths.

Figure 6.5 provides very similar results for specimens with differing amounts of confinement. The equation proposed by Sim (2014) when cover is considered yields slightly conservative predictions for all specimens in this testing program, with a minimum and maximum underestimation of 86% and 92% of f_{calc} , respectively. In all cases, when the cover modification term is included in the bar failure stress prediction, a decrease in the f_{test}/f_{calc} ratio is evident, producing ratios closer to 1.0. In addition, variation in concrete strength does not significantly affect the results of Equation 6-16.

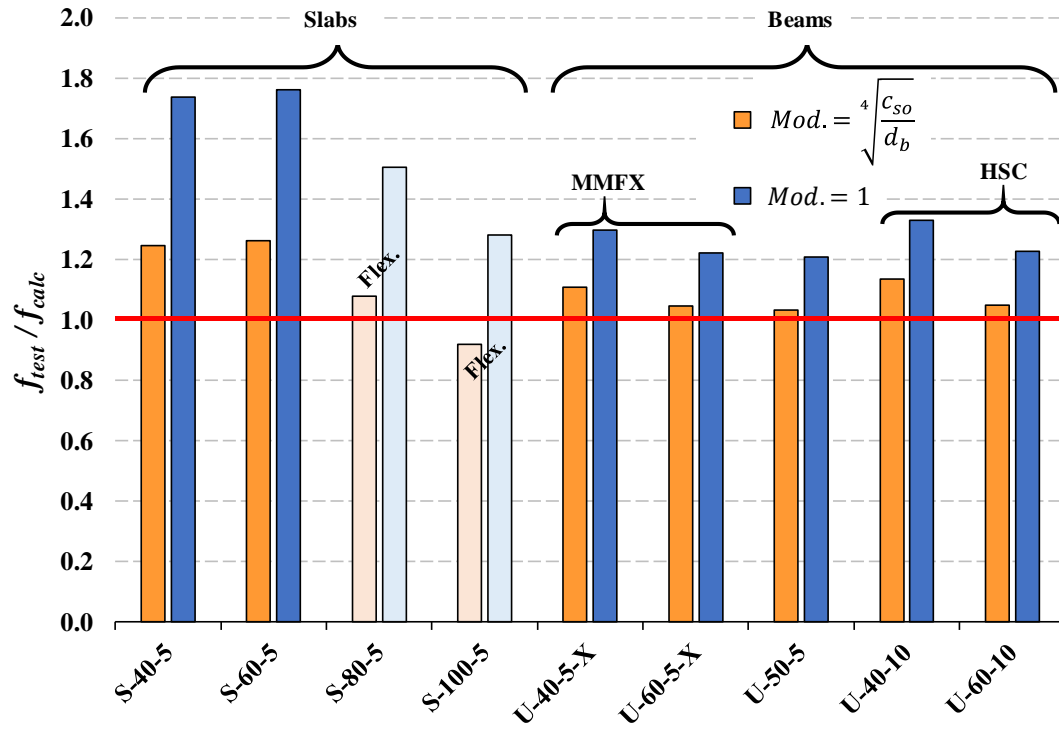


Figure 6.4: Unconfined Strength Calculation Comparison by Sim (2014) Eq. 6-16

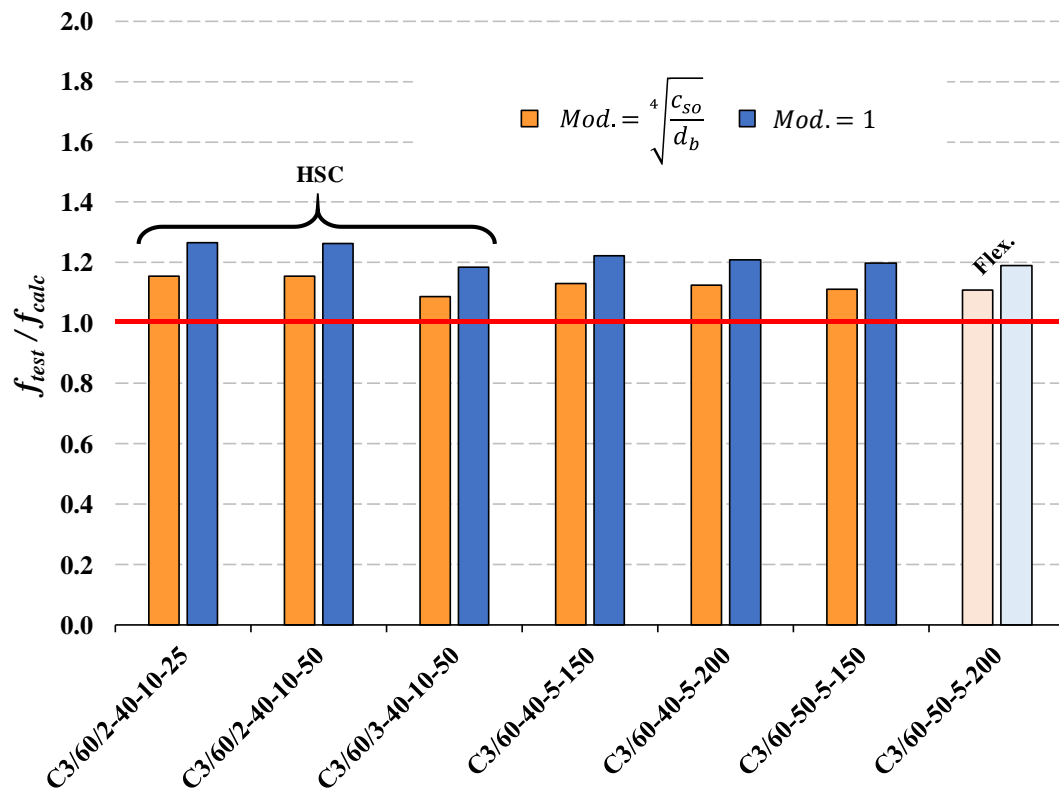


Figure 6.5: Confined Strength Calculation Comparison by Sim (2014) Eq. 6-16

6.1.4 Glucksman (2018)

A study conducted in concert with this research program included four series of experimental tests on 22 splice beam specimens containing A615 Grade 100 longitudinal bars (Phase I). The purpose of this study was to evaluate the influence of splice length and transverse reinforcement on bond strength, while also determining the effectiveness of Grade 100 transverse reinforcement on bond strength.

Upon analyzing the statistical results of four trends relating F_{test} to L_{eq} , a power trend of $8L_{eq}^{0.5}$ was selected to represent the influence of l_s on f_s when concrete strengths are normalized to 5000 psi. Concrete strengths were normalized using the fourth root ($\sqrt[4]{5000/f'_c}$) as previously recommended by Pay (2005) and Sim (2014). To reduce scatter present within the analyzed data, a cover modifier was included. Studies were performed on the primary terms that are directly related to cover: half the clear spacing between bars (c_{si}), side cover (c_{so}), and bottom cover (c_b). The linear term developed by Pay (2005) and the nonlinear term developed by Sim (2014) were also included in the investigation. The results of the investigation showed that the quarter-root of the ratio of side cover to bar diameter had the most influence on bond strength, similar to Sim (2014).

The unconfined bar stress equation for typical black steel bars takes the following form once the effects of concrete cover, normalized concrete compressive strength, and splice length were accounted for:

$$f_s = \frac{8L_{eq}^{0.5}}{A_b} \left(\frac{f'_c}{5000} \right)^{0.25} \left(\frac{c_{so}}{d_b} \right)^{0.25} \quad (6-17)$$

where:

$$A_8 = \text{area of standard No. 8 bar (in.}^2\text{)}$$

$$= 0.79 \text{ in}^2$$

$$A_b = \text{area of spliced reinforcement (in.}^2\text{)}$$

$$c_{so} = \text{side clear cover of spliced bars (in.)}$$

$$d_b = \text{nominal bar diameter (in.)}$$

$$f'_c = \text{specified compressive concrete strength (psi)}$$

$$f_s = \text{stress in lap-spliced longitudinal bar (ksi)}$$

$$L_{eq} = \text{equivalent splice length (in.)}$$

$$= l_s \frac{A_b}{A_8}$$

$$l_s = \text{splice length (in.)}$$

For beams where transverse reinforcement was present within the splice region, a separate term was developed to evaluate the additional bond strength contribution. The failure stresses of confined beams were compared to the failure stresses of identical beams without confinement steel. It was observed that this additional stress contribution was related to the total area of transverse steel crossing the plane of splitting. This relationship was observed to be linear with a coefficient of 12; therefore, the following equation was developed to capture the additional bond strength contribution of the transverse reinforcement:

$$f_{tr} = 12A_{tr_total} \quad (6-18)$$

where:

$$A_t = \text{area of one leg of transverse reinforcement (in.}^2\text{)}$$

$$\begin{aligned}
A_{tr_total} &= \text{total area of transverse reinforcement within splice region (in.}^2\text{)} \\
&= A_t N_l N_s \\
f_{tr} &= \text{bar stress contribution from the presence of transverse steel (ksi)} \\
N_l &= \text{number of legs of transverse reinforcement that cross the splitting} \\
&\quad \text{plane} \\
N_s &= \text{number of stirrups within the splice region}
\end{aligned}$$

When comparing this expression to the ratio of f_{test}/f_{calc} , a downward trend was observed. To correct for this correlation, a 0.5 power was added to the total area of transverse reinforcement term.

$$f_{tr} = 12(A_t N_l N_s)^{0.5} \quad (6-19)$$

The final equation for the bar stress of a confined splice beam was taken as a sum of the original bar stress due to the concrete strength, and the additional contribution from the transverse reinforcement. The final equation is therefore taken as a sum of Equations 6-17 and 6-19.

$$f_b = f_s + f_{tr} \quad (6-20)$$

$$f_b = \frac{8L_{eq}^{0.5}}{A_b} \left(\frac{f'_c}{5000} \right)^{0.25} \left(\frac{c_{so}}{d_b} \right)^{0.25} + 12(A_t N_l N_s)^{0.5} \quad (6-21)$$

Figure 6.6 and Figure 6.7 provide a strength comparison for unconfined and confined splice beams, respectively. Both bar plots for each unconfined and confined specimen are constructed by comparing Equation 6-21 to the measured bar stress using the cover modification term $\sqrt[4]{c_{so}/d_b}$ (orange), or using the modification factor simplified to 1.0 (blue). The orange indicates the use of this proposed expression as the cover modifying term, while the blue represents selecting this cover modification term to conservatively be one.

From Figure 6.6, it can be observed that Equation 6-21 yields unconservative results for all unconfined specimens in this testing program when the cover modification term is included. The results appear to be more unconservative for the slabs compared to the beams. When the cover modification term is excluded and taken to be one, the results improve with 78% of the unconfined specimens in this testing program yielding conservative results. The use of high-strength concrete did not seem to affect the results when compared to beams with similar splice lengths.

Figure 6.7 shows that as the amount of confinement increases within the splice region, Equation 6-21 becomes slightly more conservative. At low levels of confinement, Equation 6-21 can yield conservative or unconservative results depending on the cover modifier. In all cases, when the cover modifier is taken to be the quarter-root of the ratio between side cover and bar diameter, the results are less conservative than taking this term to be one. Similar to Sim (2014), when the cover modification term is included in the failure stress prediction, the result is a decrease in the f_{test}/f_{calc} ratio of approximately 10% for all specimens. The use of high-strength concrete does not appear to have a significant effect on the f_{test}/f_{calc} ratio.

Table 6.1 provides a summary of analysis equations for bar stress while Table 6.2 provides a statistical analysis of the results. Values are calculated for each specimen in Phases II of this testing program. Each analysis equation was performed using the cover modifier or K_{tr} , or by simplifying these terms. Note that the coefficients of variation and the coefficients of correlation for equations by Pay (2005), Sim (2014), and Glucksman (2018) produce better results when compared to the bar stress equation in ACI 318-14.

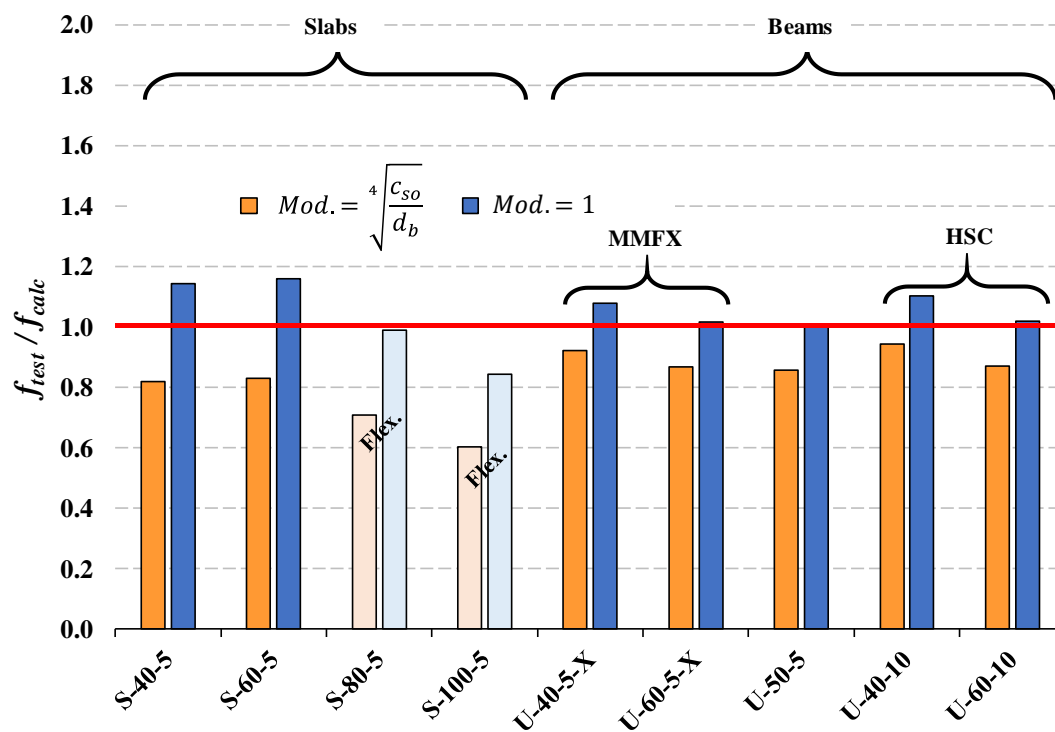


Figure 6.6: Unconfined Strength Calculation Comparison by Glucksman (2018) Eq. 6-21

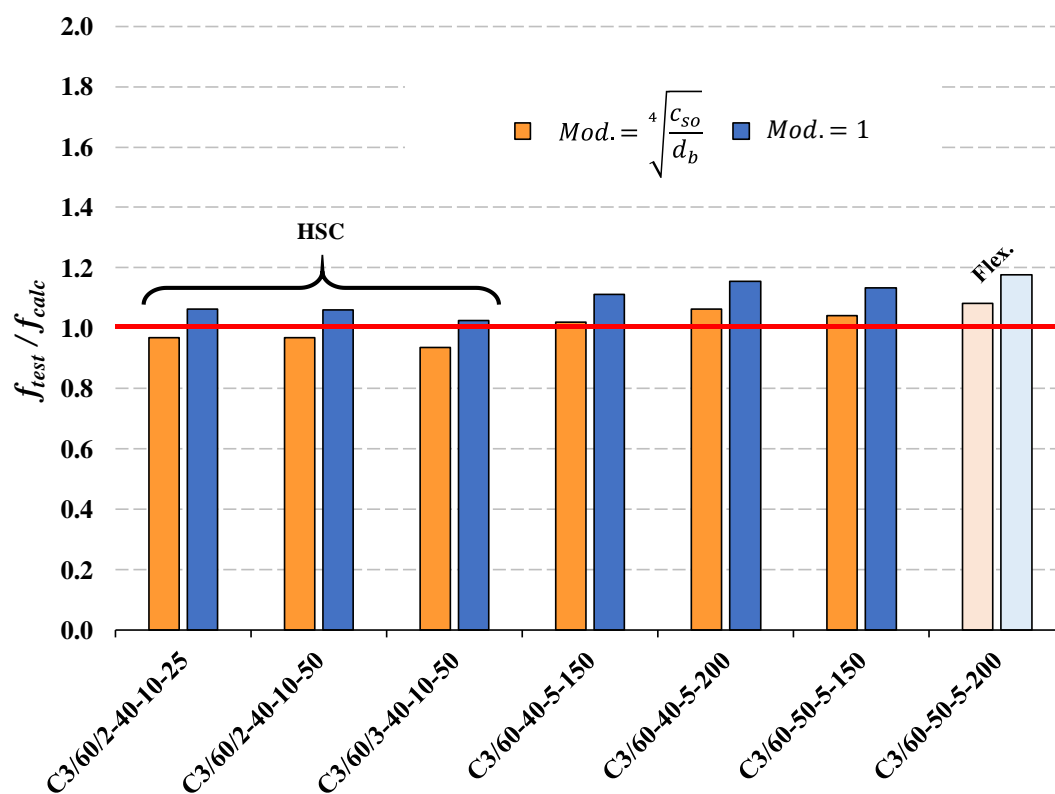


Figure 6.7: Confined Strength Calculation Comparison by Glucksman (2018) Eq. 6-21

6.1.5 Summary of Strength Comparisons

Table 6.1: f_{calc} Stress Comparison with Various Analytical Methods

		S-40-5	S-60-5	S-80-5	S-100-5	U-40-5-X	U-50-5	U-60-5-X	U-40-10	U-60-10	C3/60/2-40-10-25	C3/60/2-40-10-50	C3/60/3-40-10-50	C3/60-40-5-150	C3/60-40-5-200	C3/60-50-5-150	C3/60-50-5-200
Fleet (2019)	f_{test} (ksi)	97.9	121.0	119.2	117.0	71.0	73.2	80.8	83.6	94.2	89.4	88.4	88.2	90.4	96.8	104.6	111.3
ACI 318-14	$K_{tr} = \frac{40A_{tr}}{sn}$	89.5	133.9	178.2	228.3	59.9	73.5	87.4	79.2	118.2	84.1	86.5	88.7	82.3	89.6	105.4	114.7
	$K_{tr} = 0$	89.5	133.9	178.2	228.3	59.9	73.5	87.4	79.2	118.2	80.0	78.4	80.4	63.0	63.5	80.6	81.2
Pay (2005)	with Cover	84.2	102.9	118.8	134.4	62.2	68.9	75.1	71.5	87.3	-	-	-	-	-	-	-
	without Cover	85.0	104.0	120.0	135.8	65.4	72.5	79.0	75.2	91.9	-	-	-	-	-	-	-
Sim (2014)	with Cover	78.5	96.0	110.7	125.3	64.0	70.9	77.3	73.6	90.0	77.3	76.6	81.2	78.8	84.6	92.5	98.4
	without Cover	56.2	68.7	79.3	89.8	54.7	60.6	66.1	62.9	76.9	70.6	69.9	74.4	72.8	78.6	85.8	91.6
Glucksman (2018)	with Cover	119.3	145.9	168.3	190.5	77.1	85.4	93.1	88.7	108.3	92.2	91.4	94.2	88.6	91.0	100.5	102.7
	without Cover	85.4	104.5	120.5	136.4	65.9	73.0	79.6	75.8	92.6	84.1	83.4	86.1	81.4	83.8	92.4	94.6

Table 6.2: Statistical Analysis of f_{test}/f_{calc} for Various Analytical Methods

		Max.	Min.	Mean	Standard Deviation	COV	r^2
ACI 318-14	$K_{tr} = \frac{40A_{tr}}{sn}$	1.33	0.51	0.97	0.189	0.195	0.636
	$K_{tr} = 0$	1.52	0.51	1.07	0.252	0.235	0.452
Pay (2005) ^[1]	with Cover	1.30	0.87	1.11	0.094	0.085	0.785
	without Cover	1.16	0.86	1.04	0.086	0.083	0.772
Sim (2014)	with Cover	1.29	0.90	1.08	0.091	0.084	0.749
	without Cover	1.76	0.97	1.25	0.163	0.130	0.505
Glucksman (2018)	with Cover	1.08	0.61	0.93	0.106	0.115	0.602
	without Cover	1.19	0.86	1.06	0.079	0.074	0.736

[1] Equation only valid for unconfined specimens

6.2 Influence of Investigated Parameters

Three primary parameters were investigated in this study using test results from Phase I and Phase II of this project. Phase I testing was conducted by Glucksman (2018) that included four (4) series of splice beam tests to investigate the influence of splice length (l_s), bar spacing ($2c_{si}$), transverse reinforcement spacing (s), and transverse reinforcement yield strength (f_{yt}). In Phase II, the parameters investigated included splice length (l_s), concrete compressive strength (f'_c), and the influence of transverse reinforcement.

6.2.1 Phase I Experimental Test Results

For Series I through IV, 17 specimens failed in bond and five failed in flexure. For Series V through VII, 13 specimens failed in bond and three failed in flexure. The combined results for all seven series of splice specimen testing are documented in Table 6.3. These combined testing results were used for the investigation of several parameters and their influence on bond strength.

The U-40-5 and U-60-5 specimens in Series I were neglected in any forthcoming analyses due to problems experienced during testing, resulting in low bar stresses achieved at failure. Duplicate specimens in Series IV, U-40-5a and U-60-5a, achieved more appropriate results at failure. This provided a total of 28 specimens that failed in bond and eight specimens that failed in flexure. Of these 36 specimens, 18 contained transverse reinforcement (confined) while 18 did not (unconfined). All specimens in Series I through Series VII use the same specimen label identification. Additionally, three specimens in Series I were constructed using the minimum spliced bar spacing allowed by ACI and therefore had a slightly decreased width in the cross-section. These specimen labels contain an additional 'M' in Table 6.3 to indicate this difference.

Table 6.3: Experimental Results from Glucksman (2018) and Fleet (2019)

Series	Specimen	f_c (psi)	l_s (in.)	P_{ult} (kip)	M_{ult} (ft-k)	f_{test} (ksi)	$f_{norm}^{[4]}$ (ksi)
I	U-40-5	4740	40	44.9	180	58.2	59.0
	U-60-5	4740	60	52.7	211	68.4	69.3
	U-80-5	4740	80	77.6	310	102.2 ^[1]	103.6
	U-100-5	4740	100	78.7	315	103.7 ^[1]	105.1
	U-120-5	4740	120	78.6	314	103.6 ^[1]	105.0
	U-80-5-M	4740	80	73.3	293	97.7 ^[1]	99.0
	U-100-5-M	4740	100	73.2	293	97.5 ^[1]	98.8
	U-120-5-M	4740	120	71.8	287	95.6 ^[1]	96.9
II	C3/60-60-5-50	7360	60	80.4	322	103.3 ^[1]	93.8
	C3/60-60-5-100	7360	60	85.9	344	110.5 ^{[2][3]}	100.3
	C3/60-60-5-150	7360	60	85.1	340	109.4 ^{[2][3]}	99.3
	C4/60-60-5-100	7360	60	84.7	339	108.9 ^{[2][3]}	98.9
	C3/100-60-5-100	7360	60	86.3	345	111.0 ^{[2][3]}	100.8
III	C3/60-80-5-50	6310	80	79.4	318	101.9 ^{[1][3]}	96.1
IV	U-40-5a	6260	40	54.6	218	69.8	66.0
	U-60-5a	6260	60	69.3	277	88.9 ^[1]	84.0
	U-70-5	6260	70	73.8	295	94.9 ^[1]	89.7
	C3/60/2-40-5-50	6260	40	63.9	256	81.8	77.3
	C3/60/3-40-5-50	6260	40	70.0	280	89.8 ^[1]	84.9
	C3/100/3-40-5-50	6260	40	66.4	266	85.0	80.4
	C3/60-40-5-100	6260	40	71.4	286	91.7 ^[1]	86.7
	C3/100-40-5-100	6260	40	72.5	290	93.1 ^[1]	88.0
V	S-40-5	6240	25	11.1	44.4	97.9 ^[1]	92.6
	S-60-5	6200	37.5	13.6	54.4	121.0 ^[2]	114.7
	S-80-5	6180	50	13.4	53.6	119.2 ^{[2][3]}	113.1
	S-100-5	6490	62.5	13.2	52.8	117.0 ^{[2][3]}	109.6
VI	U-40-5-X	5670	40	55.0	220	71.0	68.8
	U-60-5-X	5310	60	61.4	245.6	80.8	79.6
	U-50-5	5400	50	55.5	222	73.2	71.8
	U-40-10	9870	40	65.0	260	83.6	70.5
	U-60-10	9700	60	73.2	292.8	94.2 ^[1]	79.8
	C3/60/2-40-10-25	10,100	40	69.5	278	89.4 ^[1]	75.0
	C3/60/2-40-10-50	9590	40	68.8	275.2	88.4 ^[1]	75.1
	C3/60/3-40-10-50	10,100	40	68.7	274.8	88.2	74.0
VII	C3/60-40-5-150	6200	40	69.9	279.6	90.4 ^[1]	85.7
	C3/60-40-5-200	6300	40	74.5	298	96.8 ^[1]	91.4
	C3/60-50-5-150	6600	50	80.1	320.4	104.6 ^[1]	97.6
	C3/60-50-5-200	6600	50	85.2	340.8	111.3 ^{[2][3]}	103.8

[1] Beyond linear-elastic limit of corresponding longitudinal bar steel

[2] Beyond yield stress of corresponding longitudinal bar steel

[3] Failed in flexure

[4] Bar stresses normalized to 5000 psi with the quarter root

6.2.2 Splice Length

6.2.2.1 Unconfined Specimens

Due to different member cross-sections, slabs and beams were separated when reviewing the test results. Figure 6.8 shows the increase in bar stress achieved in slabs as the splice length increases from 25 in. to 62.5 in. To account for the effect of variations in concrete strength among tested specimens, bar stresses normalized to a compressive strength of 5000 psi are also provided (all normalizations use the quarter root of compressive strengths). By increasing the splice length from $40d_b$ to $60d_b$, a significant increase in bar stress was achieved. While the steel reached yield, a splice failure still resulted. Once the splice length increased to $80d_b$, a flexure failure was achieved. Once a flexural failure was achieved, increasing splice length was not beneficial as the flexure capacity was fully achieved.

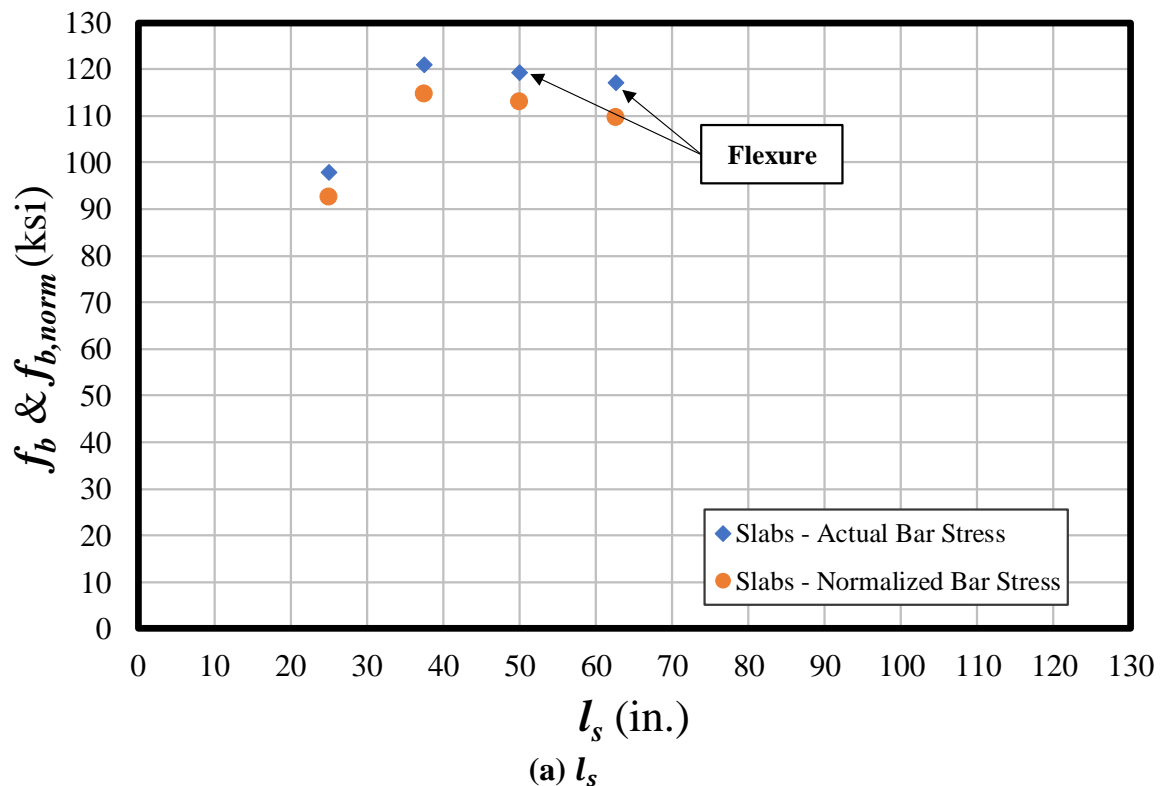


Figure 6.8: Effect of Splice Length on Bar Stress – Slabs

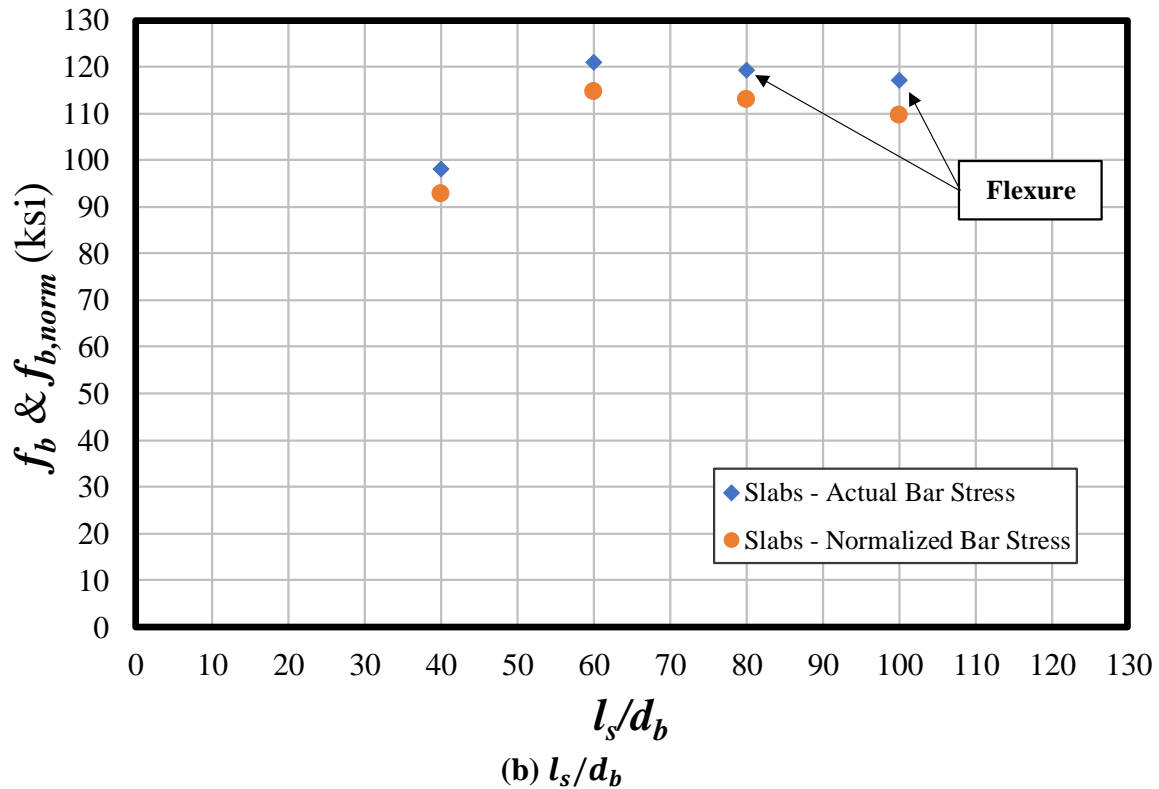
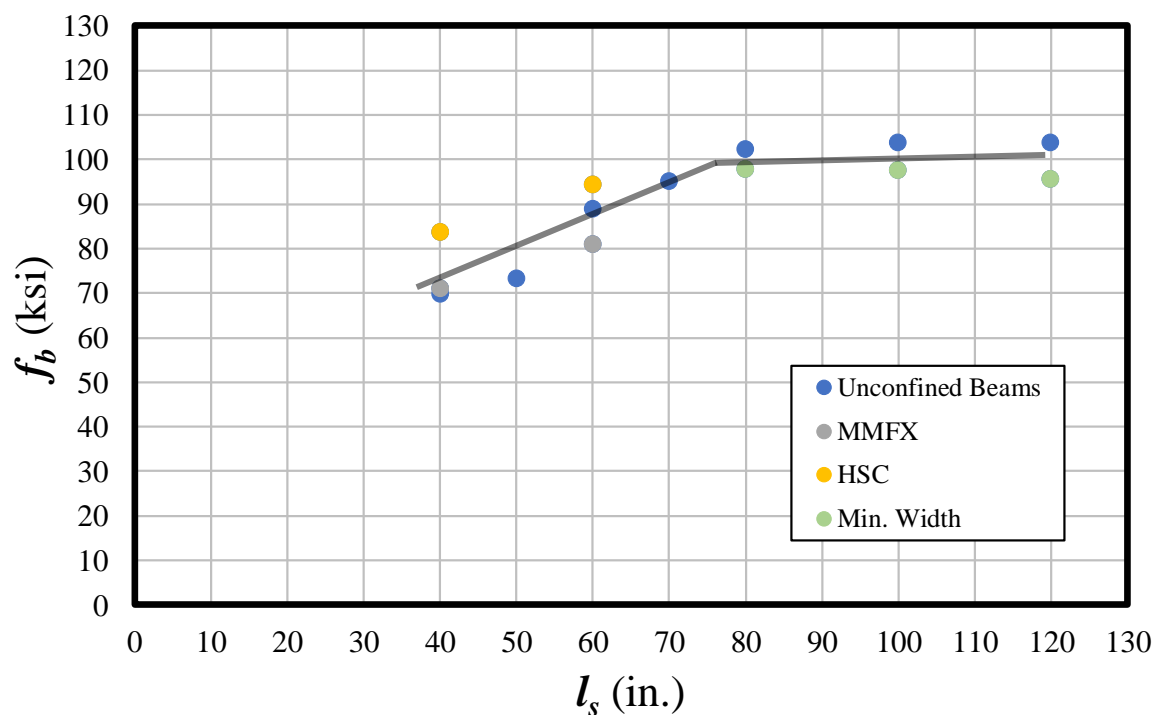


Figure 6.8: Effect of Splice Length on Bar Stress – Slabs (Continued)

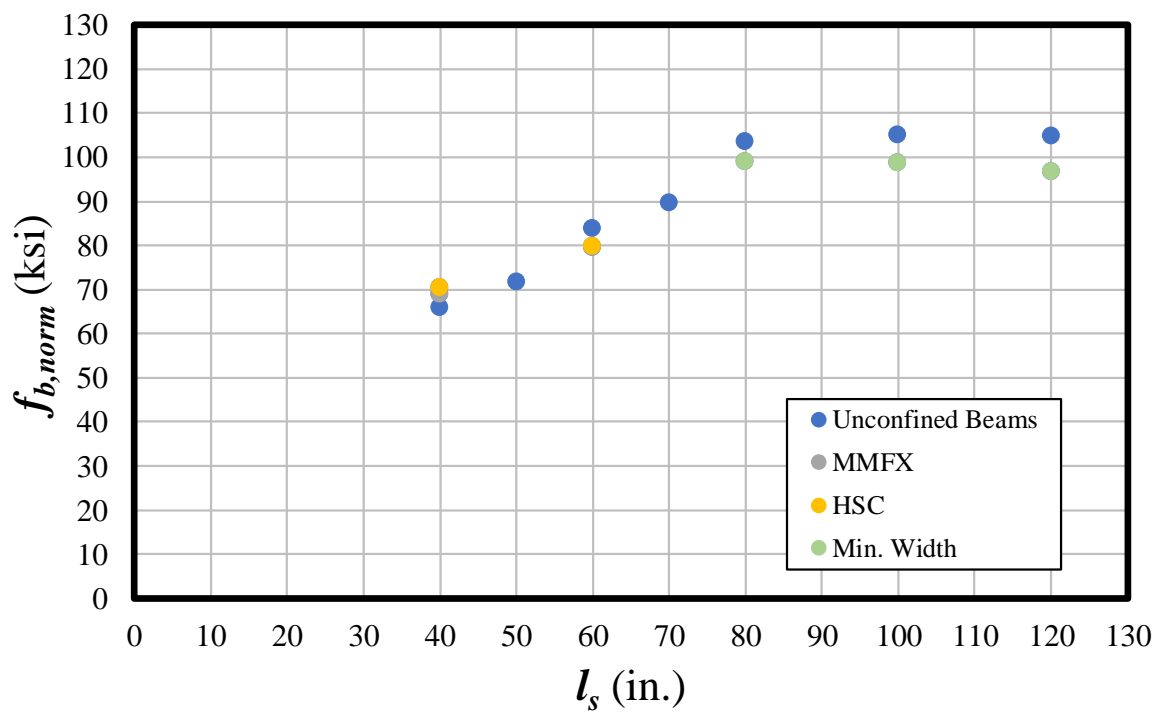
All unconfined beams from Phase I and Phase II are provided in Figure 6.9 for various splice lengths. Note that if Figure 6.9 is plotted against l_s/d_b , the plots are unchanged because all unconfined beams contained No. 8 spliced bars ($d_b = 1$ in.). Note that all MMFX, high-strength concrete, and minimum width beams are labeled. An increase in bar stress is observed for splices less than or equal to 80 in.; however, for larger splice lengths, as the embedded length increases, no additional bar stress is achieved. For the minimum width beams with large splice lengths, the bar stress appears to remain unchanged or decrease slightly as the splice length increases.

Figure 6.9(b) compares the unconfined specimen splice lengths to their failure stresses normalized to a concrete compressive strength of 5000 psi. Results from specimens with splice lengths less than 80 in. are condensed, including the high-strength concrete and MMFX specimens. This clearly shows that the quarter root normalization represents the concrete strength well.

Furthermore, the MMFX specimens performed no differently than the similar A615 splice beams at splice lengths of $40d_b$ and $60d_b$.



(a) Actual Bar Stress



(b) Normalized Bar Stress

Figure 6.9: Effect of Splice Length on Bar Stress (Unconfined)

6.2.2.2 Confined Specimens

Correlations between splice length and bar stress for confined beams when multiple different confinement pressures are plotted are not evident due to the variation in confinement (Figure 6.10). However, by isolating the confined beams constructed with 50 psi of confinement pressure along the splice, a correlation is observed between splice length and bar stress (Figure 6.11). For 50 psi confined beams with a splice length of $40d_b$, failures occurred within a range of 10 ksi (some variation of concrete strength). As splice length was increased to $60d_b$ and $80d_b$, bar stress increased and the failure mode ultimately changed from splitting to flexure.

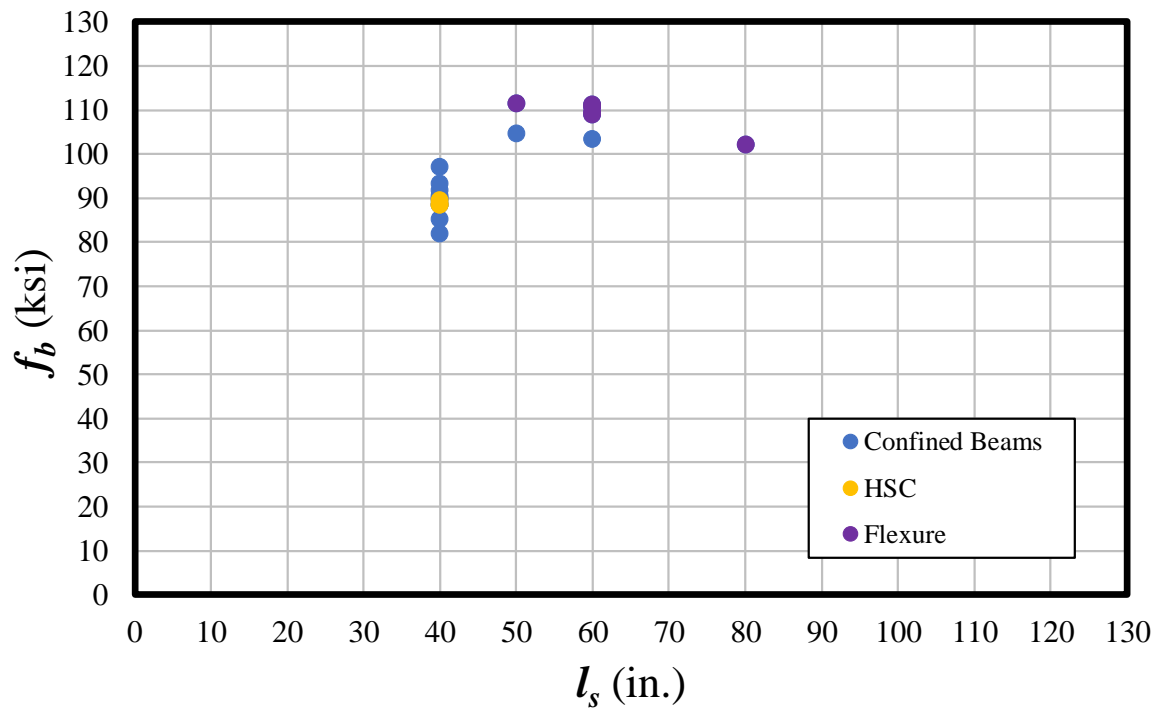


Figure 6.10: Effect of Splice Length on Actual Bar Stress

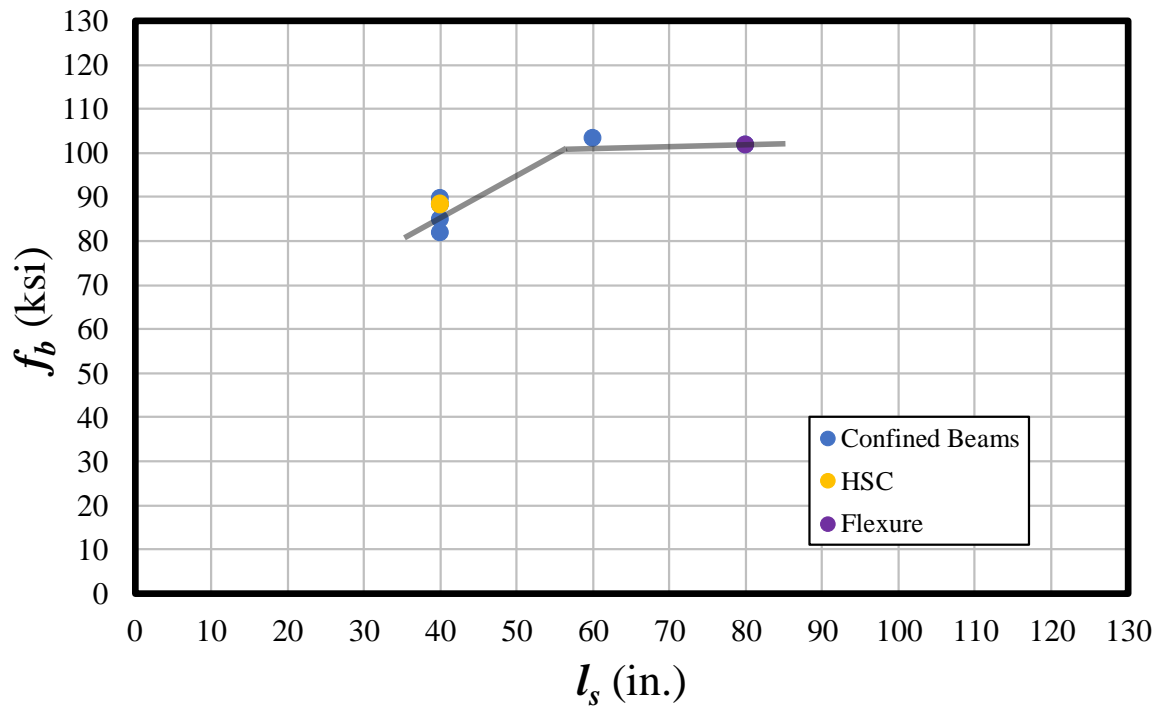


Figure 6.11: Effect of Splice Length on Actual Bar Stress (Confined 50 psi Beams)

6.2.3 Concrete Compressive Strength

6.2.3.1 Unconfined Specimens

The range of concrete strengths tested on unconfined beams in Phase I and Phase II ranged from 4740 psi to 9870 psi. Figure 6.12 shows this range and indicates which specimens contained MMFX bars, high-strength concrete, and the minimum bar spacing. No clear correlation between concrete compressive strength and bar stress is observed in this plot.

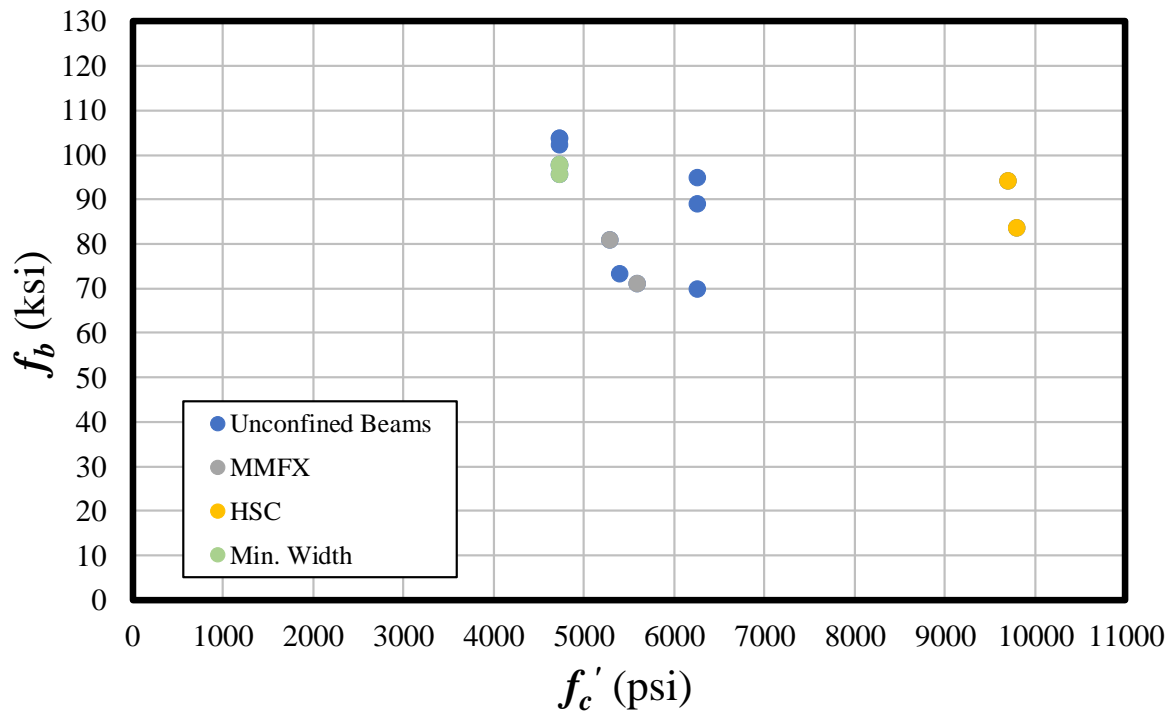
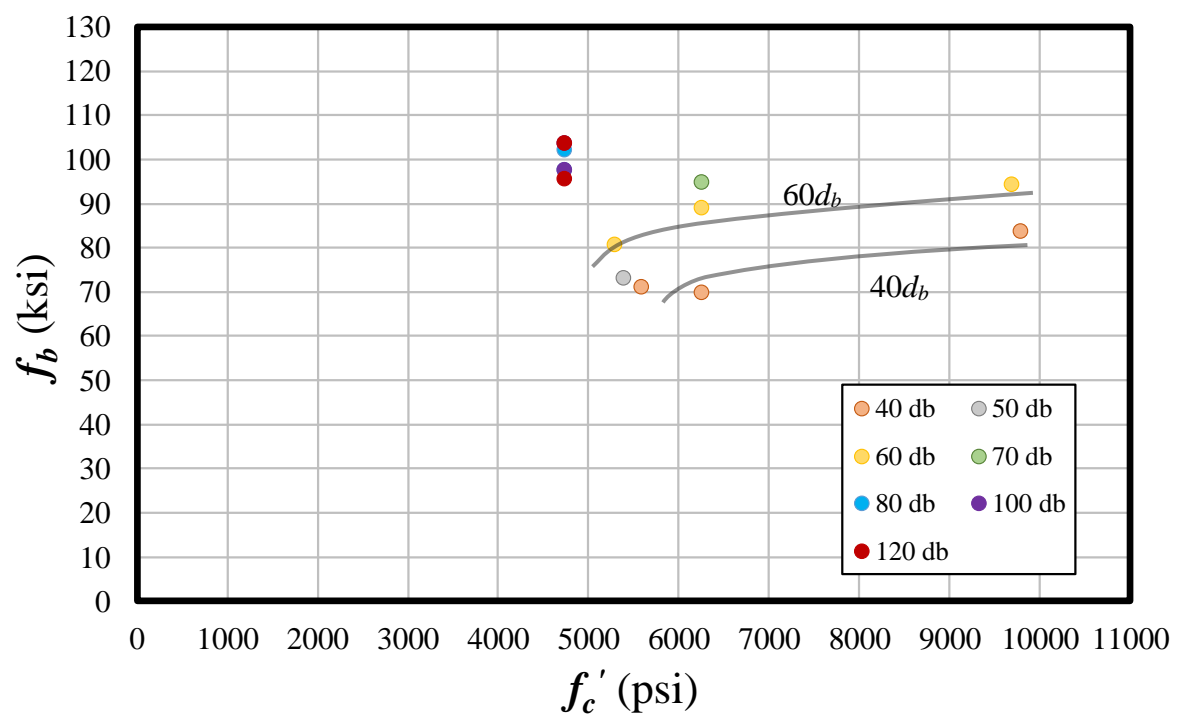
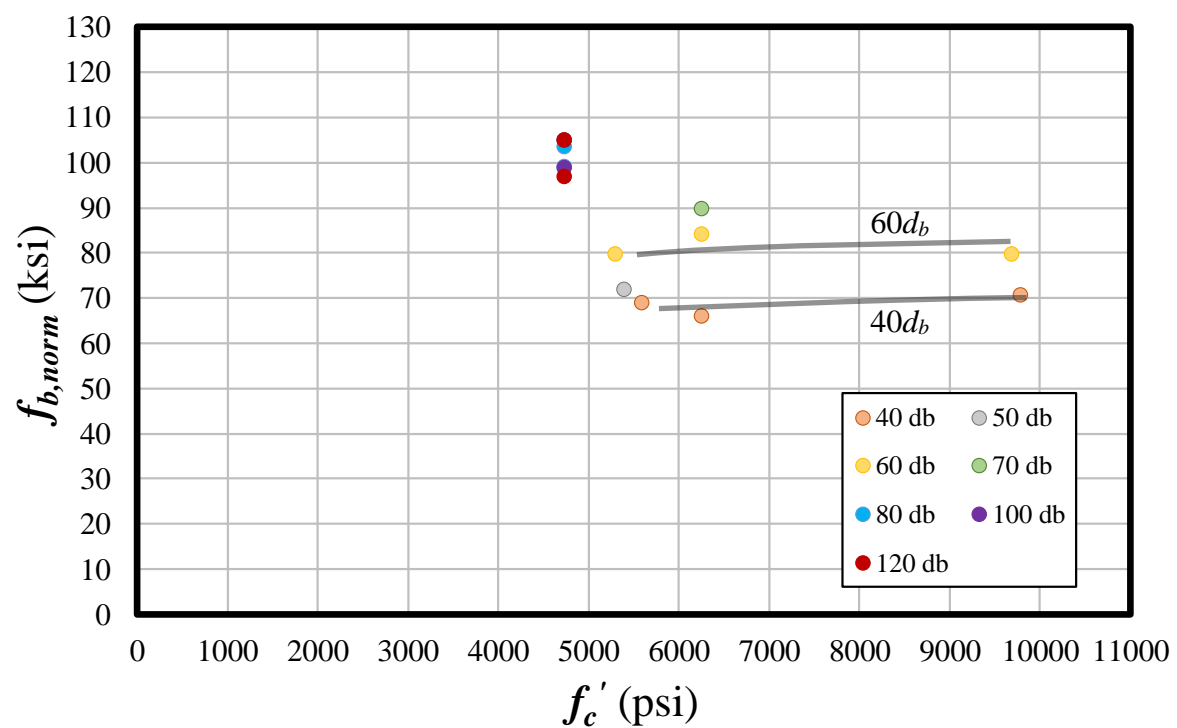


Figure 6.12: Effect of Concrete Strength on Actual Bar Stress (Unconfined)

Figure 6.13(a) provides a comparison between the concrete compressive strength and the bar stress for all unconfined beams. Slabs were not included because Series V was for a different cross-section. All specimens in Figure 6.13(a) are grouped by identical splice length, with lengths of $40d_b$ and $60d_b$ having the most specimens. There is an observed increase in bar stress as concrete compressive strength increases for a constant splice length. For the $60d_b$ unconfined beams, the relationship between compressive strength and bar stress appears to be nonlinear. Note that the cluster of beams with concrete compressive strength of 4740 psi contains the greatest splice lengths and three beams with minimum bar spacing. Figure 6.13(b) shows the effect on bar stress normalized to 5000 psi (using the quarter root), which shifts the high-strength concrete beams downward. The flat trend in the normalization supports the use of the quarter root to represent the influence of concrete compressive strength.



(a) Actual Bar Stress



(b) Normalized Bar Stress

Figure 6.13: Effect of Concrete Strength on Bar Stress by Splice Length (Unconfined)

The change in bar stress between specimens cast with normal-strength concrete and high-strength concrete is provided in Table 6.4 for $40d_b$ and $60d_b$ specimens in Phase I and Phase II. The two beams from Series VI containing MMFX reinforcing bars are included in this comparison because the behavior during testing and at failure was identical to the beams reinforced with A615 longitudinal bars. Additionally, a comparison between representing the concrete strength by the square root and the quarter root is provided. For the $60d_b$ specimens, the quarter root of the difference in concrete strengths provides a better representation when compared to the use of the square root. For splice lengths of $40d_b$, the quarter root is more accurate for Specimen U-40-5-X; however, this is untrue for Specimen U-40-5a where the square root is slightly closer in representing the change in concrete strength.

Table 6.4: Effect of High-Strength Concrete for $40d_b$ and $60d_b$ Specimens

Specimens		f_c (psi)	f_b (ksi)	f_b Increase	$\sqrt{f'_{c,HSC} / f'_{c,NSC}}$	$\sqrt[4]{f'_{c,HSC} / f'_{c,NSC}}$
$40d_b$	U-40-5a	6260	69.8	20%	25%	12%
	U-40-5-X	5600	71.0	18%	32%	15%
	U-40-10	9800	83.6	-	-	-
$60d_b$	U-60-5a	6260	88.9	6%	24%	12%
	U-60-5-X	5300	80.8	17%	35%	16%
	U-60-10	9700	94.2	-	-	-

6.2.3.2 Confined Specimens

The range of concrete strengths tested on confined beams in Phase I and Phase II ranged from 6200 psi to 10,100 psi. Figure 6.14 shows this range and indicates which specimens

contained MMFX bars, high-strength concrete, and minimum bar spacing. No clear correlation between concrete compressive strength and bar stress is observed in this plot.

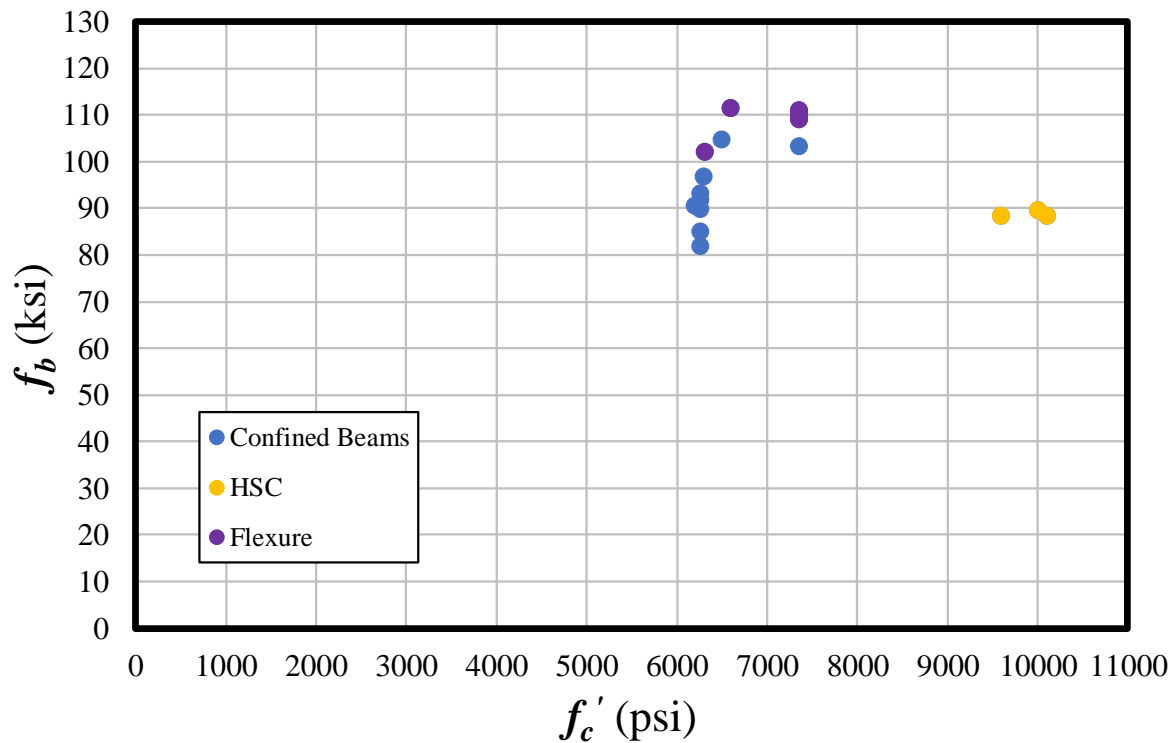
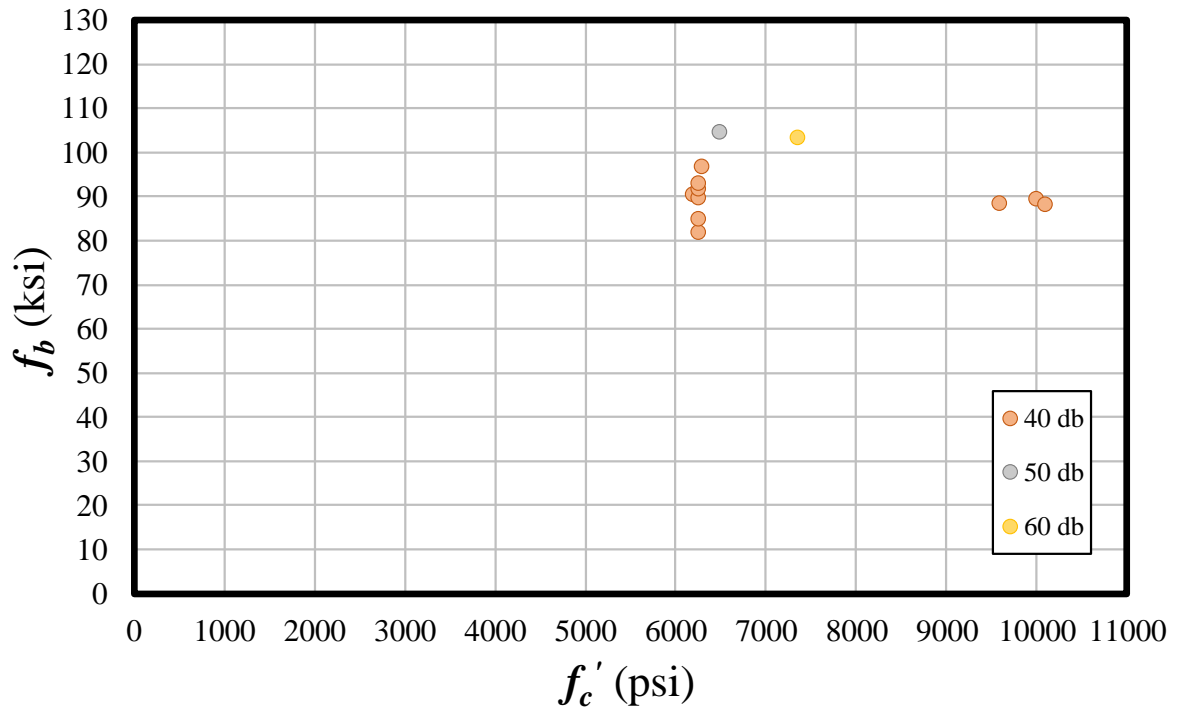


Figure 6.14: Effect of Concrete Strength on Bar Stress (Confined)

Additional parameters were isolated to observe trends among compressive strength and bar stress. Figure 6.15(a) groups confined beams that failed in splitting (no flexure) by splice length for $40d_b$, $50d_b$, $60d_b$, and $80d_b$ specimens. Only the $40d_b$ specimens contained a large range of concrete compressive strengths. In addition, the most common confinement pressure used in this testing program was 50 psi of transverse reinforcement; therefore, all $40d_b$ confined beams with 50 psi of transverse reinforcement were isolated in Figure 6.15(b). A slight positive correlation between concrete strength and bar stress was found for confined specimens; however, this may be attributed to typical scatter of the data.



6.2.4 Transverse Reinforcement

To better understand the influence of transverse reinforcement on bond strength, three parameters were found to have a strong influence on the confinement contribution to bar stress. The variables of interest are the distributed transverse reinforcement ratio (ρ_t), confinement pressure (p_c), and the average transverse reinforcement ratio (ρ_{avg}).

6.2.4.1 *Distributed Transverse Reinforcement Ratio*

Phase I of this study found that the effect of confining steel on bar stress achieved is best understood by considering the total area of transverse reinforcement present within the splice region. Although this study found a positive correlation between the confinement contribution to bar stress and the total area of transverse reinforcement present, several important confinement variables such as stirrup spacing and effective area of the stirrup in the splice plane may better describe the effect of transverse reinforcement.

The fundamental mechanics that initiate bond failure occur when tensile strength of the concrete is exceeded by the stresses developed over the lap splice. The tensile load that accumulates is resisted primarily by the concrete until cracking initiates. As bar stresses continue to increase, the transverse steel becomes responsible for resisting this stress entirely without contribution from the surrounding cracked concrete. The resisting stress or pressure occurs over the entire plane of splitting.

The distributed transverse reinforcement ratio, ρ_t , is a term used by ACI 318-14 in determining reinforcement requirements for wall and diaphragm design. The term takes the transverse reinforcement area of one confining element and compares it to the gross area of concrete over which it is confining. Figure 6.16 provides a graphic of Equation 6-22.

$$\rho_t = \frac{A_v}{A_g} = \frac{N_t A_t}{b_w s} \quad (6-22)$$

where:

A_g = gross area of concrete in splitting plane within stirrup spacing s (in.²)

A_t = area of one leg of a closed stirrup, hoop, or tie within spacing s (in.²)

A_v = area of shear reinforcement within spacing s (in.²)

b_w = beam width (in.)

N_t = number of legs on a given stirrup

s = stirrup spacing (in.)

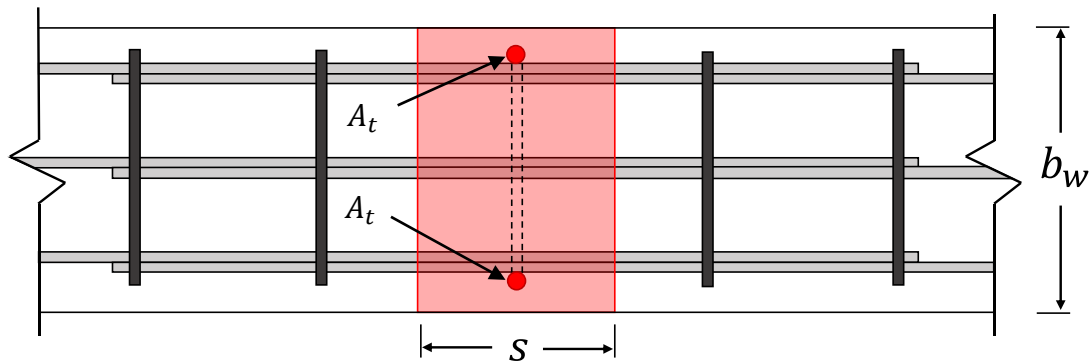
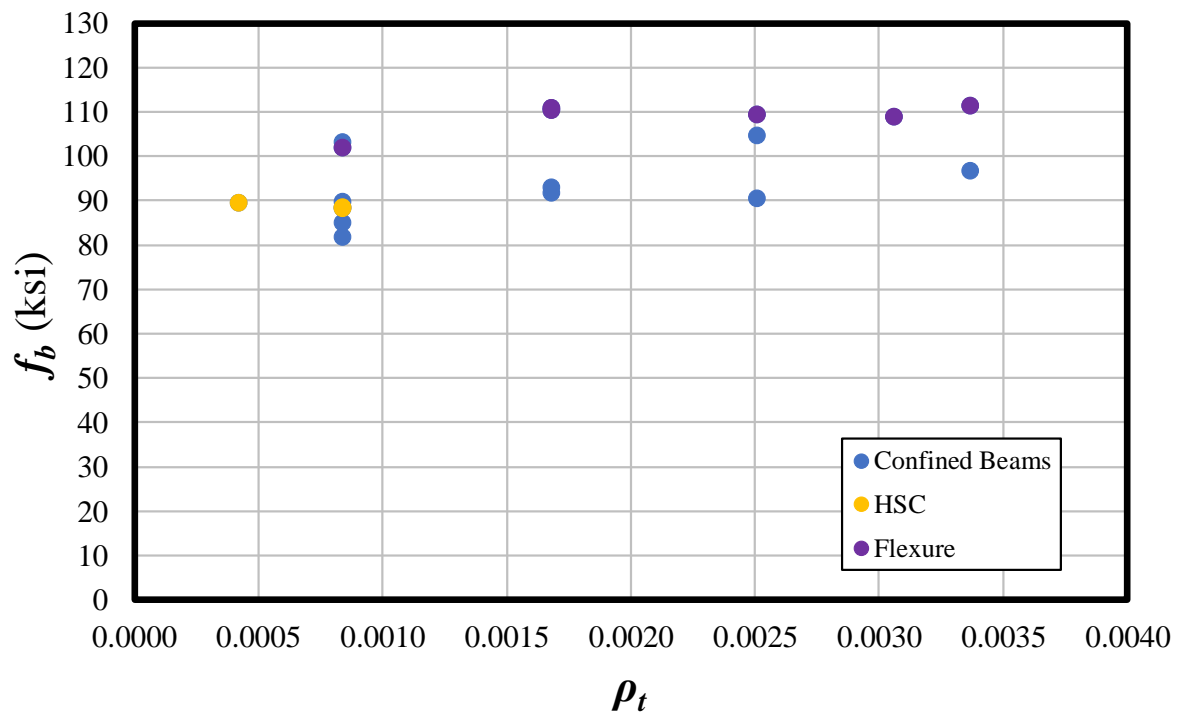


Figure 6.16: Representation of ρ_t

This ratio is helpful in describing the amount of transverse reinforcement within a region and is independent of the yield strength of the material. Glucksman (2018) concluded that the yield strength of transverse reinforcement does not improve the contribution to bar stress provided by the confinement steel; the use of ρ_t may be more appropriate as it does not consider yield strength.

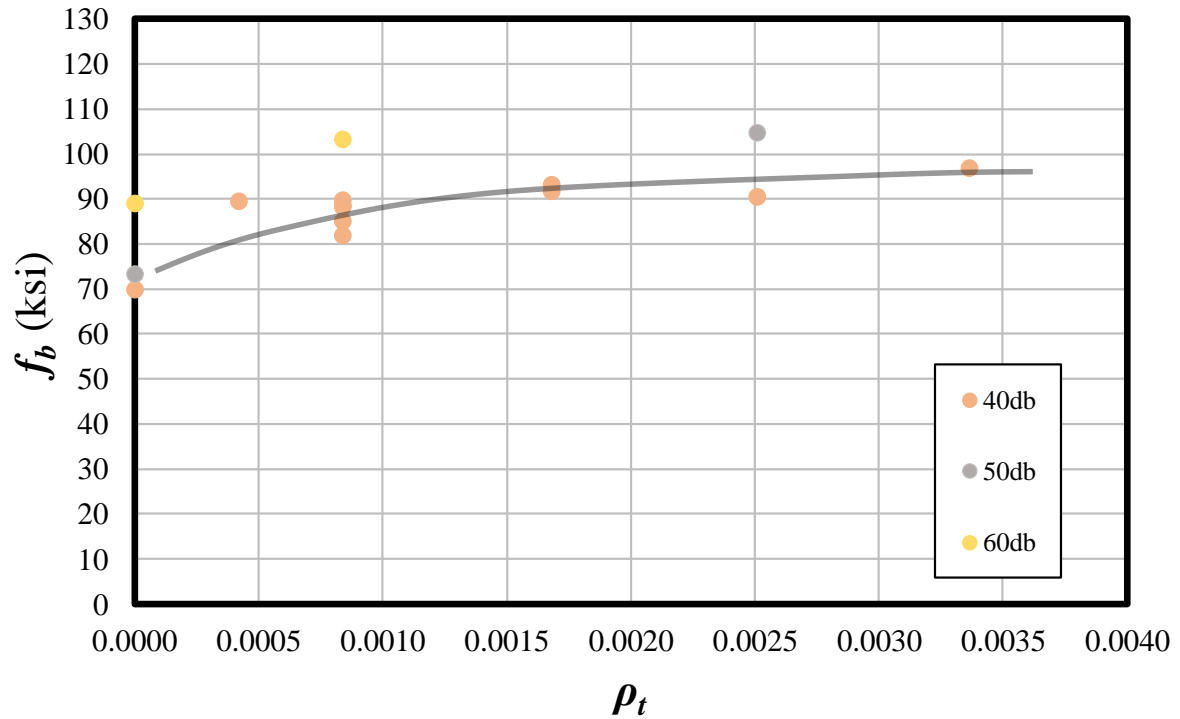
All confined specimens from Phase I and Phase II are plotted in Figure 6.17(a). Beams cast with high-strength concrete and beams that experienced a flexural failure at large stresses are

noted. Values for ρ_t range from 0.04% to 0.34% within the splice. There is a slight increasing trend in bar stress as ρ_t increases. To further evaluate, beams experiencing a flexure failure were removed and all confined beams were grouped by splice length (Figure 6.17(b)). The $40d_b$ and $60d_b$ specimens provide the most data across a large range of ρ_t values. General observed trends are noted for these two lengths of specimens. Note that a ρ_t value of zero indicates an unconfined beam of the specified splice length.



(a) All Confined Beams

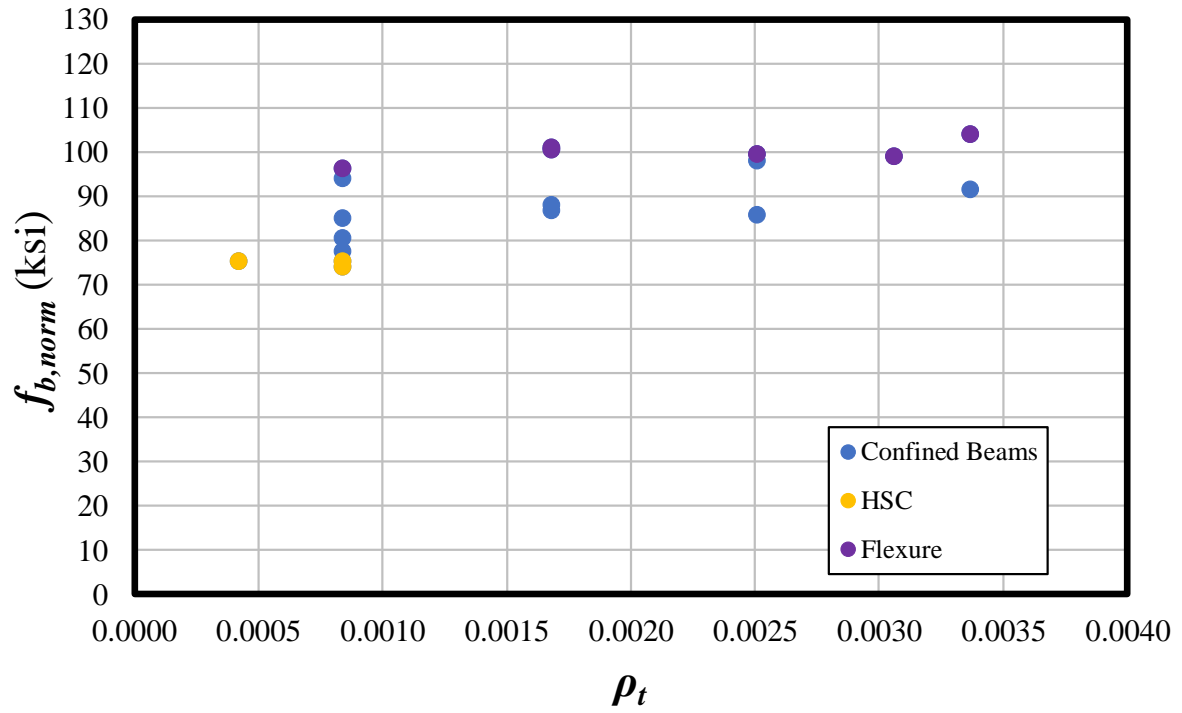
Figure 6.17: Effect of Transverse Reinforcement Ratio on Actual Bar Stress



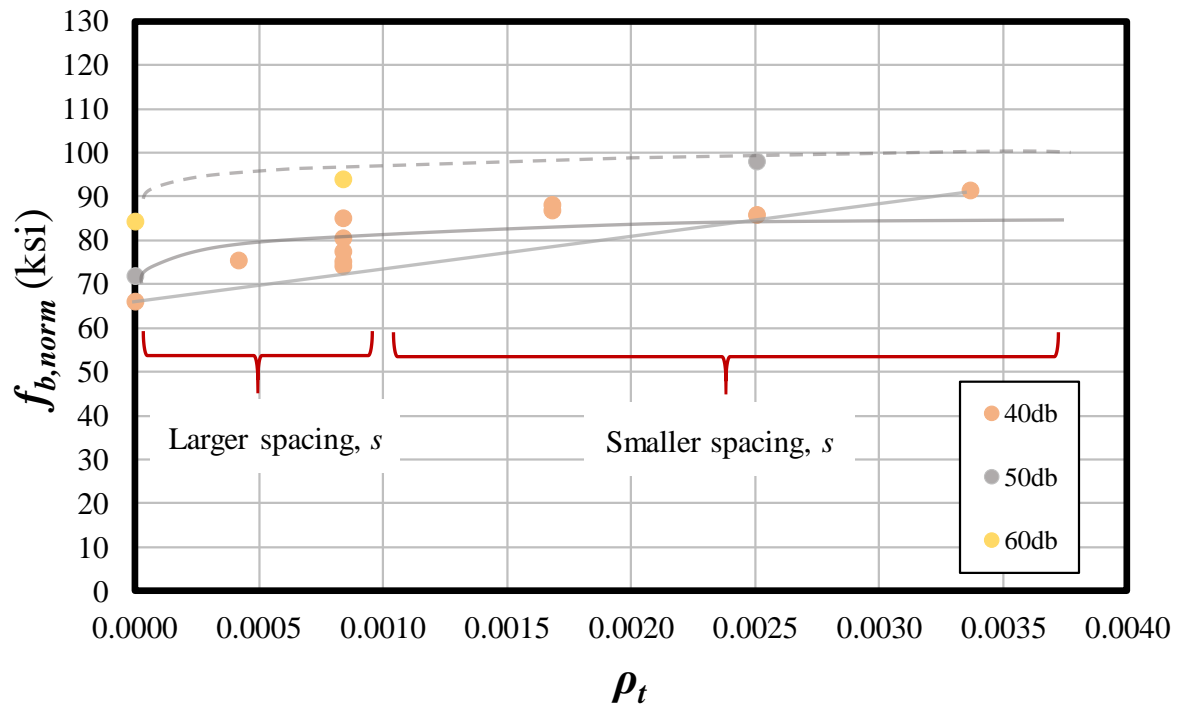
(b) Grouped by Splice Length

Figure 6.17: Effect of Transverse Reinforcement Ratio on Actual Bar Stress (Continued)

Figure 6.18(a) provides results when failure bar stresses are normalized to a concrete strength of 5000 psi. Unconfined reference values are provided in Figure 6.18(b) as well as specimens grouped by splice lengths and possible trend lines. Specimens with lower ρ_t values were observed to experience increased bar stresses with small increases in ρ_t ; however, as ρ_t increased above approximately 0.1%, a smaller increase in bond stress was observed. The region of larger stirrup spacing and lower ρ_t values exhibits more variability in bar stress contribution due to the large range of possible stirrup locations.



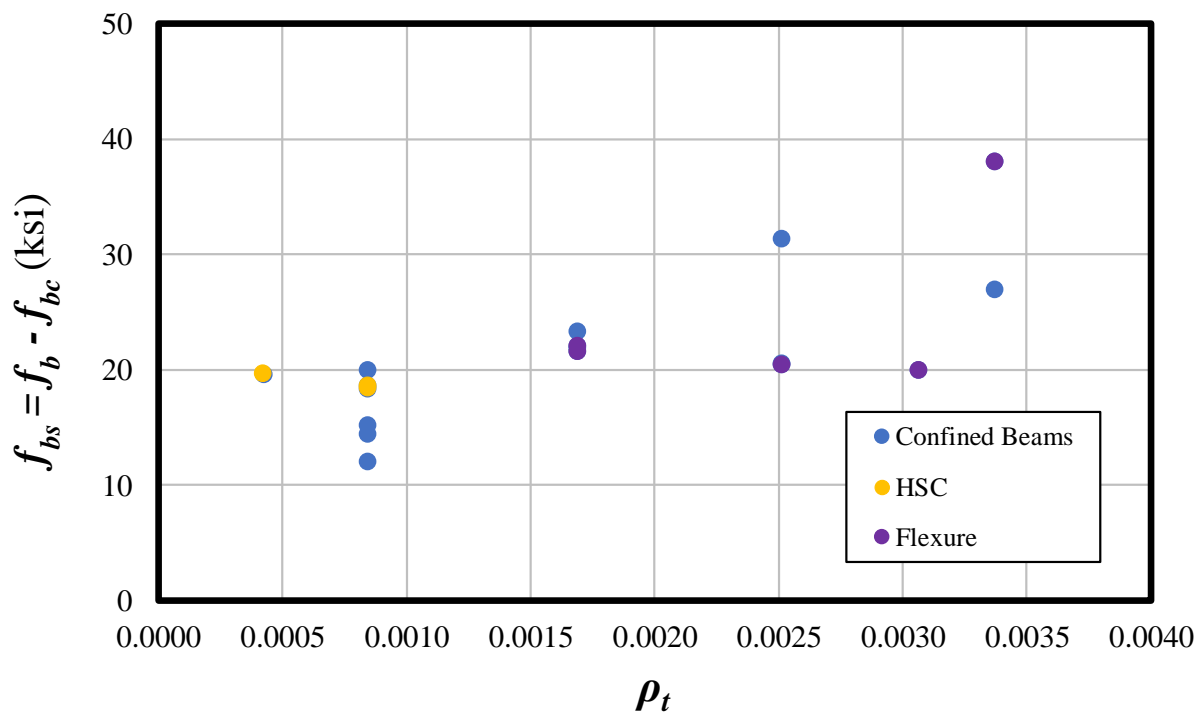
(a) All Confined Beams



(b) Grouped by Splice Length

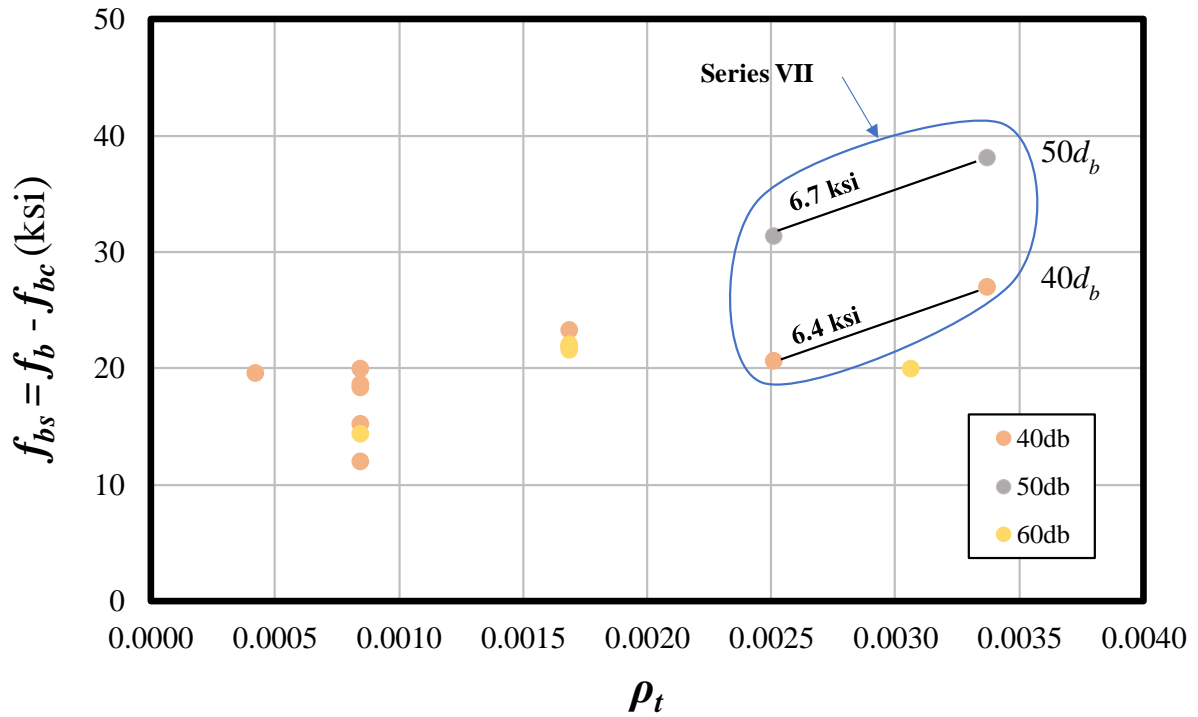
Figure 6.18: Effect of Transverse Reinforcement Ratio on Normalized Bar Stress

By subtracting the bar stress provided by the concrete (unconfined case for each confined beam, f_{bc}) from the failure bar stress of each confined beam (f_b), a value is obtained for the contribution to total bar stress provided by the transverse reinforcement (f_{bs}). Figure 6.19(a) provides f_{bs} values for all confined beams in Phase I and Phase II. Specimens cast with high-strength concrete and beams that failed in flexure are indicated. When splice lengths are isolated (Figure 6.19 (b)), trends are observed with the $40d_b$ and $50d_b$ specimens. The four beams tested in Series VII show nearly identical increases in bar stress contribution from confinement as ρ_t increases between the $40d_b$ and $50d_b$ beams. Note that specimens experiencing a flexural failure are included in Figure 6.19 (b) to show a trend in Series VII.



(a) All Confined Beams

Figure 6.19: Effect of Transverse Reinforcement Ratio on Steel Contribution to Bar Stress

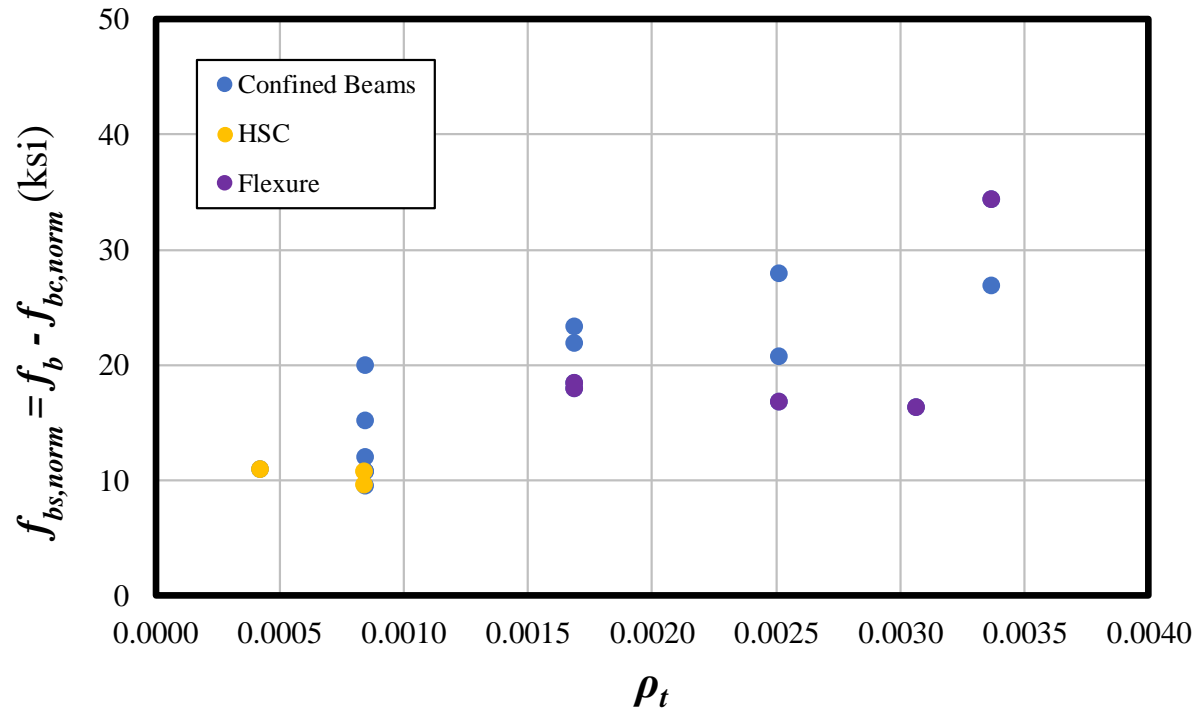


(b) Grouped by Splice Length

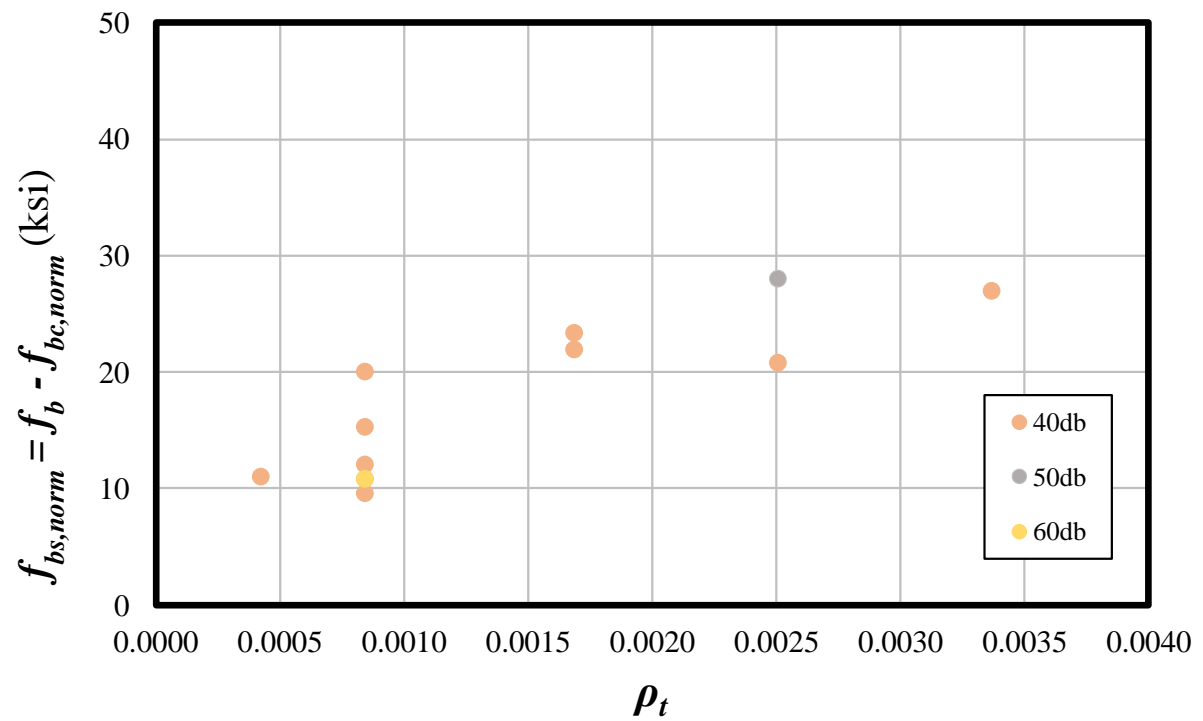
Figure 6.19: Effect of Transverse Reinforcement Ratio on Steel Contribution to Bar Stress

(Continued)

Finally, bar stress contributions (f_{bs}) were adjusted to account for differences in concrete strength. Actual failure stresses for confined beams were implemented while the unconfined counterpart beam stresses were normalized to a concrete strength of 5000 psi. Figure 6.20(a) plots the results for the confined beams. Figure 6.20(b) isolates the effect of splice length and shows that when flexure is neglected, f_{bs} increases as ρ_t increases.



(a) All Confined Beams



(b) Grouped by Splice Length

Figure 6.20: Effect of Transverse Reinforcement Ratio on Normalized Steel Contribution to Bar Stress

6.2.4.2 Confinement Pressure

The confinement pressure (p_c) for each stirrup can be calculated from the specified yield strength of the stirrup and the distributed transverse reinforcement ratio:

$$p_c = f_{yt}\rho_t \quad (6-23)$$

where:

f_{yt} = actual yield strength of transverse reinforcement (psi)

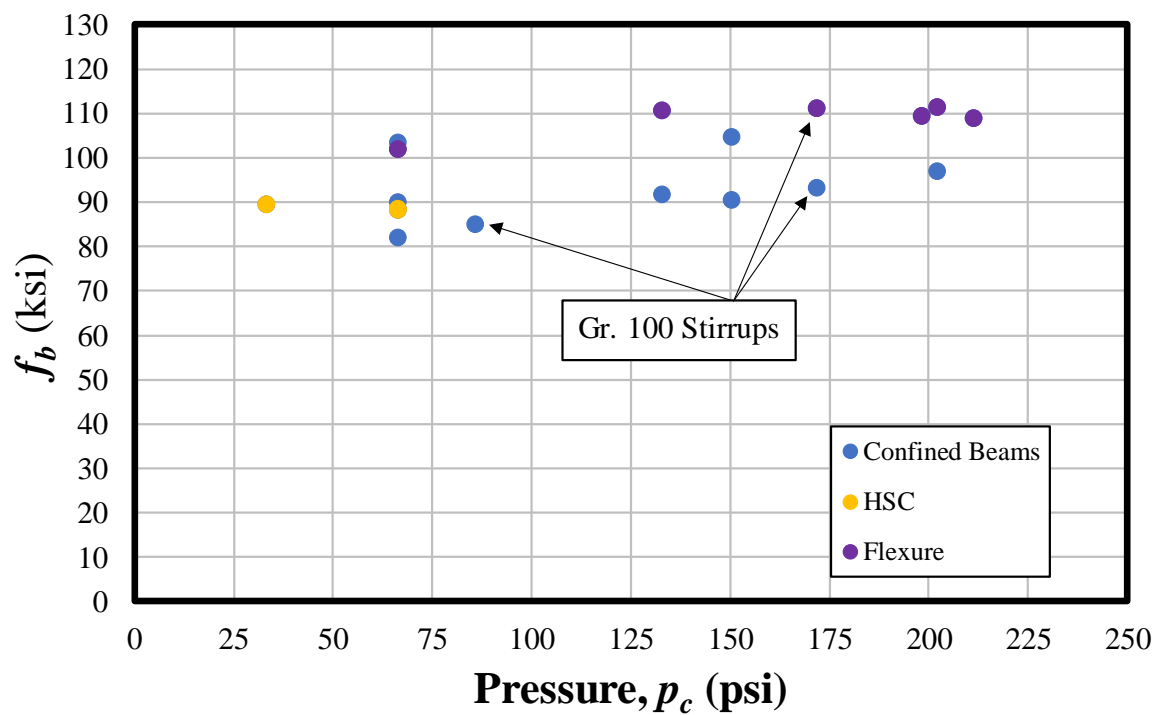
p_c = confining pressure developed by transverse reinforcing (psi)

ρ_t = distributed transverse reinforcement ratio

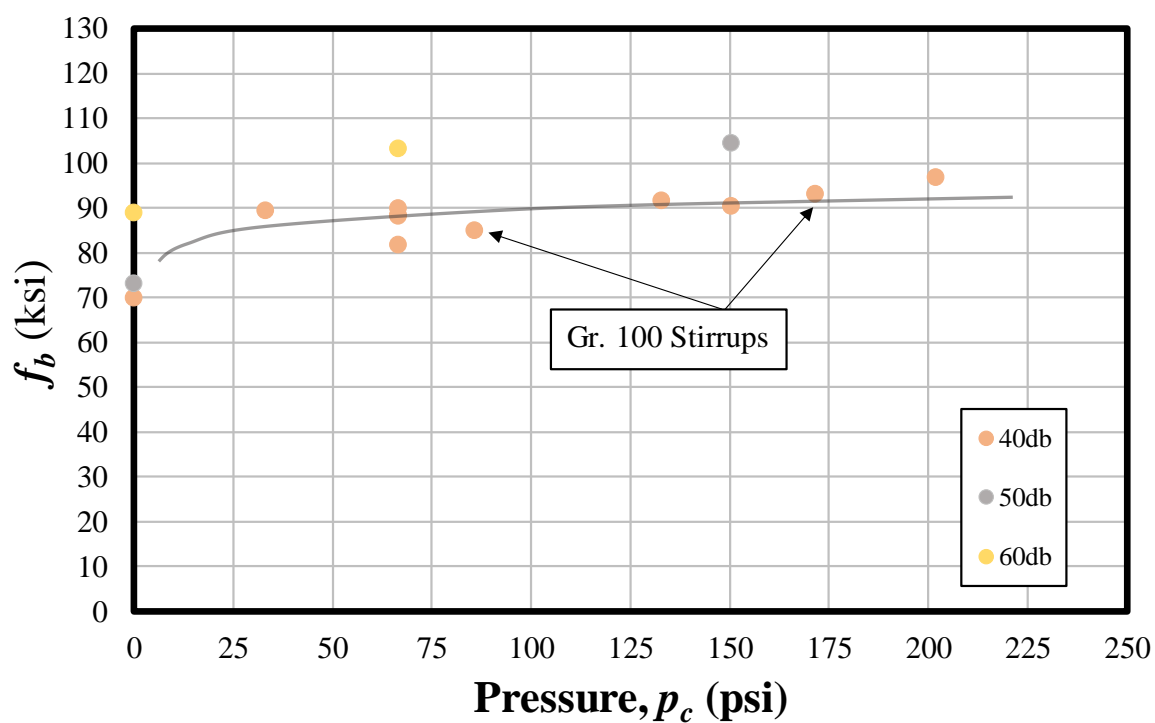
$$= \frac{A_v}{A_g} = \frac{N_t A_t}{b_w s}$$

Various confinement pressures are plotted against the failure bar stress in Figure 6.21(a). Note that this confinement bar stress is different than the nominal confinement pressure selected to design the confined specimens. The nominal value is an estimate based on general stirrup spacing and neglects the yield strength variation in the transverse reinforcement. High-strength stirrups are noted, as well as high-strength concrete beams and flexure-failed specimens. All pressures are calculated using the actual yield strength of the transverse reinforcement; therefore, specimens noted as having Grade 100 stirrups have an f_{yt} value of 102 ksi. Figure 6.21(b) isolates each specimen by splice length and shows general trends for the $40d_b$ and $60d_b$ specimens.

Findings by Glucksman (2018) indicate that the yield strength of transverse reinforcement does not influence the overall bond strength of the splice. Although there is a clear positive correlation between confinement pressure p_c and bar stress, this correlation is primarily influenced by ρ_t in the p_c equation, not f_{yt} .



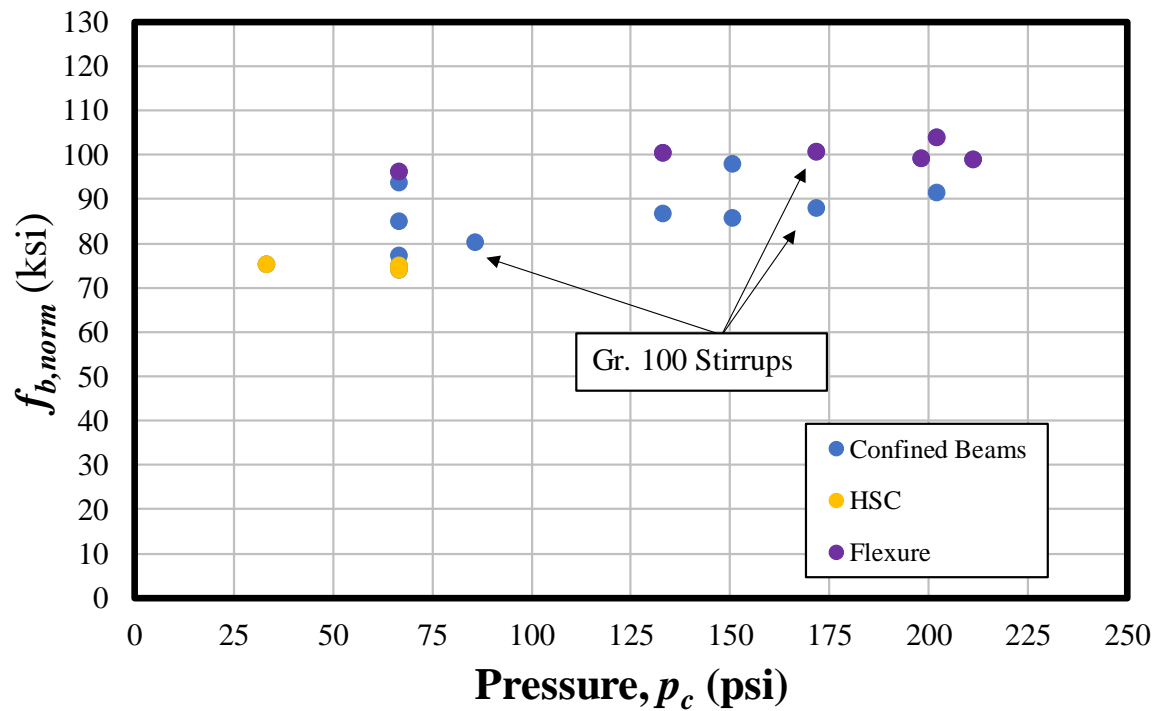
(a) All Confined Beams



(b) Grouped by Splice Length

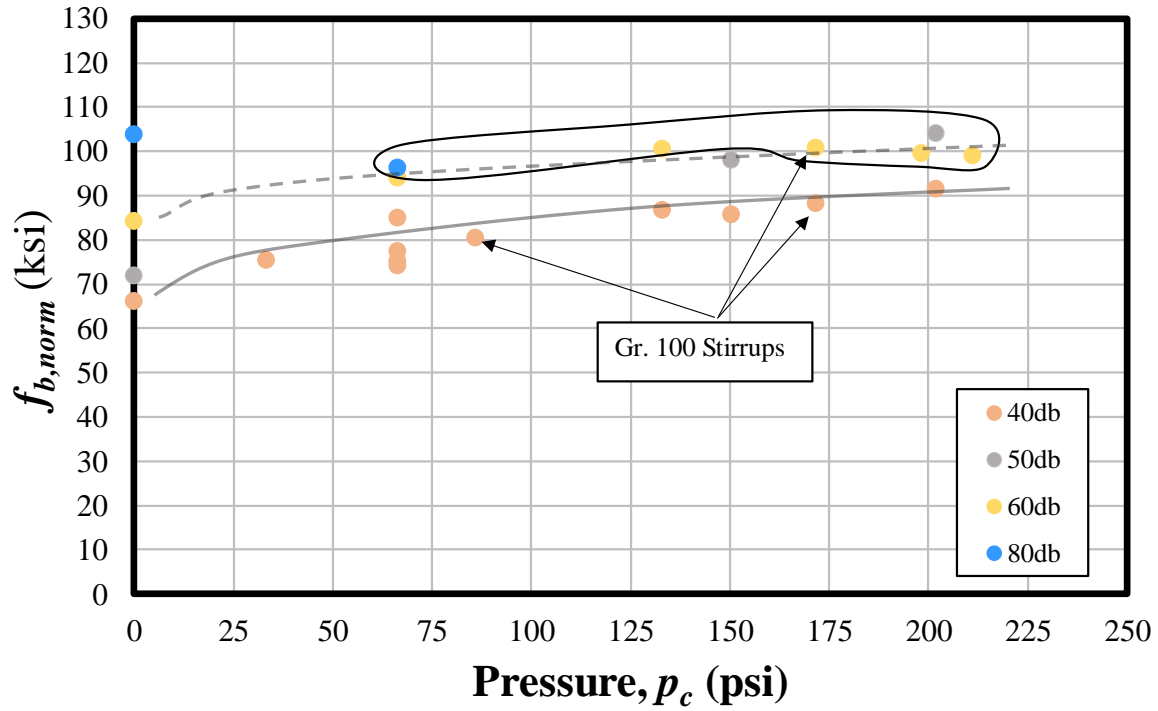
Figure 6.21: Effect of Confinement Pressure on Actual Bar Stress

When bar stress is normalized to a 5000 psi concrete compressive strength, test results with respect to confinement pressure are slightly compressed. In general, as the confining pressure around the splice increases, the bar stress increases. This normalized bar stress comparison for all confined specimens is provided in Figure 6.22(a) with beams identified that contained high-strength concrete and that experienced flexural failures. Figure 6.22(b) isolates the effect of splice length for all confined beams.



(a) All Confined Beams

Figure 6.22: Effect of Confinement Pressure on Normalized Bar Stress



(b) Grouped by Splice Length

Figure 6.22: Effect of Confinement Pressure on Normalized Bar Stress (Continued)

6.2.4.3 Average Transverse Reinforcement Ratio

The distributed transverse reinforcement ratio (ρ_t) accounts for the area of concrete being confined by each stirrup; however, the configuration of the stirrups across the entire length of the splice may change this value for end stirrups. An average can be calculated if all stirrups within the splitting plane are considered:

$$\rho_{avg} = \frac{A_{tr}}{A_{sp}} = \frac{N_s N_l A_t}{b_w l_s} \quad (6-24)$$

where:

A_{sp} = area of the splitting plane within the splice region (in.²)

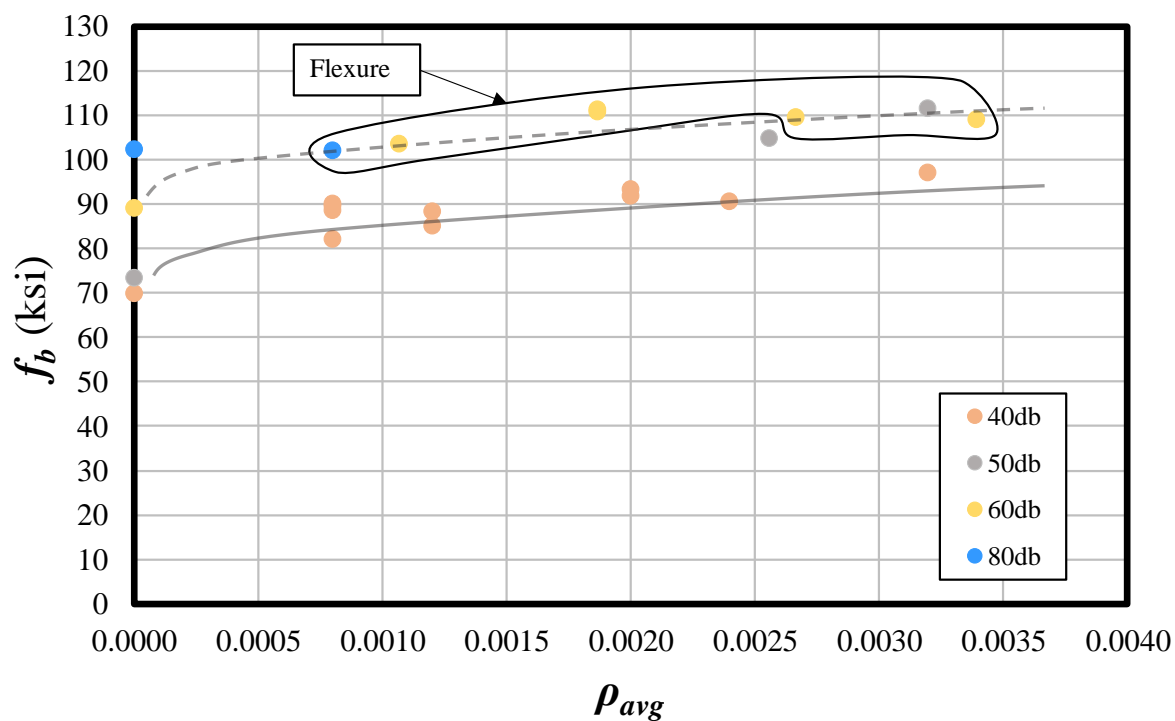
A_{tr} = *total cross-sectional area of all transverse reinforcement within spacing s that crosses the potential plane of splitting through the reinforcement being developed (in.²)*

l_s = *splice length (in.)*

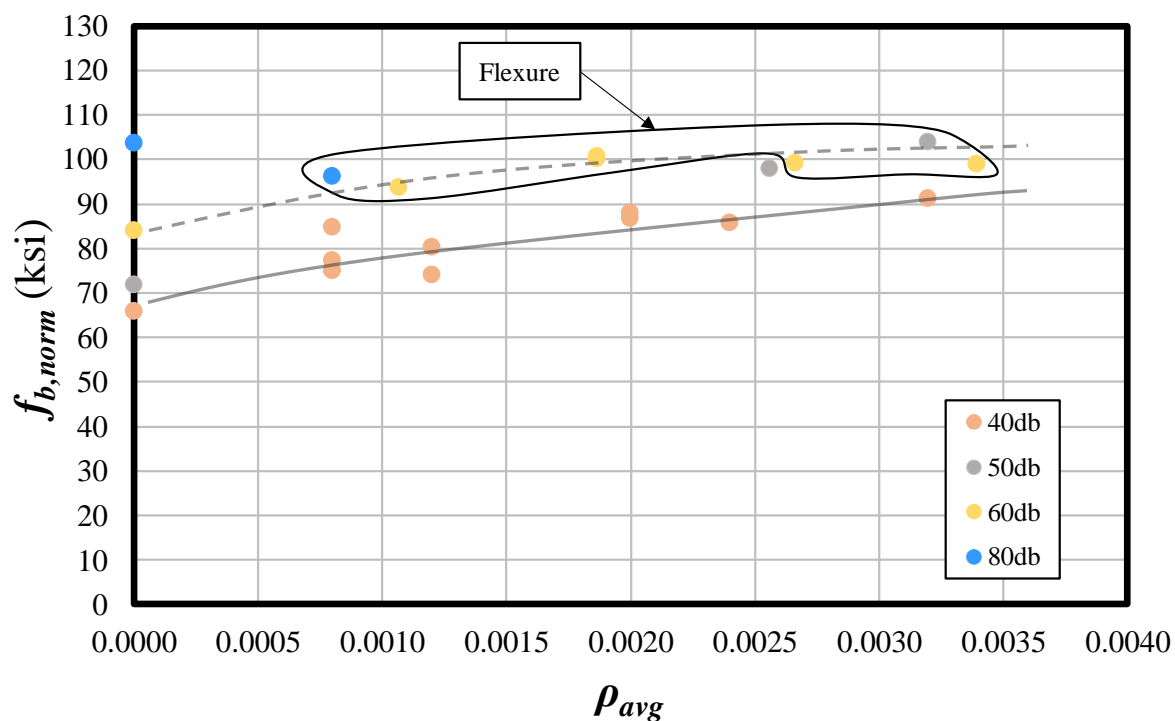
N_s = *number of stirrups along the length of splice*

Consequently, the average confinement pressure for the entire splice region can be calculated in a similar manner by replacing the distributed transverse reinforcement ratio with ρ_{avg} ; however, after analyzing the effect of ρ_t and f_{yt} on bond strength in this study, stirrup yield strength was found to contribute little to the contribution of transverse reinforcement. For a general analysis in this study, total confinement pressure was not explored as a parameter of interest.

Figure 6.23(a) provides a comparison between bar stress and average transverse reinforcement ratio, ρ_{avg} . Although some values are translated, the overall trends remain unchanged when compared to ρ_t . Figure 6.23(b) compares the average transverse reinforcement ratio to a failure bar stress normalized to a concrete compressive strength of 5000 psi. A clear positive correlation is observed for the 40 d_b specimens. A similar finding can be observed for the 60 d_b specimens.



(a) Actual Bar Stress



(b) Normalized Bar Stress

Figure 6.23: Effect of Total Transverse Reinforcement Ratio on Bar Stress, Grouped by Splice Length

6.2.4.4 Location of Transverse Reinforcement

Three specimens in Series VI contained various stirrup locations to determine a correlation between stirrup placement and its contribution to bar stress. Figure 6.24(a) provides one configuration with stirrups being placed at a 38 in. spacing and two configurations with stirrups spaced at 19 in. on-center and being arranged in different ways (Figure 6.24(b) and Figure 6.24(c)).

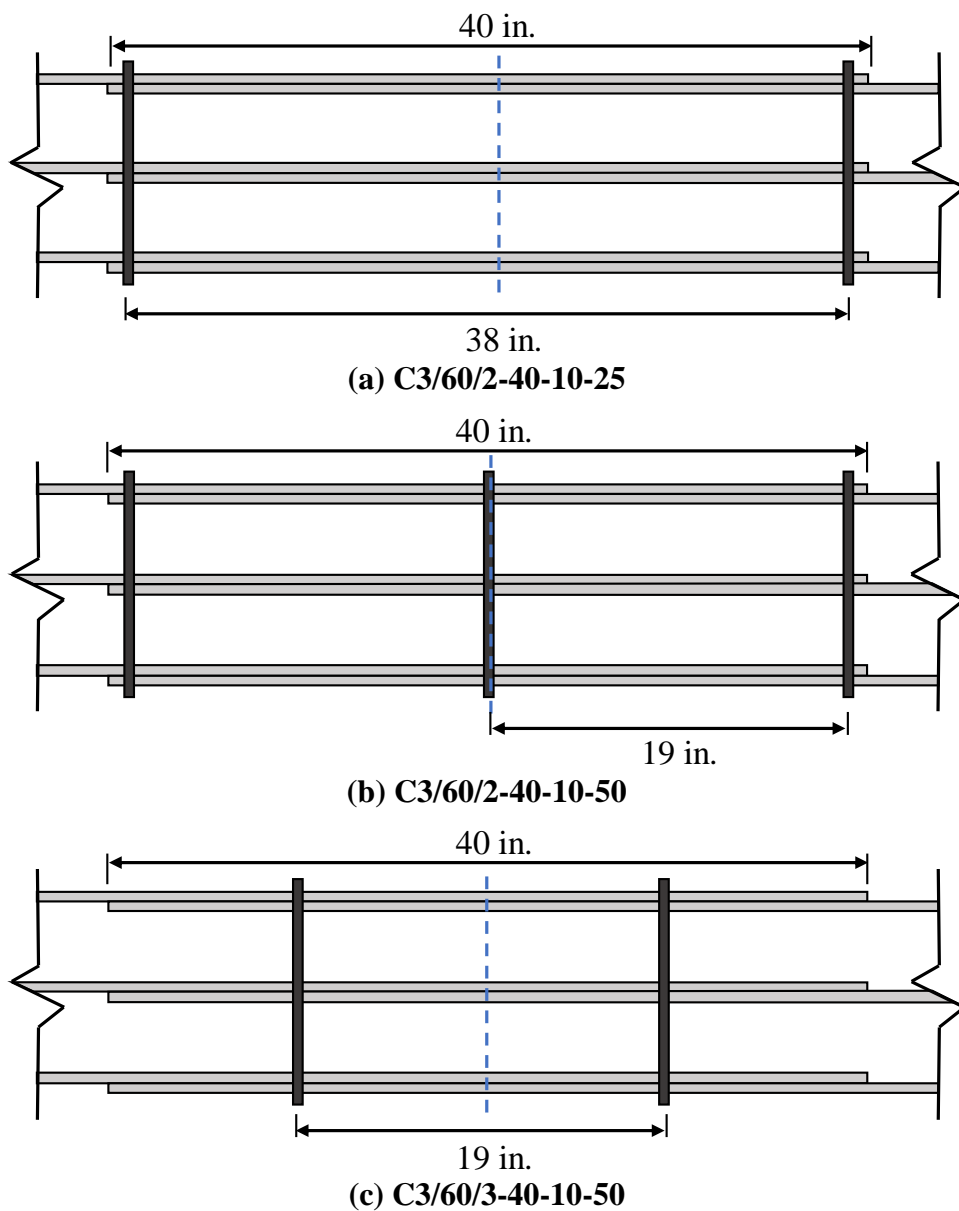


Figure 6.24: Series VI Stirrup Configurations

A comparison of failure bar stress is provided in Figure 6.25 with indicated ρ_t values. The findings from this comparison indicate that the middle stirrup is ineffective in providing additional bond strength. Additionally, when only two stirrups are placed at the ends of the splice, this configuration tends toward a higher increase in bond strength when compared to a layout where two stirrups are located closer to the middle of the splice. Similar results were found by studies conducted by Sim (2014).

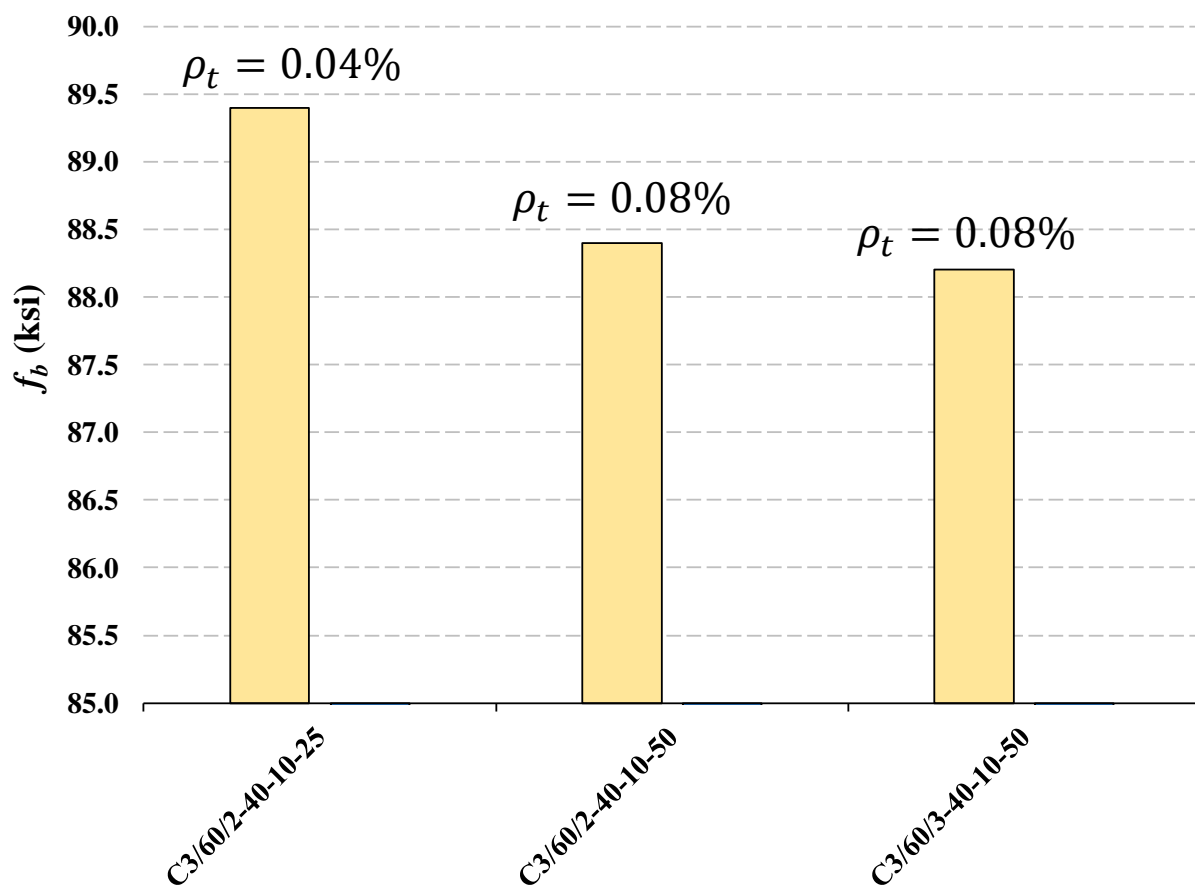


Figure 6.25: Effect of Stirrup Configuration on Bar Stress

CHAPTER 7. BOND STRENGTH MODELING

7.1 Introduction

To develop a general expression for the bond strength of concrete members spliced with high-strength reinforcing steel bars, two databases of previous unconfined and confined beam testing were compiled and analyzed to determine the best models.

7.2 Unconfined Database

For the unconfined database in this study, 132 beams were selected from the 192 unconfined, bottom cast, uncoated beams in the ACI 408 Database 10-2001. All beams that exceeded the yield strength of the spliced bars were neglected from the original database, as well as beams with concrete strengths less than 2500 psi and splice lengths less than 12 in. An additional 75 unconfined splice specimens were included from research testing on bond strength that took place after the ACI 408 Database was compiled, including the five unconfined beams from this study. Two (2) slabs from this study were included that did not experience a flexural failure; however, one slab experienced yielding of the bars. This resulted in a total of 209 unconfined specimens. Of these tests, 167 were reinforced with conventional black steel longitudinal bars while 42 contained ASTM A1035 MMFX steel reinforcing bars.

Appendix F (Table F.1) lists the specimens contained within the unconfined database. The table indicates the testing program, number of tests, splice length, bar size, ratio of splice length to bar diameter, ratio of side cover to bar diameter, and concrete compressive strength.

7.2.1 Frequency Distribution of Database Parameters

Several parameters of interest are included in the unconfined database. The frequency distribution for the 209 unconfined specimens is provided. Figure 7.1 shows the frequency distribution of concrete strength for the unconfined specimens. Approximately 62% of the unconfined specimens exhibit concrete compressive strengths between 3000 psi and 6000 psi. The largest quantity within a given distribution is 56 specimens (27%) with concrete compressive strengths between 5000 psi and 6000 psi.

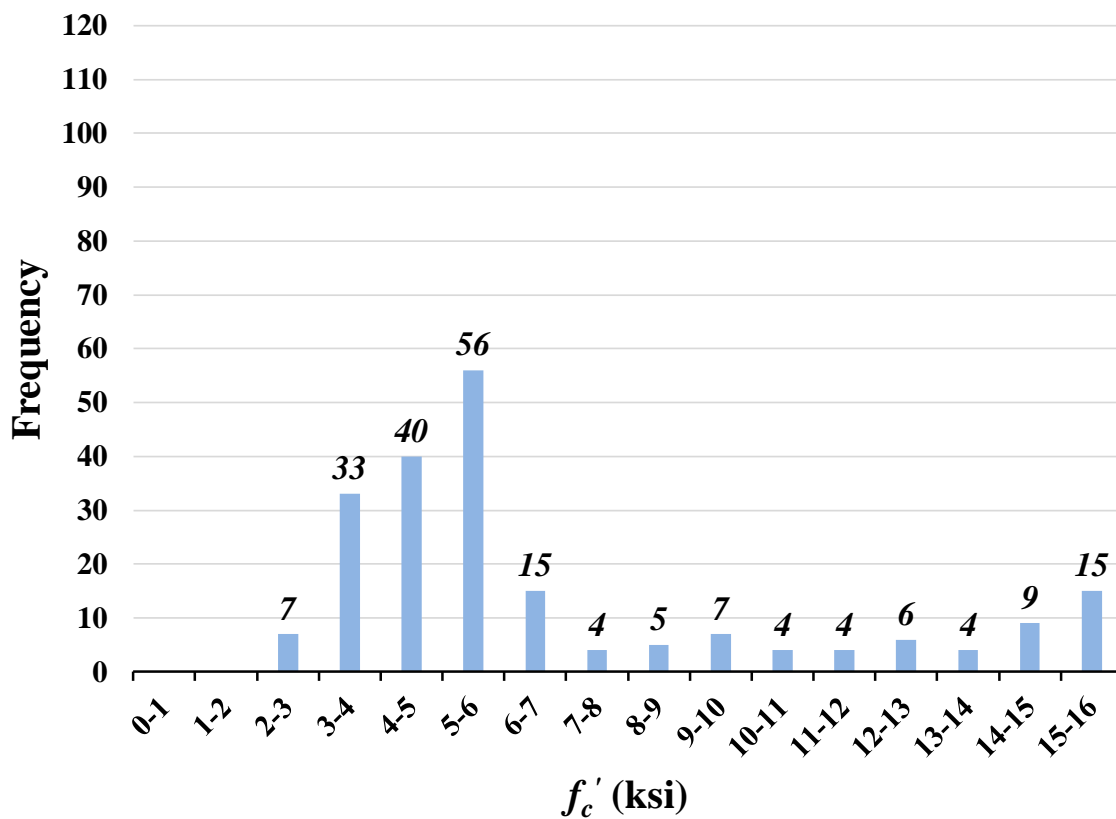


Figure 7.1: Distribution of Concrete Compressive Strength for Unconfined Database

Figure 7.2 shows the frequency distribution of bar sizes for the unconfined database. Approximately 88% of the unconfined specimens contain either No. 6, No. 8, or No. 11 spliced bars. The largest quantity within a given distribution is 106 specimens (51%) containing No. 8 longitudinal spliced bars.

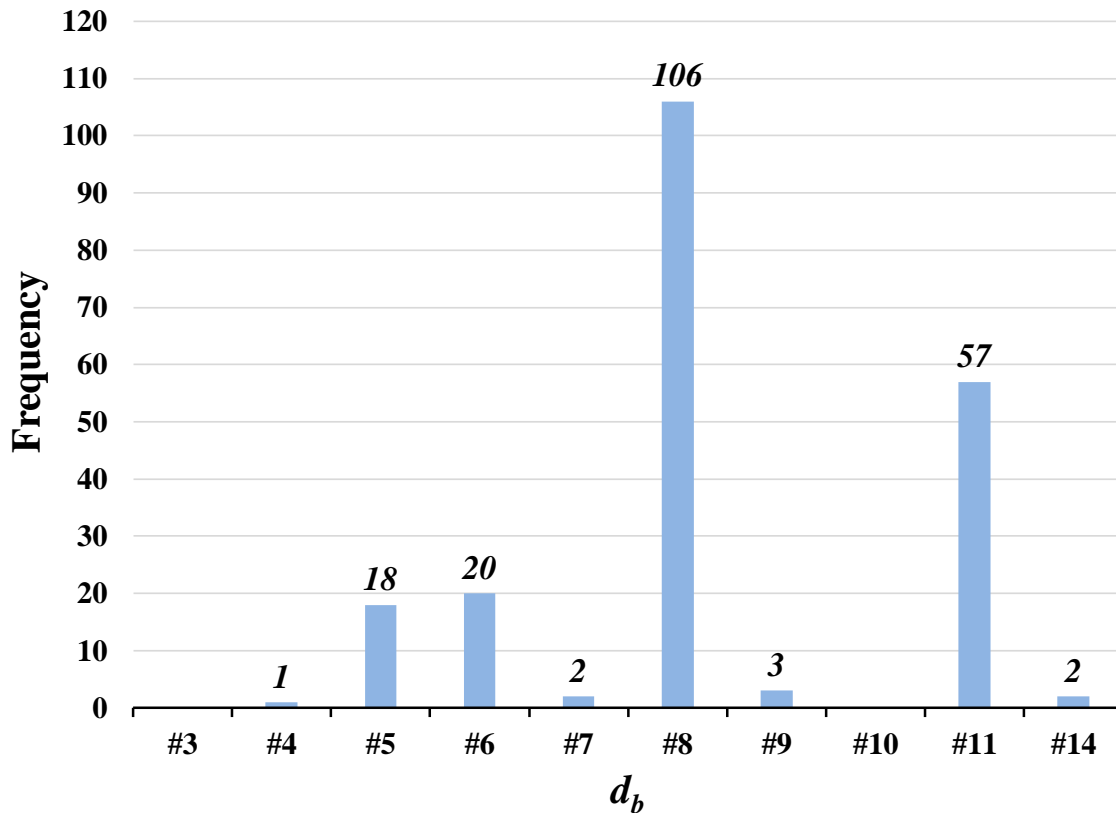


Figure 7.2: Distribution of Bar Size for Unconfined Database

Figure 7.3 shows the frequency distribution of splice lengths for the unconfined database. Approximately 74% of the unconfined specimens contain lapped splice lengths between 10 in. and 40 in. The largest quantity within a given distribution is 62 specimens (30%) containing splices between 10 in. and 20 in.

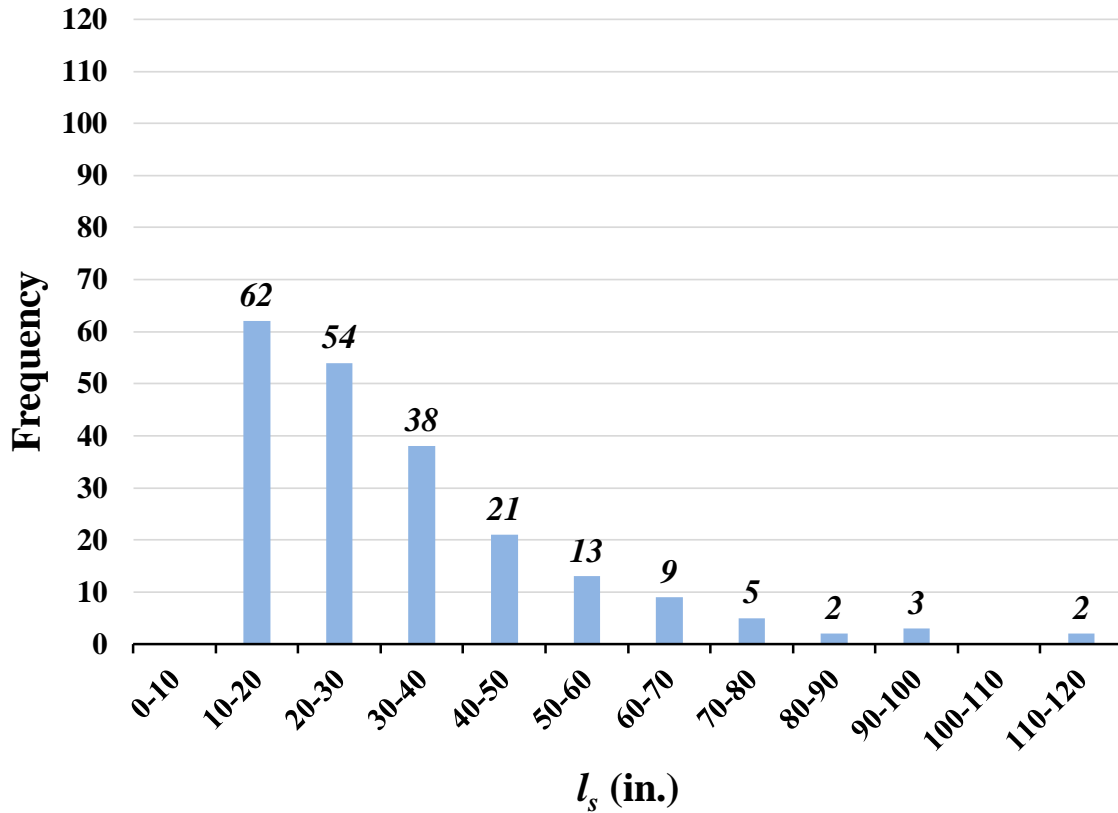


Figure 7.3: Distribution of Splice Length for Unconfined Database

Figure 7.4 shows the frequency distribution of splice length to bar diameter ratios for the unconfined database. Approximately 79% of the unconfined specimens contain ratios of splice length to bar diameter between 10 and 40. The largest quantity within a given distribution is 67 specimens (32%) containing ratios of splice length to bar diameter between 20 and 30.

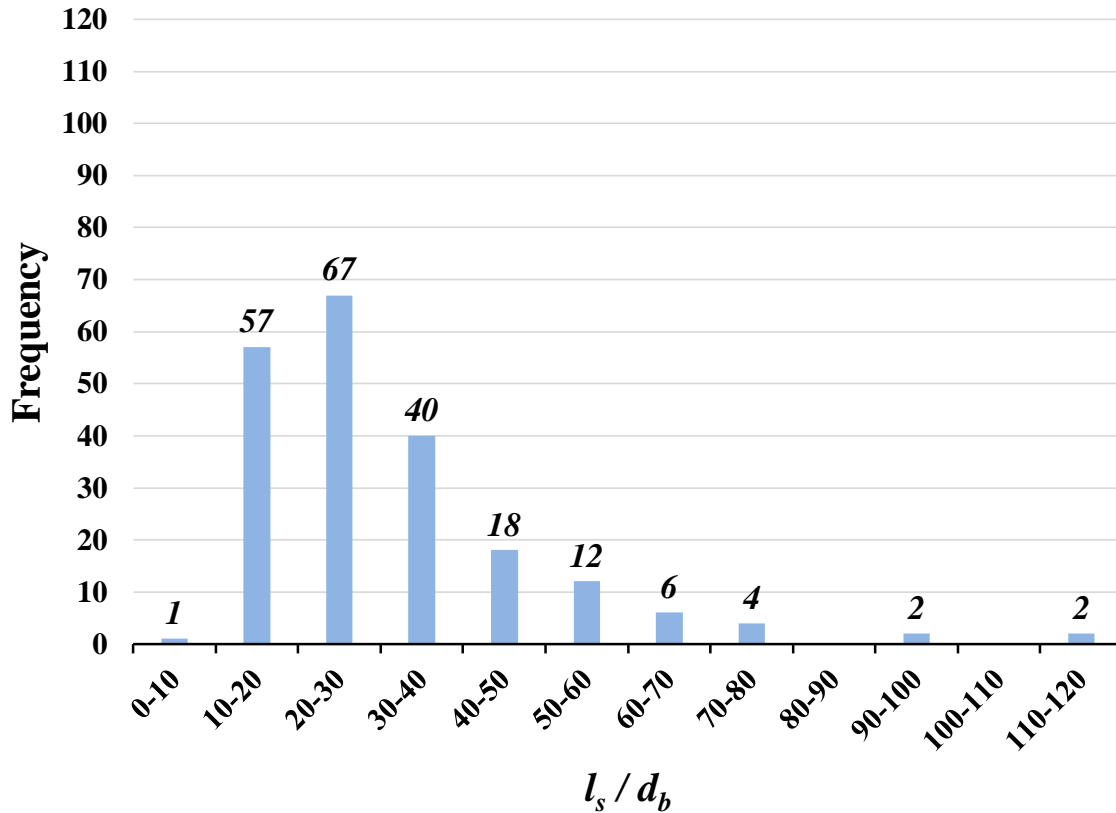


Figure 7.4: Distribution of Splice-Length-to-Bar-Diameter Ratio for Unconfined Database

Figure 7.5 shows the frequency distribution of side cover to bar diameter ratios for the unconfined database. Approximately 69% of the unconfined specimens contain ratios of side cover to bar diameter between 1.0 and 2.5. The largest quantity within a given distribution is 59 specimens (29%) containing ratios of side cover to bar diameter between 1.5 and 2.0. Note that two specimens did not have recorded side cover values and were neglected from this frequency distribution histogram.

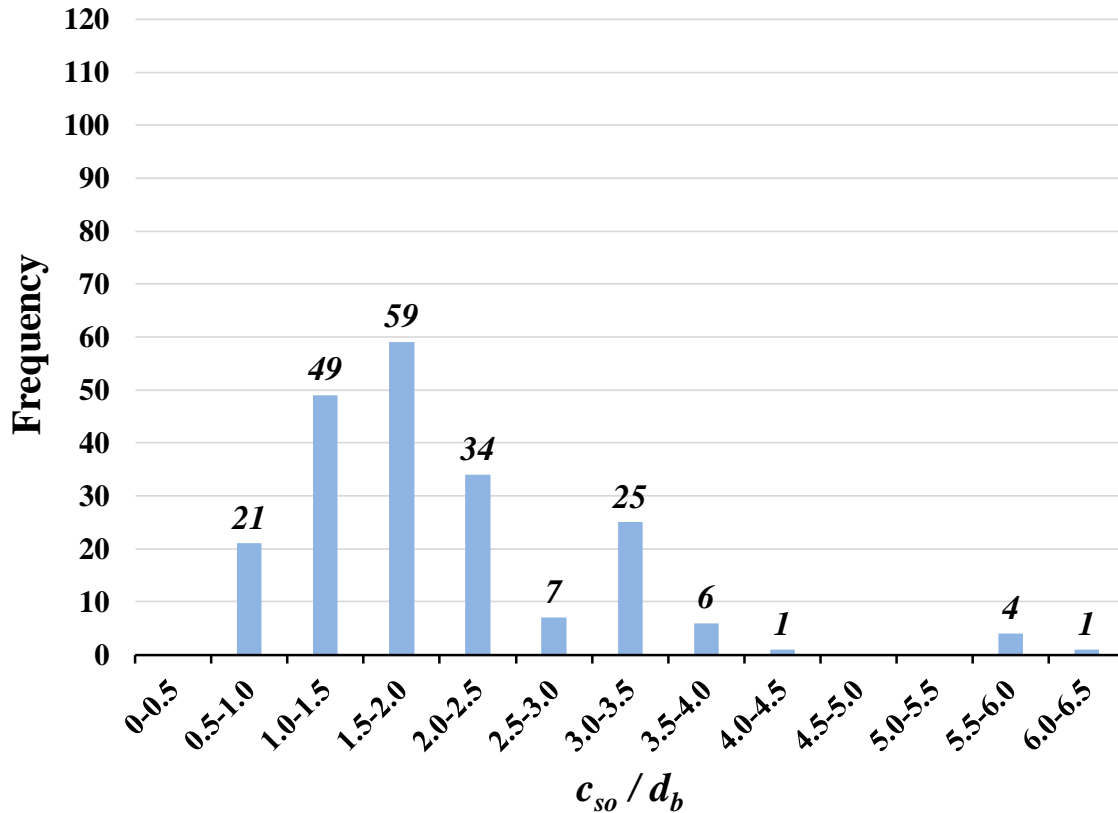


Figure 7.5: Distribution of Side-Cover-to-Bar-Diameter Ratio for Unconfined Database

7.3 Unconfined Model

An investigation was conducted to develop an equation for unconfined beams to represent the concrete contribution to total bar stress. This equation is based on trends observed over the full database of unconfined specimens and two slab specimens from this study. By comparing three previous equations for bar stress (Pay 2005, Sim 2014, Glucksman 2018), three general terms were identified to be consistent in all equations: concrete compressive strength, splice length, and a cover modifier.

7.3.1 Equation Components

Concrete compressive strength, splice length, and cover were all found to have a significant influence on the overall bar stress achieved at failure:

1. The influence of concrete compressive strength on bar stress has been best represented with the quarter root by analyses in several research programs (Darwin et al. 1996, Zuo and Darwin 2000, Canbay and Frosch 2005, Pay 2005, Sim 2014, Glucksman 2018).
2. Canbay and Frosch, Pay, Sim, and Glucksman observed that the ratio of splice length to bar diameter has a nonlinear correlation to bar stress.
3. Cover has been considered differently in various research studies. Because there are three different concrete dimensions surrounding spliced bars that can be analyzed in the database, different conclusions have been provided. Findings by Orangun, Jirsa, and Breen (1977) suggest that the ratio of a cover term to the bar diameter has a stronger correlation to the bar stress than a cover term alone. Observations on the linearity of this term have also been approached differently in research programs with some recommending a linear correlation (Pay 2005) and others recommending a nonlinear representation (Sim 2014, Glucksman 2018).

An investigation was performed to evaluate an appropriate cover modification term for a general unconfined bar stress equation.

7.3.2 Cover Investigation

The unconfined database was evaluated specifically for the effect of cover and bar spacing on bar stress. Powers for the compressive strength and splice length were selected to be 0.25 and 0.50, respectively, based on previous research. The cover modification and its power were changed to explore the influence on bar stress. A total of eight possible cover modification terms were evaluated and raised to a power to account for a potential nonlinear relationship. Table 7.1

provides the eight cover terms used in this study. Equation 7-1 was calculated for each specimen in the unconfined database with Series V slabs to determine f_{trial} values for all eight cover modifiers.

Table 7.1: Cover Modification Terms

(1) $c_{mod,1}$	$\frac{c_{so}}{d_b}$	(5) $c_{mod,5}$	$\frac{\min(c_{si}, c_b)}{d_b}$
(2) $c_{mod,2}$	$\frac{c_{si}}{d_b}$	(6) $c_{mod,6}$	$\frac{\min(c_{so}, c_b)}{d_b}$
(3) $c_{mod,3}$	$\frac{2c_{si}}{d_b}$	(7) $c_{mod,7}$	$\frac{\min(c_{so}, c_{si})}{d_b}$
(4) $c_{mod,4}$	$\frac{c_{si}}{2d_b}$	(8) $c_{mod,8}$	$\frac{\min(c_{so}, c_{si}, c_b)}{d_b}$

$$f_{trial} = (C_1)^{1.0} (f'_c)^{0.25} \left(\frac{l_s}{d_b} \right)^{0.5} (c_{mod})^z \quad (7-1)$$

where:

c_b = bottom clear cover of spliced bars (in.)

c_{mod} = cover modification term

c_{si} = half the clear spacing between spliced bars (in.)

c_{so} = side clear cover of spliced bars (in.)

C_1 = constant selected to be 1

d_b = longitudinal bar diameter (in.)

f'_c = concrete compressive strength (psi)

f_{trial} = trial bar stress for cover modification investigation (ksi)

l_s = splice or development length (in.)

z = power constant

To isolate the term of best fit for the data, f_{trial} was calculated for all eight equations and used to calculate f_{test}/f_{trial} for each specimen in the unconfined database. The coefficient of variation (COV) was then calculated for each modifier for z powers ranging from zero to one. Figure 7.6 shows the change in COV for all eight equations. Specimens that did not have recorded values for terms in the modifier were excluded in the COV calculation for that equation.

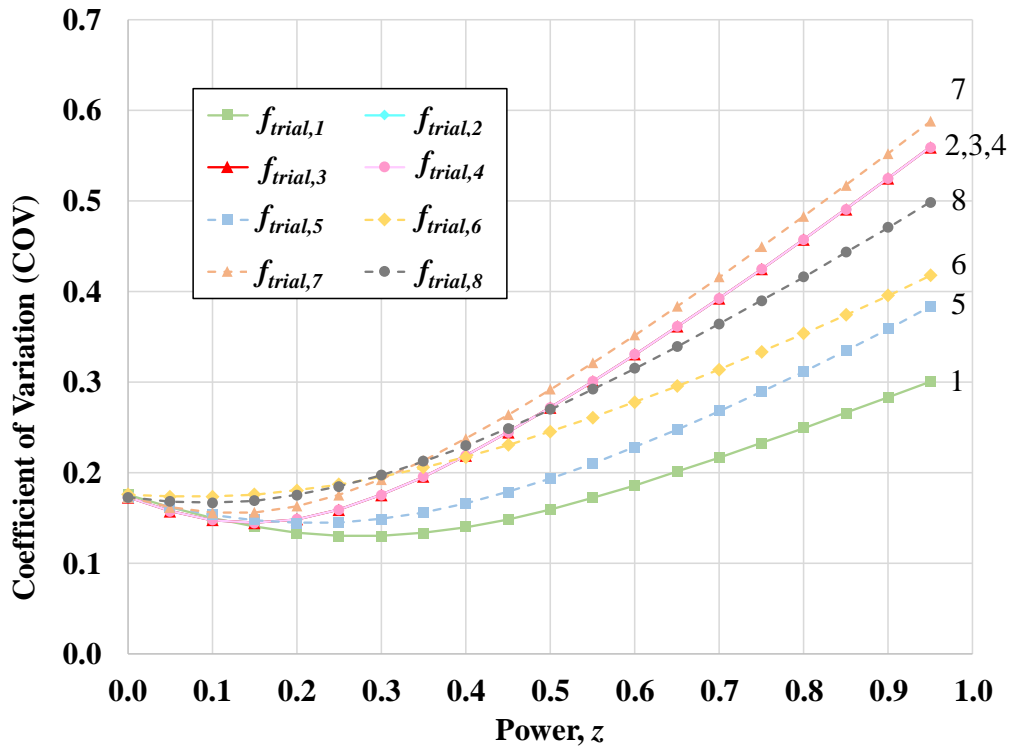


Figure 7.6: Comparison of Cover Modification Terms c_{mod}

Equations 2, 3, and 4 all result in the same COV for changing powers because the cover modifiers for these equations only differ by a constant. Equation 1 appears to fit the unconfined specimen data with the least amount of variation for all powers between zero and one. Because the COV for this equation reaches a minimum of 0.130 at a power of approximately 0.3 instead of 1, the influence of this term is assumed to be nonlinear.

When the power $z = 0.30$ and is placed on the cover term in Equation 7-1, a statistical analysis can be performed on all eight equations to further validate that side cover has the strongest influence on bond strength. Each of the eight cover modifier terms is substituted into Equation 7-1 for the comparison provided in Table 7.2.

Table 7.2: Statistical Analysis of f_{test}/f_{trial} in Cover Modifier Equations

	Eq. 1	Eq. 2	Eq. 3	Eq. 4	Eq. 5	Eq. 6	Eq. 7	Eq. 8
Max.	1.61	1.79	1.45	2.20	1.79	2.02	1.92	1.92
Min.	0.77	0.65	0.52	0.79	0.80	2.02	0.72	0.72
Mean (\bar{x})	1.09	1.15	0.93	1.41	1.24	1.18	1.18	1.25
Standard Deviation (σ)	0.14	0.20	0.16	0.25	0.18	0.23	0.23	0.25
COV	0.13	0.18	0.18	0.18	0.15	0.20	0.19	0.20
r^2	0.85	0.62	0.62	0.62	0.61	0.65	0.60	0.54

The use of the ratio between side cover and bar diameter results in the lowest coefficient of variation and the highest correlation coefficient (r^2) among the eight cover modification terms. This study finds that the ratio of side cover to bar diameter has more influence on bond strength than inner bar spacing and bottom cover; therefore c_{so}/d_b will be considered for the cover modifier in the general bar stress equation.

7.3.3 Nonlinear Regression Analysis

Based on the recommended cover modification term, the unconfined bar stress can be expressed as follows:

$$f_{bc} = (C_1)(f'_c)^x \left(\frac{l_s}{d_b} \right)^y \left(\frac{c_{so}}{d_b} \right)^z \quad (7-2)$$

where:

c_{so} = side clear cover of spliced bars (in.)

C_1 = constant

d_b = longitudinal bar diameter (in.)

f_{bc} = contribution to bond stress provided by concrete (ksi)

f'_c = concrete compressive strength (psi)

l_s = splice or development length (in.)

x, y, z = constants to be determined by nonlinear regression analysis

Although previous power values have been estimated based on past bond strength research, a nonlinear regression analysis was performed to independently evaluate the powers for each variable. By applying the natural logarithmic function to the entire equation, Equation 7-2 can be written in a more suitable way for regression analysis:

$$\ln(f_{bc}) = \ln(C_1) + x \ln(f'_c) + y \ln\left(\frac{l_s}{d_b}\right) + z \ln\left(\frac{c_{so}}{d_b}\right) \quad (7-3)$$

Nonlinear regression analysis was performed on the 207 specimens from the unconfined database in addition to two slab specimens from Phase II of this testing program. A correlation coefficient of 0.92 was generated by this analysis with a 95% confidence interval. Coefficients were rounded for convenience. All constants were determined as follows:

$$C_1 = 0.90 \quad x = 0.28 \quad y = 0.48 \quad z = 0.29$$

By substituting these values for the constants in Equation 7-3, Equation 7-4 takes the following form:

$$f_{bc} = 0.9(f'_c)^{0.28} \left(\frac{l_s}{d_b}\right)^{0.48} \left(\frac{c_{so}}{d_b}\right)^{0.29} \quad (7-4)$$

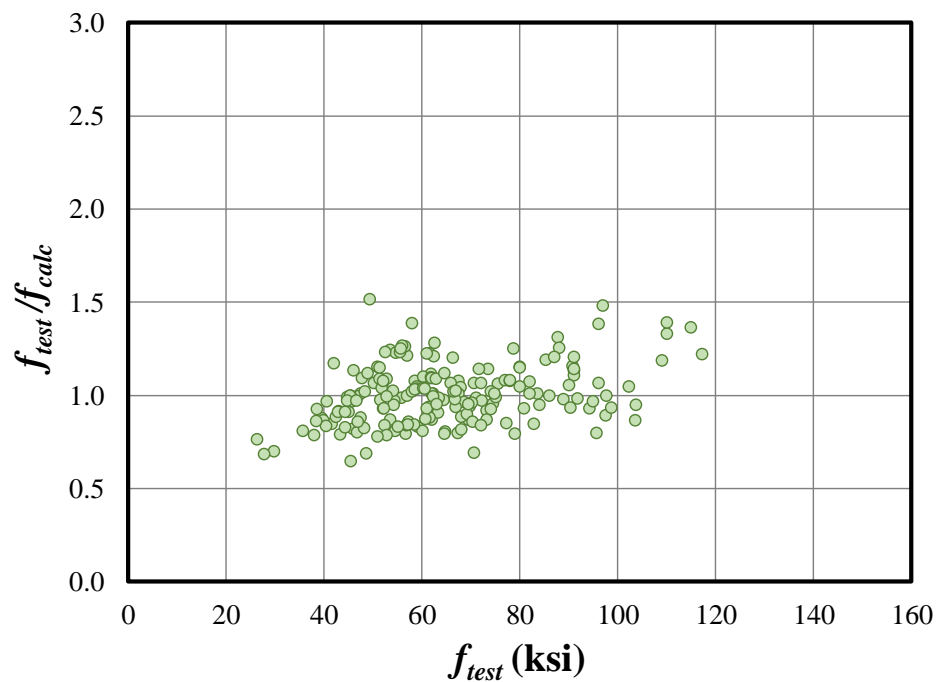
To simplify this equation for easier use, all power constants were adjusted to multiples of the quarter root. Additionally, the coefficient was adjusted to one to maintain an average f_{test}/f_{calc} value for the analyzed unconfined database beams. The expression for concrete contribution to bar stress is given by Equation 7-5:

$$f_{bc} = 1.0(f'_c)^{0.25} \left(\frac{l_s}{d_b} \right)^{0.5} \left(\frac{c_{so}}{d_b} \right)^{0.25} \quad (7-5)$$

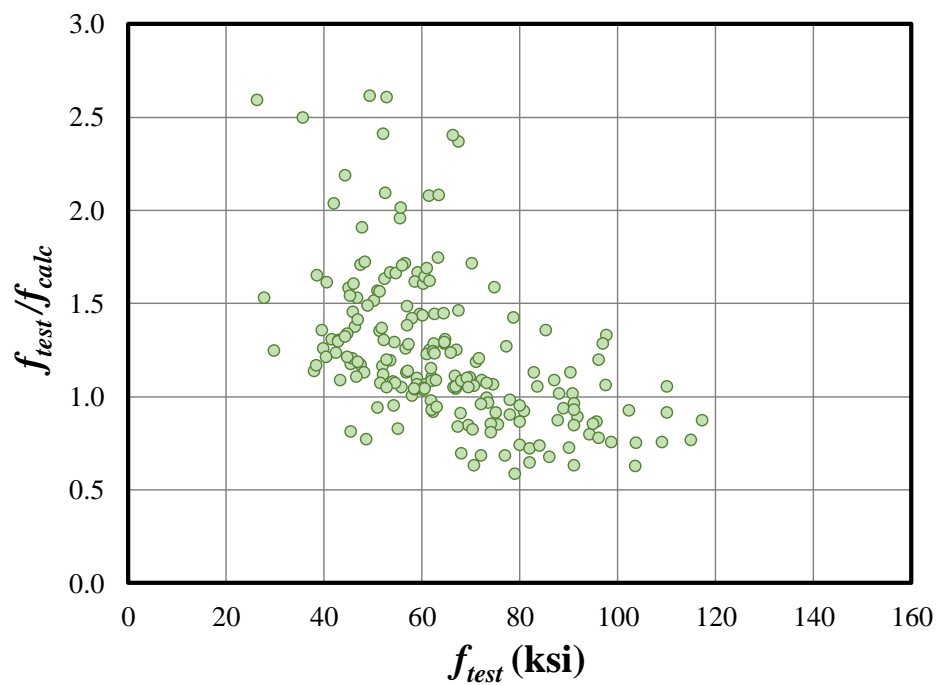
Equation 7-5 was applied to all 209 beams in the unconfined database and compared with the results using the ACI 318-14 design expression (Equation 6-3). Table 7.3 provides a statistical comparison of the results. Graphic comparisons between ACI 318-14 and the proposed unconfined equation are provided in Figure 7.7 through Figure 7.14 for different variables of interest.

Table 7.3: Statistical Analysis Comparison of f_{test}/f_{calc} for Unconfined Beams

	ACI 318-14	Proposed Equation (7-5)
Max.	2.61	1.52
Min.	0.59	0.65
Mean (\bar{x})	1.23	1.00
Standard Deviation (σ)	0.405	0.155
COV	0.328	0.155

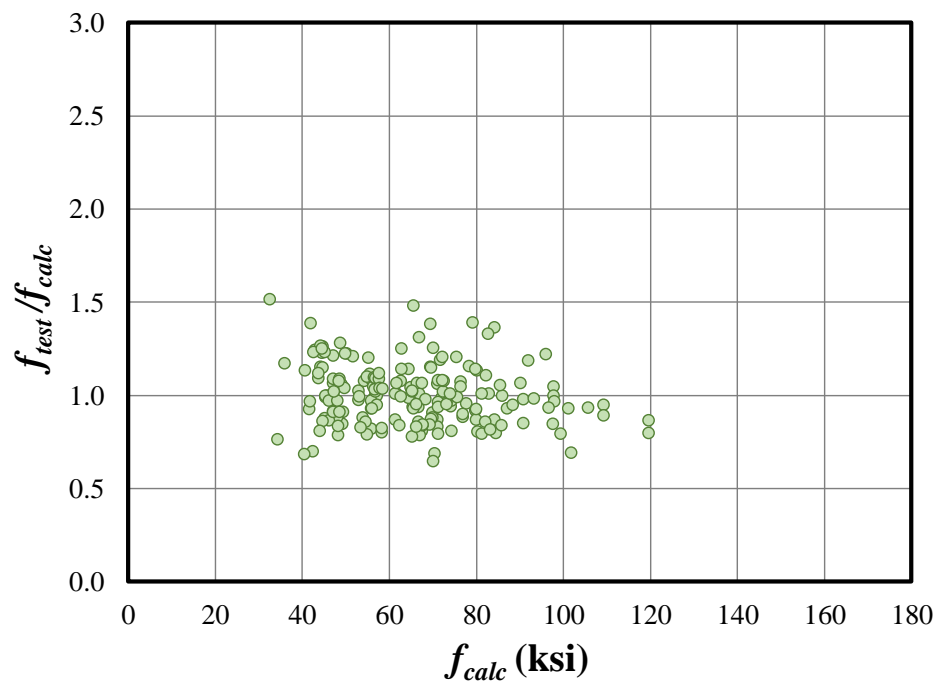


(a) Equation 7-5

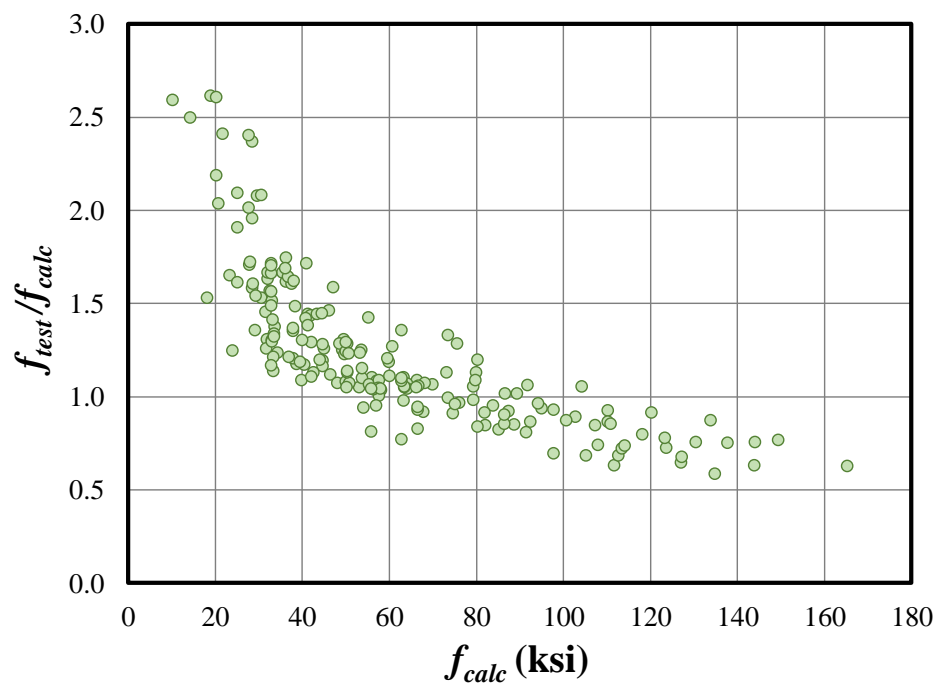


(b) ACI 318-14

Figure 7.7: Equation Comparison for Bar Stress at Failure (Unconfined)

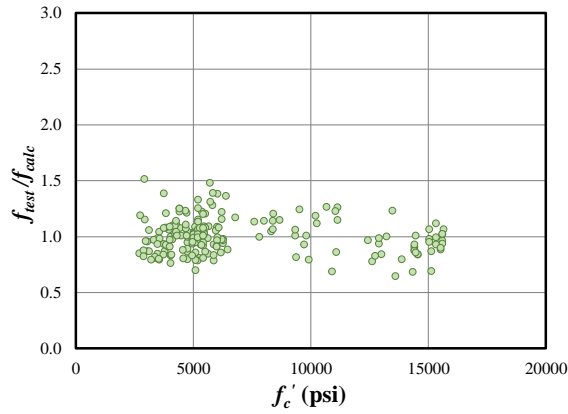


(a) Equation 7-5

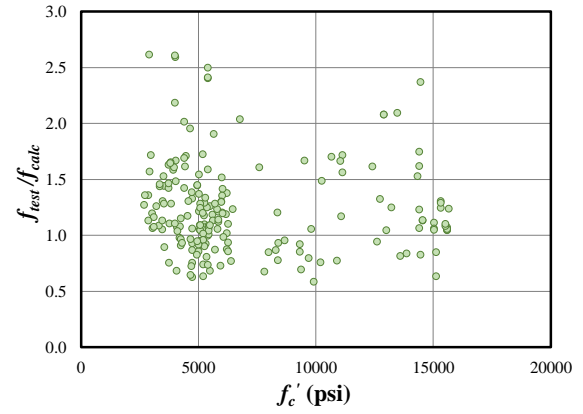


(b) ACI 318-14

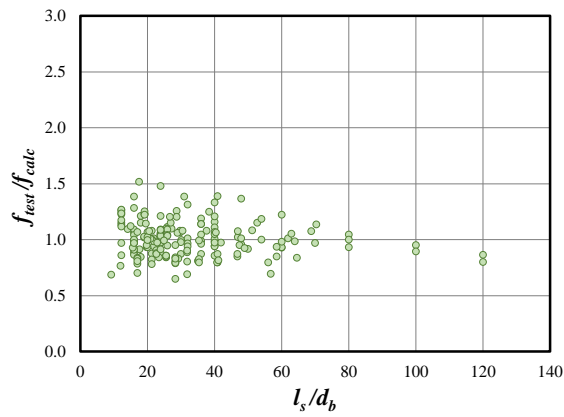
Figure 7.8: Equation Comparison for Calculated Bar Stress (Unconfined)



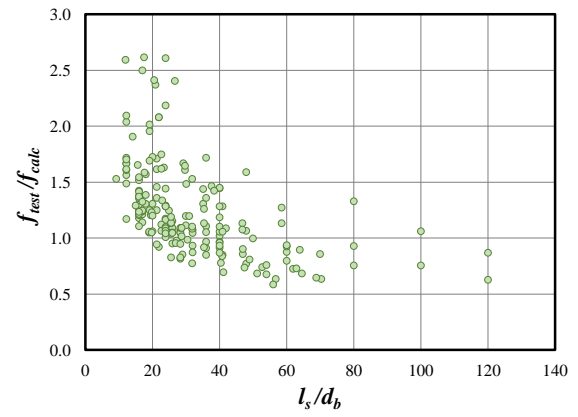
(a) Equation 7-5



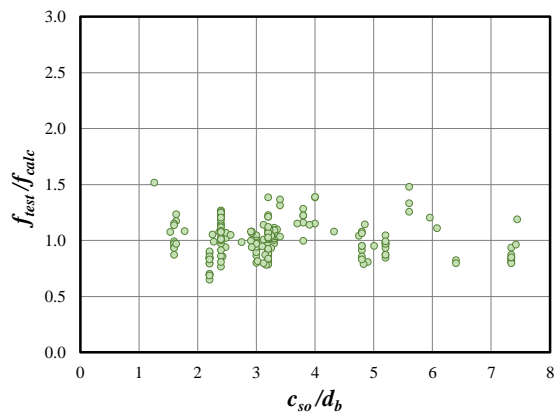
(b) ACI 318-14

Figure 7.9: Equation Comparison for Concrete Strength (Unconfined)

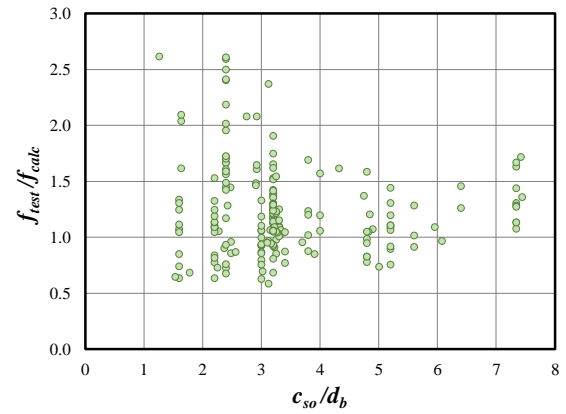
(a) Equation 7-5



(b) ACI 318-14

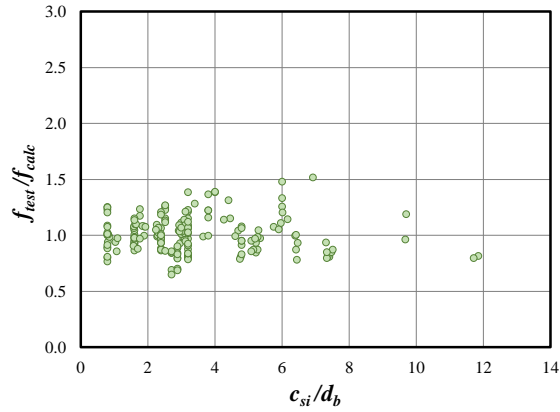
Figure 7.10: Equation Comparison for Splice Length over Bar Diameter (Unconfined)

(a) Equation 7-5

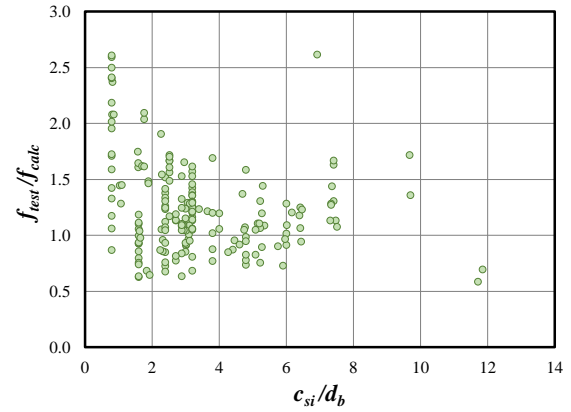


(b) ACI 318-14

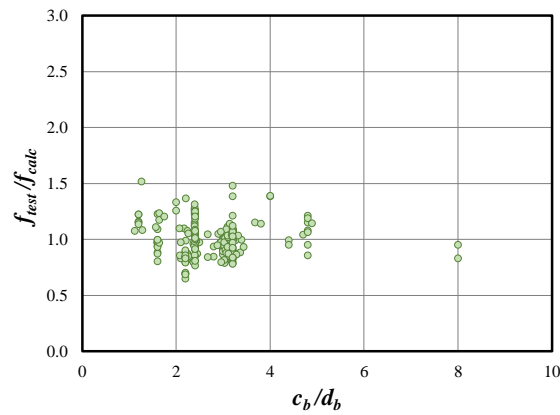
Figure 7.11: Equation Comparison for Side Cover over Bar Diameter (Unconfined)



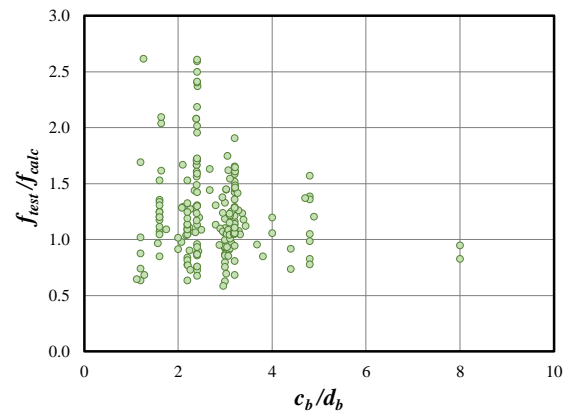
(a) Equation 7-5



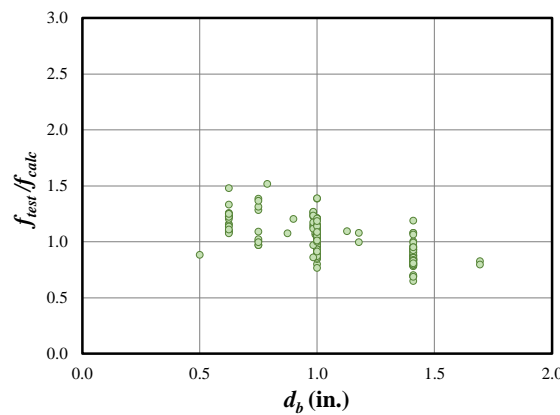
(b) ACI 318-14

Figure 7.12: Equation Comparison for Half Bar Spacing over Bar Diameter (Unconfined)

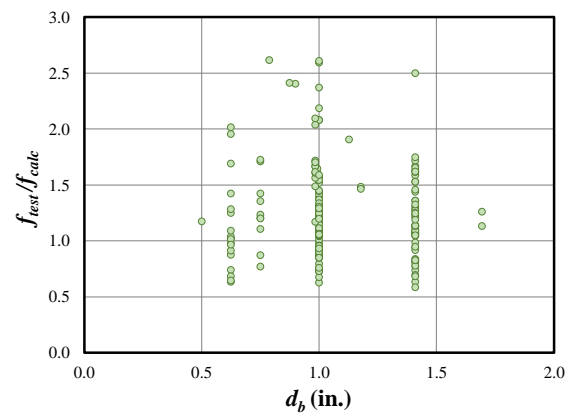
(a) Equation 7-5



(b) ACI 318-14

Figure 7.13: Equation Comparison for Bottom Cover over Bar Diameter (Unconfined)

(a) Equation 7-5



(b) ACI 318-14

Figure 7.14: Equation Comparison for Bar Diameter (Unconfined)

For all results from Figure 7.7 through Figure 7.14, scatter is reduced when Equation 7-5 is used compared to use of the design expression in ACI 318-14.

7.4 Confined Database

The database for confined specimens used in this study contains the 286 confined, bottom cast, uncoated beams from the original ACI 408 Database 10-2001. An additional 70 confined beams were included from research testing on bond strength that took place after the ACI 408 Database was compiled, including the six confined beams that failed in splitting from this study. From this total, exclusion criteria were selected and implemented, removing all beams with a splice length less than 12 in. and concrete strengths less than 2500 psi. Furthermore, specimens with only one stirrup within the splice region and specimens consisting of only one splice were excluded. Therefore, the total number of specimens selected in the database was 322 confined beams. Of these tests, 85 specimens reached yielding of the longitudinal bars before failure, 281 specimens were reinforced with conventional black steel longitudinal bars, and 41 contained ASTM A1035 MFX reinforcing bars.

Appendix F (Table F.2) lists the specimens contained within the confined database and indicates the testing program, number of tests, splice length, bar size, ratio of splice length to bar diameter, ratio of side cover to bar diameter, and concrete compressive strength. Additionally, beam pairs were selected from various tests that contained a confined beam with an identical unconfined specimen. A total of 101 beam pairs were used in this study.

7.4.1 Frequency Distribution of Database Parameters

Several parameters of interest are included in the confined database. The frequency distribution for all 322 confined specimens was evaluated. Figure 7.15 shows the frequency distribution of concrete compressive strengths for the confined database. Approximately 58% of the confined specimens exhibit concrete compressive strengths between 3000 psi and 6000 psi. The largest quantity within a given distribution is 85 specimens (26%) with concrete compressive strengths between 4000 psi and 5000 psi.

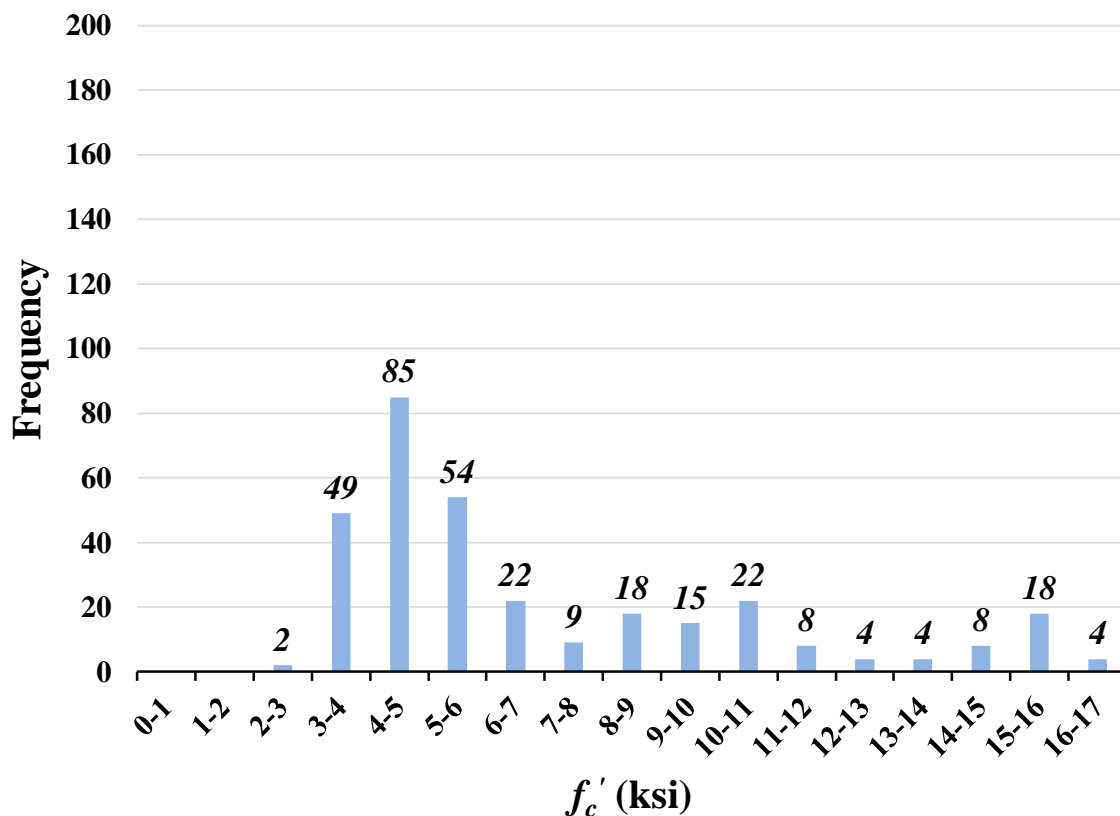


Figure 7.15: Distribution of Concrete Compressive Strength for Confined Database

Figure 7.16 shows the frequency distribution of spliced bar sizes for the confined database. Approximately 94% of the confined specimens contain either No. 6, No. 8, or No. 11 bars. The largest quantity within a given distribution is 193 specimens (60%) containing No. 8 longitudinal bars.

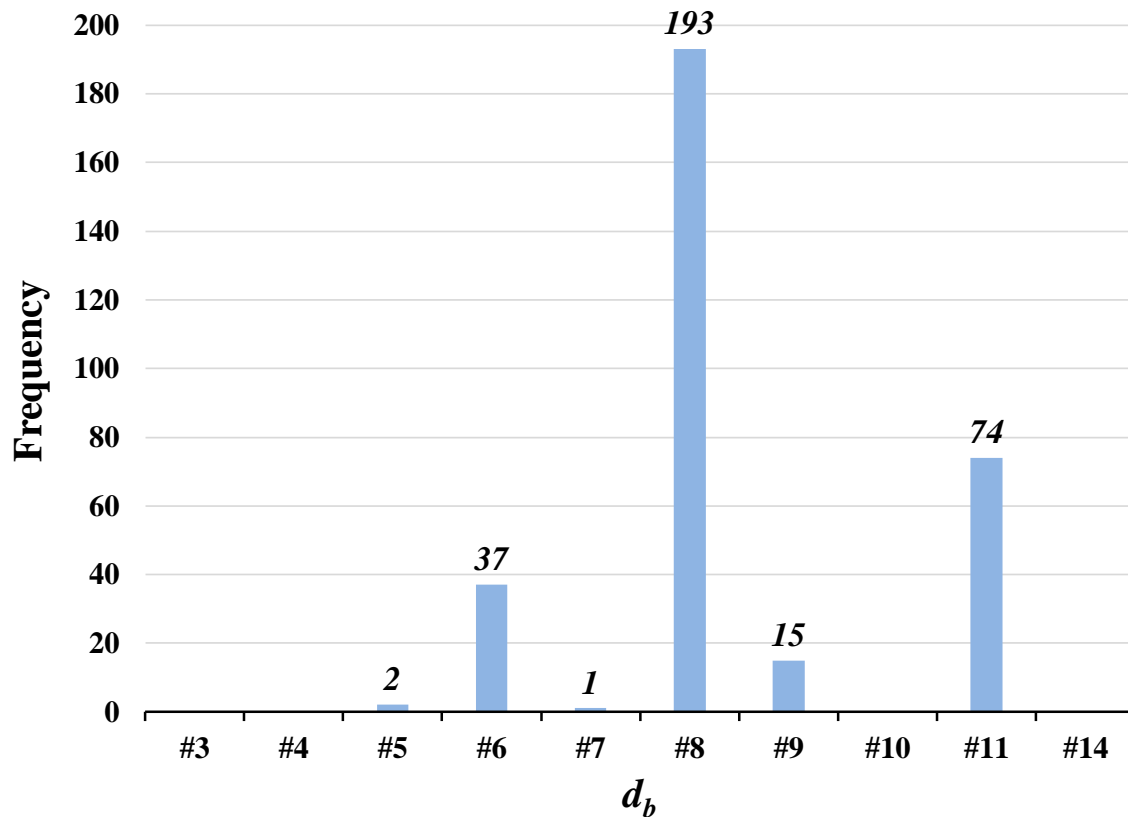


Figure 7.16: Distribution of Bar Size for Confined Database

Figure 7.17 shows the frequency distribution of longitudinal lapped splice lengths in the confined database. Approximately 89% of the confined specimens contain lapped splice lengths between 10 in. and 40 in. The largest quantity within a given distribution is 136 specimens (42%) containing splices between 20 in. and 30 in.

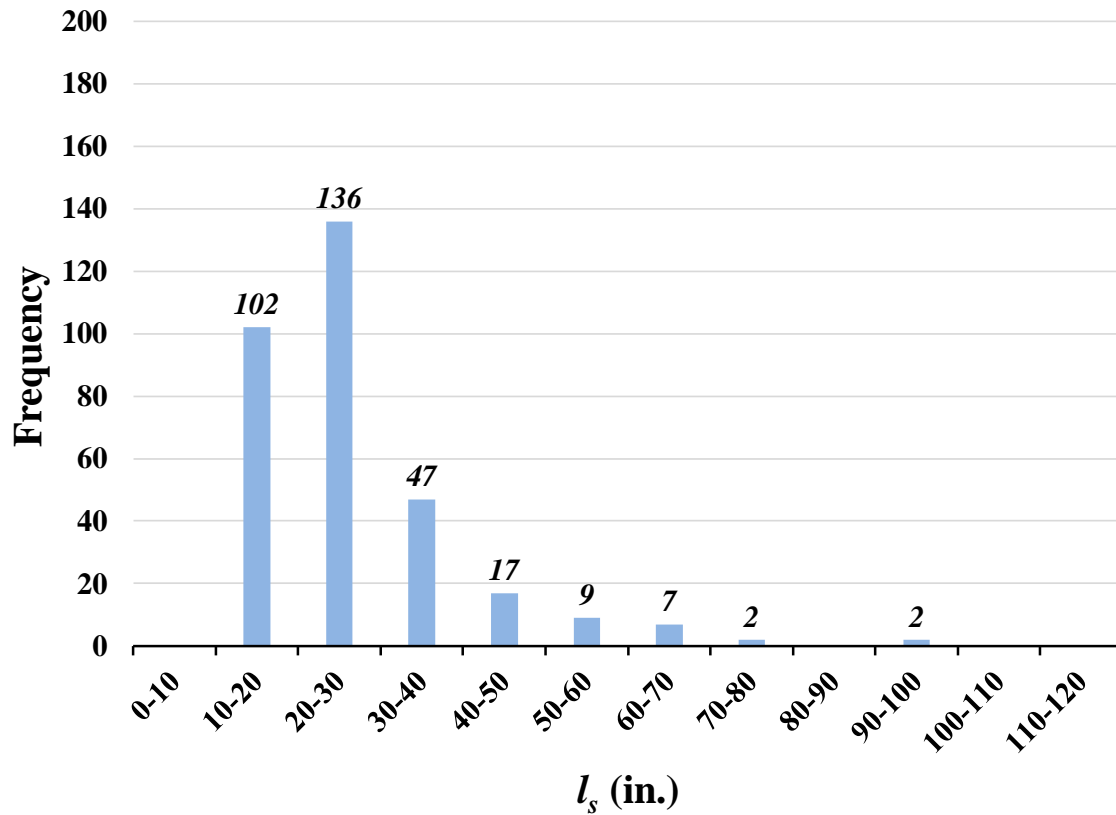


Figure 7.17: Distribution of Splice Length for Confined Database

Figure 7.18 shows the frequency distribution of splice-length-to-bar-diameter ratios in the confined database. Approximately 91% of the confined specimens contain ratios of splice length to bar diameter between 10 and 40. The largest quantity within a distribution is 130 specimens (40%) containing ratios of splice length to bar diameter between 10 and 20.

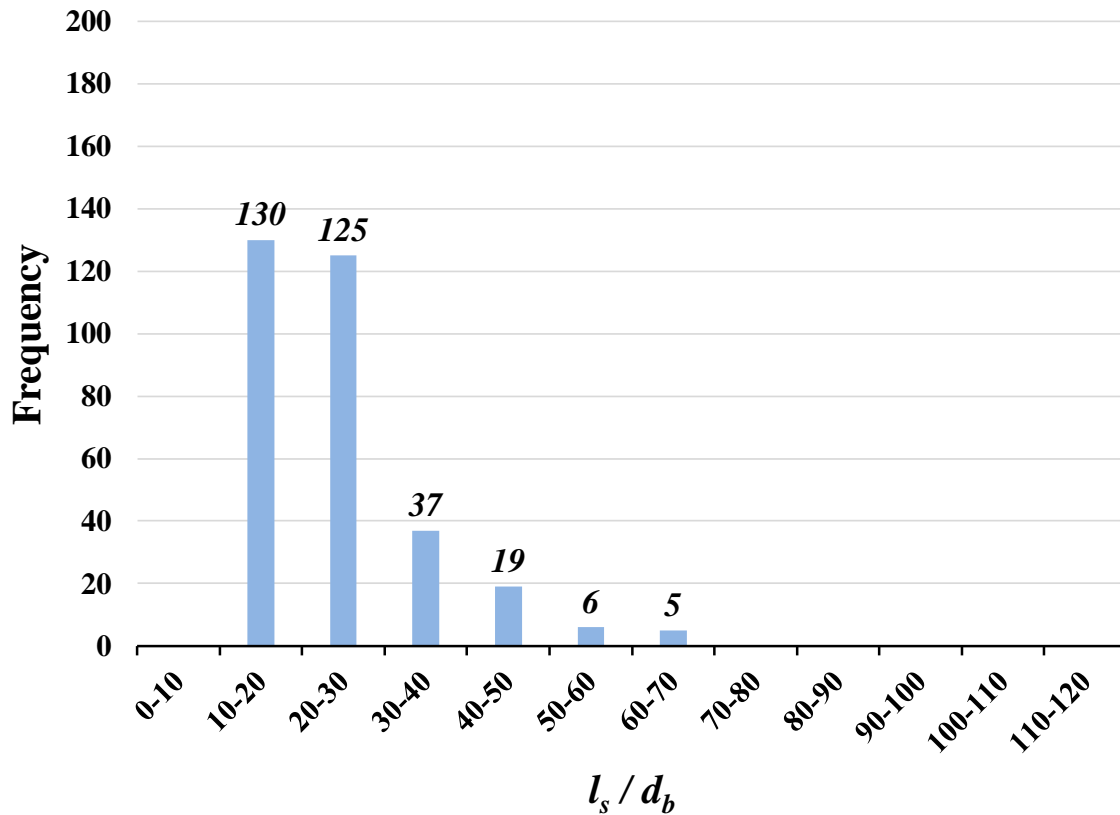


Figure 7.18: Distribution of Splice-Length-to-Bar-Diameter Ratio for Confined Database

Figure 7.19 shows the frequency distribution of side-cover-to-bar-diameter ratios in the confined database. Approximately 87% of the confined specimens contain ratios of side cover to bar diameter between 1.0 and 2.5. The largest quantity within a given distribution is 102 specimens (32%) containing ratios of side cover to bar diameter between 1.5 and 2.0.

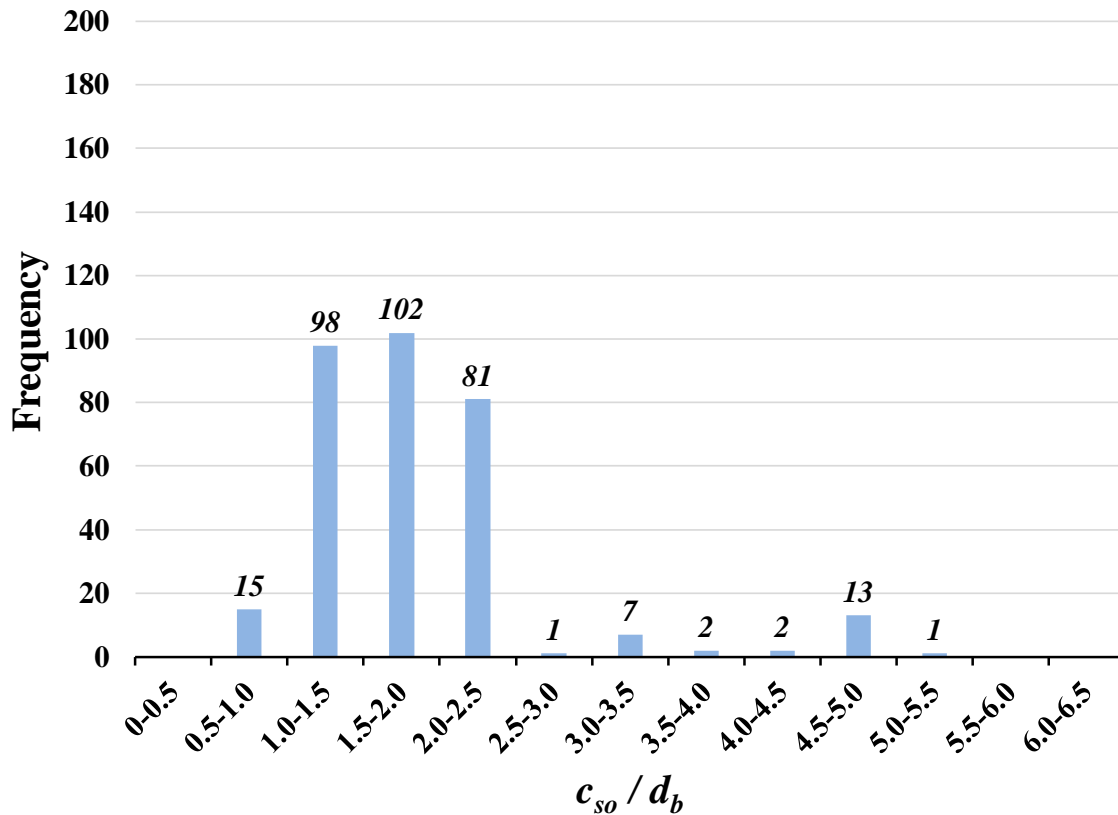


Figure 7.19: Distribution of Side-Cover-to-Bar-Diameter Ratio for Confined Database

Figure 7.20 shows the frequency distribution of total transverse reinforcement areas across the splitting plane for the confined database. Approximately 77% of the confined specimens contain total areas of transverse reinforcement between 0.35 in.² and 2.0 in.². The largest quantity within a given distribution is 104 specimens (32%) containing total areas of transverse reinforcement between 0.5 in.² and 1.0 in.².

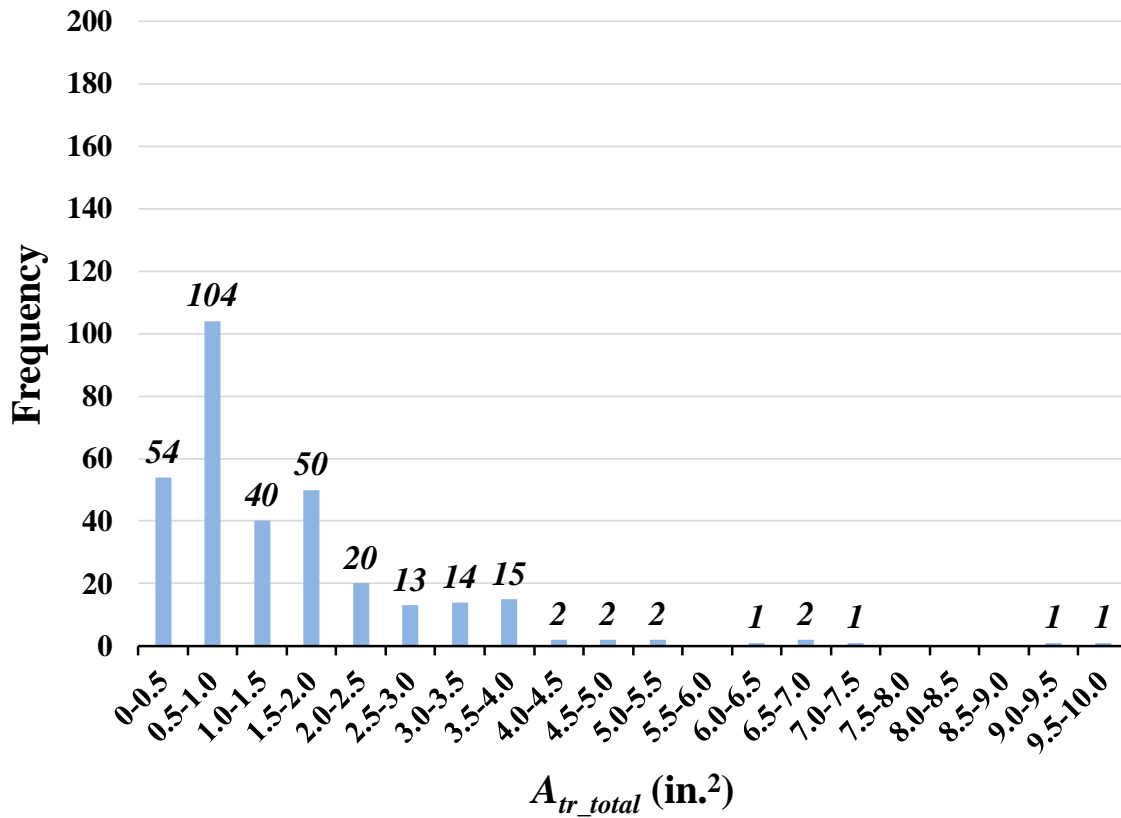


Figure 7.20: Distribution of Total Transverse Reinforcement Area for Confined Database

Figure 7.21 shows the frequency distribution of distributed transverse reinforcement ratios for the confined database. Approximately 66% of the confined specimens contain distributed transverse reinforcement ratios between 0.1% and 0.5%. The largest quantity within a given distribution is 67 specimens (21%) containing distributed transverse reinforcement ratios between 0.1% and 0.2%.

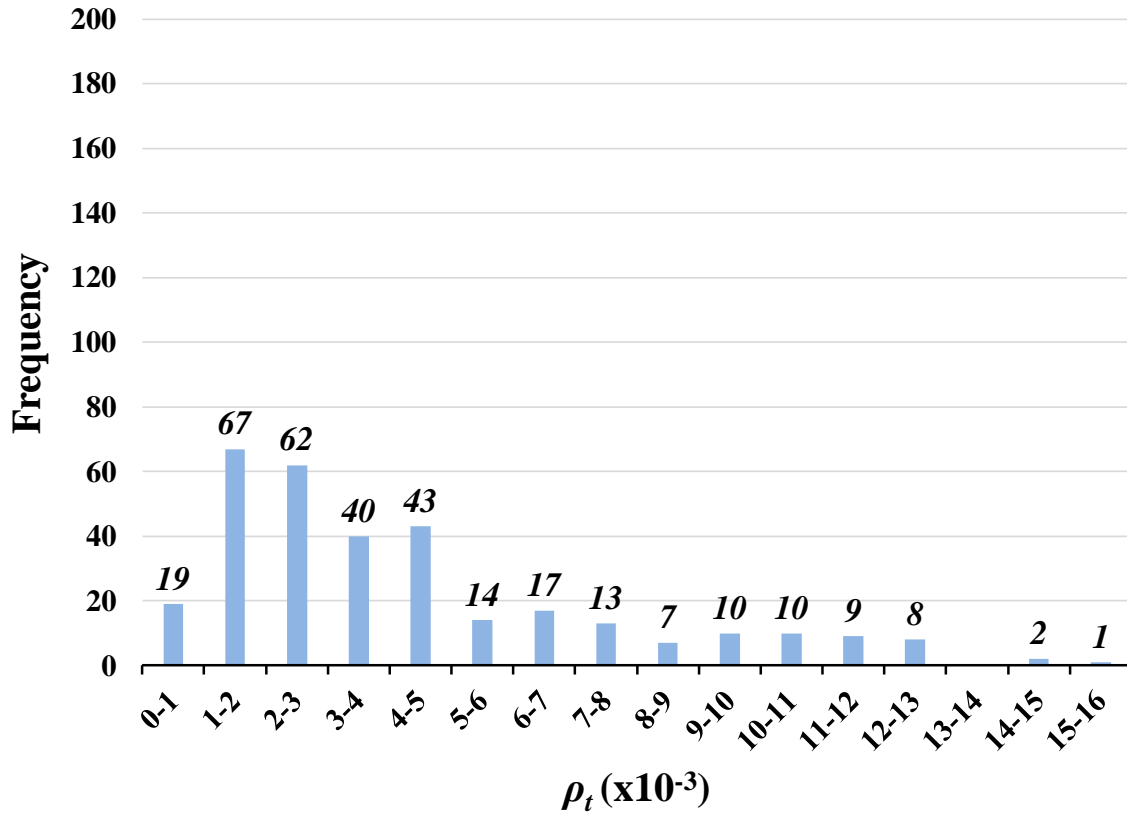


Figure 7.21: Distribution of ρ_t for Confined Database

7.5 Confinement Model

7.5.1 Model

A model was developed that explores the effect of transverse reinforcement location on bond strength of confined concrete members. This transverse reinforcement location model is based on the understanding that bond stress distribution across a splice is nonlinear (Thompson et al. 1975, Azizinamini et al. 1999, Canbay and Frosch 2005, Sim 2014). Because stresses are not constant across the splice, stirrups in different locations may experience different amounts of tensile resisting stress. Figure 7.22 (from Canbay and Frosch (2005)) illustrates how this concept applies to shorter splices and how it changes as the splice length increases.

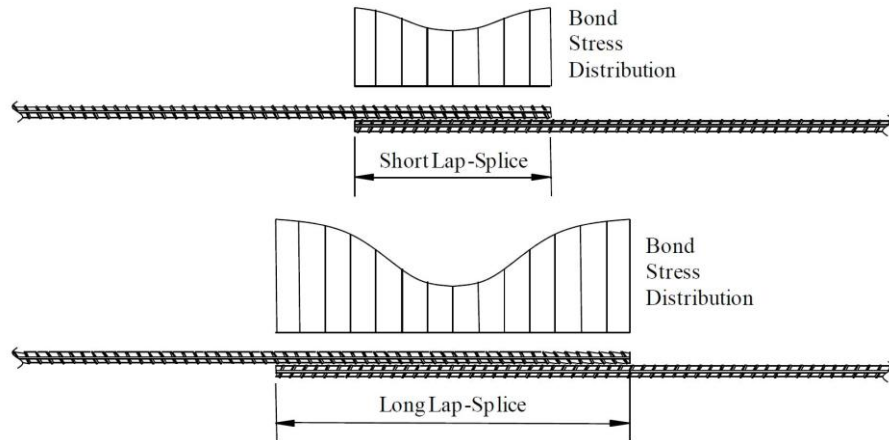


Figure 7.22: Nonlinear Bond Stress Distribution (Canbay and Frosch, 2005)

Further research by Sim (2014) found that when the total area of transverse reinforcement in the splitting plane is constant, stirrups placed at the ends of the splice experience greater strains than stirrups located directly in the middle of the splice. Differences in bar stress at failure were observed including no increase in longitudinal bar stress provided by stirrups located mid-splice and a 30% increase when only end stirrups were provided rather than being distributed. These results align closely with Series VI testing in this research program.

Based on this behavior, a model needs to consider bond stress distribution and stirrup location. The location of a stirrup along the splice determines its effectiveness in resisting tensile stress. Assumptions made to develop this Effective Confinement (EC) model include:

1. Stirrups are limited by their yield strength.
2. The splice zone may be discretized into five (5) regions: two regions of full effectiveness from confinement at the ends, one region of no effectiveness from confinement in the middle, and two regions of partial effectiveness in between.

A typical EC model with six stirrups distributed along the splice is provided in Figure 7.23 and shows the location of each region. Note that the red lines indicate the percent contribution value of each stirrup based on its location along the splice.

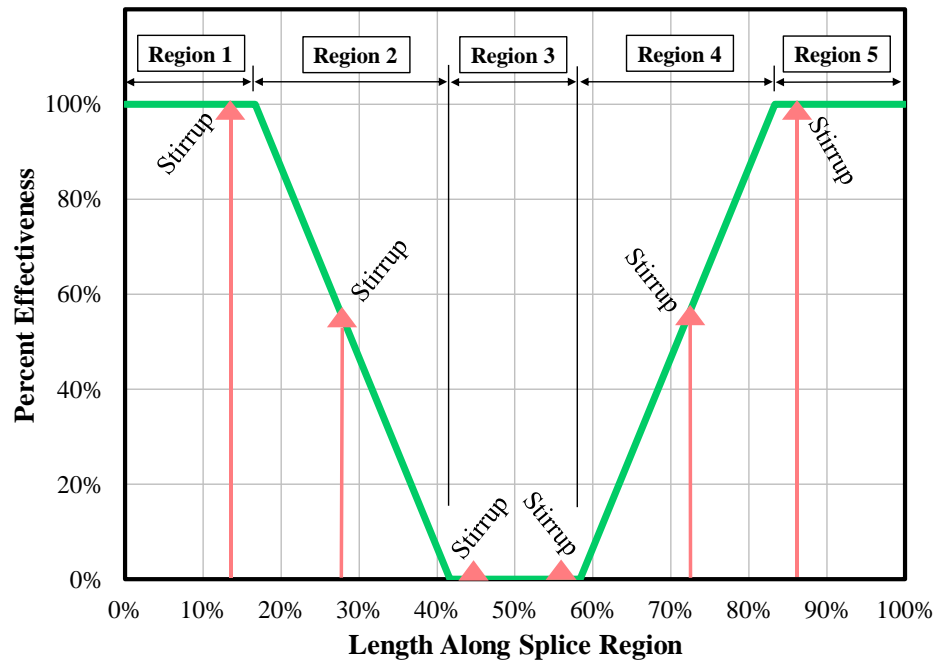


Figure 7.23: Typical Model Regions

Four models were generated in this study, each with different region lengths across the splice. All models are symmetric about the midpoint of the splice to reflect the symmetrical distribution of bond stresses across a symmetrically-loaded beam. The differences between these models are described in Table 7.4 followed by graphical configurations for all four models in Figure 7.24.

Table 7.4: Trial Model Region Dimensions

Potential Models	Lengths of Model Regions				
	Region 1	Region 2	Region 3	Region 4	Region 5
A	$l_s/6$	$l_s/3$	0	$l_s/3$	$l_s/6$
B	$0.15l_s$	$l_s/5$	$0.3l_s$	$l_s/5$	$0.15l_s$
C	$l_s/6$	$l_s/4$	$l_s/6$	$l_s/4$	$l_s/6$
D	$l_s/6$	$l_s/6$	$l_s/3$	$l_s/6$	$l_s/6$

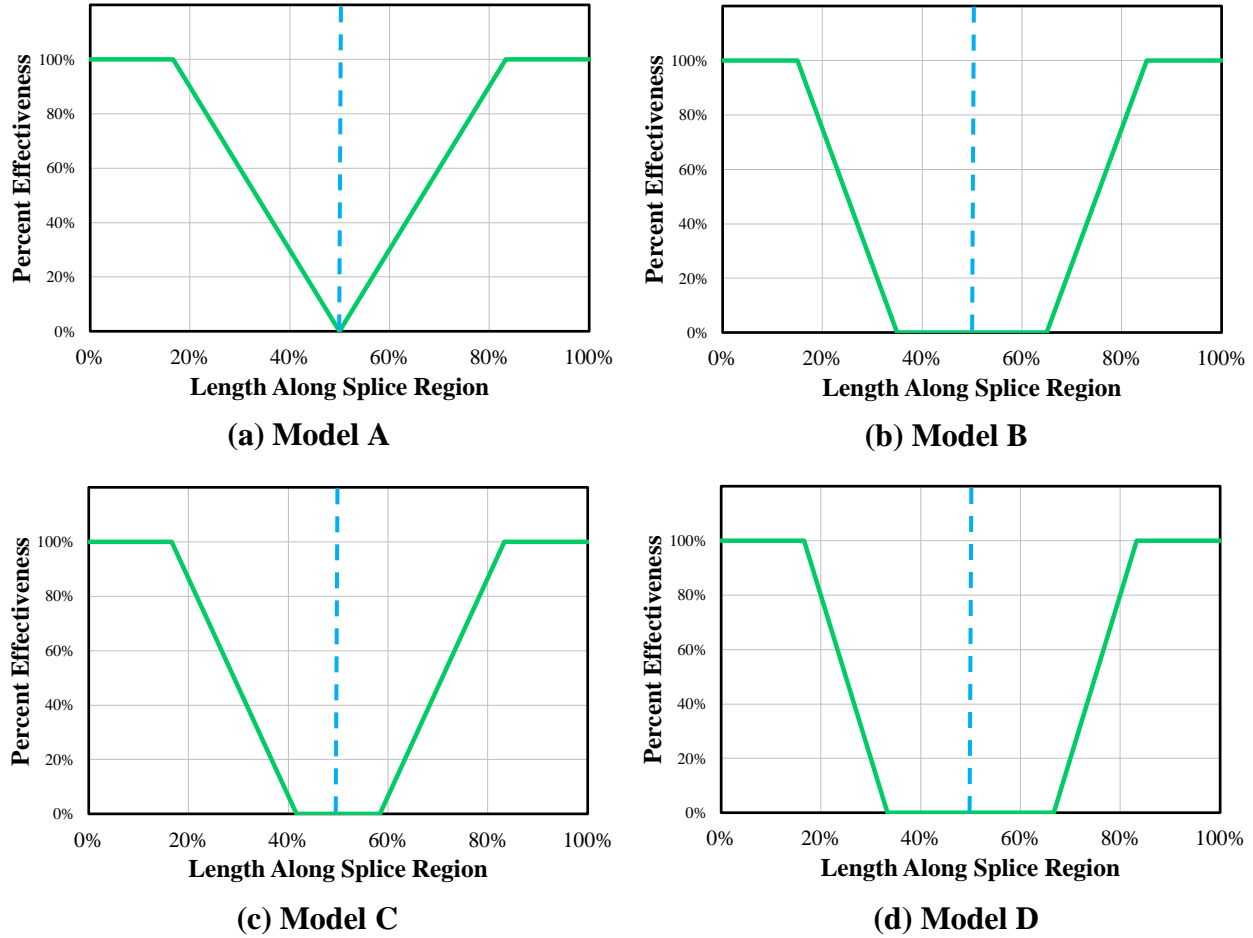


Figure 7.24: Potential Effective Confinement Models

To determine the effectiveness of a stirrup along the splice length, all four models require knowing the location of that stirrup. The total number of effective stirrups ($N_{s,eff}$) along the splice is calculated by summing all percent contributions. For example, given a splice length of 50 in. with three stirrups spaced at quarter points, all four models indicate that the middle stirrup provides no additional tensile resistance (0%). However, the other two stirrups are located within the linear interpolation range and can be either 50% (Model B and D), 67% (Model C), or 75% (Model A) effective, depending on the model. Model A outputs the most stirrup efficiency with $N_{s,eff} = 0 + 0.75 + 0.75 = 1.5$ effective stirrups while Models B and D output $N_{s,eff} = 0 + 0.5 + 0.5 = 1$ effective stirrup for this case.

7.5.2 Model Application

The number of effective stirrups within the splice region $N_{s,eff}$ can be determined by equating the effective stress developed in the transverse reinforcement to the additional stress in the longitudinal bars.

$$N_l A_t f_{yt} N_{s,eff} = N_b A_b (f_b - f_{bc}) \quad (7-6)$$

where:

A_b = area of one longitudinal reinforcing bar (in.²)

A_t = area of one stirrup leg (in.²)

f_b = total bar stress at failure of confined specimen (ksi)

f_{bc} = bar stress at failure of identical unconfined specimen; concrete contribution to bar stress (ksi)

f_{yt} = yield strength of transverse reinforcement (ksi)

N_b = number of longitudinal reinforcing bars

N_l = number of legs of transverse reinforcement crossing the splice plane

Note that the term $(f_b - f_{bc})$ represents the additional stress (f_{bs}) gained from the presence of confinement steel within the splice. The stress obtained from an unconfined specimen is subtracted from the total bar stress of each confined specimen where design parameters between the two specimens are identical, except the presence of confinement. This equation is also a measure of equilibrium between the force crossing the splitting plane and the force transferred from the transverse reinforcement to the longitudinal reinforcement. The final rearranged equation takes the following form:

$$N_{s,eff} = \frac{N_b A_b (f_b - f_{bc})}{N_l A_t f_{yt}} \quad (7-7)$$

Confined beam tests in Series VI and VII were conducted to isolate the additional bond strength provided from the transverse reinforcement. These tests allow for comparing beams with varying amounts of confinement steel to an identical beam with no transverse reinforcement. By running each of these beams through all four models, the ratio (Equation 7-8) of the number of effective stirrups $N_{s,eff}$ to the number of actual stirrups present N_s could be investigated. This ratio k represents the percent contribution of transverse reinforcement toward increasing bond strength. This value should always be less than or equal to one.

$$k = \frac{N_{s,eff}}{N_s} \quad (7-8)$$

where:

k = percent contribution of transverse reinforcement in splice region

$N_{s,eff}$ = number of effective stirrups within the splice region

N_s = number of stirrups within the splice region

To visualize how the value of k changes as the number of stirrups is increased within the splice, a spectrum of possible spacings was determined for a range of N_s values from 1 to 15, resulting in an upper and lower bound for possible model results. Additionally, an average stirrup spacing was implemented to determine an average k_{calc} value. Note that all stirrups are assumed to be evenly spaced and symmetric about the center of the splice. Table 7.5 shows the possible spacings and k values for each model. Spacing limits were determined from the following:

$$s_{min} = \frac{l_s}{N_s + 1} \quad s_{avg} = \frac{l_s}{N_s} \quad s_{max} = \frac{l_s}{N_s - 1}$$

Table 7.5: Model Boundaries

N_s	Possible Spacings (s)			k_{calc}											
				A			B			C			D		
	Min	Avg	Max	Min	Avg	Max	Min	Avg	Max	Min	Avg	Max	Min	Avg	Max
1	-	-	-	-	0	-	-	0	-	-	0	-	-	0	-
2	$l_s/3$	$l_s/2$	l_s	0.50	0.75	1.0	0.08	0.50	1.0	0.33	0.67	1.0	0	0.50	1.0
3	$l_s/4$	$l_s/3$	$l_s/2$	0.50	0.67	0.67	0.33	0.61	0.67	0.44	0.67	0.67	0.33	0.67	0.67
4	$l_s/5$	$l_s/4$	$l_s/3$	0.60	0.69	0.75	0.38	0.50	0.54	0.47	0.58	0.67	0.40	0.50	0.50
5	$l_s/6$	$l_s/5$	$l_s/4$	0.60	0.64	0.70	0.40	0.50	0.60	0.53	0.59	0.67	0.40	0.48	0.60
6	$l_s/7$	$l_s/6$	$l_s/5$	0.62	0.67	0.73	0.44	0.50	0.58	0.51	0.56	0.64	0.43	0.50	0.60
7	$l_s/8$	$l_s/7$	$l_s/6$	0.61	0.65	0.71	0.43	0.48	0.57	0.52	0.59	0.67	0.43	0.49	0.57
8	$l_s/9$	$l_s/8$	$l_s/7$	0.62	0.67	0.71	0.43	0.50	0.58	0.52	0.58	0.63	0.41	0.50	0.57
9	$l_s/10$	$l_s/9$	$l_s/8$	0.62	0.67	0.69	0.44	0.51	0.56	0.53	0.59	0.63	0.44	0.52	0.56
10	$l_s/11$	$l_s/10$	$l_s/9$	0.64	0.67	0.70	0.44	0.50	0.54	0.54	0.59	0.62	0.45	0.50	0.53
11	$l_s/12$	$l_s/11$	$l_s/10$	0.64	0.66	0.69	0.45	0.50	0.55	0.54	0.58	0.62	0.45	0.50	0.55
12	$l_s/13$	$l_s/12$	$l_s/11$	0.64	0.67	0.70	0.47	0.50	0.54	0.55	0.58	0.62	0.46	0.50	0.54
13	$l_s/14$	$l_s/13$	$l_s/12$	0.64	0.66	0.69	0.46	0.49	0.54	0.55	0.58	0.61	0.46	0.50	0.54
14	$l_s/15$	$l_s/14$	$l_s/13$	0.64	0.67	0.69	0.46	0.50	0.54	0.55	0.59	0.61	0.46	0.50	0.54
15	$l_s/16$	$l_s/15$	$l_s/14$	0.64	0.67	0.69	0.47	0.50	0.53	0.56	0.59	0.61	0.47	0.51	0.53

The k_{calc} values vs. N_s for each model are shown in Figure 7.25. Note that for a particular number of specified stirrups within the splice region, each model provides a range of possible percent contributions with an upper bound and a lower bound based on stirrup spacing. For lower values of N_s , the possible values of k_{calc} that each model can predict is large. As more stirrups are included within the splice region, this range of k_{calc} values converges upon one distinct constant in all four models. The large amount of initial scatter in the model is a result of the range of possible stirrup locations along the anchorage length. Spacing variability permits stirrups to be placed in regions of varying effectiveness, lending to a large range of k_{calc} values. It should also be noted that regardless of model accuracy, all four models approached a distinct value after approximately four stirrups were placed within the splice region.

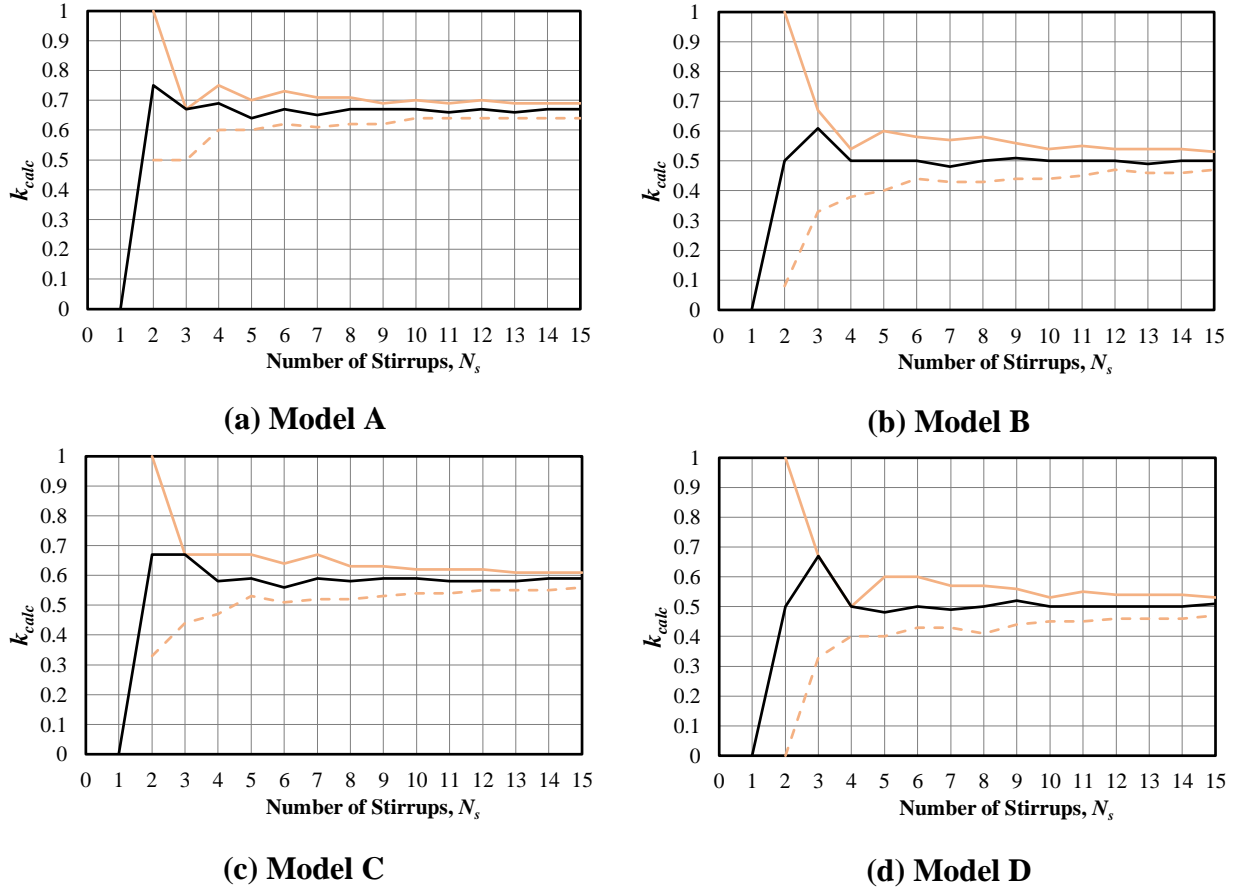


Figure 7.25: Potential Ranges of k_{calc}

Values of k_{test} were calculated in two trials for several beams from Phase I and Phase II of this testing program, as well as from Sim (2014). The value of k_{test} was calculated by substituting Equation 7-7 into Equation 7-8 to produce the following equation:

$$k_{test} = \frac{N_b A_b (f_b - f_{bc})}{N_s N_l A_t f_{yt}} \quad (7-9)$$

For Trial 1, measured values of f_{yt} were used to obtain initial k_{test} percentages for comparison. Nominal confined bar stress at failure and unconfined bar stress at failure were used; therefore, any differences in concrete strength between the confined and unconfined specimens were not included. The results of Trial 1 are provided in Table 7.6.

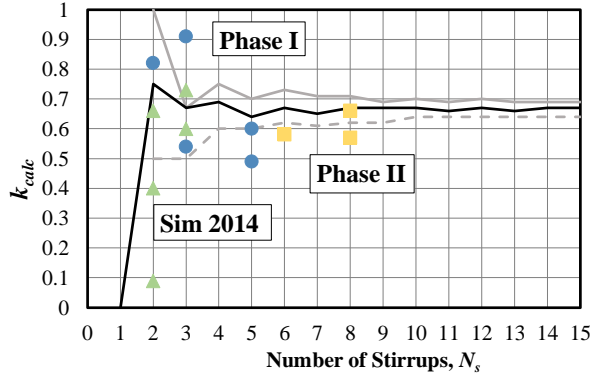
Table 7.6: Effective Confinement Test Specimens

Program	Specimen	l_s (in.)	f'_c (psi)	f_{test} (ksi)	N_s	Trial 1		Trial 2		
						$N_{s,eff}$	k_{test}	$f_{norm}^{[1]}$ (ksi)	$N_{s,eff}$	k_{test}
Phase I: Glucksman (2018)	U-40-5a	40	6260	69.8	-	-	-	-	-	-
	C3/60/2-40-5-50	40	6260	81.8	2	1.64	0.82	70.8	1.98	0.99
	C3/60/3-40-5-50	40	6260	89.8	3	2.73	0.91	70.8	3.41	1.14 ^[2]
	C3/100/3-40-5-50	40	6260	85.0	3	1.61	0.54	70.8	2.55	0.85
	C3/60-40-5-100	40	6260	91.7	5	2.99	0.60	70.8	3.75	0.75
	C3/100-40-5-100	40	6260	93.1	5	2.46	0.49	70.8	4.00	0.80
Phase II: Fleet (2019)	C3/60-40-5-150	40	6200	90.4	6	3.47	0.58	70.7	3.54	0.59
	C3/60-40-5-200	40	6300	96.8	8	4.54	0.57	71.0	4.63	0.58
	U-50-5	50	5400	73.2	-	-	-	-	-	-
	C3/60-50-5-150	50	6600	104.6	8	5.29	0.66	76.7	5.01	0.63
Sim (2014)	B-8-S-24	24	4400	44.2	-	-	-	-	-	-
	B-8-S-24-C1	24	4400	51.5	2	1.31	0.66	44.2	1.31	0.66
	B-8-S-24-C2	24	4400	48.7	2	0.81	0.40	44.2	0.81	0.40
	B-8-S-24-C3	24	4400	54.3	3	1.81	0.60	44.2	1.81	0.60
	M-8-S-48	48	5400	74.7	-	-	-	-	-	-
	M-8-S-48-C1	48	5400	97.1	2	2.21	1.11 ^[2]	74.7	2.21	1.11 ^[2]
	M-8-S-48-C2	48	5400	76.6	2	0.19	0.09	74.7	0.19	0.09
	M-8-S-48-C3	48	5400	97.0	3	2.20	0.73	74.7	2.20	0.73

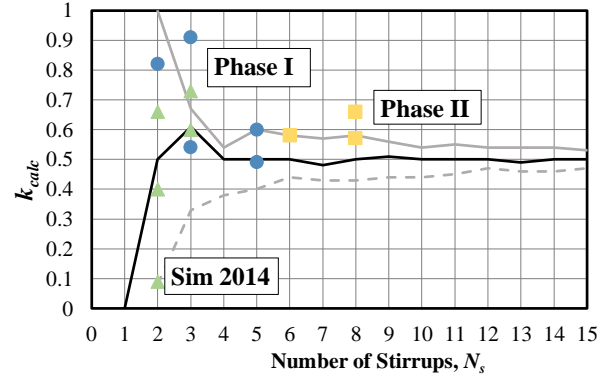
[1] Values reflect the unconfined concrete strength, normalized to the concrete strength of the confined beam

[2] Experimental test performed better than model prediction

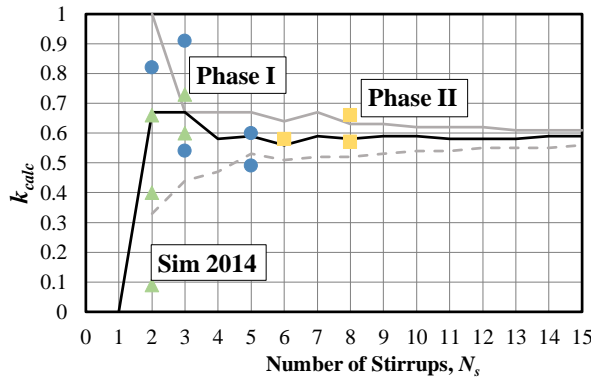
Trial 1 k_{test} values are plotted in Figure 7.26. Three specimens from Phase II are shown as yellow squares, five specimens from Phase I are shown as blue circles, and six specimens by Sim (2014) are shown as green triangles.



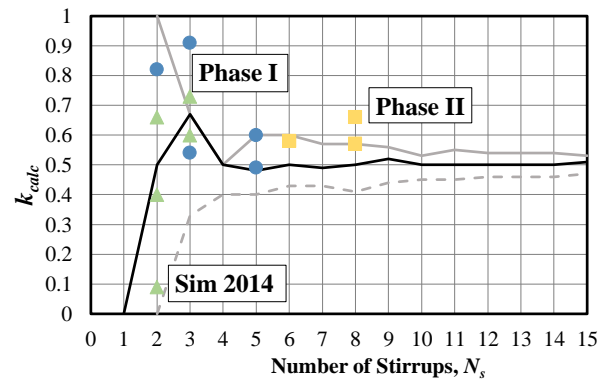
(a) Model A



(b) Model B



(c) Model C



(d) Model D

Figure 7.26: Trial 1 k_{test} vs. k_{calc}

Note that one specimen from Sim (2014) exceeded $k = 1$ in Trial 1 and is not included in Figure 7.26. Additionally, one specimen from Sim (2014) resulted in a k_{test} value of only 9%. This beam was constructed with two No. 4 Grade 60 stirrups placed in the middle of a 48 in. lap splice. It was concluded in this test that the addition of transverse reinforcement had essentially no effect on bond strength. Another beam achieved a k_{test} of 40% that contained two No. 3 Grade 60 stirrups in the middle of a 24 in. lap splice and slightly contributed to a higher bond strength. Figure 7.26 supports these findings.

In Trial 2, yield strength and variability in concrete strength were handled differently. According to Glucksman (2018), yield strength of the transverse reinforcement is negligible in determining the additional bond strength contribution. Therefore, yield strength f_{yt} in Equation 7-9 was taken to be a lower bound of 60 ksi for all beams, regardless of grade.

To account for the variation in concrete strength between the confined beam and its unconfined counterpart, a general normalization function was implemented. It has been previously supported that the representation of concrete strength in a spliced member without transverse reinforcement is best described by a power of 0.25 (Darwin et al. 1996, Zuo and Darwin 2000, Canbay and Frosch 2005, Pay 2005, Sim 2014, Glucksman 2018). The failure stresses of all baseline unconfined beams were normalized to the concrete strength of the confined specimen of interest. Equation 7-10 was used to normalize the longitudinal failure stress (f_{orig}) that reflects the difference in concrete strength between the unconfined beam and the confined beam.

$$f_{norm} = f_{orig} \sqrt[4]{\frac{f_{target}}{f'_c}} \quad (7-10)$$

where:

- f'_c = concrete cylinder strength (psi)
- f_{norm} = new normalized longitudinal bar stress at failure (ksi)
- f_{orig} = original longitudinal bar stress at failure (ksi)
- f_{target} = normalization target strength (psi)

Table 7.6 presents the calculated f_{norm} and k_{test} values for Trial 2. A comparison between k_{test} and k_{calc} is plotted for all four models in Figure 7.27.

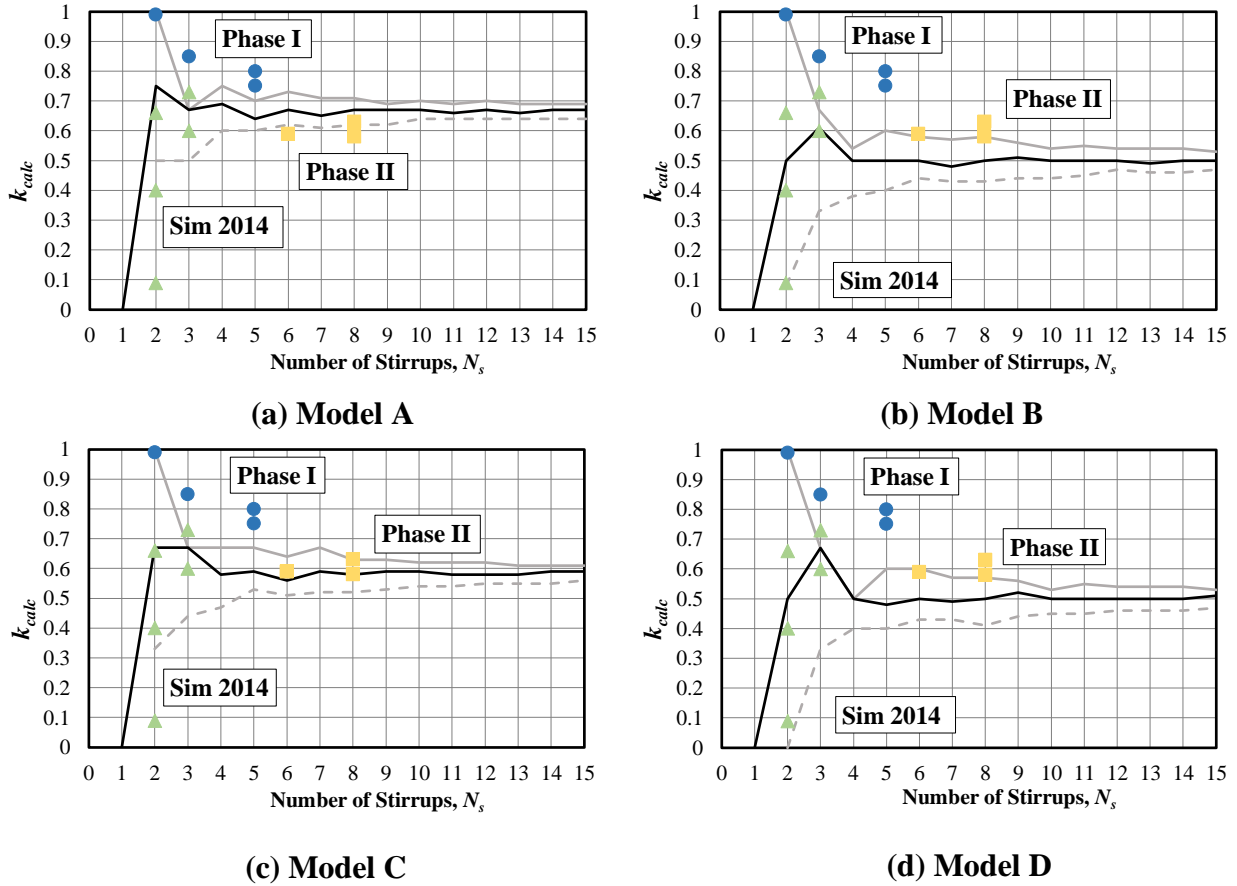


Figure 7.27: Trial 2 k_{test} vs. k_{calc}

Note that one beam from Glucksman (2018) and Sim (2014) produced k_{test} values of 1.14 and 1.11, respectively, due to the high contribution from the transverse reinforcement when three stirrups were placed along the splice. These tests are not shown in Figure 7.27.

Each model from both trials was compared to determine a best fit. Model A shows that many k_{test} values were below the k_{calc} convergence average of 67%, indicating that more stirrups were effective in the model than observed from the test. In addition, the lower bound for k_{calc} minimizes at 0.50 (2 or 3 stirrups) and does not capture values below this minimum. Model C fits the test data slightly better and results in a convergence k_{calc} value of 59%; however, the model is unable to accommodate lower k_{test} values because the lower bound reaches a minimum of 33%.

Models B and D closely fit the test data and provide reasonable bounds for the k_{calc} term. Both converge on a value of 50%, suggesting that when a reasonable distribution of transverse reinforcement is provided in the splice region, only half of those stirrups fully contribute to any additional bond strength. In other words, over the splice length, half of the stirrups are considered fully effective. For simplicity purposes, Model D was selected based on the ease in calculating the five region lengths as 1/3-regions (Fully effective regions sum to $l_s/3$, interpolated regions sum to $l_s/3$, and region of no effectiveness is $l_s/3$).

7.5.3 Steel Contribution Term, f_{bs}

Equation 7-6 relates the vertical force resisted by the transverse reinforcement and the horizontal force resisted by the longitudinal reinforcement. By rearranging the equation to solve for the transverse steel contribution, Equation 7-11 results. Note that the amount of force transferred from the vertical stirrups to the longitudinal bars (p) is assumed to be 100% of the vertical tension resisting force:

$$f_{bs} = \frac{F_{horiz}}{A_b N_b} = \frac{p F_{vert}}{A_b N_b} \quad (7-11)$$

where:

A_b = area of one longitudinal reinforcing bar (in.^2)

f_{bs} = bar stress contribution from the presence of transverse steel (ksi)

F_{horiz} = horizontal force transferred to the longitudinal reinforcement by the transverse reinforcement (kip)

F_{vert} = vertical force provided by transverse reinforcement (kip)

N_b = number of longitudinal reinforcing bars

p = transfer factor between vertical and horizontal force; Assumed to be 1

The force developed in the vertical transverse steel is limited by the yield strength of each stirrup; therefore, the product of stirrup force resistance and the total number of effective stirrups results in the vertical contribution force (Equation 7-12).

$$F_{vert} = N_{s,eff} R_s \quad (7-12)$$

where:

A_t = area of one stirrup leg (in.^2)

f_{yt} = yield strength of transverse reinforcement (ksi)

k = percent contribution of transverse reinforcement in splice region

N_l = number of legs of transverse reinforcement that cross the splitting plane

N_l = number of stirrups along the splice

$N_{s,eff}$ = number of effective stirrups within the splice region

= kN_s

R_s = resistance force provided by one stirrup (kip)

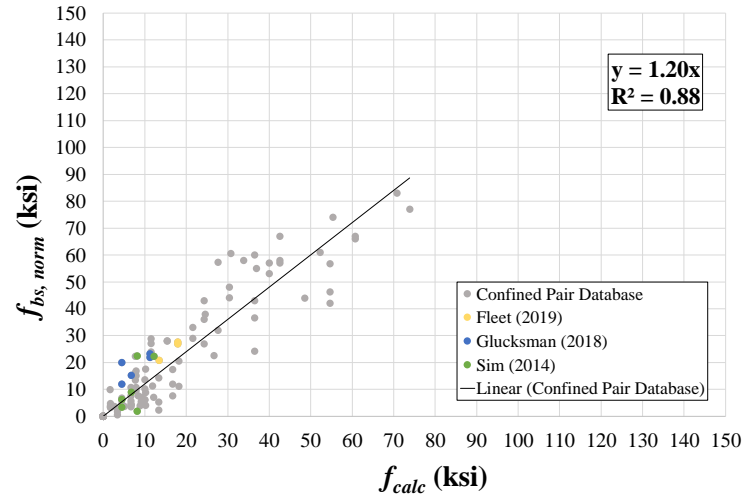
= $N_l A_t f_{yt}$

Substituting Equation 7-12 in Equation 7-11 results in the following:

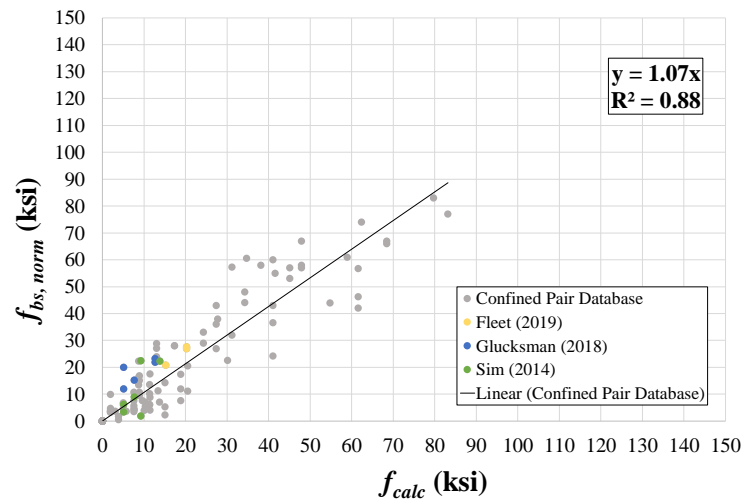
$$f_{bs} = \frac{pkN_s N_l A_t f_{yt}}{A_b N_b} \quad (7-13)$$

The value of p is taken to be one because it is assumed that the entire vertical force in the stirrups is transferred to the longitudinal steel. As previously discussed, in the model study k was found to converge to a value between 0.4 and 0.6. To further explore the value of k , the normalized steel contribution stress (f_{bs}) from each specimen in the confined pair database was plotted against Equation 7-13 for different values of k ranging from 40% to 65%. A linear trend is included, and

its slope should approach a value of one as k approaches the correct value. Figure 7.28(c) indicates that a contribution of 50% is most appropriate for the bar stress equation. This value is also consistent with findings by Sim (2014). Note that the normalized steel contribution stress is equal to the failure stress less the contribution from the concrete ($f_{bs, norm} = f_b - f_{bc, norm}$).

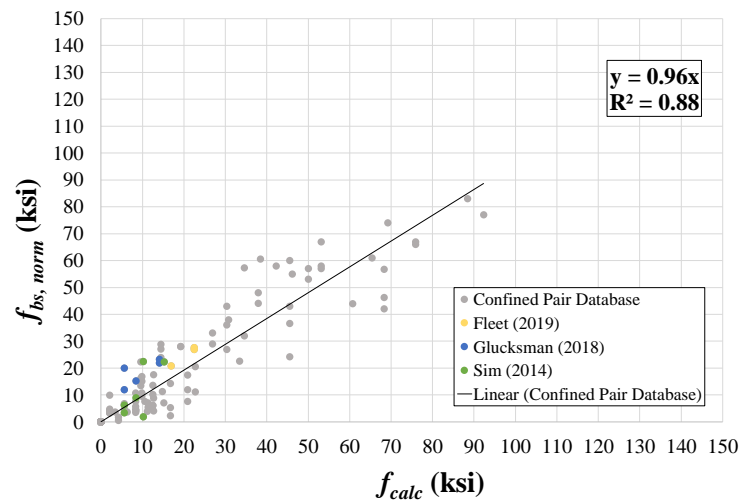


(a) $k = 40\%$

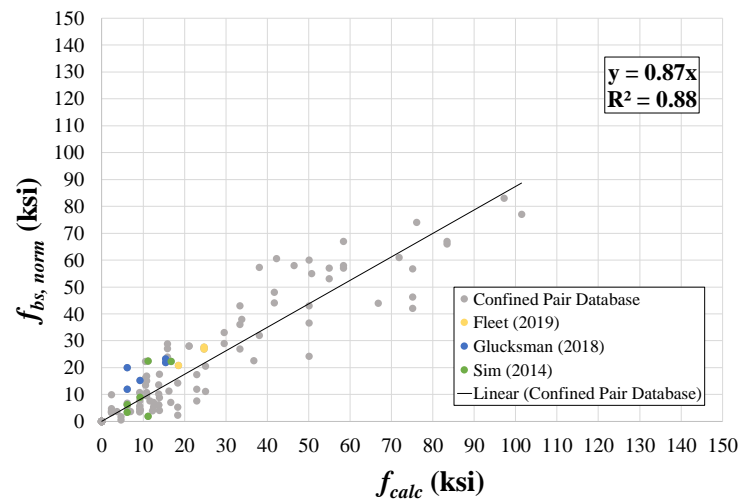


(b) $k = 45\%$

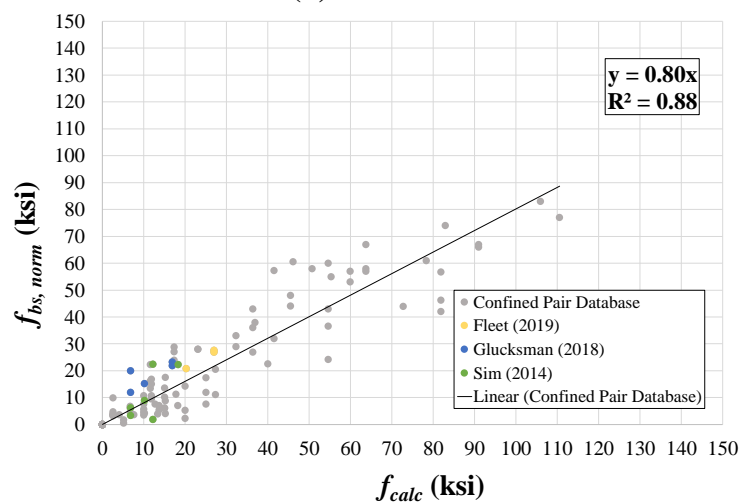
Figure 7.28: Normalized Steel Contribution to Bar Stress vs. Proposed Equation



(c) $k = 50\%$



(d) $k = 55\%$



(e) $k = 60\%$

Figure 7.28: Normalized Steel Contribution to Bar Stress vs. Proposed Equation (Continued)

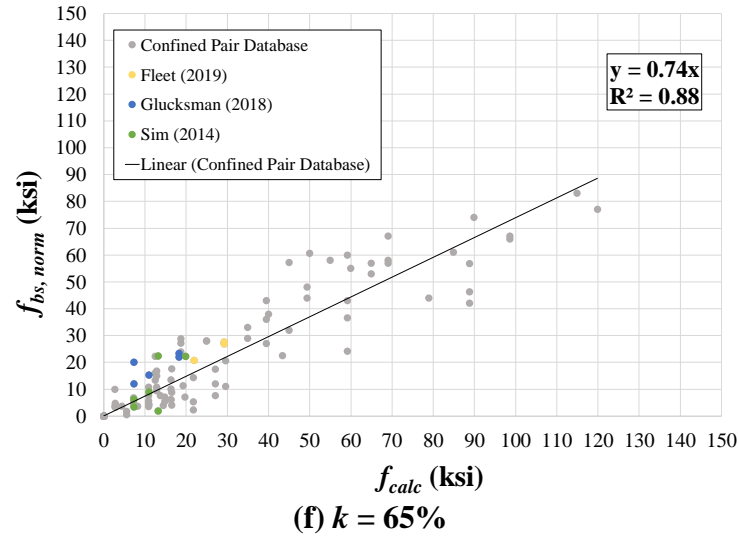


Figure 7.28: Normalized Steel Contribution to Bar Stress vs. Proposed Equation (Continued)

By substituting a value of 0.5 for k , the final equation for the stress contribution from transverse reinforcement results in Equation 7-14. As shown in Figure 7.28(c), the test results fit very well with the model.

$$f_{bs} = \frac{f_{yt} N_s N_l A_t}{2 N_b A_b} \quad (7-14)$$

7.6 Bond Model

The total bar stress at failure can be considered the sum of the concrete contribution and the added contribution of any transverse reinforcement within the lap splice (Equation 7-15):

$$f_b = f_{bc} + f_{bs} \quad (7-15)$$

where:

f_b = total bond strength (ksi)

f_{bc} = contribution to bond strength provided by concrete (ksi)

f_{bs} = contribution to bond strength provided by transverse steel (ksi)

By substituting Equations 7-5 and 7-14 into Equation 7-15, the final expression for bar stress takes the following form:

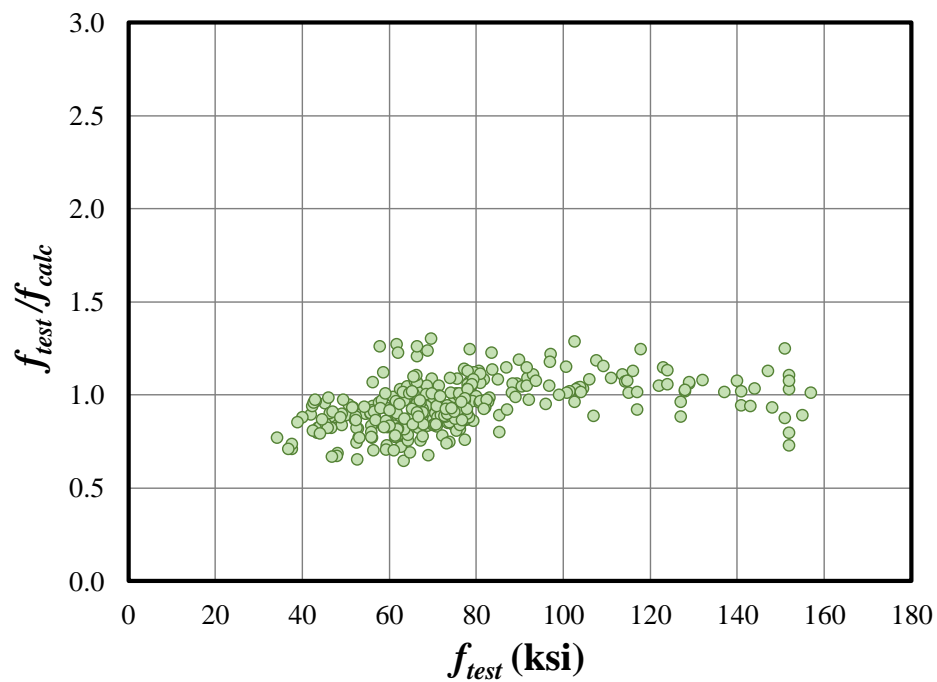
$$f_b = (f'_c)^{0.25} \left(\frac{l_s}{d_b} \right)^{0.5} \left(\frac{c_{so}}{d_b} \right)^{0.25} + \frac{N_s N_l A_t f_{yt}}{2 N_b A_b} \quad (7-16)$$

This expression is applicable for the development of unconfined and confined beams containing bars of all steel grades. Equation 7-16 was applied to the 322 beams in the confined database to evaluate its performance. For comparative purposes, the results provided by the ACI 318-14 design expression (Equation 6-3) are also included.

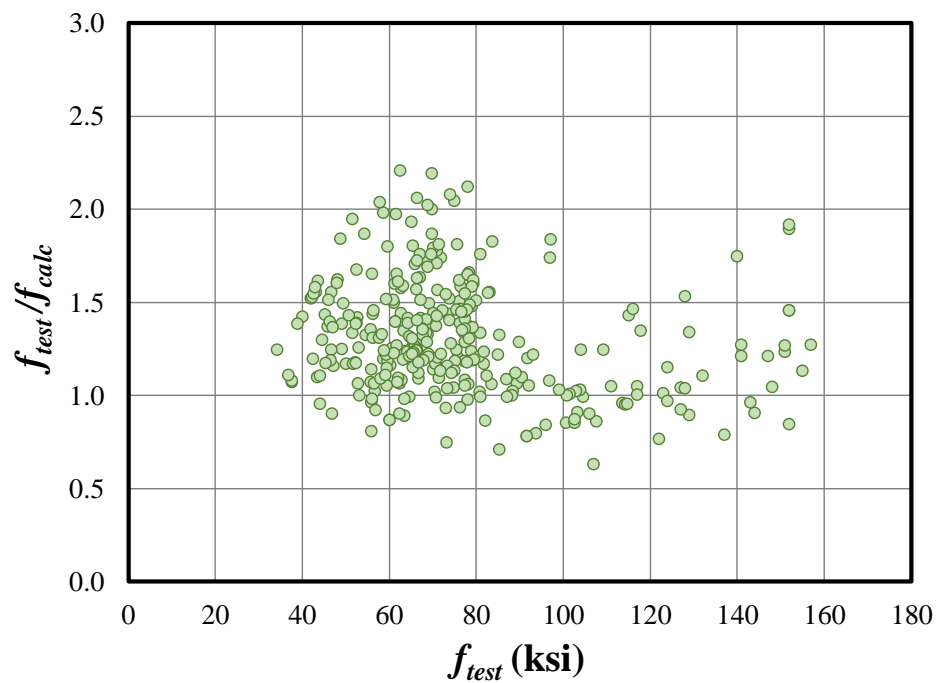
Table 7.7 provides a statistical comparison of the results. Graphic comparisons between ACI 318-14 and proposed expression (Equation 7-16) are provided in Figure 7.29 through Figure 7.37 for different variables of interest.

Table 7.7: Statistical Analysis Comparison of f_{test}/f_{calc} for Confined Beams

	ACI 318-14	Proposed Equation (7-16)
Max.	2.21	1.30
Min.	0.63	0.64
Mean (\bar{x})	1.30	0.94
Standard Deviation (σ)	0.300	0.129
COV	0.230	0.136

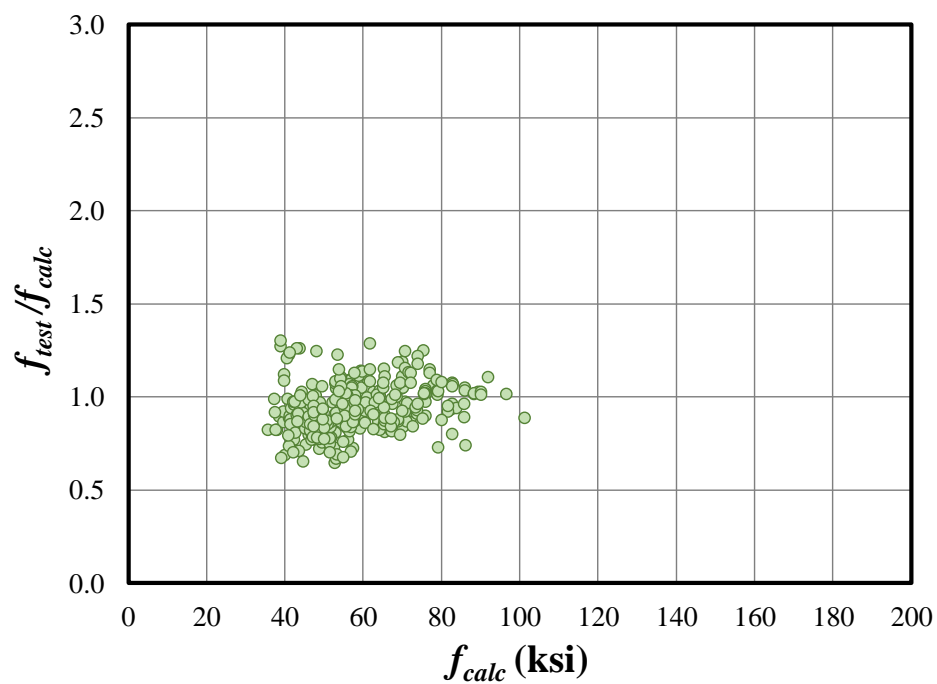


(a) Equation 7-16

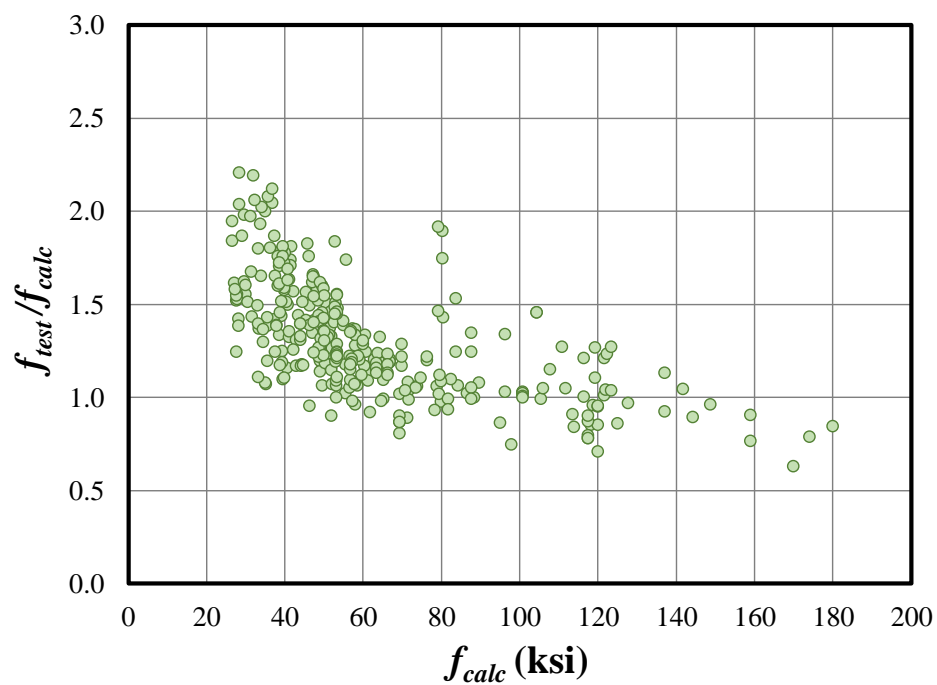


(b) ACI 318-14

Figure 7.29: Equation Comparison for Bar Stress at Failure (Confined)

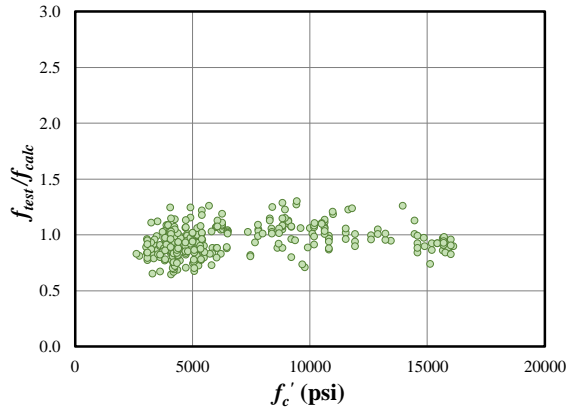


(a) Equation 7-16

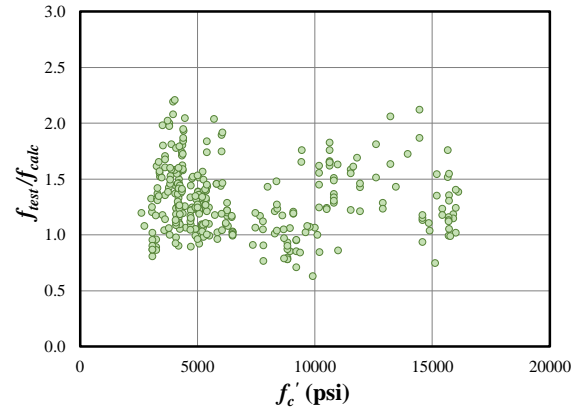


(b) ACI 318-14

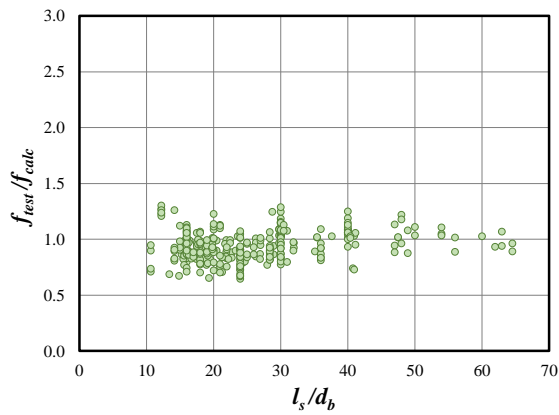
Figure 7.30: Equation Comparison for Calculated Bar Stress (Confined)



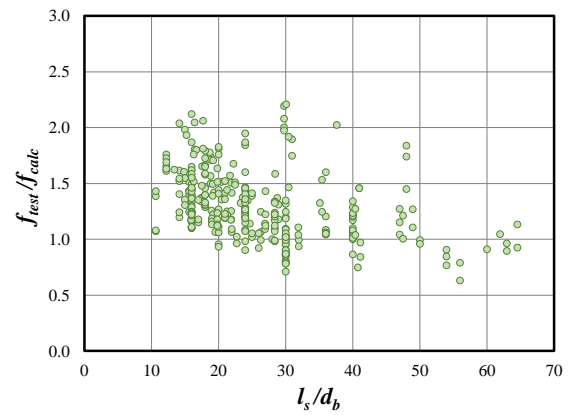
(a) Equation 7-16



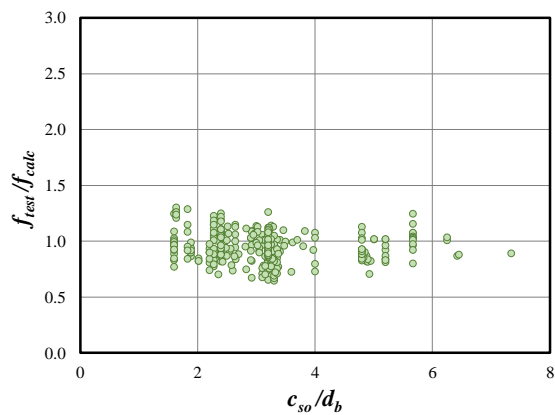
(b) ACI 318-14

Figure 7.31: Equation Comparison for Concrete Strength (Confined)

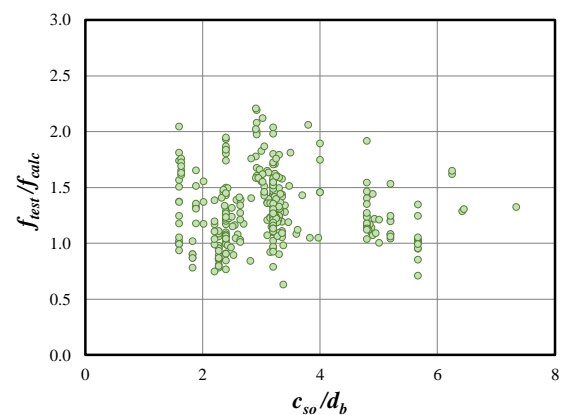
(a) Equation 7-16



(b) ACI 318-14

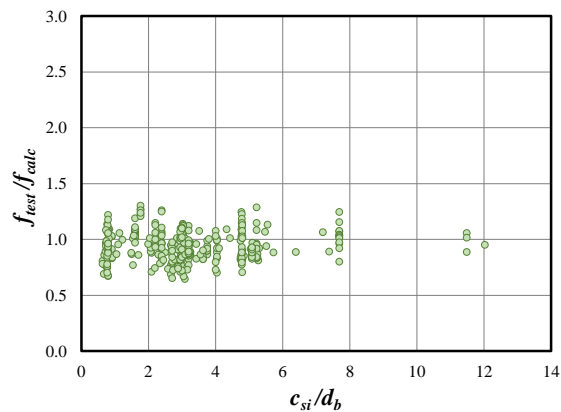
Figure 7.32: Equation Comparison for Splice Length over Bar Diameter (Confined)

(a) Equation 7-16

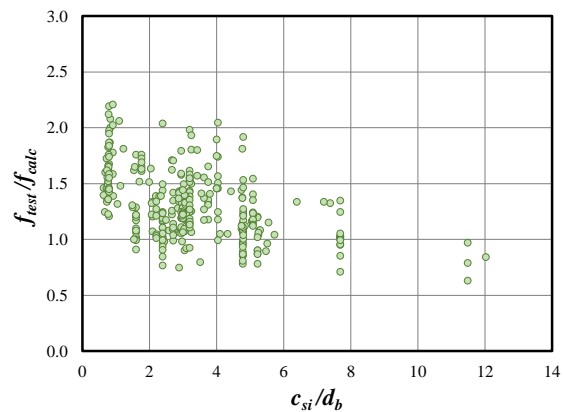


(b) ACI 318-14

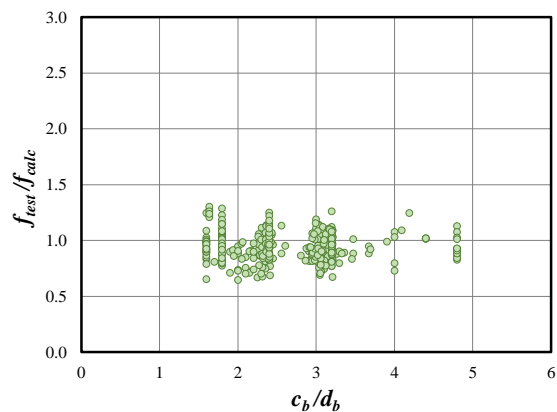
Figure 7.33: Equation Comparison for Side Cover over Bar Diameter (Confined)



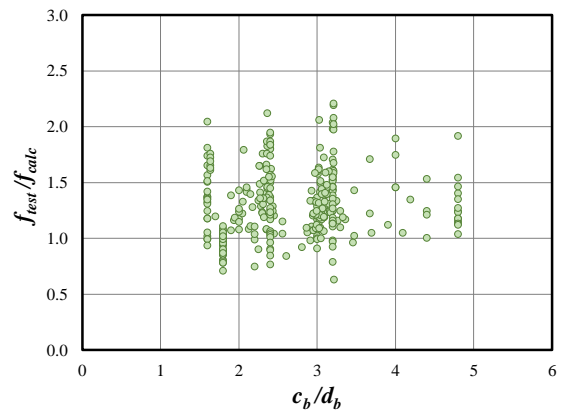
(a) Equation 7-16



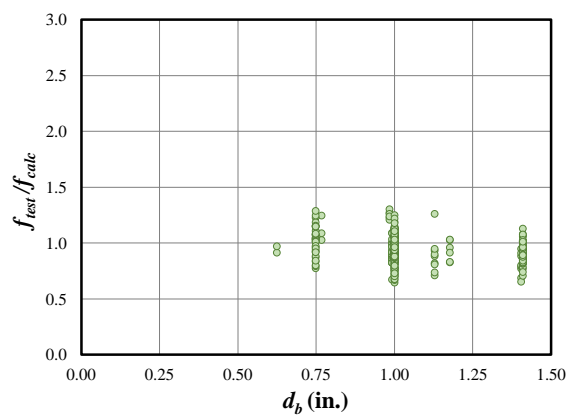
(b) ACI 318-14

Figure 7.34: Equation Comparison for Half Bar Spacing over Bar Diameter (Confined)

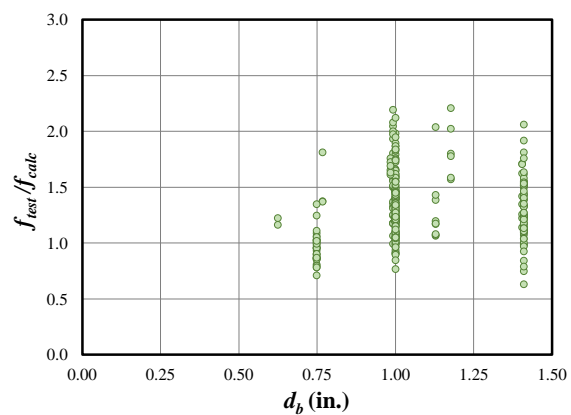
(a) Equation 7-16



(b) ACI 318-14

Figure 7.35: Equation Comparison for Bottom Cover over Bar Diameter (Confined)

(a) Equation 7-16



(b) ACI 318-14

Figure 7.36: Equation Comparison for Bar Diameter (Confined)

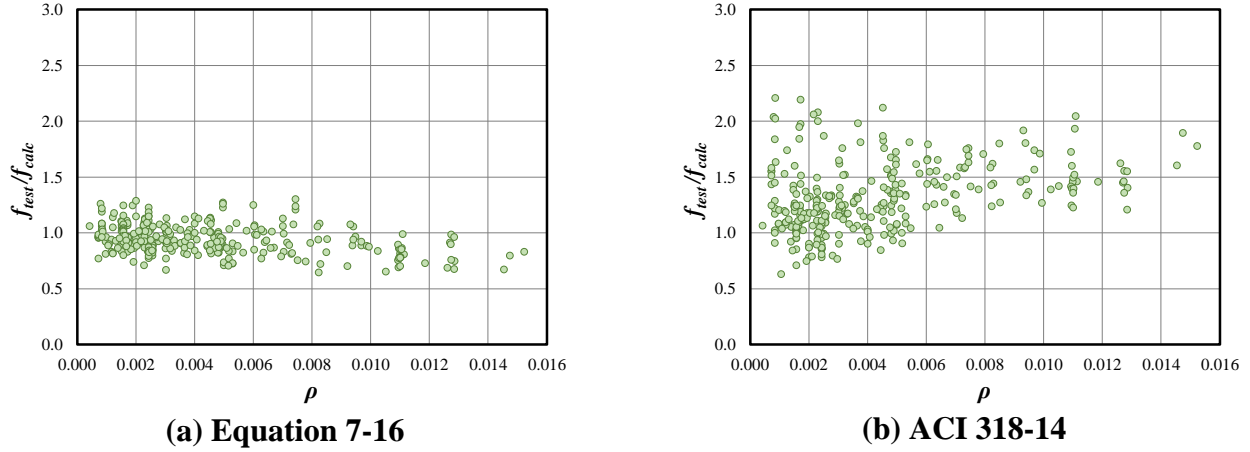


Figure 7.37: Equation Comparison for Transverse Reinforcement Ratio (Confined)

For all results from Figure 7.29 through Figure 7.37, scatter is reduced when Equation 7-16 is implemented compared to the design expression in ACI 318-14.

7.7 Recommendations

The following expression is proposed for the development and splicing of reinforcing steel:

$$f_b = (f'_c)^{0.25} \left(\frac{l_s}{d_b} \right)^{0.5} \left(\frac{c_{so}}{d_b} \right)^{0.25} + \frac{N_s N_l A_t f_{yt}}{2 N_b A_b} \quad (7-17)$$

where:

A_b = area of one longitudinal reinforcing bar (in.²)

A_t = area of one stirrup leg (in.²)

c_{so} = side clear cover of spliced bars (in.)

d_b = longitudinal bar diameter (in.)

f_b = total bond strength (ksi)

f'_c = concrete compressive strength (psi)

f_{yt} = yield strength of transverse reinforcement = 60 ksi

l_s = splice or development length (in.)

N_b = number of longitudinal reinforcing bars

N_l = number of legs of transverse reinforcement crossing the splice plane

N_s = number of stirrups in the splice region

The value recommended for f_{yt} is 60 ksi after findings from Glucksman (2018) indicate that transverse reinforcement with a yield strength of 100 ksi has no additional effect on bond strength when compared to transverse reinforcement having a yield strength of 60 ksi.

For design purposes, Equation 7-17 can be rearranged and solved for the splice length in terms of bar diameter in order to achieve the design stress f_y .

$$\left(\frac{l_s}{d_b}\right)^{0.5} = \frac{(f_y - f_{bs})}{(f'_c)^{0.25}} \left(\frac{d_b}{c_{so}}\right)^{0.25} \quad (7-18)$$

where:

$$f_{bs} = \left(\frac{f_{yt}}{2}\right) \left(\frac{N_s N_l A_t}{N_b A_b}\right) N_s$$

Solving for l_s/d_b results in Equation 7-19:

$$\frac{l_s}{d_b} = \frac{(f_y - f_{bs})^2}{\sqrt{f'_c}} \sqrt{\frac{d_b}{c_{so}}} \quad (7-19)$$

Note that the cover modifier can be conservatively taken as one for typical beams (Equation 7-20). For slabs which provide large bar spacings, use of the cover modifier has a significant effect and should be considered. For slabs, c_{so} should be calculated as half the inner bar spacing, c_{si} .

$$\frac{l_s}{d_b} = \frac{(f_y - f_{bs})^2}{\sqrt{f'_c}} \quad (7-20)$$

CHAPTER 8. SUMMARY AND CONCLUSIONS

8.1 Summary

For the implementation of high-strength reinforcement in practice, it is essential that the stresses required by use of these bars be properly developed. Therefore, the objective of this study was to evaluate the development of high-strength reinforcing steel and establish a design expression for the development and splicing of this steel. Two phases of experimental tests were conducted. Phase I of this research program was conducted by Glucksman (2018) which investigated the influence of splice length and transverse reinforcement on bond strength, as well as the effectiveness of high-strength transverse reinforcement over four series of beam tests. Phase II of this research program was the focus of this study. Testing in this phase complemented the testing conducted in the first four series. Of specific interest in this phase of research were the following:

1. Bar development in slabs
2. Effect of high-strength concrete (10,000 psi)
3. Effect of different stress-strain relationships of the high-strength steel (ASTM A615 vs. ASTM A1035)
4. Effect of transverse reinforcement location

8.2 Slab Testing

Four reinforced concrete slabs with splice lengths ranging from $40d_b$ to $100d_b$ were tested in this program. Based on testing, the following findings are provided:

1. Longitudinal cracking was consistently observed above each of the four splices, regardless of final failure mode. For splitting failures, spalling was minimal.

2. For shorter splice lengths ($\leq 60d_b$), bond failures occurred by splitting of the side and top cover around the splice. As splice length increased, the failure mode transitioned to flexure at the supports evidenced by crushing of the concrete in the compression zone. For these specimens with No. 5 bars spaced at 6 in., it was possible to develop the full strength of the ASTM A615 Grade 100 reinforcement with a splice length of $80d_b$.

8.3 Beam Testing

A total of 12 reinforced concrete beams were tested to explore the influence of splice length, concrete compressive strength, bar type, and transverse reinforcement on the bond strength of members spliced with high-strength reinforcement. Seven beams contained varying amounts of confining steel within the splice region while five were unconfined.

8.3.1 Unconfined

1. Longitudinal cracking initiated near the ends of the splice and propagated toward the middle of the beam.
2. Primary cracks surfaced along the tension face at a larger spacing than the slab specimens, (approximately three times the spacing).
3. Only bond failures were observed for unconfined specimens.
4. Failure of the unconfined beams was brittle and explosive, regardless of splice length, and was typically preceded by extensive amounts of longitudinal cracking at the ends of the splice.
5. The use of high-strength concrete allowed for an increase in bond strength of approximately 18% to 20% for unconfined $40d_b$ beams when compared to similar

specimens cast with normal-strength concrete. Unconfined $60d_b$ beams experienced increases in bond strength of 6% and 17% when high-strength concrete was implemented.

6. The quarter root provides a more accurate representation of the effect of concrete compressive strength on bond strength for normal-strength and high-strength concrete when compared to the square root.
7. Beams containing ASTM A1035 spliced bars behaved similarly to beams spliced with ASTM A615 Grade 100 bars when failure occurred within the linear-elastic region of the steel response.

8.3.2 Confined

1. For confined beams, primary flexural cracks formed directly above the transverse reinforcement at all stirrup locations with the exception of stirrups placed close to the end of the splice. In this case, the primary flexural crack formed at the end of the splice.
2. The presence of transverse reinforcement did not prevent propagation of longitudinal cracks but did contain the growth of these cracks.
3. Failure of confined beams was generally less explosive. When confinement pressures were low, a splitting failure mode was typical; however, as this pressure was increased for a given splice length through the addition of more transverse reinforcement, the failure mode shifted from bond to flexure initiated by crushing of the concrete in the compression zone.
4. When stirrups were placed at the end of a given splice, the potential for the longitudinal bars to slip out from this confinement under increased loading was high. It appears that the bars slipped out after failure, but due to the brittle nature of the failure, this could not be confirmed.

5. In general, an increase in bond strength was observed for confined beams as the transverse reinforcement ratio ρ_t increased. A larger increase in bar stress was observed for small values of ρ_t when compared to an unconfined specimen.
6. The effect of f_{yt} on the bond strength contribution from transverse reinforcement is negligible based on comparisons using the transverse reinforcement ratio (which is not dependent on f_{yt}) and the confinement pressure (which is dependent on f_{yt}).

8.4 **Bond Modeling**

The total bar stress achieved in a specimen was considered as the sum of the individual contributions from the concrete and the transverse steel (Equation 8-1). This theory has been supported by several previous findings and proposed models (ACI 408 2003, Canbay and Frosch 2005, Sim 2014, Glucksman 2018). Various bond models were explored using existing data to develop the components of this general design expression.

$$f_b = f_{bc} + f_{bs} \quad (8-1)$$

where:

f_b = total bond strength (ksi)

f_{bc} = contribution to bond strength provided by concrete (ksi)

f_{bs} = contribution to bond strength provided by transverse steel (ksi)

8.4.1 **Unconfined**

A comparison of bar stress equation recommendations from previous studies indicates three parameters in common that have a significant influence on bond strength. Concrete compressive strength, splice length, and cover were investigated using a database of bottom-cast

specimens without transverse reinforcement to determine this influence. The ratio of side cover to bar diameter was selected for a cover modifier due to its minimum coefficient of variation and high coefficient of correlation across multiple powers. By performing a nonlinear regression analysis, Equation 8-2 was found to be the best fit for the concrete contribution to bar stress:

$$f_{bc} = 0.9(f'_c)^{0.28} \left(\frac{l_s}{d_b} \right)^{0.48} \left(\frac{c_{so}}{d_b} \right)^{0.29} \quad (8-2)$$

where:

c_{so} = side clear cover of spliced bars (in.)

d_b = longitudinal bar diameter (in.)

f'_c = concrete compressive strength (psi)

l_s = splice or development length (in.)

This equation was simplified for design by rounding the power constants and adjusting the coefficients, resulting in Equation 8-3.

$$f_{bc} = (f'_c)^{0.25} \left(\frac{l_s}{d_b} \right)^{0.5} \left(\frac{c_{so}}{d_b} \right)^{0.25} \quad (8-3)$$

This equation which was independently developed supports the findings by Sim (2014) for an expression that determines the expected bar stress for an unconfined reinforced concrete specimen. In fact, the same equation is provided.

8.4.2 Confined

By analyzing the difference in bar stress between pairs of unconfined and confined beams with identical details, the contribution to steel bar stress was isolated. Through this analysis, a physical model for evaluating the effectiveness of stirrups within the splice region based on stirrup location was developed, as shown in Figure 8.1.

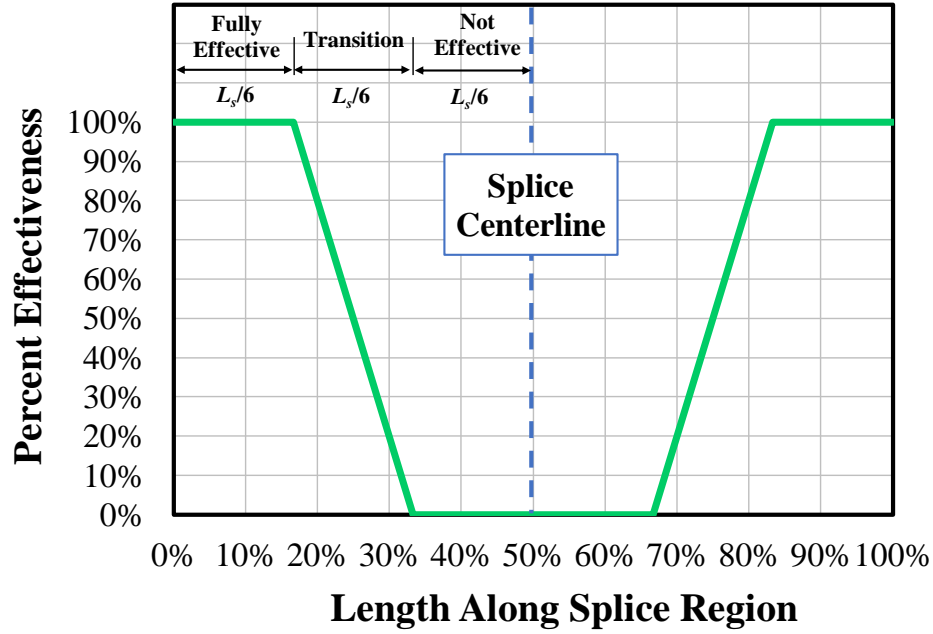


Figure 8.1: Proposed Effective Confinement Model

The percent contribution of transverse reinforcement was calculated for a selection of beam specimens tested by Glucksman (2018), Sim (2014), and this study. The exact location of these stirrups was known and percent contributions were compared to the selected model for comparison. The proposed model represents the test results well.

A parametric study indicates that the proposed model converges on an average of 50% of the stirrups across the splice being effective once four or more stirrups are provided using a consistent spacing. The increase in bar force developed in the spliced bars (F_{long}) was found to be equivalent to the vertical force provided by the effective transverse reinforcement (F_{trans}). This relationship is displayed in Figure 8.2.

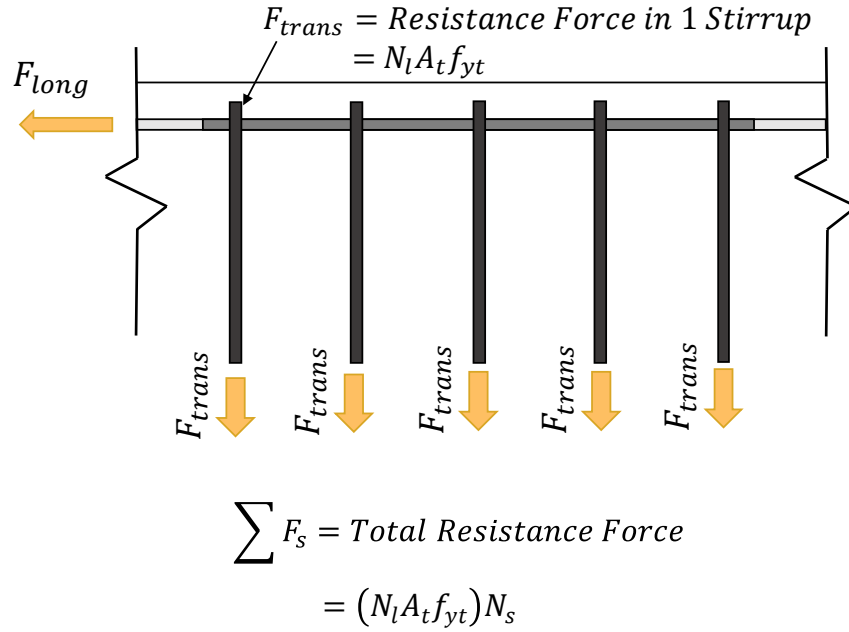


Figure 8.2: Total Effective Force from Transverse Reinforcement

By equating the longitudinal force with the transverse force, an expression for the transverse steel contribution can be derived in Equation 8-4:

$$F_{long} = F_{trans}$$

$$(A_b f_{bs}) N_b = (N_l A_t f_{yt}) (k N_s) \quad (8-4)$$

By substituting a value of 0.5 for the percent contribution term k , the number of effective stirrups is included in the equation. Therefore, the stress contribution from the transverse steel to bar stress developed can be expressed according to Equation 8-5.

$$f_{bs} = \frac{(N_l A_t f_{yt})}{N_b A_b} \left(\frac{N_s}{2} \right) \quad (8-5)$$

where:

A_b = area of one longitudinal reinforcing bar (in.^2)

A_t = area of one stirrup leg (in.^2)

f_{yt} = yield strength of transverse reinforcement (ksi)

N_b = number of longitudinal reinforcing bars

N_l = number of legs of transverse reinforcement crossing the splice plane

N_s = number of stirrups in the splice region

While the percent contribution factor (50%) was determined using the model illustrated in Figure 8.1, Equation 8-5 supports findings by Sim (2014) for an expression that determines the additional bar stress provided by transverse reinforcement for confined reinforced concrete specimens. Again, this evaluation independently results in the same expression. Additionally, the transverse steel yield strength, f_{yt} , is fixed at 60 ksi for this expression based on findings by Glucksman (2018) indicating that transverse reinforcement with a yield strength of 100 ksi has no additional effect on bond strength when compared to transverse reinforcement having a yield strength of 60 ksi; therefore, a simplified expression takes the following form where f_{bs} is in ksi:

$$f_{bs} = \frac{30N_s(N_l A_t)}{N_b A_b} \quad (8-6)$$

where:

A_b = area of one longitudinal reinforcing bar (in.^2)

A_t = area of one stirrup leg (in.^2)

N_b = number of longitudinal reinforcing bars

N_l = number of legs of transverse reinforcement crossing the splice plane

N_s = number of stirrups in the splice region

8.4.3 Design Recommendations

Based on the results from comparing various models to describe the contributions of concrete and steel to the overall bar stress, the following analytical expression was developed for reinforced concrete members:

$$f_b = f_{bc} + f_{bs}$$

$$f_b = (f'_c)^{0.25} \left(\frac{l_s}{d_b} \right)^{0.5} \left(\frac{c_{so}}{d_b} \right)^{0.25} + \frac{30N_s(N_l A_t)}{N_b A_b} \quad (8-7)$$

where:

A_b = area of one longitudinal reinforcing bar (in.²)

A_t = area of one stirrup leg (in.²)

c_{so} = bar cover modifier term

for beams = side clear cover (in.)

for slabs = 1/2 clear bar spacing (in.)

d_b = longitudinal bar diameter (in.)

f_b = total bond strength (ksi)

f'_c = concrete compressive strength (psi)

l_s = splice length (in.)

N_b = number of longitudinal reinforcing bars

N_l = number of legs of transverse reinforcement crossing the splice plane

N_s = number of stirrups in the splice region

For design, Equation 8-7 can be rearranged to solve for the required development length in terms of bar diameter given a required stress, f_b . In design, the yield strength, f_y replaces f_b .

$$\frac{l_s}{d_b} = \frac{(f_y - f_{bs})^2}{\sqrt{f'_c}} \sqrt{\frac{d_b}{c_{so}}} \quad (8-8)$$

If desired, the cover factor $\sqrt{d_b/c_{so}}$ can be conservatively taken to 1.0 for beams and slabs. This provides some conservatism for beams but may be too conservative for slabs depending on bar size and spacing. It is strongly recommended in beams that transverse reinforcement always be provided. Test results indicate that regardless of splice length, splitting failures occur when confinement is absent. Because of the importance of transverse reinforcement location on bond strength, a minimum of four stirrups should be provided across the splice at equal bar spacings. It is also recommended that the end stirrup be placed at a minimum of 2 in. from the end of the splice to avoid the potential for longitudinal bar slip.

8.5 Further Research

To better understand the behavior and development of high-strength steel in spliced reinforced concrete members, it is suggested that further research be conducted on the development of high-strength reinforcing steel with an emphasis on the following topics:

1. Stirrup Configuration: Conduct testing on various stirrup layouts within the splice to determine the influence of transverse reinforcement spacing.
2. Stirrup Concentration: Conduct testing on splice beams that have transverse reinforcement concentrations within $l_s/6$ from the splice ends (varying the length of the fully effective region).

3. Distributed Transverse Reinforcement Ratio: Conduct testing on splice beams with the same splice length and different values of ρ_t to determine the transition between bond failure and the initiation of flexural failure.
4. Continuous Nonlinear Confinement Model: Develop an alternate confinement model that more closely reflects the distribution of bond stresses across the splice to determine the effectiveness of stirrup location.
5. Nonlinear Response of ASTM A1035 Steel: Conduct beam testing using ASTM A1035 longitudinal steel to produce bond failures in the nonlinear region of the stress-strain curve.

REFERENCES

- Abrams, D. A., 1913, "Tests of Bond between Concrete and Steel," *University of Illinois Bulletin*, No. 71, The University of Illinois, Urbana-Champaign, IL., 238 pp.
- ACI Committee 234, 2000, *Guide for the Use of Silica Fume in Concrete*, ACI 234R-96, American Concrete Institute, Farmington Hills, MI., 51 pp.
- ACI Committee 318, 2014, *Building Code Requirements for Structural Concrete and Commentary*, ACI 318-14, American Concrete Institute, Farmington Hills, MI., 519 pp.
- ACI Committee 408, 2003, *Bond and Development of Straight Reinforcing Bars in Tension*, ACI 408R-03, American Concrete Institute, Farmington Hills, MI., 49 pp.
- ASTM A1035, 2016, "Standard Specification for Deformed and Plain, Low-Carbon, Chromium, Steel Bars for Concrete Reinforcement," American Society of Testing and Materials International, West Conshohocken, PA., 8 pp.
- ASTM A370, 2018, "Standard Test Methods and Definitions for Mechanical Testing of Steel Products," American Society of Testing and Materials International, West Conshohocken, PA., 50 pp.
- ASTM A615, 2016, "Standard Specification for Deformed and Plain Carbon-Steel Bars for Concrete Reinforcement," American Society of Testing and Materials International, West Conshohocken, PA., 8 pp.
- ASTM C1231, 2015, "Standard Practice for Use of Unbonded Caps in Determination of Compressive Strength of Hardened Cylindrical Concrete Specimens," American Society of Testing and Materials International, West Conshohocken, PA., 5 pp.
- ASTM C1240, 2015, "Standard Specification for Silica Fume Used in Cementitious Mixtures," American Society of Testing and Materials International, West Conshohocken, PA., 7 pp.

- ASTM C143, 2015, “Standard Test Method for Slump of Hydraulic-Cement Concrete,” American Society of Testing and Materials International, West Conshohocken, PA., 4 pp.
- ASTM C150, 2018, “Standard Specification for Portland Cement,” American Society of Testing and Materials International, West Conshohocken, PA., 9 pp.
- ASTM C192, 2016, “Standard Practice for Making and Curing Concrete Test Specimens in the Laboratory,” American Society of Testing and Materials International, West Conshohocken, PA., 8 pp.
- ASTM C31, 2018, “Standard Practice for Making and Curing Concrete Test Specimens in the Field,” American Society of Testing and Materials International, West Conshohocken, PA., 6 pp.
- ASTM C39, 2018, “Standard Test Method for Compressive Strength of Cylindrical Concrete Specimens,” American Society of Testing and Materials International, West Conshohocken, PA., 8 pp.
- ASTM C469, 2014, “Standard Test Method for Static Modulus of Elasticity and Poisson’s Ratio of Concrete in Compression,” American Society of Testing and Materials International, West Conshohocken, PA., 5 pp.
- ASTM C470, 2015, “Standard Specification for Molds for Forming Concrete Test Cylinders Vertically,” American Society of Testing and Materials International, West Conshohocken, PA., 5 pp.
- ASTM C496, 2017, “Standard Test Method for Splitting Tensile Strength of Cylindrical Concrete Specimens,” American Society of Testing and Materials International, West Conshohocken, PA., 5 pp.

- ASTM C989, 2018, "Standard Specification for Slag Cement for Use in Concrete and Mortars," American Society of Testing and Materials International, West Conshohocken, PA., 7 pp.
- ASTM E8, 2016, "Standard Test Methods for Tension Testing of Metallic Materials," American Society of Testing and Materials International, West Conshohocken, PA., 30 pp.
- ATC-115, 2014, "Roadmap for the Use of High-Strength Reinforcement in Reinforced Concrete Design," Applied Technology Council, Redwood City, CA., 197 pp.
- Azizinamini, A., Pavel, R., Hatfield, E., and Ghosh, S. K., 1999, "Behavior of Lap-Spliced Reinforcing Bars Embedded in High-Strength Concrete," *ACI Structural Journal*, Vol. 96, No. 5, pp. 826-835.
- Azizinamini, A., Stark, M., Roller, J. J., and Ghosh, S. K., 1993, "Bond Performance of Reinforcing Bars Embedded in High-Strength Concrete," *ACI Structural Journal*, Vol. 90, No. 5, pp. 554-561.
- Canbay, E., and Frosch, R. J., 2005, "Bond Strength of Lap-Spliced Bars," *ACI Structural Journal*, Vol. 102, No. 4, July-Aug., pp. 605-614.
- Chamberlin, S. J., 1958, "Spacing of Spliced Bars in Beams," *ACI Journal, Proceedings*, Vol. 54, No. 8, Feb., pp. 689-697.
- Chinn, J., Ferguson, P. M., and Thompson, J. N., 1955, "Lapped Splices in Reinforced Concrete Beams," *ACI Journal, Proceedings*, Vol. 52, No. 10, Oct., pp. 201-213.
- Clemeña, G. G., and Virmani, Y. P., 2004, "Comparing the Chloride Resistance of Reinforcing Bars," *Concrete International*, Vol. 25, No. 11, pp. 39-49.
- Darwin, D., Browning, J. P., Nguyen, T. V., Locke, C. E., 2002, "Mechanical and Corrosion Properties of a High-Strength, High Chromium Reinforcing Steel for Concrete," *SM Report* No. 66, University of Kansas Center for Research, Lawrence, KS., Mar., 169 pp.

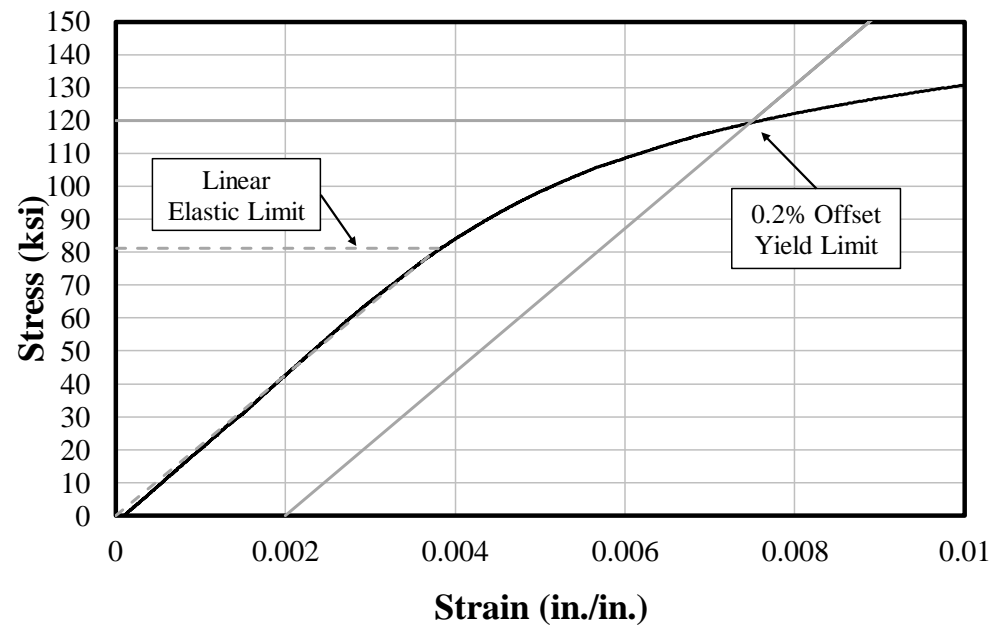
- Darwin, D., McCabe, S. L., Idun, E. K., and Schoenekase, S. P., 1992, "Development Length Criteria: Bars Not Confined by Transverse Reinforcement," *ACI Structural Journal*, Vol. 89, No. 6, Nov.-Dec., pp. 709-720.
- Darwin, D., and Zuo, J., 2002, "Discussion of Proposed Changes to ACI 318 in ACI 318-02 Discussion and Closure," *Concrete International*, Vol. 24, No. 1, Jan., pp. 91-101.
- Darwin, D., Zuo, J., Tholen, M. L., and Idun, E. K., 1996, "Development Length Criteria for Conventional and High Relative Rib Area Reinforcing Bars," *ACI Structural Journal*, Vol. 93, No. 3, May-June, pp. 347-359.
- El-Hacha, R., El-Agroudy, H., and Rizkalla, S. H., 2006, "Bond Characteristics of High-Strength Steel Reinforcement," *ACI Structural Journal*, Vol. 103, No. 6, pp. 771-782.
- Eligehausen, R., Popov, E. P., and Bertero, V. V., 1983, "Local Bond Stress-Slip Relationships of Deformed Bars Under Generalized Excitations," *Report No. UCB/EERC-82/23*, Earthquake Engineering Research Center, University of California at Berkeley, CA., 169 pp.
- Esfahani, M. R., and Vijaya Rangan, B. V., 1998, "Local Bond Strength of Reinforcing Bars in Normal-Strength and High-Strength Concrete (HSC)," *ACI Structural Journal*, Vol. 95, No. 2, Mar.-Apr., pp. 96-106.
- Ferguson, P. M., and Breen, J. E., 1965, "Lapped Splices for High-Strength Reinforcing Bars," *ACI Journal, Proceedings*, Vol. 62, No. 9, Sept., pp. 1063-1078.
- Ferguson, P. M., and Thompson, J. N., 1962, "Development Length for Large High Strength Reinforcing Bars in Bond," *ACI Journal, Proceedings*, Vol. 59, No. 7, July, pp. 887-922.
- Ferguson, P. M., and Thompson, J. N., 1965, "Development Length for Large High Strength Reinforcing Bars," *ACI Journal, Proceedings*, Vol. 62, No. 1, Jan., pp. 71-94.

- Glucksman, R., 2018, “Bond Strength of ASTM A615 Grade 100 Reinforcement for Beams,” Master’s Thesis, Lyles School of Civil Engineering, Purdue University, West Lafayette, IN., 226 pp.
- Hibbeler, R. C., 2011, “Mechanics of Materials,” 8th Ed., *Pearson Prentice Hall*, Upper Saddle River, NJ., 695 pp.
- Hognestad, E., 1951, “A Study of Combined Bending and Axial Load in Reinforced Concrete Members,” *University of Illinois Bulletin Series*, No. 399, The University of Illinois, Urbana-Champaign, IL., 128 pp.
- Hognestad, E., 1962, “High-Strength Bars as Concrete Reinforcement - Part 2: Flexural Cracking,” *Journal, PCA Research and Development Laboratories*, Vol. 4, No. 1, pp. 46-63.
- Hosny, A., Seliem, H. M., Rizkalla, S. H., and Zia, P., 2012, “Development Length of Unconfined Conventional and High-Strength Steel Reinforcing Bars,” *ACI Structural Journal*, Vol. 109, No. 5, Sept.-Oct., pp. 655-664.
- Jirsa, J. O., and Breen, J. E., 1981, “Influence of Casting Position and Shear on Development and Splice Length - Design Recommendation,” *Research Report* No. 242-3F, Center for Transportation Research, The University of Texas at Austin, Austin, TX., 51 pp.
- Johnston, D. W., and Zia, P., 1982, “Bond Characteristics of Epoxy-Coated Reinforcing Bars,” *Report* No. FHWA/NC/82-002, Department of Civil Engineering, North Carolina State University, Raleigh, NC., Aug., 176 pp.
- Kluge, R. W., and Tuma, E. C., 1945, “Lapped Bar Slices in Concrete Beams,” *ACI Journal, Proceedings*, Vol. 42, Sept., pp. 13-33.
- Kosmatka, S. H., Kerkhoff B., and Panarese, W. C., 2017, “Design and Control of Concrete Mixtures,” 14th Ed., EB001, Portland Cement Association, Skokie, IL., 358 pp.

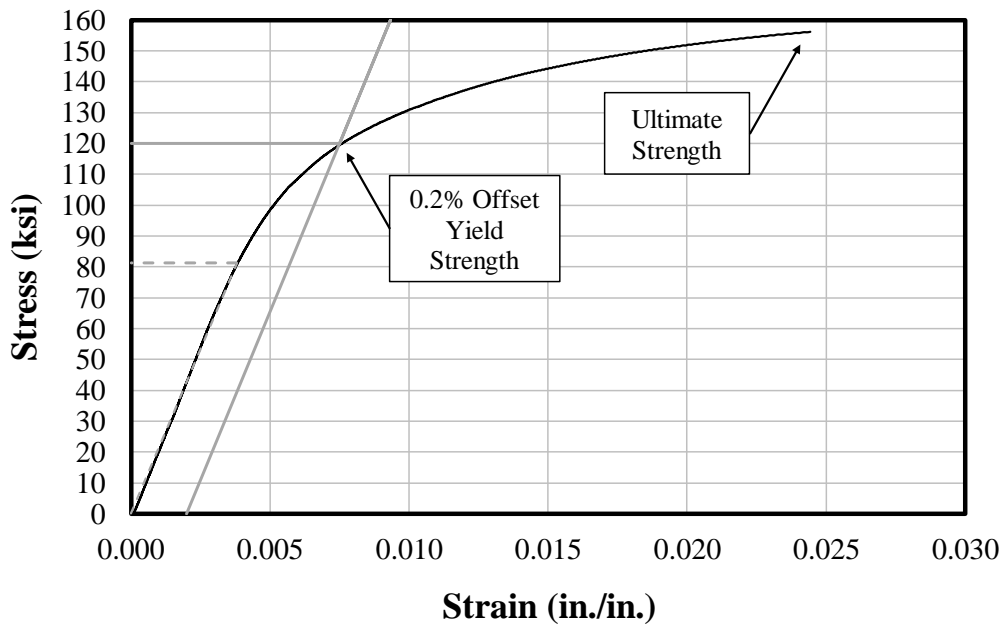
- Lutz, L. A., and Gergely, P., 1967, "Mechanics of Bond and Slip of Deformed Bars in Concrete," ACI Journal, *Proceedings*, Vol. 64, No. 11, Nov., pp. 711-721.
- Mathey, R., and Watstein, D., 1961, "Investigation of Bond in Beam and Pull-Out Specimens with High-Yield-Strength Deformed Bars," ACI Journal, *Proceedings*, Vol. 58, No. 9, Mar., pp. 1071-1090.
- McCormac, J. C., and Brown, R. H., 2016, "Design of Reinforced Concrete," 10th Ed., Wiley, Hoboken, NJ., 672 pp.
- Miller, Mark A., 2012, "Section 900 - Materials Details," *Standard Specifications*, Indiana Department of Transportation, Indianapolis, IN., pp. 784-1039.
- Morita, S., and Fujii, S., 1982, "Bond Capacity of Deformed Bars Due to Splitting of Surrounding Concrete," *Proceedings of the International Conference on Bond in Concrete*, Scotland, June 14-16., Applied Science Publishers, London, U.K., pp. 331-341.
- Orangun, C. O., Jirsa, J. O., and Breen, J. E., 1977, "Reevaluation of Test Data on Development Length and Splices," ACI Journal, *Proceedings*, Vol. 74, No. 3, Mar., pp. 114-122.
- Pay, A. C., 2005, "Bond Behavior of Unconfined Steel and Fiber Reinforced Polymer (FRP) Bar Splices in Concrete Beams," Ph.D. Dissertation, Lyles School of Civil Engineering, Purdue University, West Lafayette, IN., 313 pp.
- Rezansoff, T., Konkankar, U. S., and Fu, Y. C., 1992, "Confinement Limits for Tension Lap Splices under Static Loading," *Canadian Journal of Civil Engineering*, Vol. 19, No. 3, pp. 447-453.
- Richter, B. P., 2012, "A New Perspective on the Tensile Strength of Lap Splices in Reinforced Concrete Members," Master's Thesis, Lyle's School of Civil Engineering, Purdue University, West Lafayette, IN., 165 pp.

- Seliem, H. M., Hosny, A., Rizkalla, S., Zia, P., Briggs, M., Miller, S., Darwin, D., Browning, J., Glass, G. M., Hoyt, K., Donnelly, K., and Jirsa, J. O., 2009, "Bond Characteristics of ASTM A1035 Steel Reinforcing Bars," *ACI Structural Journal*, Vol. 106, No. 4, July-Aug., pp. 530-539.
- Sim, C., 2014, "Structural and Corrosion Performance of Concrete Bridge Decks Reinforced with Corrosion-Resistant Reinforcing Steel," Ph.D. Dissertation, Lyles School of Civil Engineering, Purdue University, West Lafayette, IN., 563 pp.
- Tepfers, R., 1973, "A Theory of Bond Applied to Overlapping Tensile Reinforcement Splices for Deformed Bars," *Publication 73:2*, Division of Concrete Structures, Chalmers University of Technology, Goteborg, Sweden, 328 pp.
- Thompson, M. A., Jirsa, J. O., Breen, J. E., and Meinheit, D. F., 1975, "The Behavior of Multiple Lap Splices in Wide Sections," *Research Report No. 154-1*, Center for Highway Research, The University of Texas at Austin, Austin, TX., Feb., 75 pp.
- Treece, R. A., and Jirsa, J. O., 1989, "Bond Strength of Epoxy-Coated Reinforcing Bars," *ACI Materials Journal*, Vol. 86, No. 2, Mar.-Apr., pp. 167-174.
- Trejo, D., Monteiro, P. J., Thomas, G., and Wang, X., 1994, "Mechanical Properties and Corrosion Susceptibility of Dual-Phase Steel in Concrete," *Cement and Concrete Research*, Vol. 24, No. 7, pp. 1245-1254.
- Zuo, J., and Darwin, D., 1998, "Bond Strength of High Relative Rib Area Reinforcing Bars," *SM Report No. 46*, University of Kansas Center for Research, Lawrence, KS., 350 pp.
- Zuo, J., and Darwin, D., 2000, "Splice Strength of Conventional and High Relative Rib Area Bars in Normal and High-Strength Concrete," *ACI Structural Journal*, Vol. 97, No. 4, July-Aug., pp. 630-641.

APPENDIX A. STEEL STRESS-STRAIN CURVES

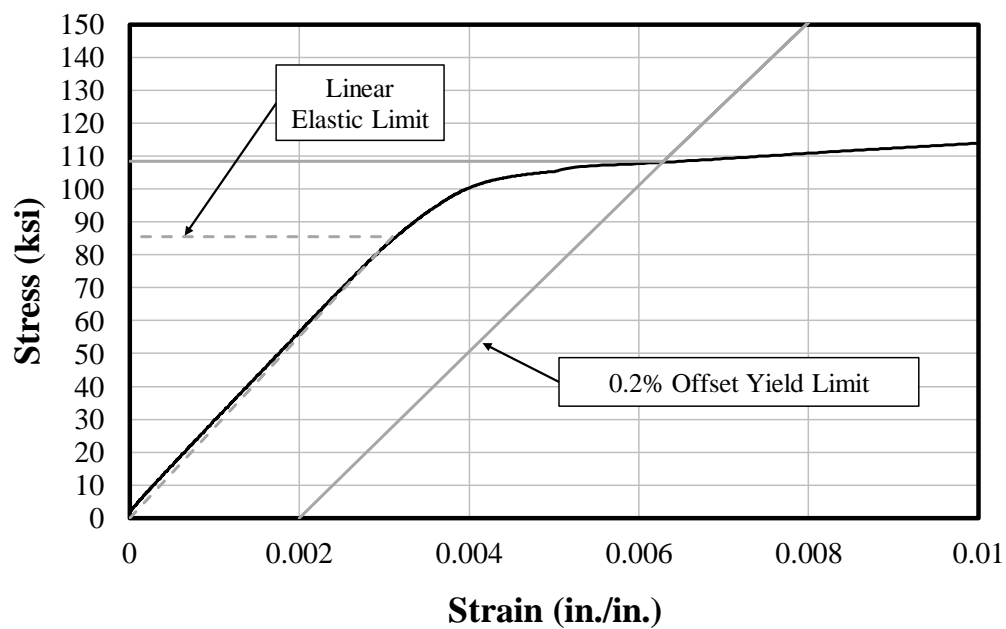


(a) Initial Behavior Limits

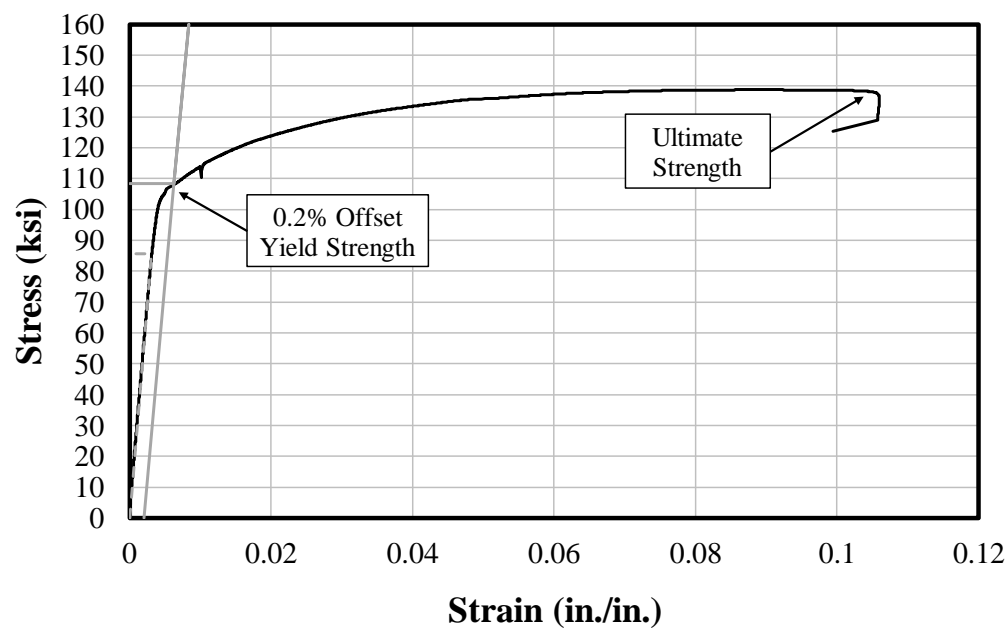


(b) Full Behavior

Figure A.1: A1035 Gr. 100 No. 8 Longitudinal Bar (MMFX) Stress Strain Curve

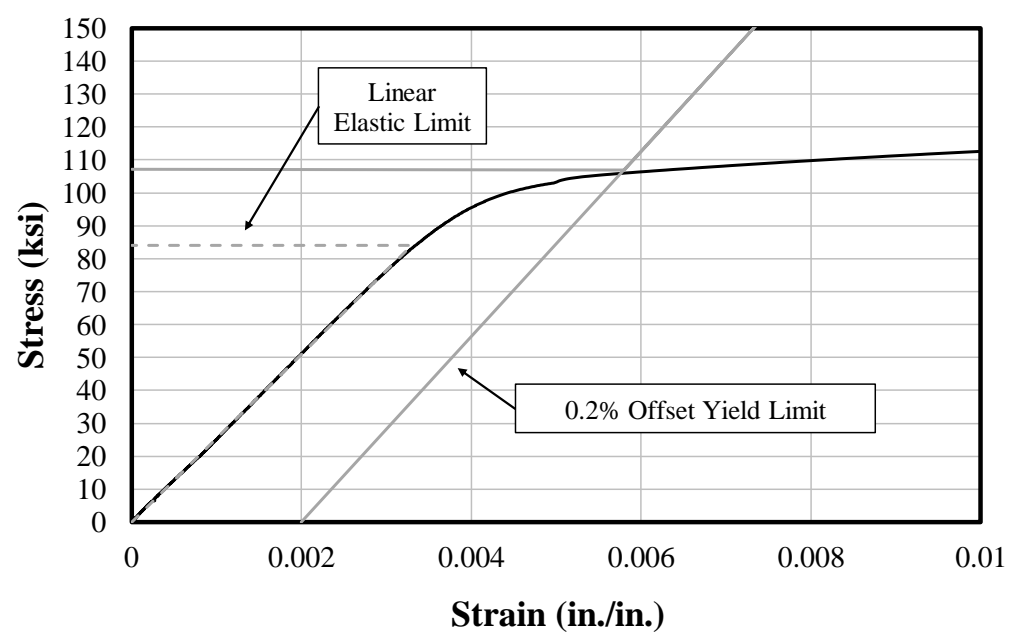


(a) Initial Behavior Limits

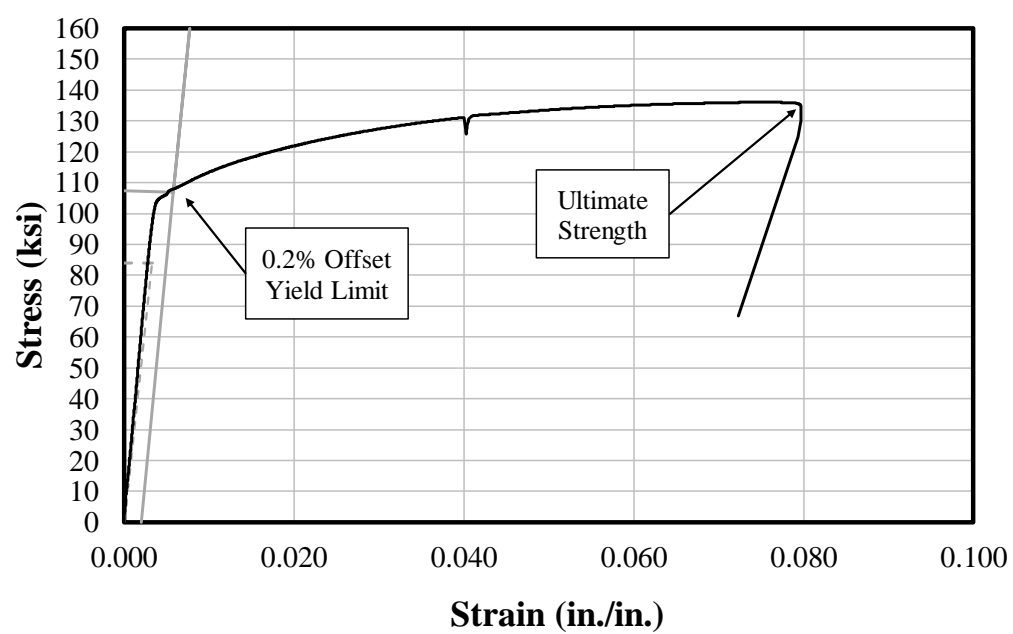


(b) Full Behavior

Figure A.2: A615 Gr. 100 No. 8 Longitudinal Bar - Stress Strain Curve

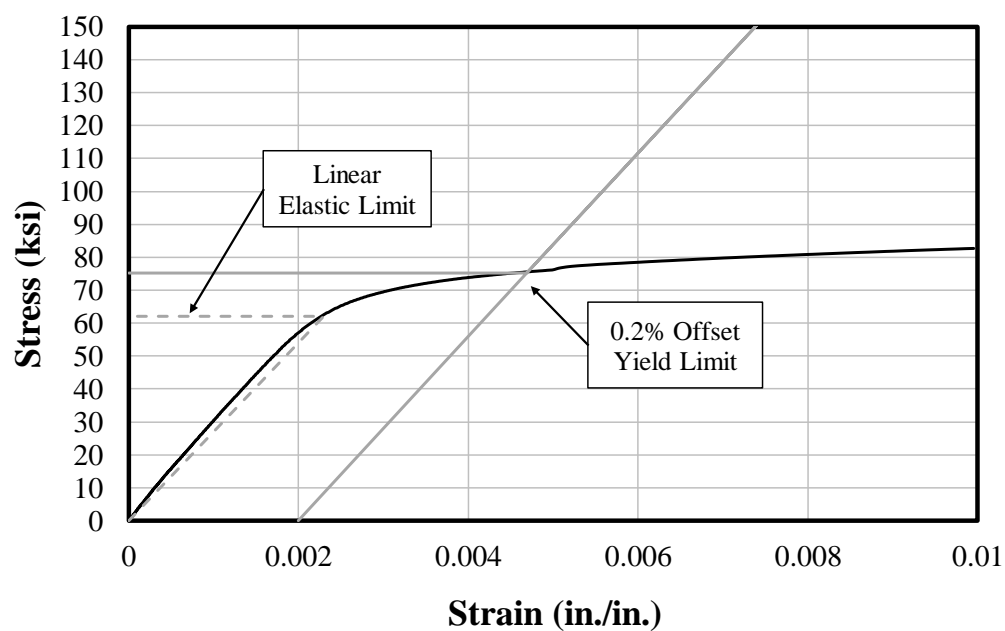


(a) Initial Behavior Limits

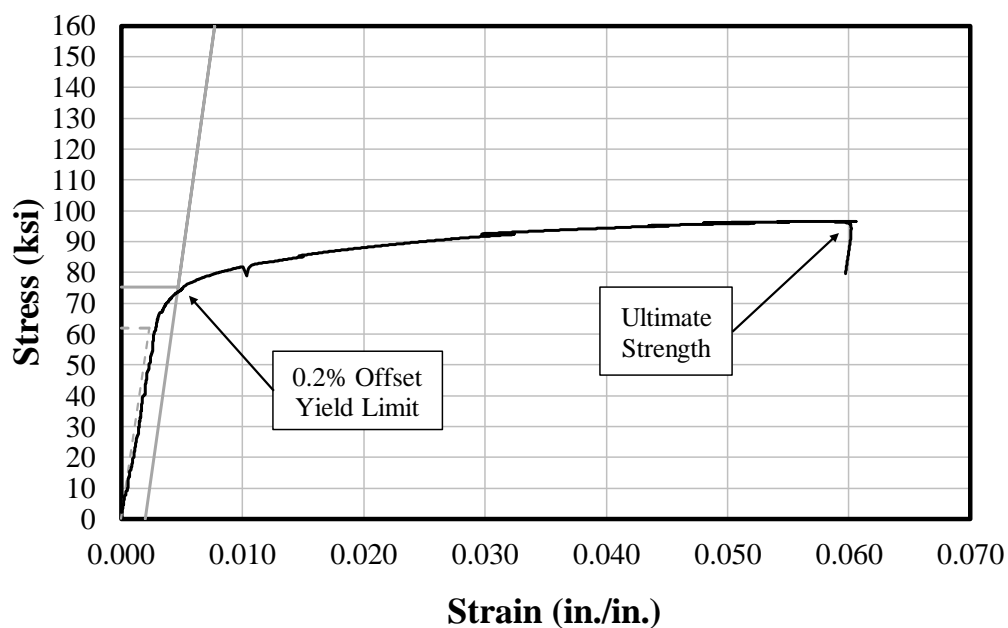


(b) Full Behavior

Figure A.3: A615 Gr. 100 No. 5 Longitudinal Bar - Stress Strain Curve



(a) Initial Behavior Limits



(b) Full Behavior

Figure A.4: A615 Gr. 60 No. 3 Transverse Bar (Series VI) - Stress Strain Curve

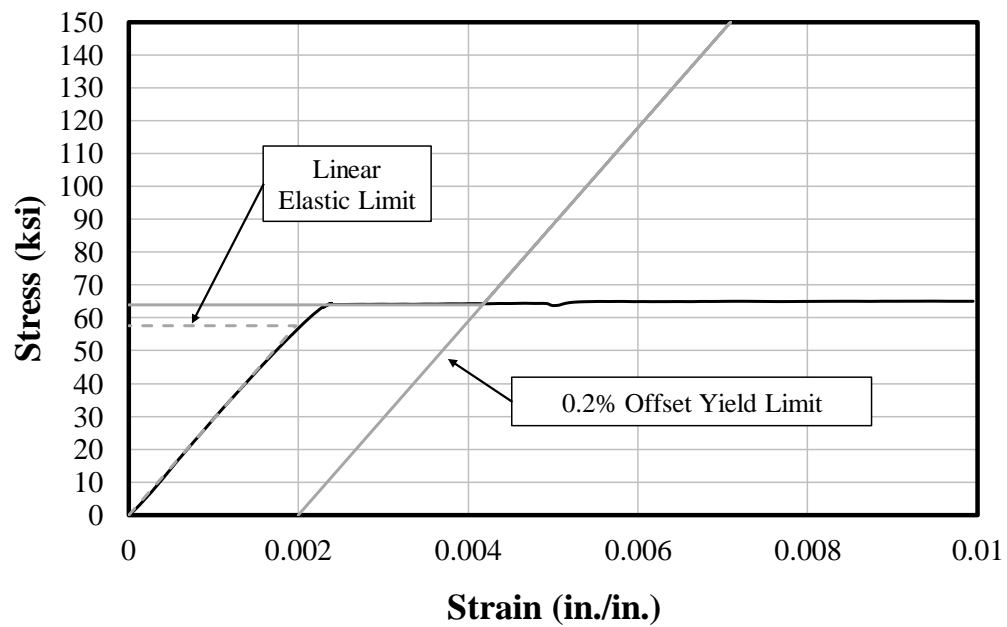


Figure A.5: A615 Gr. 60 No. 3 Transverse Bar (Series VII) - Stress Strain Curve

Note: Full stress-strain behavior was not measured due to a broken break-away extensometer during coupon testing. Post-processed data indicates an ultimate strength of 98 ksi after typical stress-strain behavior up to failure, similar to Figure A.4(b).

APPENDIX B. SLAB CONSTRUCTION AS-BUILT DIMENSIONS

Dimensions were measured for all slabs after failure at the locations shown in Figure B.1. The total slab width b_w accounts for four (4) splices of No. 5 bars, or 5 in. Bottom cover is measured between the two inner splices for the south, middle, and north locations. Percent error values indicate comparisons between the measured values and the original design values specified in Table B.1.

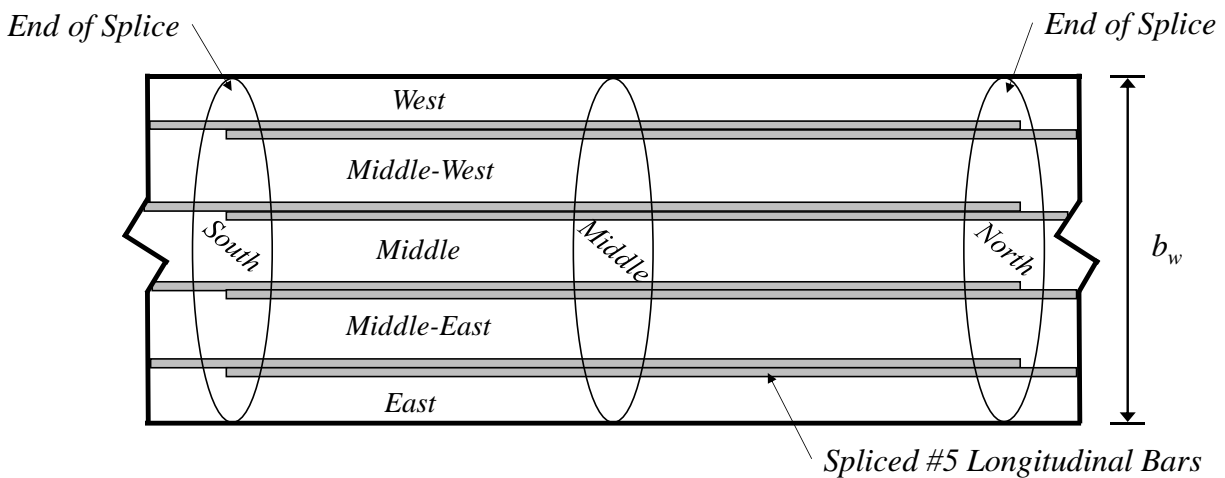


Figure B.1: Slab Splice Region Layout for As-Built Dimensions

Table B.1: Slab Design Dimensions

Location Along Width	Design Value (in.)
West	2-3/8
Middle-West	4-3/4
Middle	4-3/4
Middle-East	4-3/4
East	2-3/8
Total (b_w)	24
Bottom Cover (c_b)	3/4

Table B.2: S-40-5

Transverse Location	Longitudinal Location					
	South (in.)	% Error	Middle (in.)	% Error	North (in.)	% Error
West	2.464	3.7%	1.872	-21.2%	1.875	-21.1%
Middle-West	5.829	22.7%	5.106	7.5%	5.553	16.9%
Middle	6.423	35.2%	5.838	22.9%	6.813	43.4%
Middle-East	4.958	4.4%	4.263	-10.3%	4.628	-2.6%
East	1.969	-17.1%	2.177	-8.3%	2.935	23.6%
Total	26.643	11.0%	24.256	1.1%	26.804	11.7%
Bottom Cover	0.789	5.2%	0.786	4.8%	0.824	9.9%

Table B.3: S-60-5

Transverse Location	Longitudinal Location					
	South (in.)	% Error	Middle (in.)	% Error	North (in.)	% Error
West	2.115	-10.9%	2.078	-12.5%	2.026	-14.7%
Middle-West	4.759	0.2%	4.985	4.9%	5.210	9.7%
Middle	5.481	15.4%	5.156	8.5%	4.863	2.4%
Middle-East	4.867	2.5%	4.841	1.9%	4.731	-0.4%
East	2.011	-15.3%	1.989	-16.3%	2.434	2.5%
Total	24.233	1.0%	24.049	0.2%	24.264	1.1%
Bottom Cover	0.759	1.2%	.777	3.6%	.893	19.1%

Table B.4: S-80-5

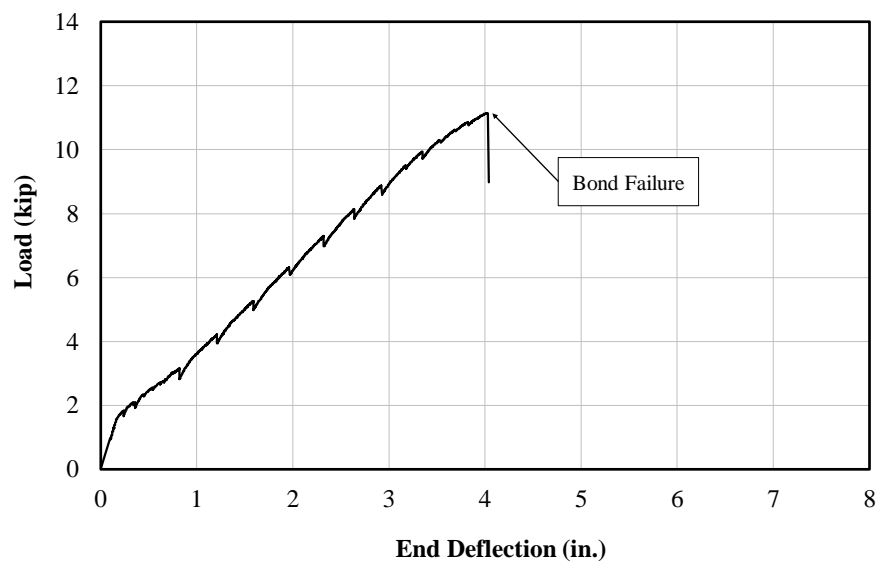
Transverse Location	Longitudinal Location					
	South (in.)	% Error	Middle (in.)	% Error	North (in.)	% Error
West	2.370	-0.2%	2.344	-1.3%	2.715	14.3%
Middle-West	4.917	3.5%	4.927	3.7%	5.076	6.9%
Middle	4.762	0.2%	4.904	3.2%	5.098	7.3%
Middle-East	5.014	5.5%	4.768	0.4%	4.651	-2.1%
East	1.998	-15.9%	1.783	-24.9%	1.834	-22.8%
Total	24.059	0.2%	23.724	-1.2%	24.373	1.6%
Bottom Cover	0.744	-0.8%	0.804	7.1%	0.787	4.9%

Table B.5: S-100-5

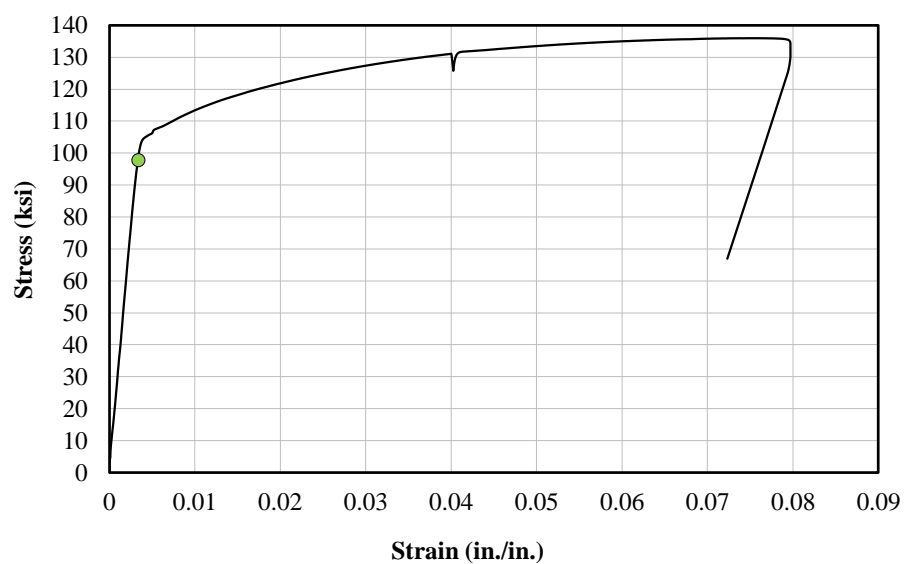
Transverse Location	Longitudinal Location					
	South (in.)	% Error	Middle (in.)	% Error	North (in.)	% Error
West	0.916	-61.4%	1.840	-22.5%	2.395	0.8%
Middle-West	4.921	3.6%	4.659	-1.9%	4.424	-6.9%
Middle	4.933	3.9%	5.234	10.2%	5.470	15.2%
Middle-East	5.284	11.2%	4.998	5.2%	4.573	-3.7%
East	2.719	14.5%	2.261	-4.8%	2.112	-11.1%
Total	23.773	-0.9%	23.992	0.0%	23.973	-0.1%
Bottom Cover	0.732	-2.4%	0.767	2.3%	0.790	5.3%

APPENDIX C. LOAD DEFLECTION CURVES

Load-deflection responses are constructed from end load and end deflection data for all specimens in this testing program. All load and deflection values are averages of the north and south ends, unless noted otherwise. The stress-strain response for the longitudinal steel in each specimen is provided to give an indication of longitudinal steel behavior at failure. Maximum load, maximum midspan deflection, maximum end deflection, and bar stress at failure are also provided for each specimen.



(a) Load-Deflection*



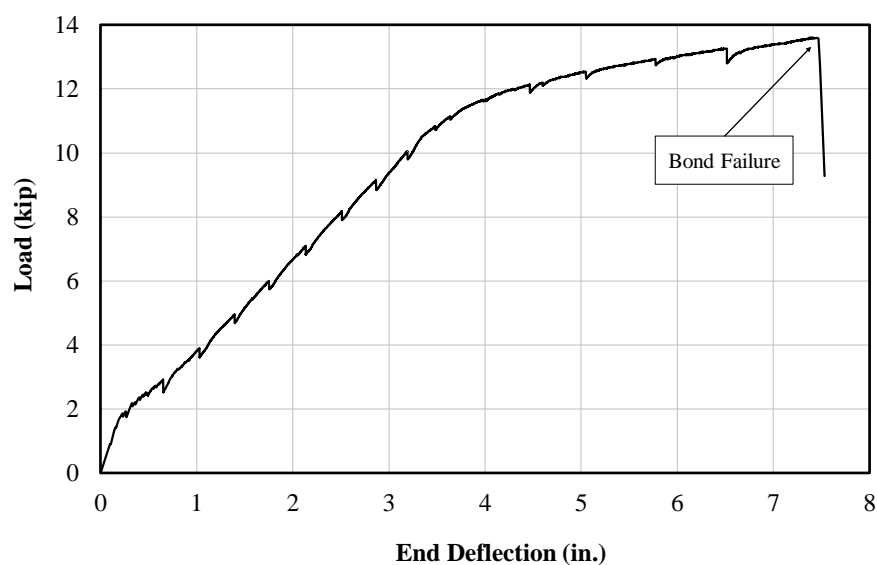
(b) Stress-Strain (A615 Gr. 100 No. 5)

Figure C.1: S-40-5

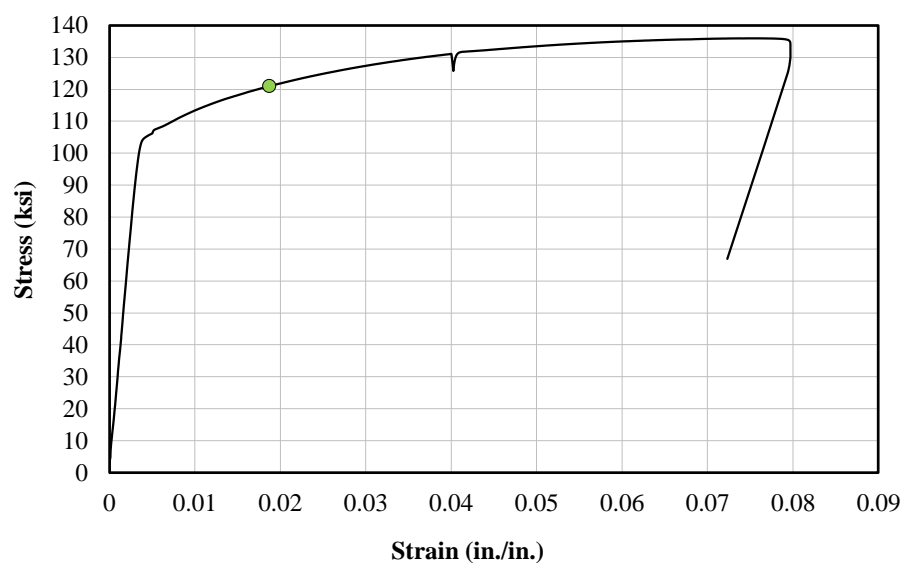
*Response reflects the south end deflection and twice the southeast load cell reading.

Table C.1: S-40-5 Maximum Testing Values

Load (kip)	Avg. End Deflection (in.)	Avg. Midspan Deflection (in.)	Bar Stress (ksi)
11.1	4.0	2.2	97.9



(a) Load-Deflection*



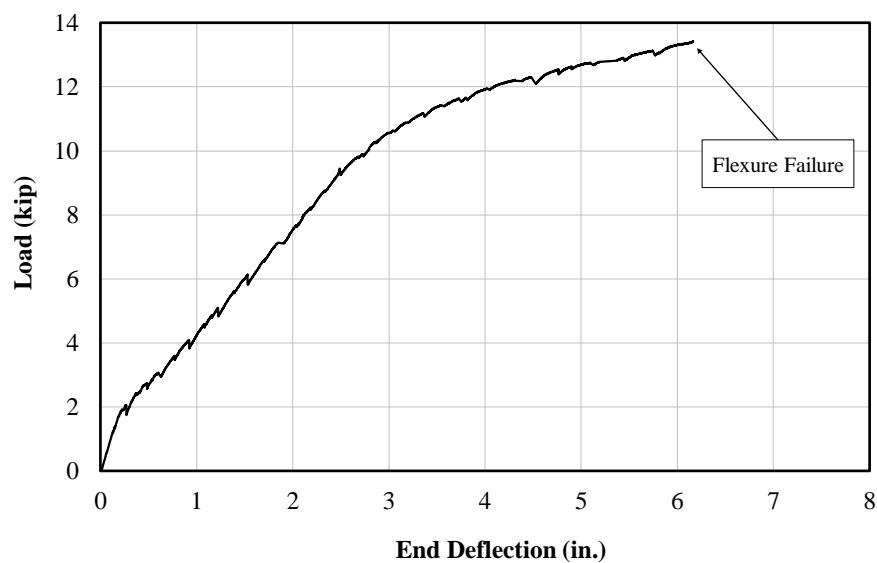
(b) Stress-Strain (A615 Gr. 100 No. 5)

Figure C.2: S-60-5

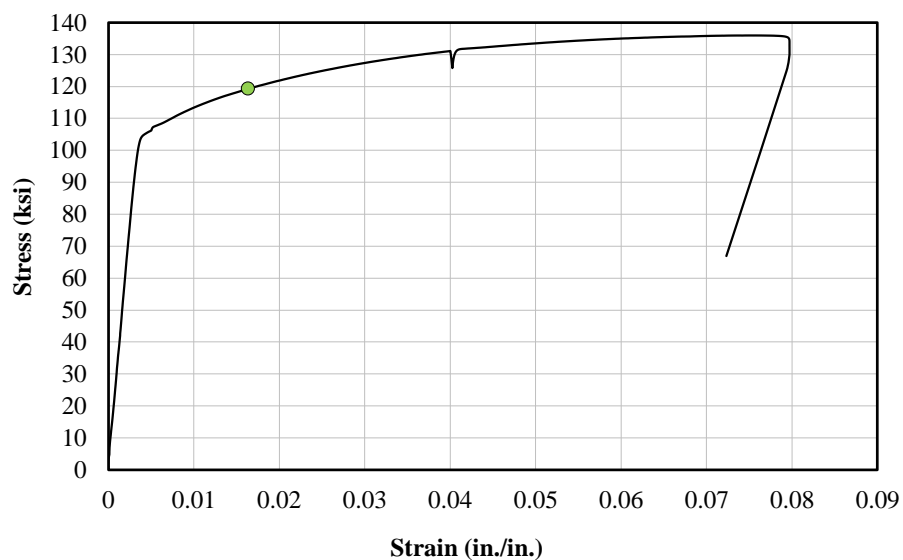
*Response reflects the north end deflection and twice the northwest load cell reading.

Table C.2: S-60-5 Maximum Testing Values

Load (kip)	Avg. End Deflection (in.)	Avg. Midspan Deflection (in.)	Bar Stress (ksi)
13.6	7.5	3.7	121.0



(a) Load-Deflection*



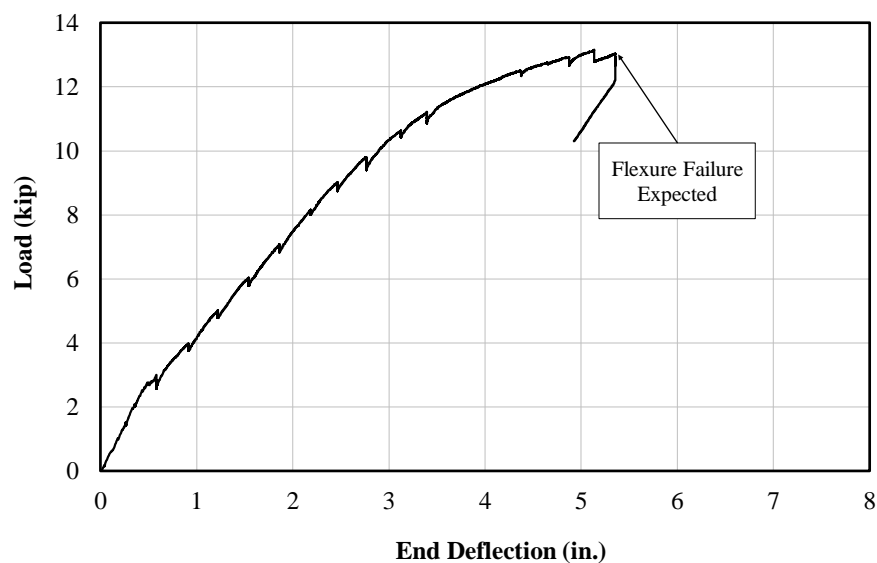
(b) Stress-Strain (A615 Gr. 100 No. 5)

Figure C.3: S-80-5

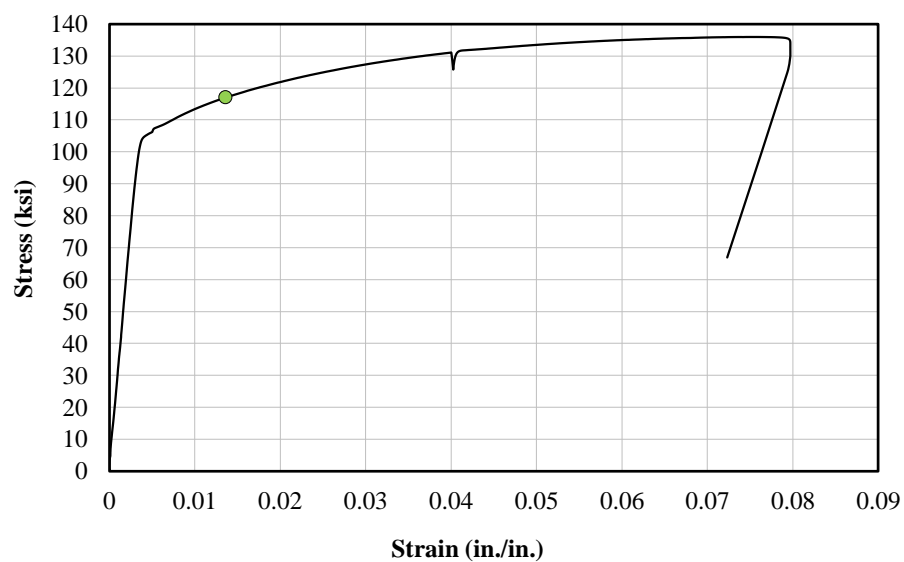
*Response reflects the south end deflection and twice the southwest load cell reading.

Table C.3: S-80-5 Maximum Testing Values

Load (kip)	Avg. End Deflection (in.)	Avg. Midspan Deflection (in.)	Bar Stress (ksi)
13.4	6.2	2.9	119.2



(a) Load-Deflection*



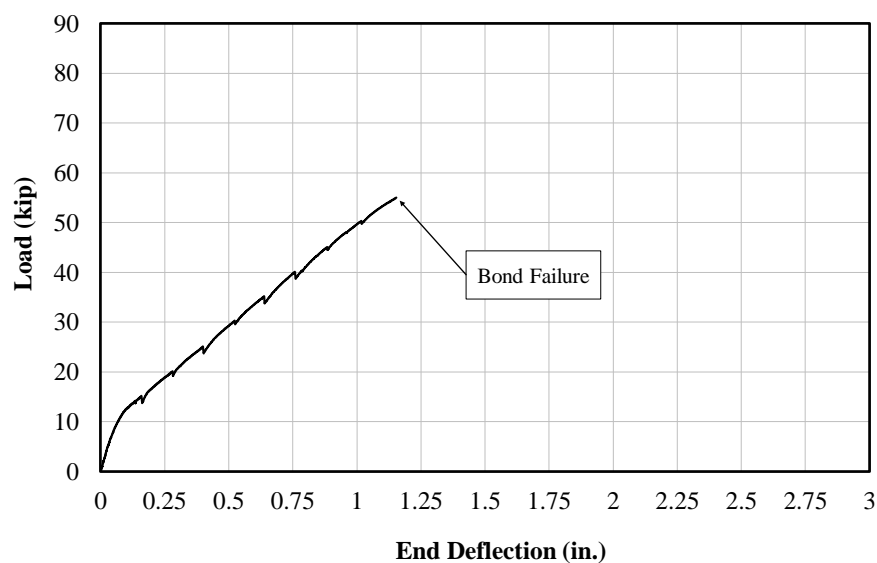
(b) Stress-Strain (A615 Gr. 100 No. 5)

Figure C.4: S-100-5

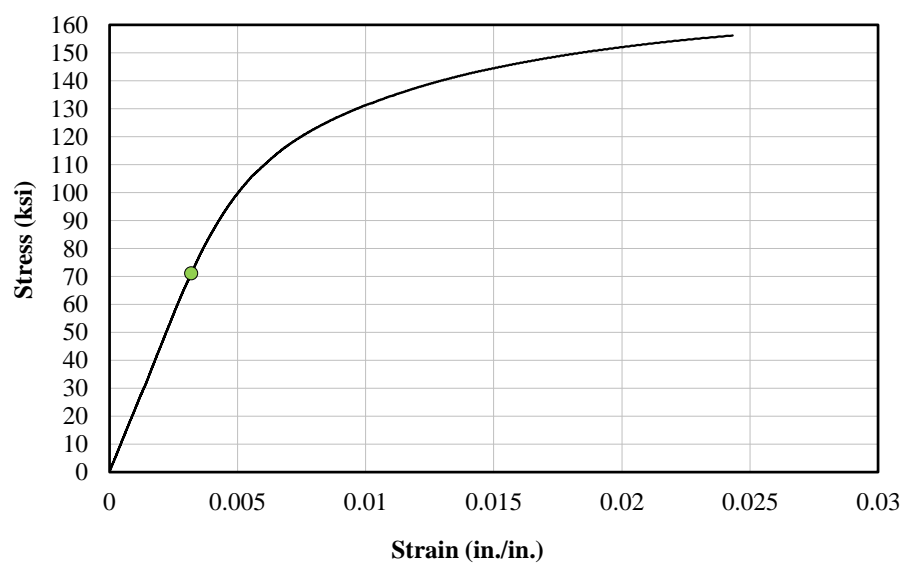
*Response reflects the south end deflection and twice the southwest load cell reading.

Table C.4: S-100-5 Maximum Testing Values

Load (kip)	Avg. End Deflection (in.)	Avg. Midspan Deflection (in.)	Bar Stress (ksi)
13.2	5.4	2.2	117.0



(a) Load-Deflection

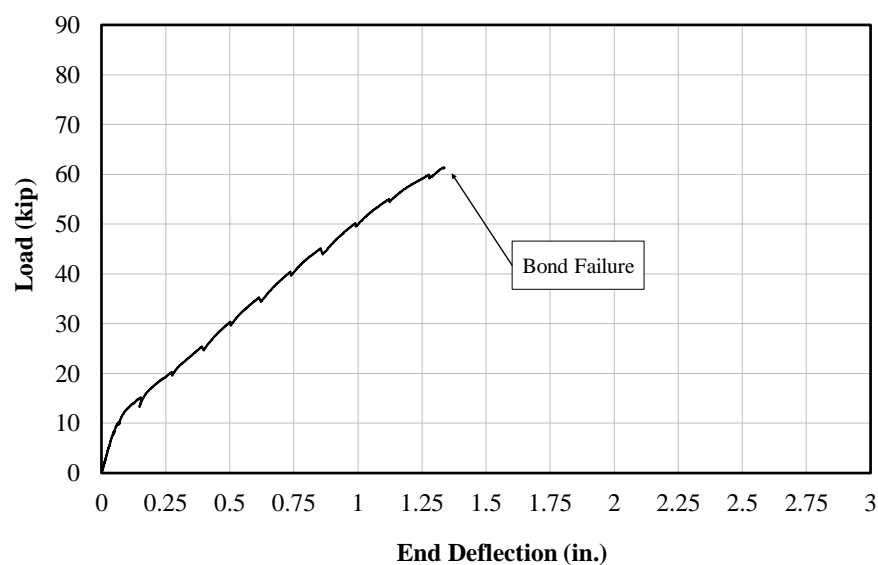


(b) Stress-Strain (A1035 Gr. 100 No. 8)

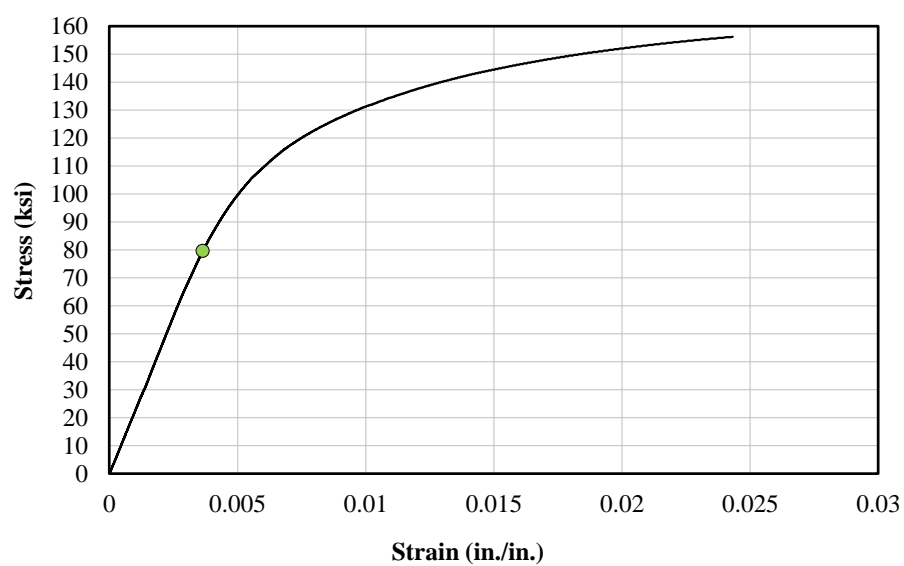
Figure C.5: U-40-5-X

Table C.5: U-40-5-X Maximum Testing Values

Load (kip)	Avg. End Deflection (in.)	Avg. Midspan Deflection (in.)	Bar Stress (ksi)
55.0	1.2	0.9	71.0



(a) Load-Deflection

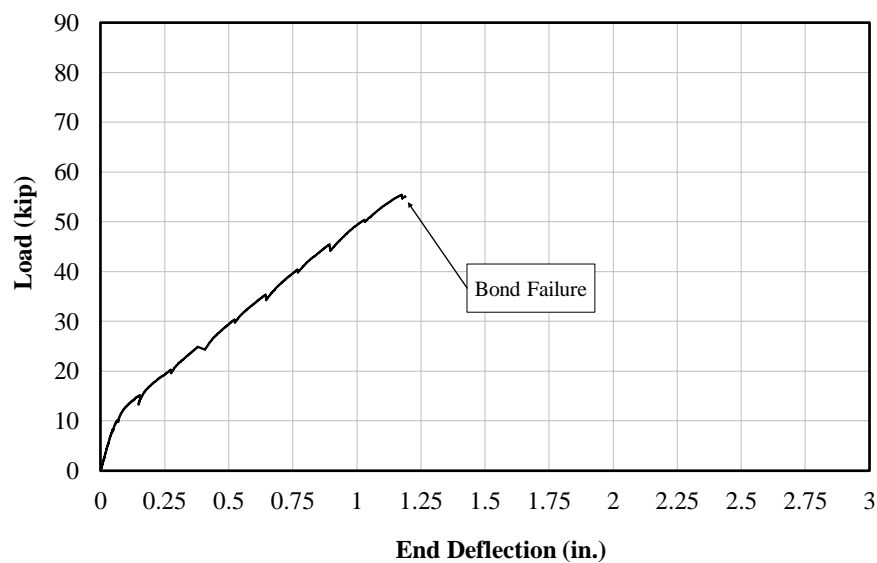


(b) Stress-Strain (A1035 Gr. 100 No. 8)

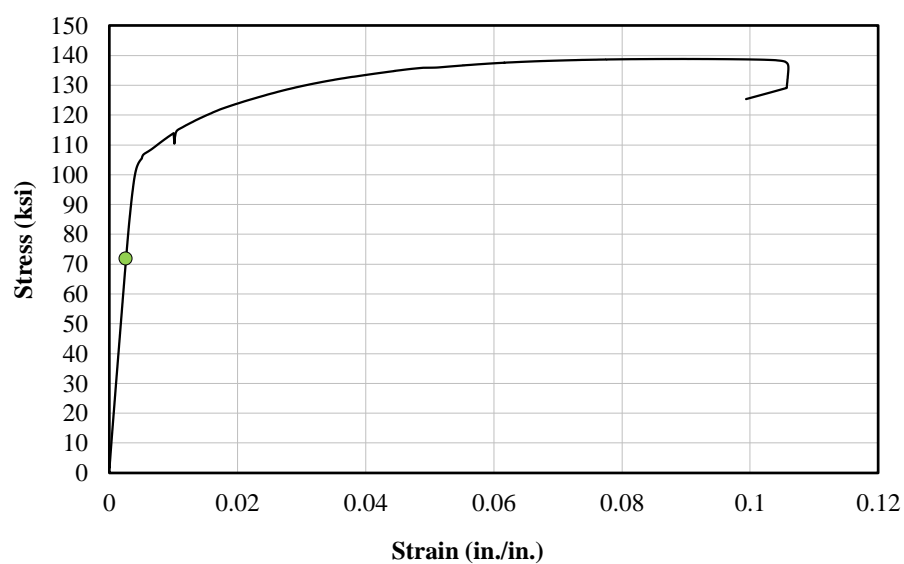
Figure C.6: U-60-5-X

Table C.6: U-60-5-X Maximum Testing Values

Load (kip)	Avg. End Deflection (in.)	Avg. Midspan Deflection (in.)	Bar Stress (ksi)
61.4	1.3	1.1	79.6



(a) Load-Deflection

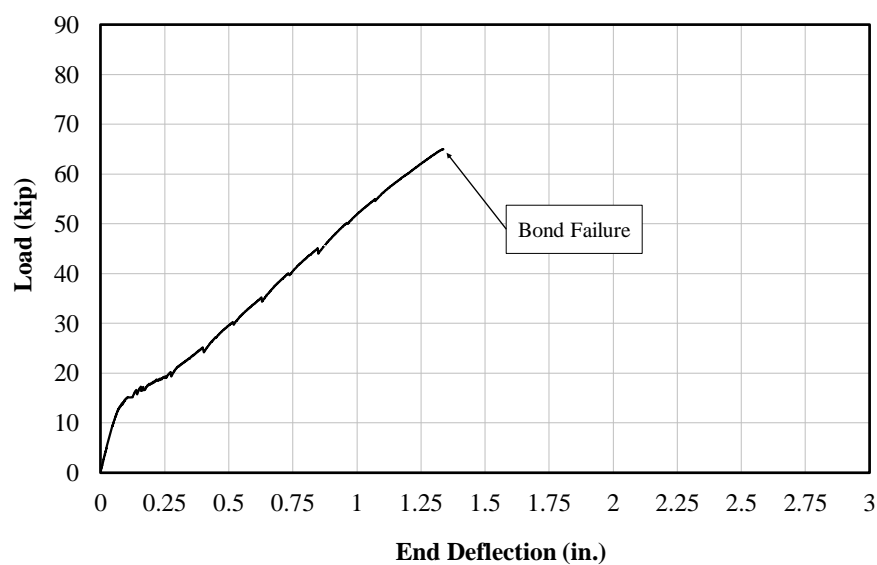


(b) Stress-Strain (A615 Gr. 100 No. 8)

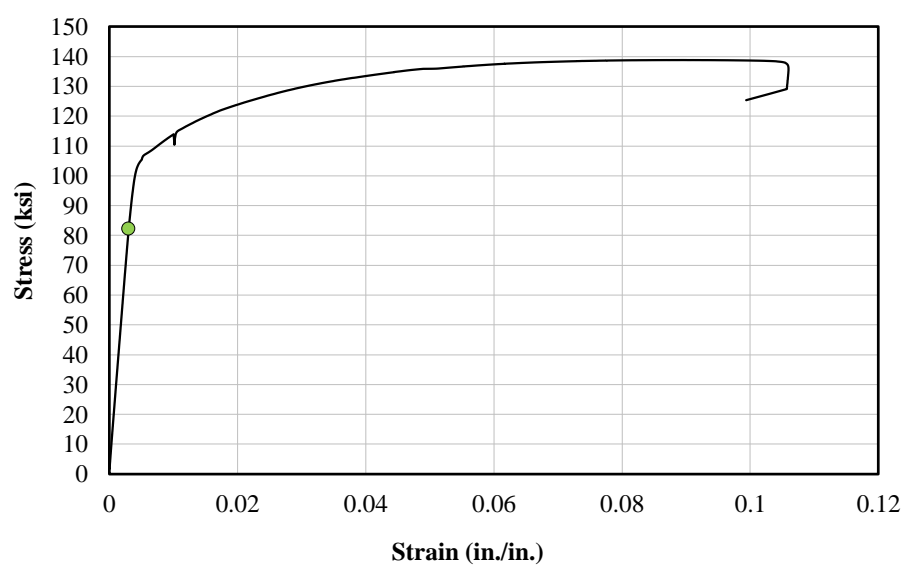
Figure C.7: U-50-5

Table C.7: U-50-5 Maximum Testing Values

Load (kip)	Avg. End Deflection (in.)	Avg. Midspan Deflection (in.)	Bar Stress (ksi)
55.5	1.2	1.0	71.8



(a) Load-Deflection

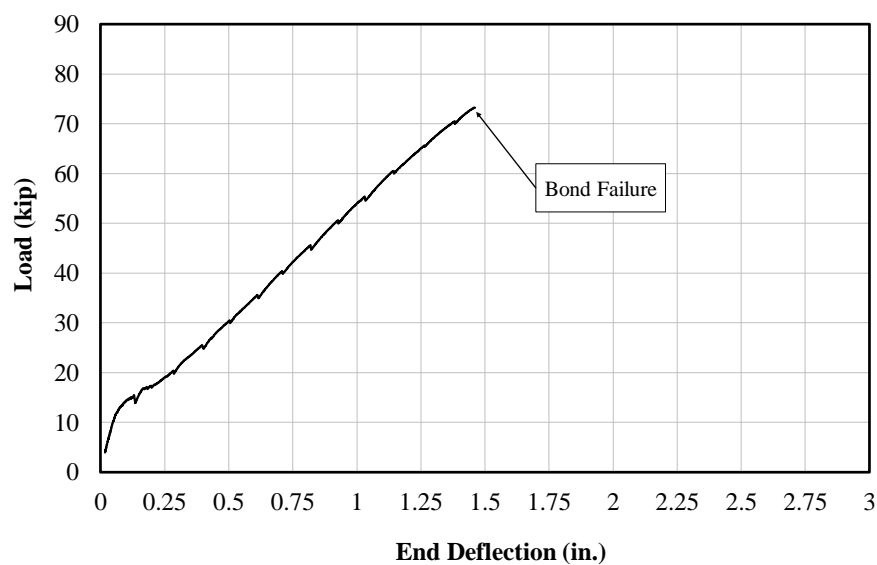


(b) Stress-Strain (A615 Gr. 100 No. 8)

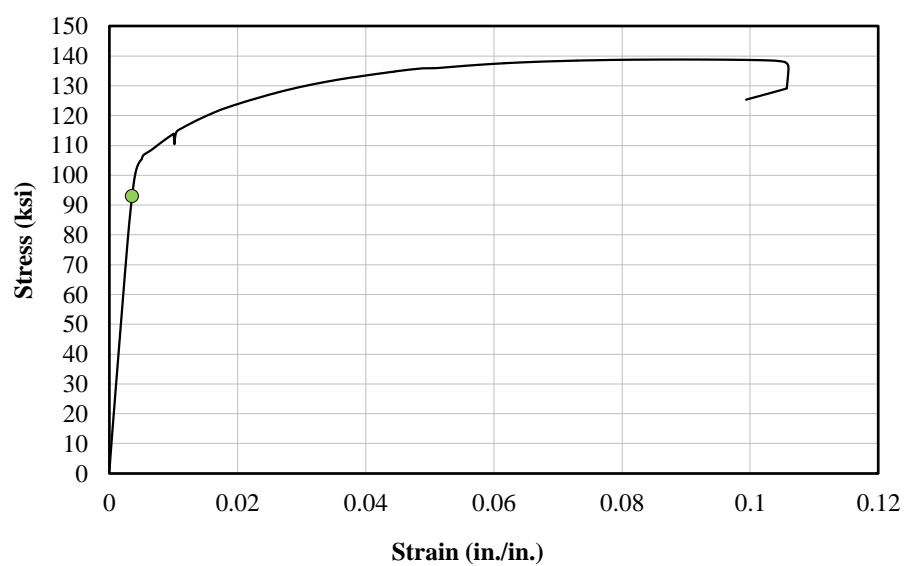
Figure C.8: U-40-10

Table C.8: U-40-10 Maximum Testing Values

Load (kip)	Avg. End Deflection (in.)	Avg. Midspan Deflection (in.)	Bar Stress (ksi)
65.0	1.3	1.0	82.3



(a) Load-Deflection



(b) Stress-Strain (A615 Gr. 100 No. 8)

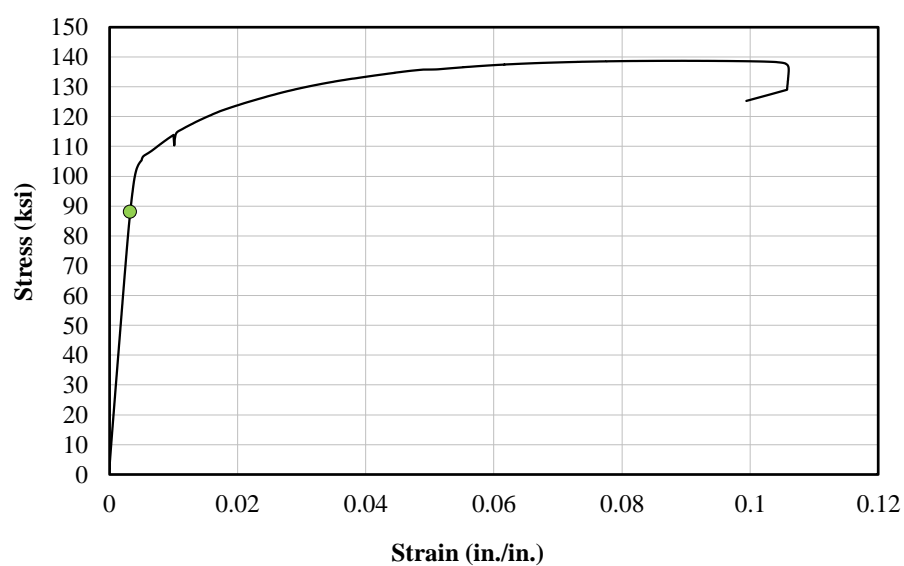
Figure C.9: U-60-10

Table C.9: U-60-10 Maximum Testing Values

Load (kip)	Avg. End Deflection (in.)	Avg. Midspan Deflection (in.)	Bar Stress (ksi)
73.2	1.5	0.9	92.9



(a) Load-Deflection

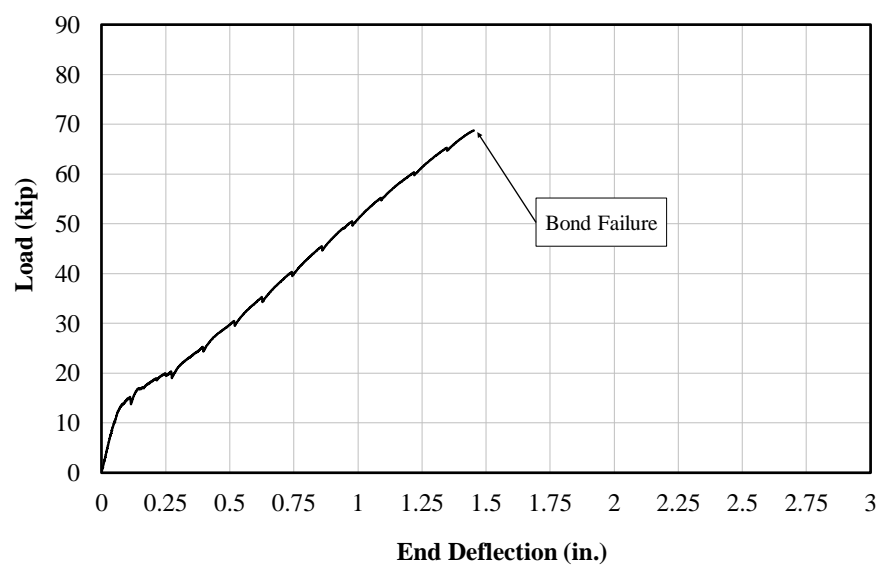


(b) Stress-Strain (A615 Gr. 100 No. 8)

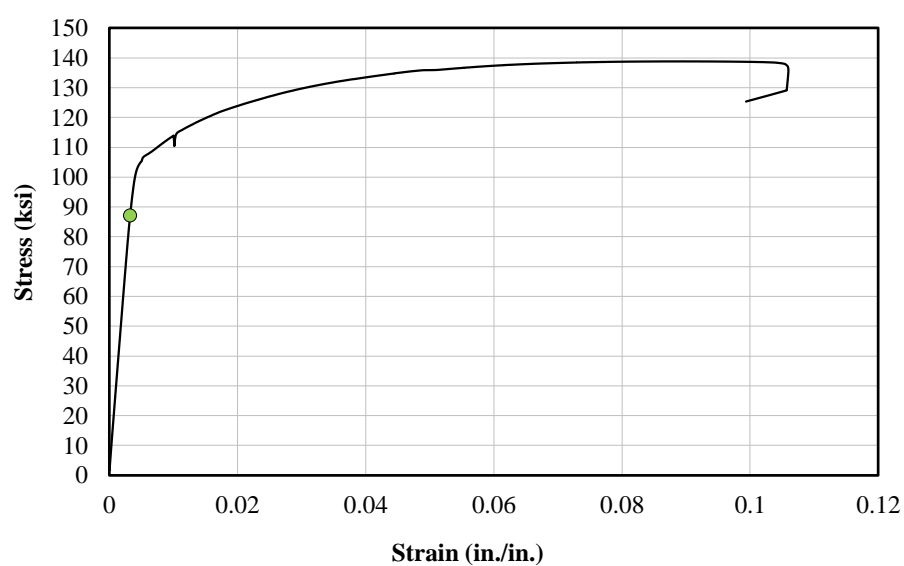
Figure C.10: C3/60/2-40-10-25

Table C.10: C3/60/2-40-10-25 Maximum Testing Values

Load (kip)	Avg. End Deflection (in.)	Avg. Midspan Deflection (in.)	Bar Stress (ksi)
69.5	1.5	1.1	88.1



(a) Load-Deflection

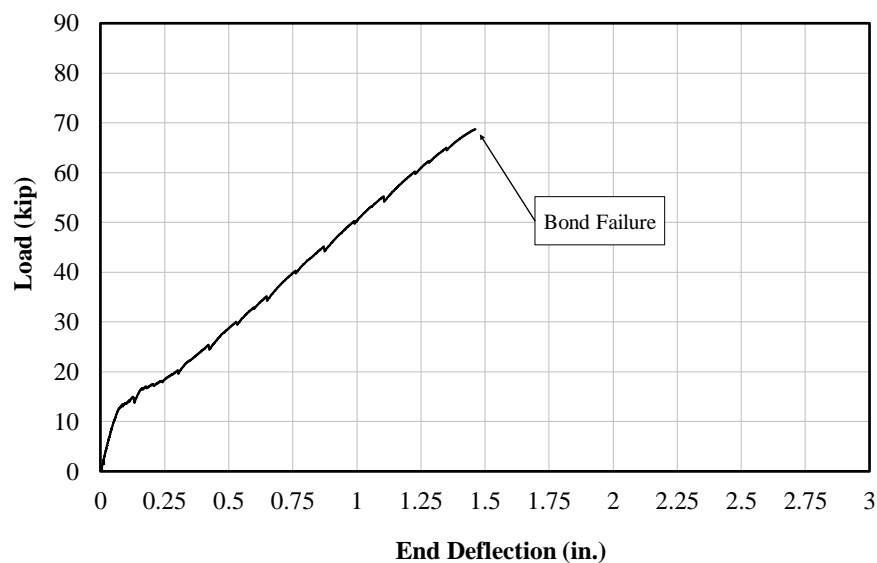


(b) Stress-Strain (A615 Gr. 100 No. 8)

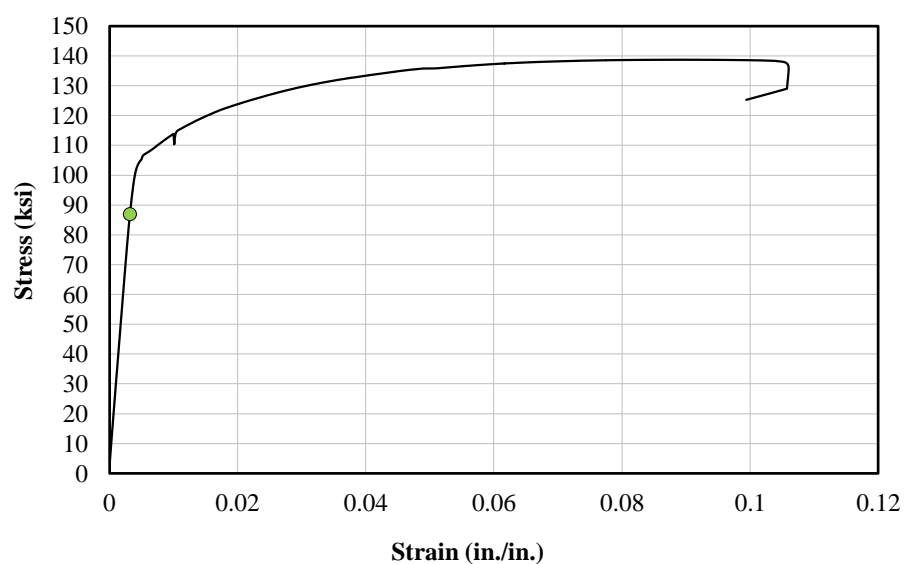
Figure C.11: C3/60/2-40-10-50

Table C.11: C3/60/2-40-10-50 Maximum Testing Values

Load (kip)	Avg. End Deflection (in.)	Avg. Midspan Deflection (in.)	Bar Stress (ksi)
68.8	1.5	1.1	87.1



(a) Load-Deflection

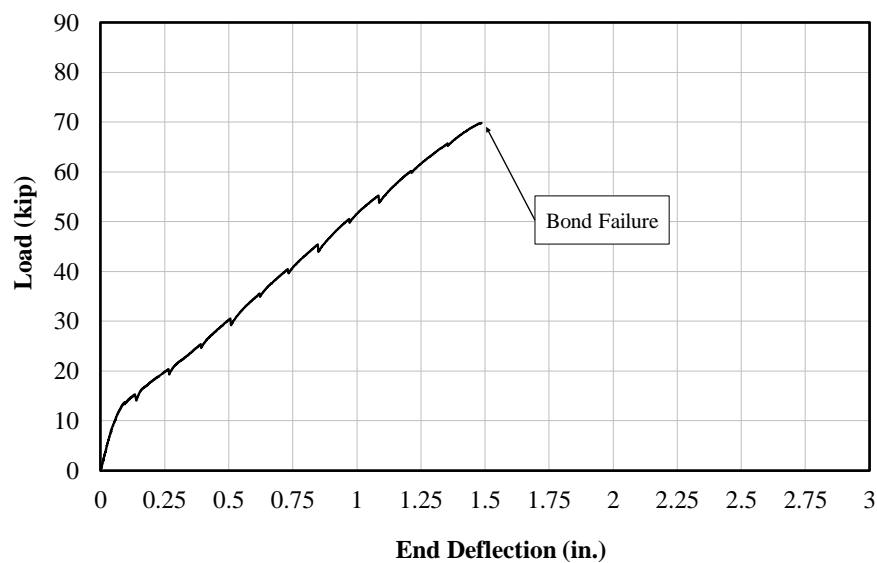


(b) Stress-Strain (A615 Gr. 100 No. 8)

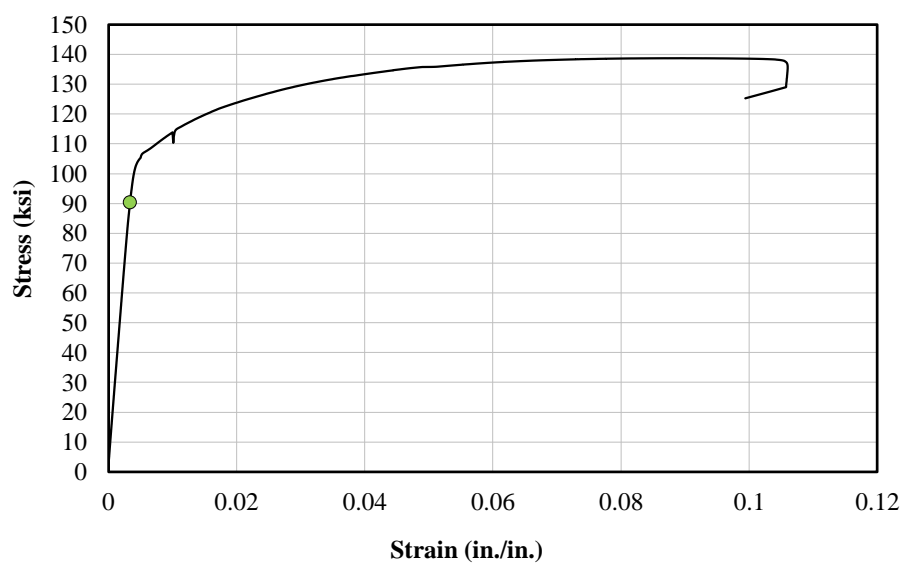
Figure C.12: C3/60/3-40-10-50

Table C.12: C3/60/3-40-10-50 Maximum Testing Values

Load (kip)	Avg. End Deflection (in.)	Avg. Midspan Deflection (in.)	Bar Stress (ksi)
68.7	1.5	1.1	86.8



(a) Load-Deflection

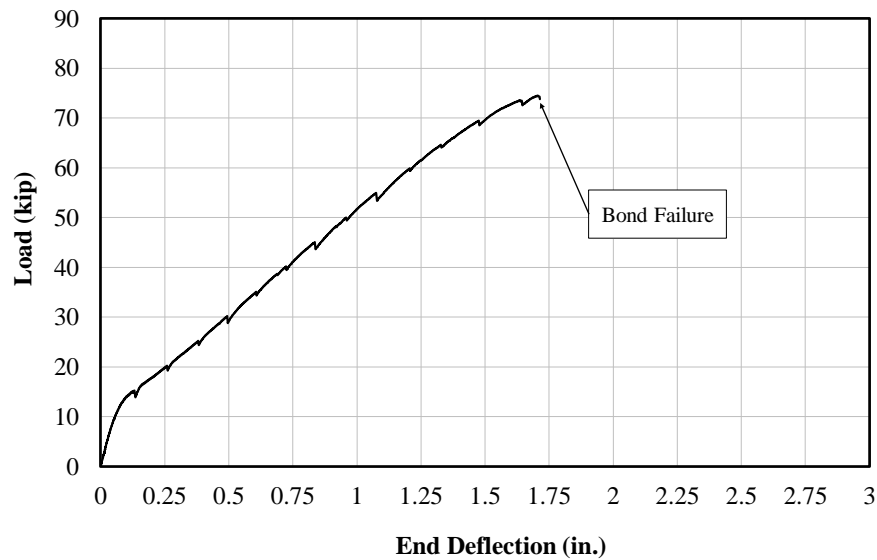


(b) Stress-Strain (A615 Gr. 100 No. 8)

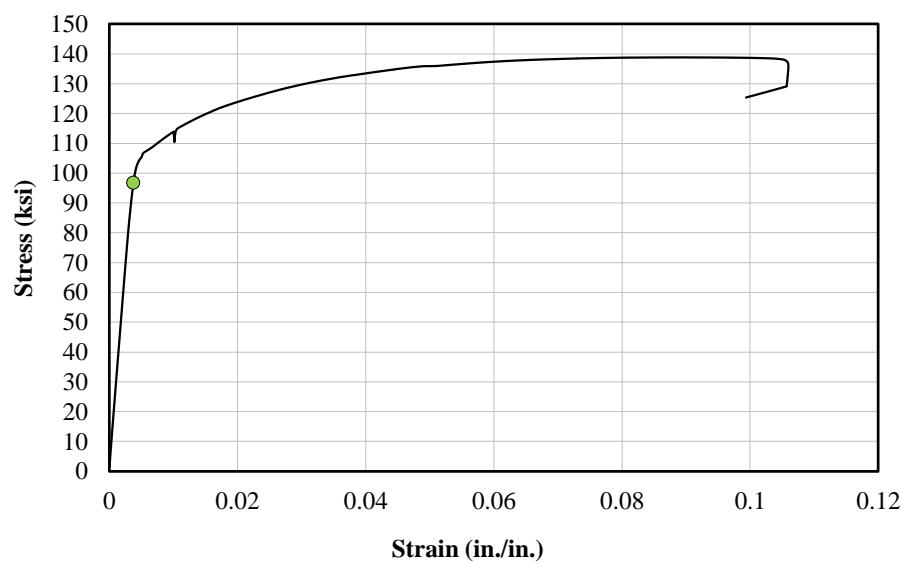
Figure C.13: C3/60-40-5-150

Table C.13: C3/60-40-5-150 Maximum Testing Values

Load (kip)	Avg. End Deflection (in.)	Avg. Midspan Deflection (in.)	Bar Stress (ksi)
69.9	1.5	1.1	90.4



(a) Load-Deflection

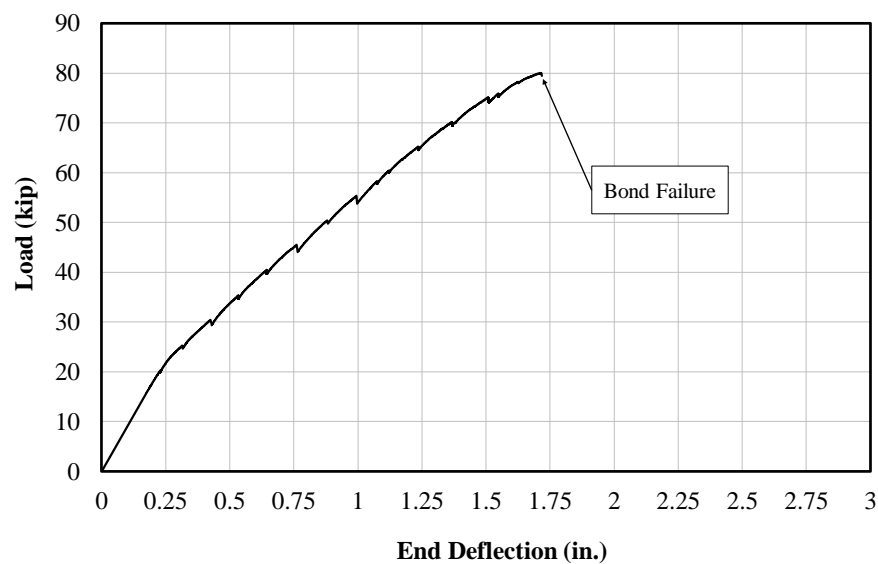


(b) Stress-Strain (A615 Gr. 100 No. 8)

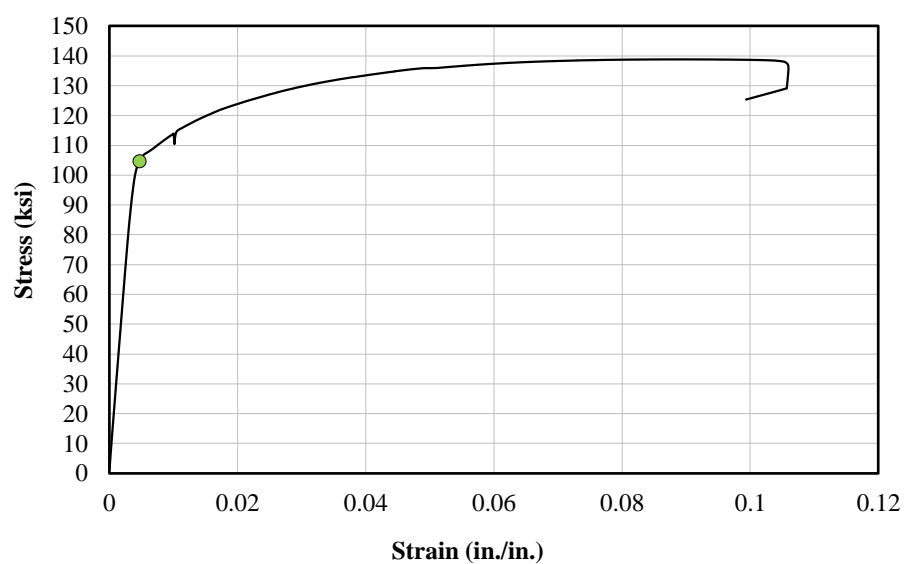
Figure C.14: C3/60-40-5-200

Table C.14: C3/60-40-5-200 Maximum Testing Values

Load (kip)	Avg. End Deflection (in.)	Avg. Midspan Deflection (in.)	Bar Stress (ksi)
74.5	1.7	1.4	96.8



(a) Load-Deflection

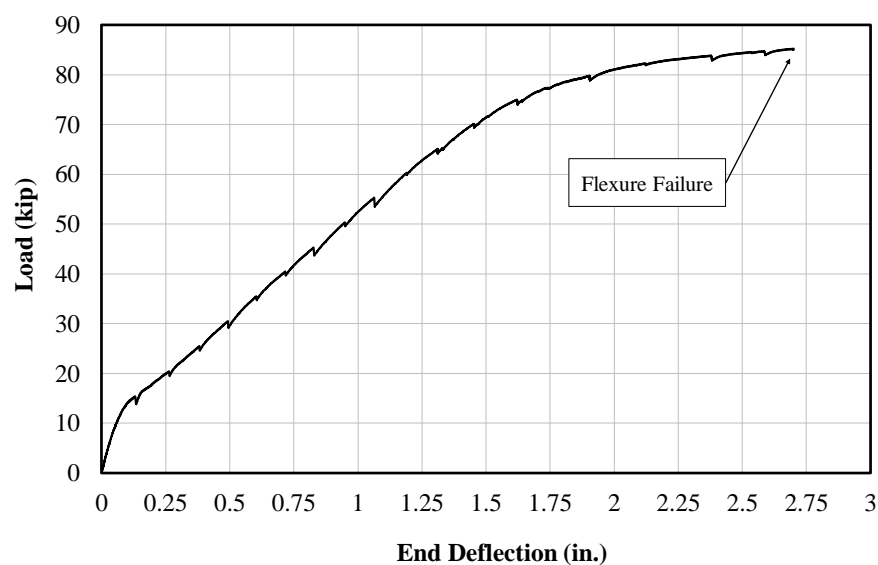


(b) Stress-Strain (A615 Gr. 100 No. 8)

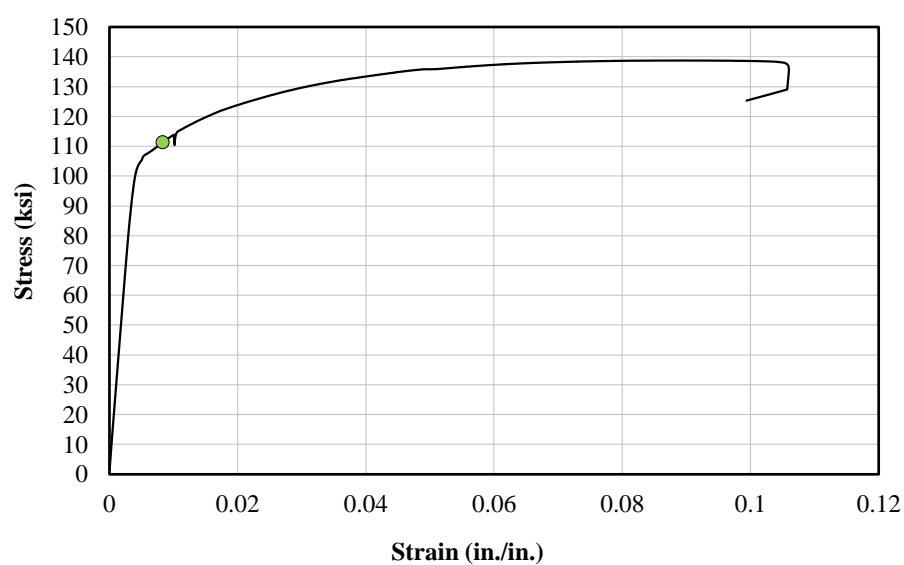
Figure C.15: C3/60-50-5-150

Table C.15: C3/60-50-5-150 Maximum Testing Values

Load (kip)	Avg. End Deflection (in.)	Avg. Midspan Deflection (in.)	Bar Stress (ksi)
80.1	1.7	1.3	104.6



(a) Load-Deflection



(b) Stress-Strain (A615 Gr. 100 No. 8)

Figure C.16: C3/60-50-5-200

Table C.16: C3/60-50-5-200 Maximum Testing Values

Load (kip)	Avg. End Deflection (in.)	Avg. Midspan Deflection (in.)	Bar Stress (ksi)
85.2	2.7	2.0	111.3

APPENDIX D. CRACK WIDTH PROPAGATION

All cracks are measured from specimen centerline and remain within the constant moment region. Four (4) cracks were monitored in each test. The average crack width growth was plotted for each test specimen. A typical test specimen showing any regions of interest and locations of these cracks is provided in Figure D.1.

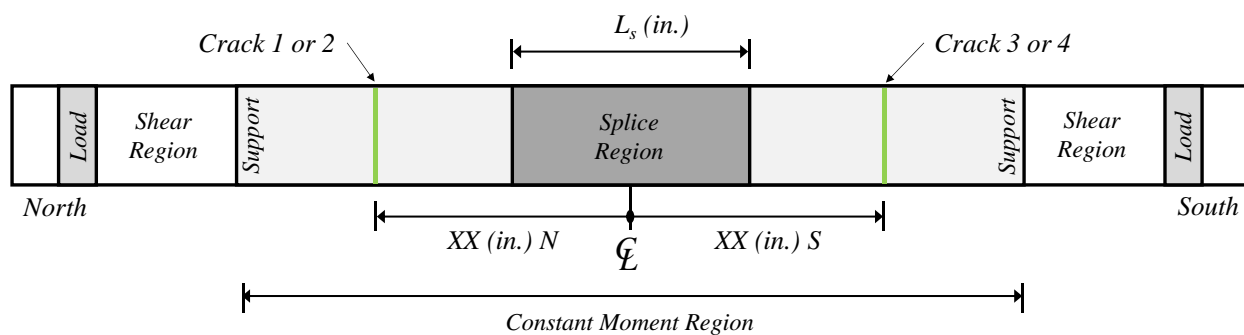


Figure D.1: Typical Specimen Crack Monitoring Diagram

Table D.1: S-40-5 Crack Width Summary

Load (kip)	Moment (ft-kip)	Bar Stress (ksi)	Crack Widths (1/1000 in.)					
			Crack 1	Crack 2	Crack 3	Crack 4	Max.	Avg.
			33" N	20" N	19.5" S	30" S		
2.0	8.0	17.6	3	6	3	3	6	4
3.0	12.0	26.3	4	9	4	5	9	6
4.0	16.0	35.1	7	10	5	6	10	7
5.0	20.0	43.8	9	11	7	8	11	9
6.0	24.0	52.5	10	13	9	10	13	11
7.0	28.0	61.3	11	15	9	14	15	12
8.0	32.0	70.1	14	15	12	16	16	14

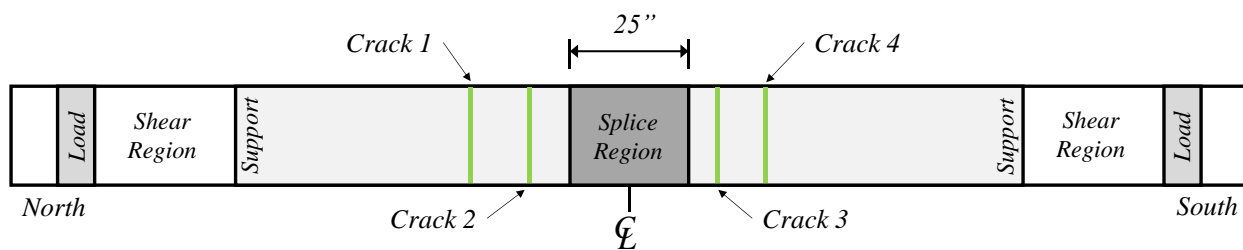
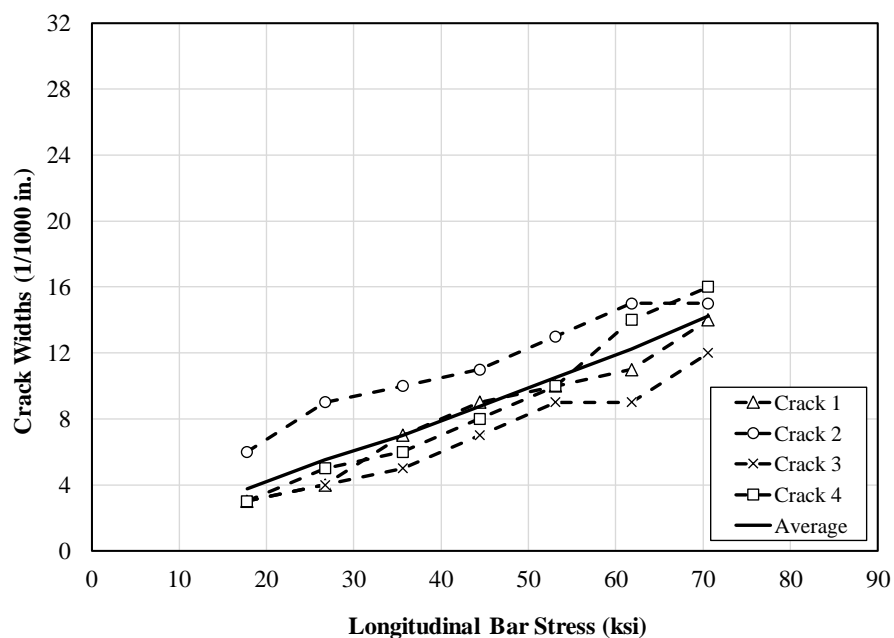
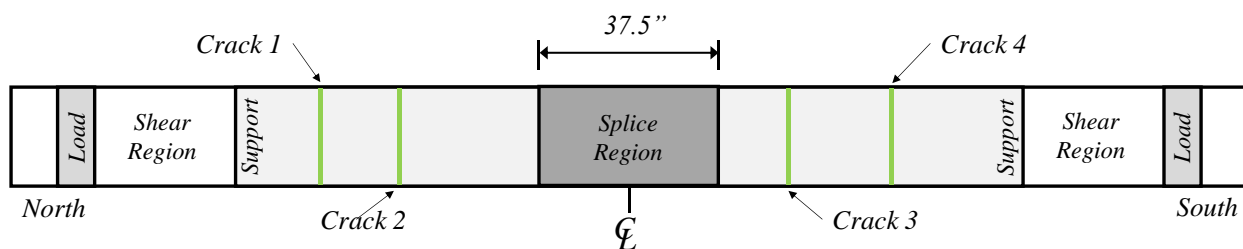
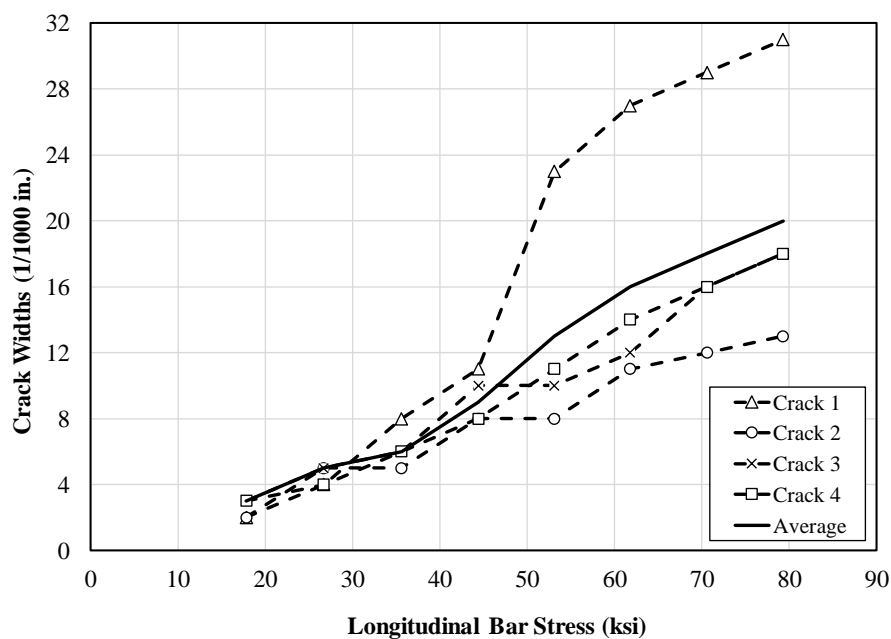
**(a) Crack Locations****(b) Crack Widths****Figure D.2: S-40-5**

Table D.2: S-60-5 Crack Width Summary

Load (kip)	Moment (ft-kip)	Bar Stress (ksi)	Crack Widths (1/1000 in.)					
			Crack 1	Crack 2	Crack 3	Crack 4	Max.	Avg.
			48" N	37" N	23.5" S	39.5" S		
2.0	8.1	17.8	2	2	3	3	3	3
3.0	12.0	26.7	4	5	5	4	5	5
4.0	16.0	35.6	8	5	6	6	8	6
5.0	20.0	44.4	11	8	10	8	11	9
6.0	24.0	53.1	23	8	10	11	23	13
7.0	28.0	61.8	27	11	12	14	27	16
8.0	32.0	70.6	29	12	16	16	29	18
9.0	36.0	79.3	31	13	18	18	31	20



(a) Crack Locations



(b) Crack Widths

Figure D.3: S-60-5

Table D.3: S-80-5 Crack Width Summary

Load (kip)	Moment (ft-kip)	Bar Stress (ksi)	Crack Widths (1/1000 in.)					
			Crack 1	Crack 2	Crack 3	Crack 4	Max.	Avg.
			50" N	31" N	30.5" S	46" S		
2.0	8.0	17.8	4	3	2	3	4	3
3.0	12.0	26.7	5	4	2	4	5	4
4.0	16.0	35.6	6	5	2	6	6	5
5.0	20.0	44.4	10	8	3	9	10	8
6.0	24.0	53.1	10	10	3	10	10	8
7.0	28.0	61.8	13	13	5	11	13	11

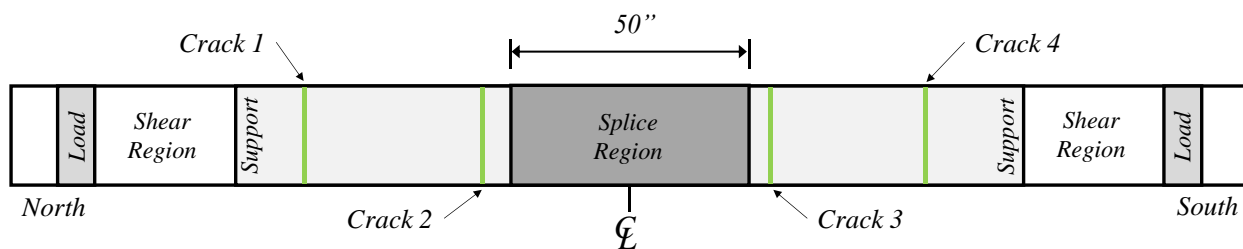
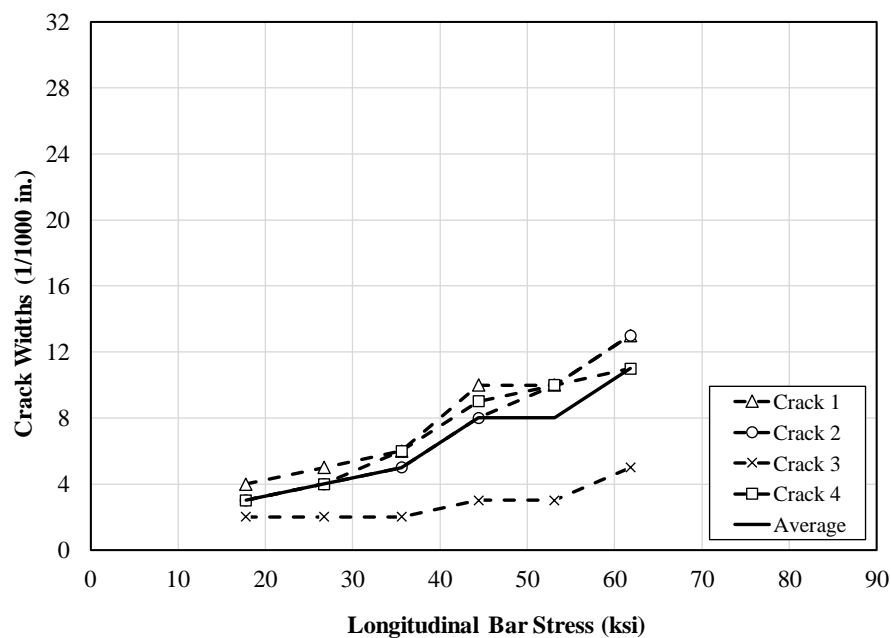
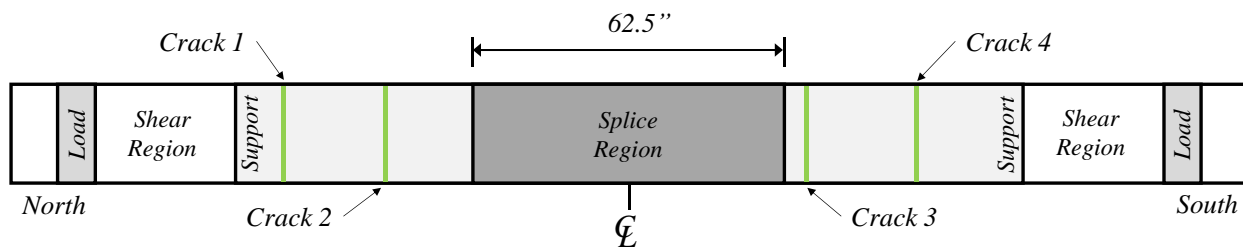
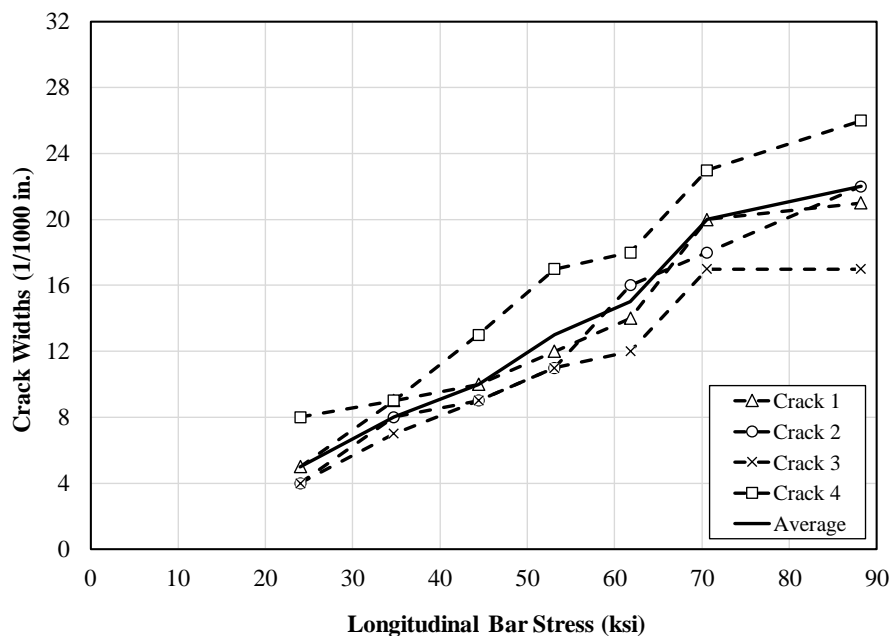
**(a) Crack Locations****(b) Crack Widths****Figure D.4: S-80-5**

Table D.4: S-100-5 Crack Width Summary

Load (kip)	Moment (ft-kip)	Bar Stress (ksi)	Crack Widths (1/1000 in.)				Max.	Avg.
			Crack 1	Crack 2	Crack 3	Crack 4		
			56" N	41" N	34" S	46" S		
2.7	11.0	24.0	5	4	4	8	8	5
3.9	15.7	34.6	9	8	7	9	9	8
5.0	20.0	44.3	10	9	9	13	13	10
6.0	23.9	52.9	12	11	11	17	17	13
7.0	28.0	61.7	14	16	12	18	18	15
8.0	31.8	70.5	20	18	17	23	23	20
10.0	40.0	88.1	21	22	17	26	26	22



(a) Crack Locations

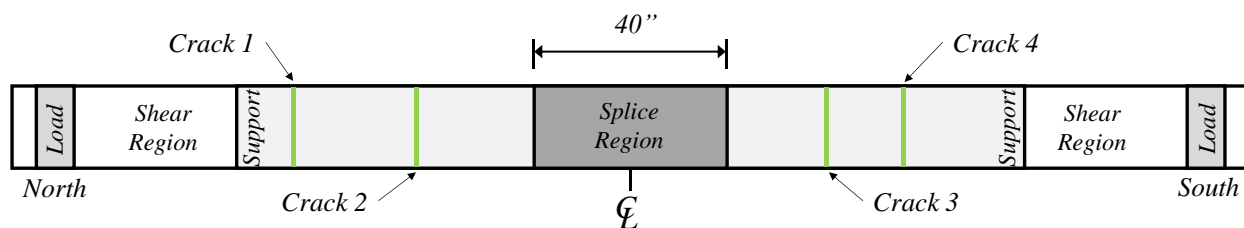


(b) Crack Widths

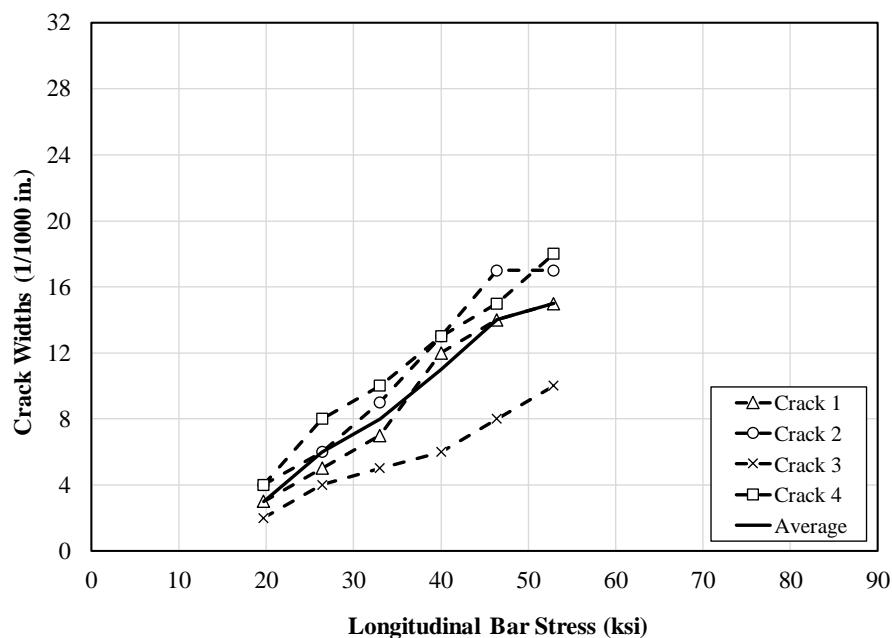
Figure D.5: S-100-5

Table D.5: U-40-5-X Crack Width Summary

Load (kip)	Moment (ft-kip)	Bar Stress (ksi)	Crack Widths (1/1000 in.)					
			Crack 1	Crack 2	Crack 3	Crack 4	Max.	Avg.
			83" N	45" N	48" S	65" S		
15.0	60.1	19.7	3	4	2	4	4	3
20.2	80.7	26.4	5	6	4	8	8	6
25.2	100.7	33.0	7	9	5	10	10	8
30.4	121.6	40.0	12	13	6	13	13	11
35.3	141.1	46.4	14	17	8	15	17	14
40.2	160.9	52.9	15	17	10	18	18	15



(a) Crack Locations



(b) Crack Widths

Figure D.6: U-40-5-X

Table D.6: U-60-5-X Crack Width Summary

Load (kip)	Moment (ft-kip)	Bar Stress (ksi)	Crack Widths (1/1000 in.)					
			Crack 1	Crack 2	Crack 3	Crack 4	Max.	Avg.
			65" N	51" N	54" S	70" S		
15.0	59.8	19.7	3	4	4	3	4	4
20.2	80.8	26.7	4	6	5	6	6	5
25.2	101.0	33.3	5	7	6	7	7	6
30.2	120.6	39.9	5	10	11	9	11	9
35.1	140.3	46.5	7	12	12	11	12	11
40.4	161.6	53.4	10	12	13	12	13	12
45.1	180.4	59.4	12	15	13	14	15	14

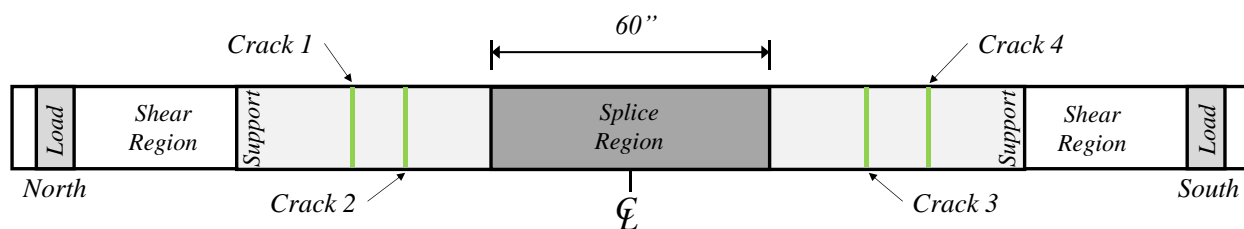
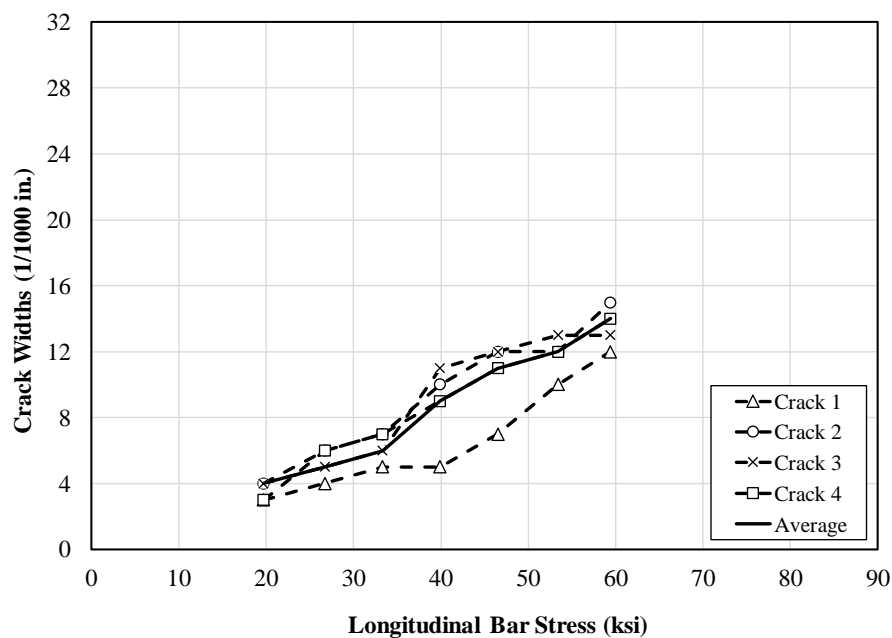
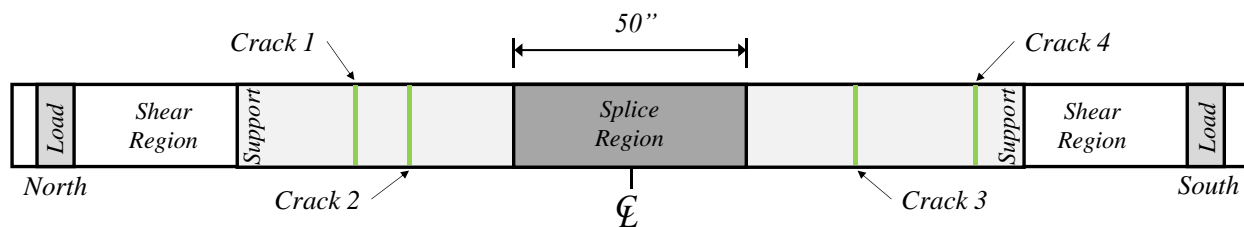
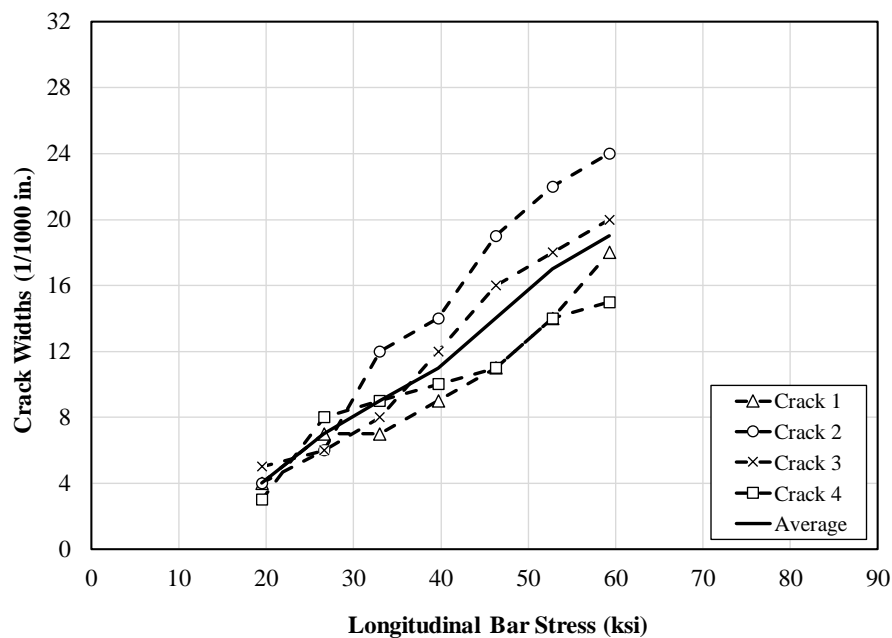
**(a) Crack Locations****(b) Crack Widths****Figure D.7: U-60-5-X**

Table D.7: U-50-5 Crack Width Summary

Load (kip)	Moment (ft-kip)	Bar Stress (ksi)	Crack Widths (1/1000 in.)				Max.	Avg.
			Crack 1	Crack 2	Crack 3	Crack 4		
			68" N	47" N	47" S	84" S		
14.8	59.2	19.5	4	4	5	3	5	4
20.2	80.6	26.6	7	6	6	8	8	7
25.0	100.1	33.0	7	12	8	9	12	9
30.1	120.2	39.7	9	14	12	10	14	11
35.0	140.1	46.3	11	19	16	11	19	14
40.0	160.1	52.8	14	22	18	14	22	17
45.1	180.4	59.3	18	24	20	15	24	19



(a) Crack Locations

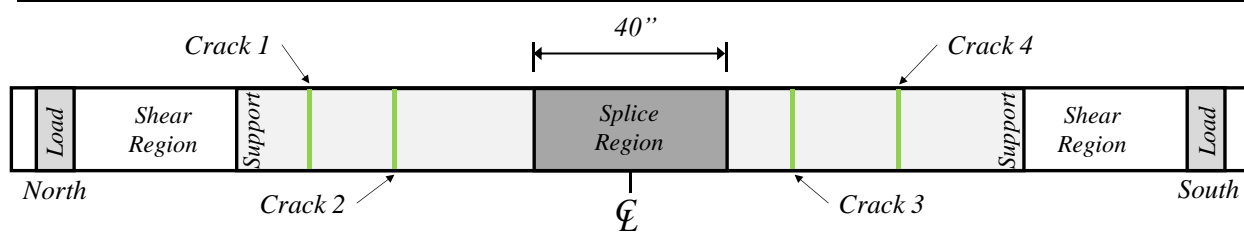


(b) Crack Widths

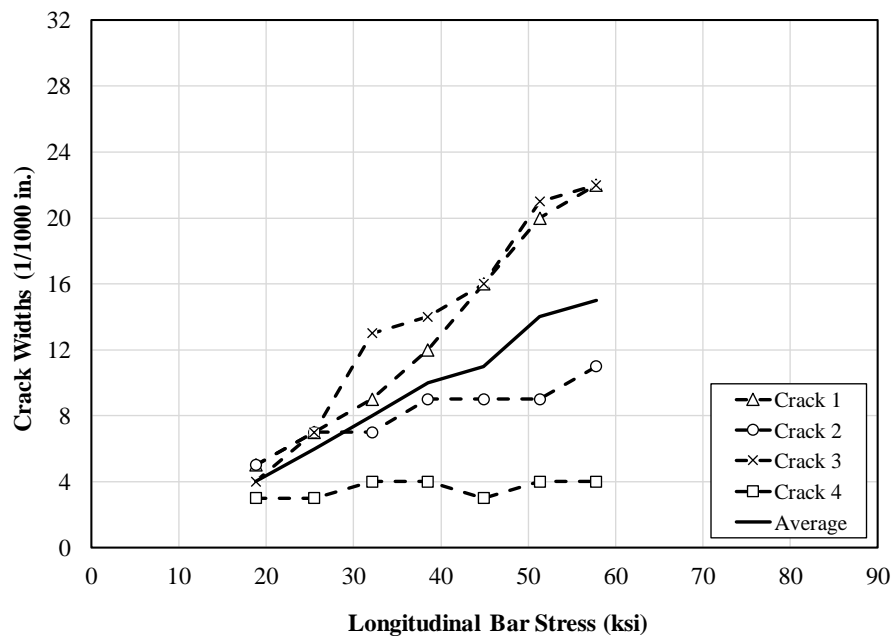
Figure D.8: U-50-5

Table D.8: U-40-10 Crack Width Summary

Load (kip)	Moment (ft-kip)	Bar Stress (ksi)	Crack Widths (1/1000 in.)					
			Crack 1	Crack 2	Crack 3	Crack 4	Max.	Avg.
			76" N	46" N	35" S	60" S		
14.8	59.1	18.8	5	5	4	3	5	4
20.0	79.9	25.5	7	7	7	3	7	6
25.2	100.7	32.1	9	7	13	4	13	8
30.2	120.8	38.5	12	9	14	4	14	10
35.2	140.6	44.9	16	9	16	3	16	11
40.1	160.2	51.3	20	9	21	4	21	14
45.1	180.4	57.8	22	11	22	4	22	15



(a) Crack Locations



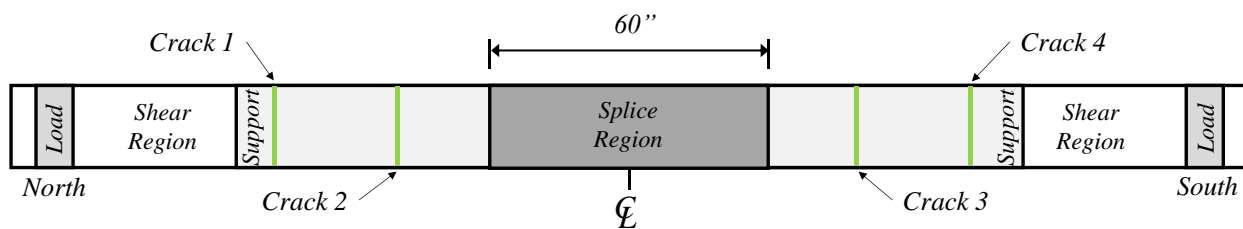
(b) Crack Widths

Figure D.9: U-40-10

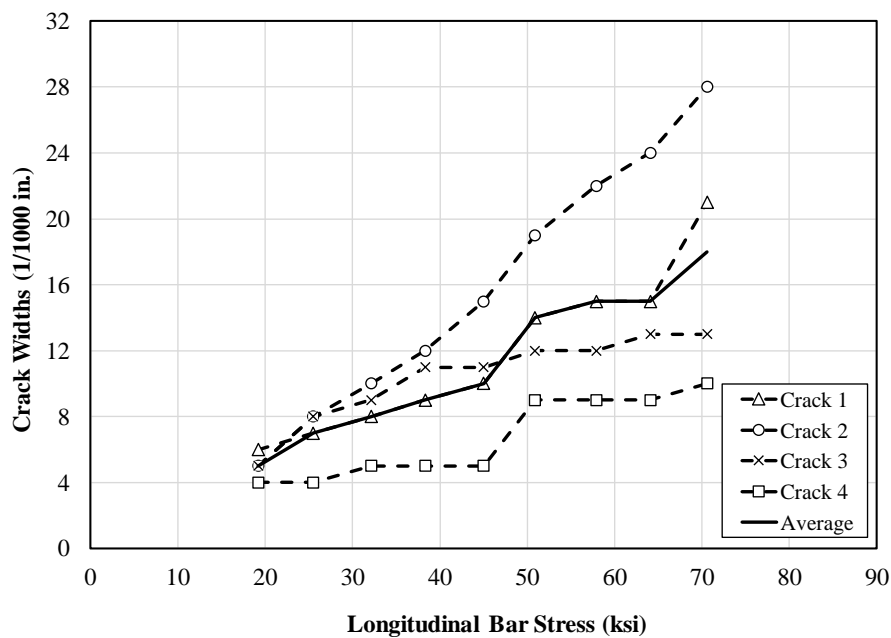
Note: Crack 4 did not grow larger for U-40-10 due to the presence of a nearby primary crack.

Table D.9: U-60-10 Crack Width Summary

Load (kip)	Moment (ft-kip)	Bar Stress (ksi)	Crack Widths (1/1000 in.)				Max.	Avg.
			Crack 1	Crack 2	Crack 3	Crack 4		
			90" N	43" N	44" S	84" S		
15.1	60.3	19.2	6	5	5	4	6	5
20.0	80.0	25.5	7	8	8	4	8	7
25.2	100.7	32.1	8	10	9	5	10	8
30.1	120.3	38.3	9	12	11	5	12	9
35.2	140.8	45.0	10	15	11	5	15	10
39.8	159.0	50.9	14	19	12	9	19	14
45.2	180.9	57.9	15	22	12	9	22	15
50.0	200.2	64.1	15	24	13	9	24	15
55.1	220.2	70.6	21	28	13	10	28	18



(a) Crack Locations

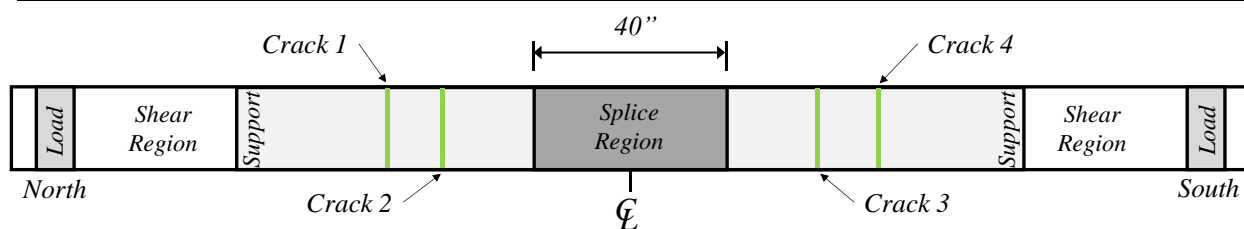


(b) Crack Widths

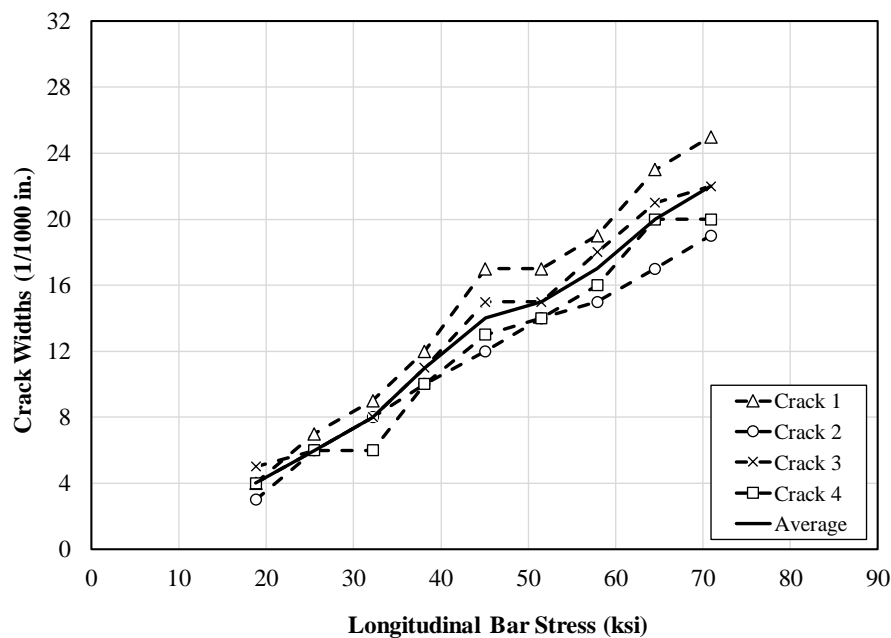
Figure D.10: U-60-10

Table D.10: C3/60/2-40-10-25 Crack Width Summary

Load (kip)	Moment (ft-kip)	Bar Stress (ksi)	Crack Widths (1/1000 in.)				Max.	Avg.
			Crack 1	Crack 2	Crack 3	Crack 4		
			53" N	40" N	38" S	53" S		
14.8	59.0	18.8	4	3	5	4	5	4
20.0	80.0	25.5	7	6	6	6	7	6
25.3	101.1	32.2	9	8	8	6	9	8
29.9	119.8	38.1	12	10	11	10	12	11
35.3	141.2	45.1	17	12	15	13	17	14
40.3	161.0	51.5	17	14	15	14	17	15
45.2	180.9	57.9	19	15	18	16	19	17
50.4	201.5	64.5	23	17	21	20	23	20
55.2	221.0	70.9	25	19	22	20	25	22



(a) Crack Locations

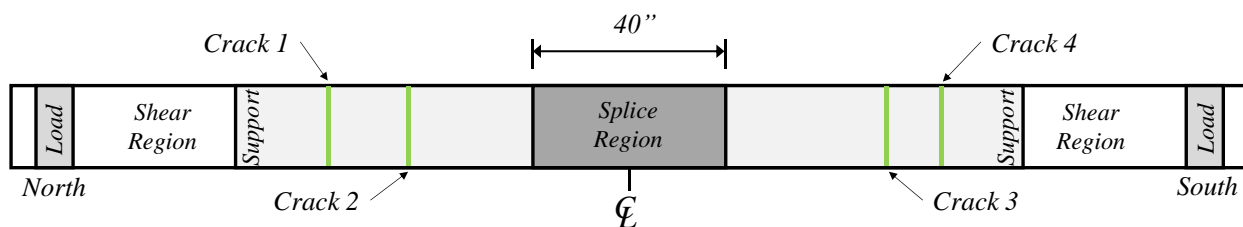


(b) Crack Widths

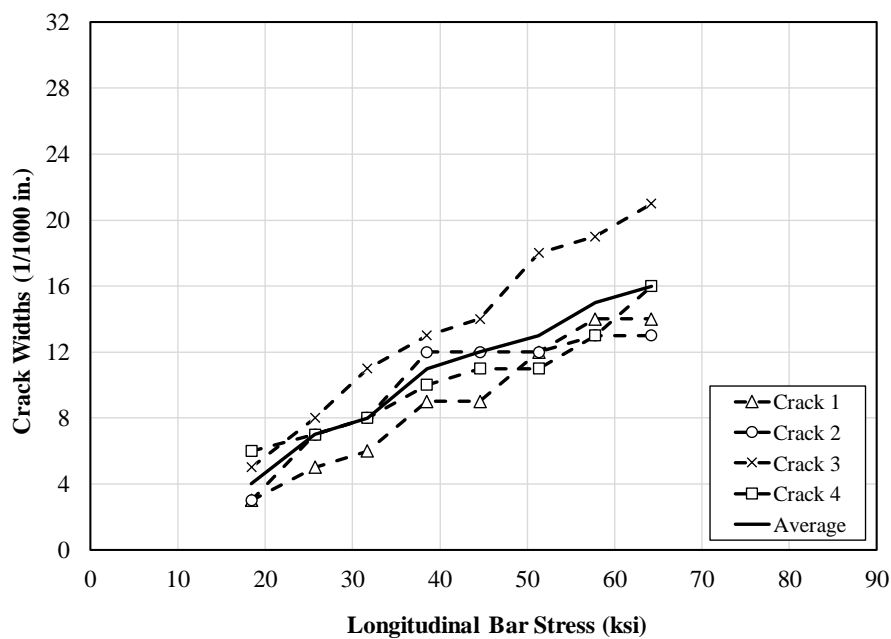
Figure D.11: C3/60/2-40-10-25

Table D.11: C3/60/2-40-10-50 Crack Width Summary

Load (kip)	Moment (ft-kip)	Bar Stress (ksi)	Crack Widths (1/1000 in.)				Max.	Avg.
			Crack 1	Crack 2	Crack 3	Crack 4		
			74" N	53" N	62" S	80" S		
14.5	58.1	18.4	3	3	5	6	6	4
20.2	81.0	25.7	5	7	8	7	8	7
25.0	100.0	31.7	6	8	11	8	11	8
30.4	121.4	38.5	9	12	13	10	13	11
35.1	140.3	44.6	9	12	14	11	14	12
40.3	161.0	51.3	12	12	18	11	18	13
45.3	181.3	57.8	14	13	19	13	19	15
50.3	201.2	64.2	14	13	21	16	21	16



(a) Crack Locations



(b) Crack Widths

Figure D.12: C3/60/2-40-10-50

Table D.12: C3/60/3-40-10-50 Crack Width Summary

Load (kip)	Moment (ft-kip)	Bar Stress (ksi)	Crack Widths (1/1000 in.)				Max.	Avg.
			Crack 1	Crack 2	Crack 3	Crack 4		
			76" N	46" N	44" S	77" S		
14.0	56.1	17.7	5	3	5	4	5	4
20.3	81.3	25.7	6	5	6	7	7	6
25.4	101.6	32.1	6	7	9	8	9	8
30.1	120.3	38.0	9	8	13	12	13	11
35.2	140.6	44.6	9	8	13	13	13	11
40.3	161.3	51.2	10	8	17	16	16	13
45.1	180.3	57.3	12	10	18	20	20	15
50.2	200.8	63.9	15	14	21	24	24	19
55.1	220.4	70.3	16	20	23	25	25	21

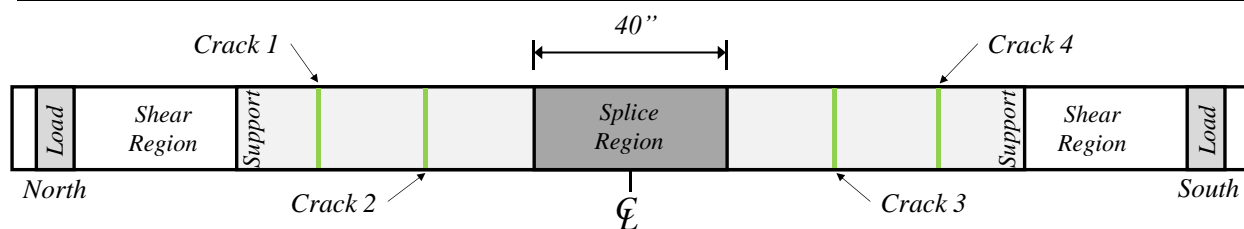
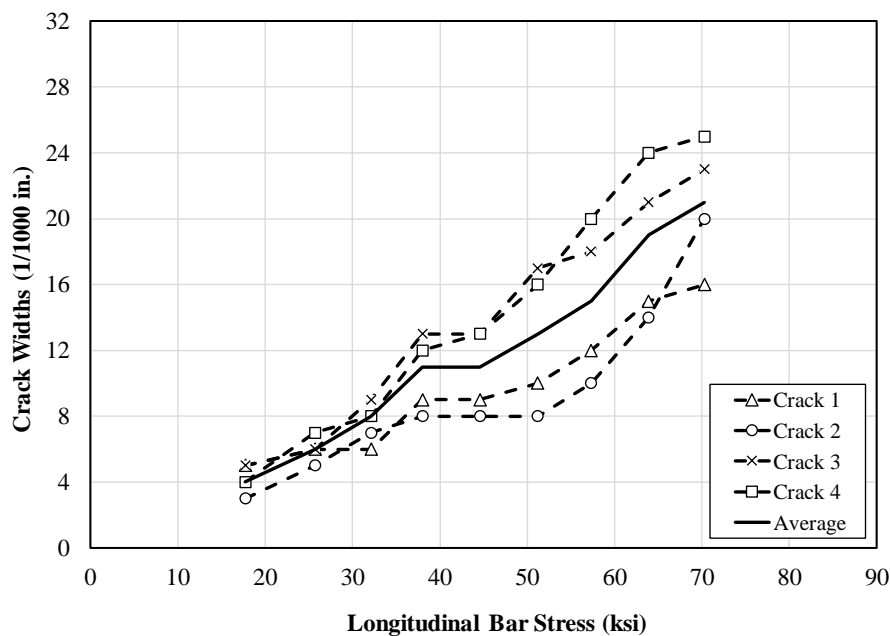
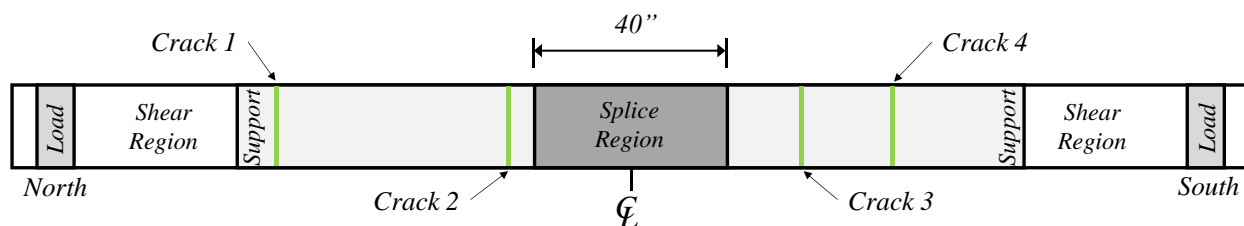
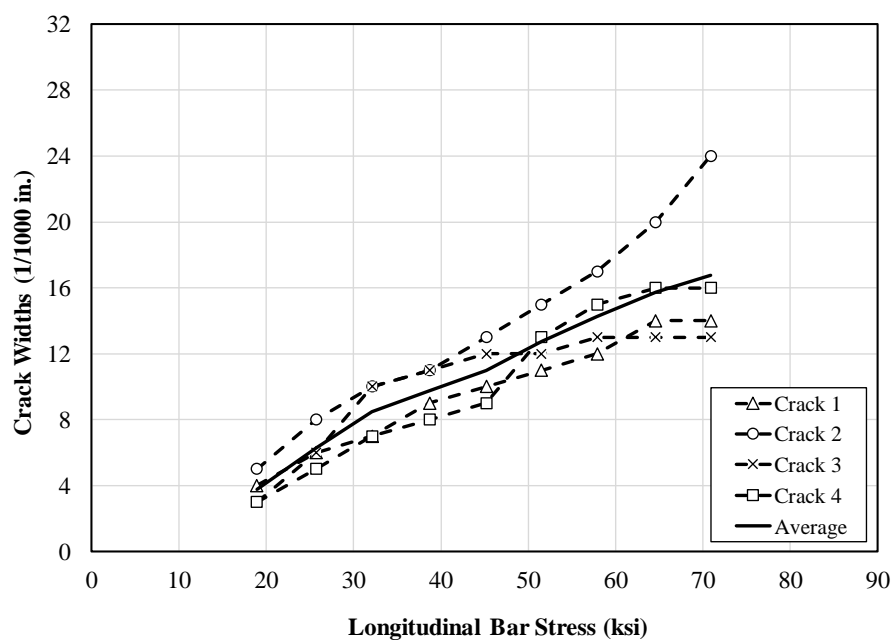
**(a) Crack Locations****(b) Crack Widths****Figure D.13: C3/60/3-40-10-50**

Table D.13: C3/60-40-5-150 Crack Width Summary

Load (kip)	Moment (ft-kip)	Bar Stress (ksi)	Crack Widths (1/1000 in.)				Max.	Avg.
			Crack 1	Crack 2	Crack 3	Crack 4		
			92" N	26" N	36" S	56" S		
14.8	59.2	18.9	4	5	3	3	5	4
20.2	80.8	25.7	6	8	6	5	8	6
25.2	100.8	32.1	7	10	10	7	10	9
30.4	121.6	38.7	9	11	11	8	11	10
35.4	141.6	45.2	10	13	12	9	13	11
40.3	161.2	51.5	11	15	12	13	15	13
45.2	181.0	57.9	12	17	13	15	17	14
50.4	201.7	64.6	14	20	13	16	20	16
55.1	220.5	70.9	14	24	13	16	24	17



(a) Crack Locations

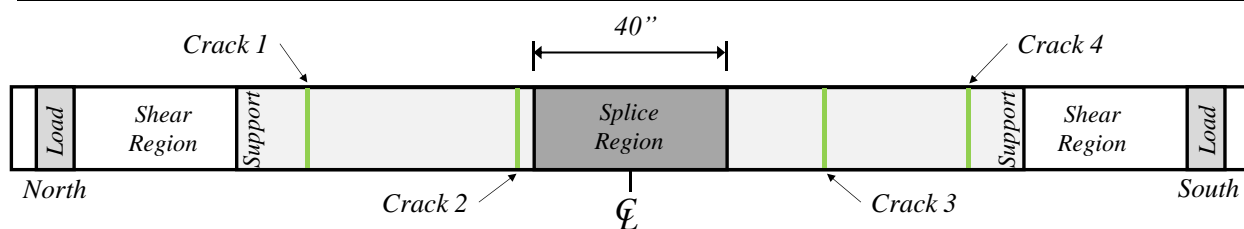


(b) Crack Widths

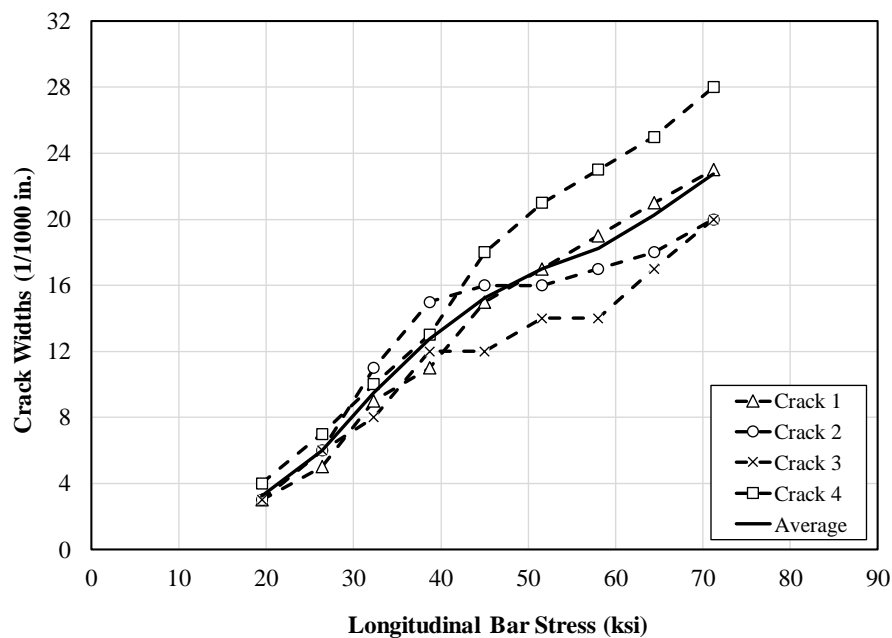
Figure D.14: C3/60-40-5-150

Table D.14: C3/60-40-5-200 Crack Width Summary

Load (kip)	Moment (ft-kip)	Bar Stress (ksi)	Crack Widths (1/1000 in.)				Max.	Avg.
			Crack 1	Crack 2	Crack 3	Crack 4		
			75" N	23" N	43" S	83" S		
15.3	61.3	19.5	3	3	3	4	4	3
20.8	83.1	26.4	5	6	6	7	7	6
25.3	101.4	32.3	9	11	8	10	11	10
30.4	121.6	38.7	11	15	12	13	15	13
35.3	141.1	45.0	15	16	12	18	18	15
40.3	161.4	51.6	17	16	14	21	21	17
45.4	181.4	58.0	19	17	14	23	23	18
50.3	201.2	64.4	21	18	17	25	25	20
55.4	221.4	71.2	23	20	20	28	28	23



(a) Crack Locations

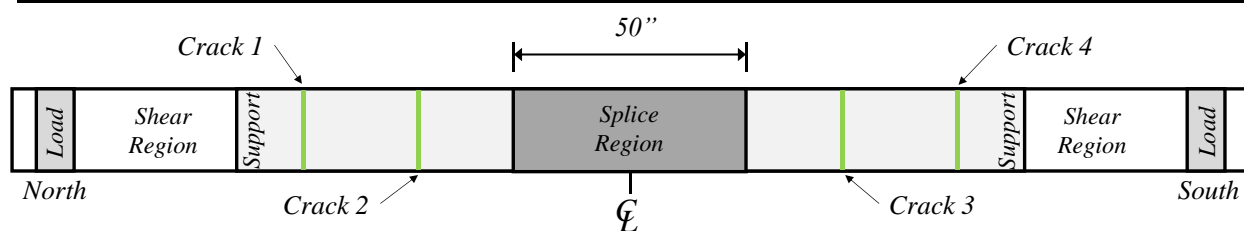


(b) Crack Widths

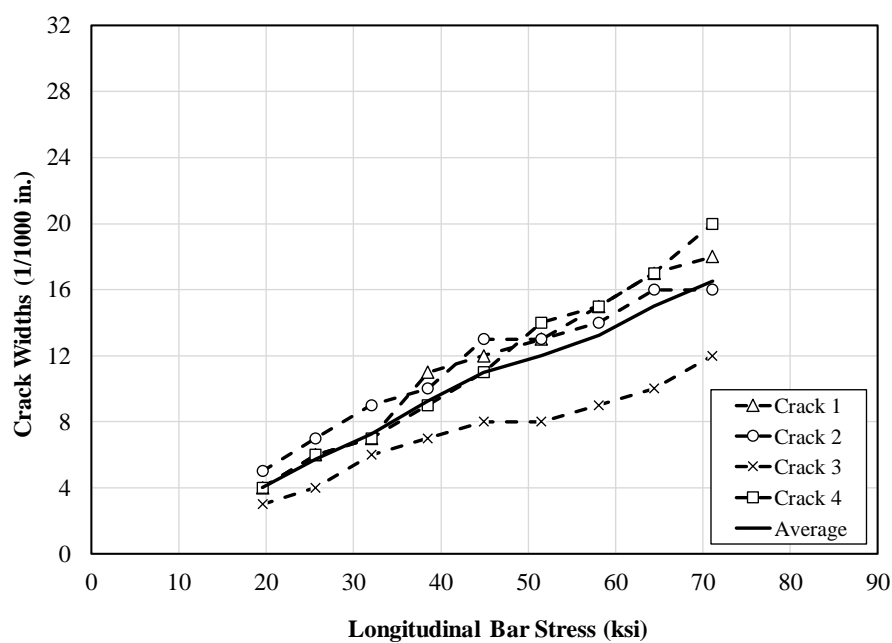
Figure D.15: C3/60-40-5-200

Table D.15: C3/60-50-5-150 Crack Width Summary

Load (kip)	Moment (ft-kip)	Bar Stress (ksi)	Crack Widths (1/1000 in.)				Max.	Avg.
			Crack 1	Crack 2	Crack 3	Crack 4		
			82" N	42" N	41" S	75" S		
15.4	61.6	19.6	4	5	3	4	5	4
20.2	80.8	25.7	6	7	4	6	7	6
25.2	100.8	32.0	7	9	6	7	9	7
30.3	121.2	38.5	11	10	7	9	11	9
35.2	140.8	44.9	12	13	8	11	13	11
40.3	161.2	51.5	13	13	8	14	14	12
45.4	181.6	58.1	15	14	9	15	15	13
50.3	201.2	64.4	17	16	10	17	17	15
55.3	221.2	71.1	18	16	12	20	20	17



(a) Crack Locations

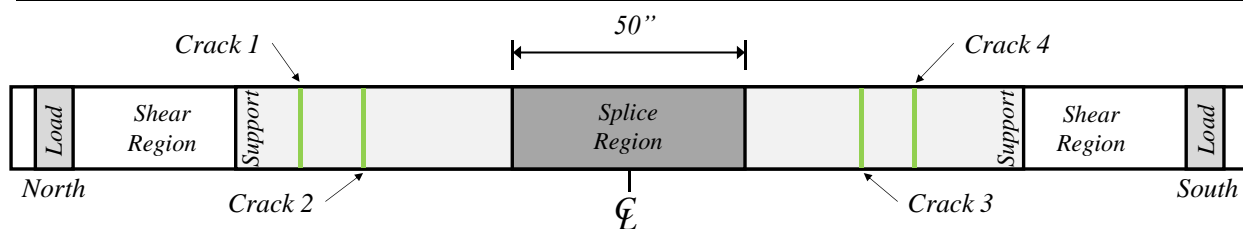


(b) Crack Widths

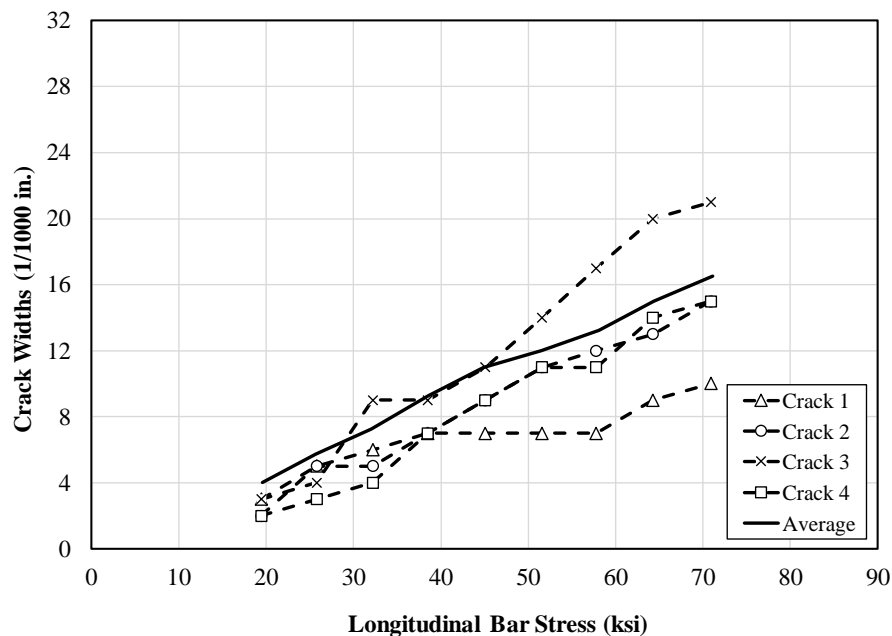
Figure D.16: C3/60-50-5-150

Table D.16: C3/60-50-5-200 Crack Width Summary

Load (kip)	Moment (ft-kip)	Bar Stress (ksi)	Crack Widths (1/1000 in.)				Max.	Avg.
			Crack 1	Crack 2	Crack 3	Crack 4		
			83" N	62" N	45" S	60" S		
15.3	61.2	19.4	3	2	3	2	3	3
20.3	81.2	25.8	5	5	4	3	5	4
25.4	101.4	32.2	6	5	9	4	9	6
30.3	121.3	38.5	7	7	9	7	9	8
35.4	141.6	45.1	7	9	11	9	11	9
40.4	161.5	51.6	7	11	14	11	14	11
45.2	180.9	57.8	7	12	17	11	17	12
50.3	201.2	64.3	9	13	20	14	20	14
55.2	220.8	70.9	10	15	21	15	21	15



(a) Crack Locations



(b) Crack Widths

Figure C.17: C3/60-50-5-200

APPENDIX E. BEAM CONSTRUCTION AS-BUILT DIMENSIONS

Dimensions were measured for all beams after failure at the locations shown in Figure E.1. The total beam width b_w accounts for three (3) splices of No. 8 bars, or 6 in. Bottom cover is measured along the middle splice for the south, middle, and north longitudinal locations. Percent error values indicate comparisons between the measured values and the original design values specified in Table E.1.

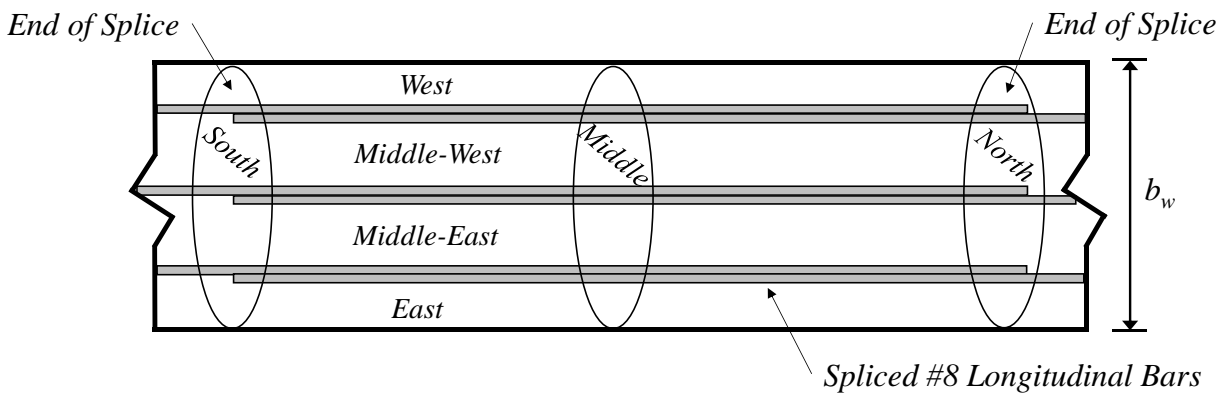


Figure E.1: Beam Splice Region Layout for As-Built Dimensions

Table E.1: Beam Design Dimensions

Location Along Width	Design Value (in.)
West	1-7/8
Middle-West	2
Middle-East	2
East	1-7/8
Total (b_w)	13-3/4
Bottom Cover (c_b)	1-7/8

Table E.2: U-40-5-X

Transverse Location	Longitudinal Location					
	South (in.)	% Error	Middle (in.)	% Error	North (in.)	% Error
West	1.668	-11.0%	1.697	-9.5%	1.738	-7.3%
Middle-West	1.981	-0.9%	1.904	-4.8%	1.717	-14.2%
Middle-East	1.993	-0.3%	2.024	1.2%	2.088	4.4%
East	2.111	12.6%	1.878	0.2%	1.781	-5.0%
Total	13.753	0.0%	13.503	-1.8%	13.324	-3.1%
Bottom Cover	2.081	11.0%	2.039	8.7%	1.823	-2.8%

Table E.3: U-60-5-X

Transverse Location	Longitudinal Location					
	South (in.)	% Error	Middle (in.)	% Error	North (in.)	% Error
West	1.919	2.3%	2.120	13.0%	2.041	8.8%
Middle-West	2.016	0.8%	1.856	-7.2%	1.868	-6.6%
Middle-East	1.652	-17.4%	1.817	-9.2%	2.024	1.2%
East	2.193	16.9%	1.904	1.5%	1.660	-11.5%
Total	13.779	0.2%	13.696	-0.4%	13.592	-1.2%
Bottom Cover	1.871	-0.2%	1.917	2.2%	1.908	1.8%

Table E.4: U-50-5

Transverse Location	Longitudinal Location					
	South (in.)	% Error	Middle (in.)	% Error	North (in.)	% Error
West	1.931	3.0%	1.848	-1.4%	1.682	-10.3%
Middle-West	1.763	-11.9%	1.805	-9.8%	2.124	6.2%
Middle-East	2.137	6.9%	2.187	9.3%	2.207	10.4%
East	1.949	3.9%	2.075	10.7%	1.900	1.3%
Total	13.780	0.2%	13.915	1.2%	13.913	1.2%
Bottom Cover	1.857	-1.0%	1.847	-1.5%	1.815	-3.2%

Table E.5: U-40-10

Transverse Location	Longitudinal Location					
	South (in.)	% Error	Middle (in.)	% Error	North (in.)	% Error
West	2.009	7.1%	1.822	-2.8%	1.674	-10.7%
Middle-West	1.783	-10.9%	1.794	-10.3%	1.853	-7.4%
Middle-East	1.663	-16.9%	1.846	-7.7%	2.201	10.1%
East	2.070	10.4%	2.000	6.7%	2.088	11.4%
Total	13.525	-1.6%	13.462	-2.1%	13.816	0.5%
Bottom Cover	1.893	1.0%	1.916	2.2%	1.888	0.7%

Table E.6: U-60-10

Transverse Location	Longitudinal Location					
	South (in.)	% Error	Middle (in.)	% Error	North (in.)	% Error
West	2.086	11.3%	2.160	15.2%	1.814	-3.3%
Middle-West	2.143	7.1%	2.188	9.4%	2.021	1.1%
Middle-East	1.663	-16.9%	1.893	-5.4%	1.872	-6.4%
East	2.001	6.7%	2.159	15.1%	2.345	25.1%
Total	13.893	1.0%	14.400	4.7%	14.052	2.2%
Bottom Cover	1.952	4.1%	1.982	5.7%	1.934	3.1%

Table E.7: C3/60/2-40-10-25

Transverse Location	Longitudinal Location					
	South (in.)	% Error	Middle (in.)	% Error	North (in.)	% Error
West	1.993	6.3%	2.030	8.2%	2.275	21.3%
Middle-West	1.569	-21.6%	1.802	-9.9%	1.849	-7.6%
Middle-East	1.668	-16.6%	1.756	-12.2%	1.547	-22.7%
East	2.224	18.6%	2.178	16.2%	1.953	4.1%
Total	13.453	-2.2%	13.766	0.1%	13.623	-0.9%
Bottom Cover	2.013	7.3%	2.009	7.1%	1.924	2.6%

Table E.8: C3/60/2-40-10-50

Transverse Location	Longitudinal Location					
	South (in.)	% Error	Middle (in.)	% Error	North (in.)	% Error
West	1.741	-7.1%	1.935	3.2%	2.007	7.0%
Middle-West	1.663	-16.9%	1.922	-3.9%	1.885	-5.8%
Middle-East	1.677	-16.2%	1.563	-21.9%	1.431	-28.5%
East	2.393	27.6%	2.395	27.7%	2.235	19.2%
Total	13.474	-2.0%	13.815	0.5%	13.558	-1.4%
Bottom Cover	2.104	12.2%	1.926	2.7%	1.800	-4.0%

Table E.9: C3/60/3-40-10-50

Transverse Location	Longitudinal Location					
	South (in.)	% Error	Middle (in.)	% Error	North (in.)	% Error
West	2.073	10.5%	2.234	19.1%	2.292	22.2%
Middle-West	1.452	-27.4%	1.574	-21.3%	1.665	-16.8%
Middle-East	1.702	-14.9%	1.633	-18.4%	1.566	-21.7%
East	2.11	12.5%	2.123	13.2%	2.035	8.5%
Total	13.336	-3.0%	13.564	-1.4%	13.557	-1.4%
Bottom Cover	1.795	-4.3%	1.910	1.8%	1.865	-0.5%

Table E.10: C3/60-40-5-150

Transverse Location	Longitudinal Location					
	South (in.)	% Error	Middle (in.)	% Error	North (in.)	% Error
West	2.060	9.9%	1.808	-3.6%	1.722	-8.2%
Middle-West	1.840	-8.0%	1.792	-10.4%	1.831	-8.5%
Middle-East	2.011	0.6%	1.883	-5.9%	1.832	-8.4%
East	2.060	9.9%	2.247	19.8%	2.421	29.1%
Total	13.971	1.6%	13.730	-0.1%	13.806	0.4%
Bottom Cover	1.882	0.4%	1.845	-1.6%	1.910	1.9%

Table E.11: C3/60-40-5-200

Transverse Location	Longitudinal Location					
	South (in.)	% Error	Middle (in.)	% Error	North (in.)	% Error
West	2.478	32.1%	2.369	26.4%	2.069	10.3%
Middle-West	1.768	-11.6%	1.839	-8.1%	2.010	0.5%
Middle-East	1.901	-5.0%	1.857	-7.2%	1.853	-7.4%
East	1.820	-2.9%	2.004	6.9%	2.045	9.0%
Total	13.967	1.6%	14.069	2.3%	13.977	1.6%
Bottom Cover	1.878	0.2%	1.836	-2.1%	1.717	-8.4%

Table E.12: C3/60-50-5-150

Transverse Location	Longitudinal Location					
	South (in.)	% Error	Middle (in.)	% Error	North (in.)	% Error
West	2.117	12.9%	2.113	12.7%	2.072	10.5%
Middle-West	1.680	-16.0%	1.622	-18.9%	1.711	-14.5%
Middle-East	1.798	-10.1%	1.661	-17.0%	1.638	-18.1%
East	2.078	10.8%	2.427	29.4%	2.241	19.5%
Total	13.673	-0.6%	13.823	0.5%	13.662	-0.6%
Bottom Cover	1.824	-2.7%	1.980	5.6%	1.818	-3.0%

Table E.13: C3/60-50-5-200

Transverse Location	Longitudinal Location					
	South (in.)	% Error	Middle (in.)	% Error	North (in.)	% Error
West	1.991	6.2%	1.691	-9.8%	1.743	-7.0%
Middle-West	2.044	2.2%	1.908	-4.6%	1.800	-10.0%
Middle-East	2.074	3.7%	1.969	-1.6%	1.888	-5.6%
East	2.243	19.6%	2.363	26.0%	2.486	32.6%
Total	14.352	4.4%	13.932	1.3%	13.917	1.2%
Bottom Cover	1.815	-3.2%	1.911	1.9%	1.958	4.4%

APPENDIX F. STEEL DATABASE

Table F.1: Summary of Unconfined Lap-Splice Specimen Database

Reference	No. of Tests	l_s (in.)	d_b (No.)	l_s/d_b	c_{so}/d_b	f_c' (psi)
Azizinamini, Pavel, Hatfield and Ghosh; 1997	27	13-80	8, 11	9.2-56.7	0.98-2.13	5080-15,591
Chamberlin; 1956	1	12	4	24	4.00	4540
Chinn, Ferguson, and Thompson; 1955	11	12.5-24.0	6, 11	14.4-32.0	1.41-3.92	3580-7480
Choi, Hadje-Ghaffari, Darwin, and McCabe; 1990, 1991	7	12-24	5, 6, 8, 11	16.0-19.2	1.42-3.20	5360-6010
Cleary, Ramirez; 1991	1	12	6	16.0	4.33	3990
Darwin, Tholen, Idun, and Zuo; 1995	13	16-40	5, 8, 11	16.0-28.3	2.00-3.35	3830-5250
El-Hacha, Hossam El-Agroudy, and Sami H. Rizkalla; 2006	3	12-36	6	16-48	2.84-3.17	5713-6380
Ferguson and Breen; 1965	18	18.0-82.5	8, 11	18-80	1.42-3.26	2690-5620
Ferguson and Thompson; 1965	4	49.4-63.3	11	35.0-44.9	3.30 ^[1]	2730-3410
Fleet and Frosch; 2019	7	25-60	5, 8	40-60	1.88-3.80	5300-9800
Glucksman and Frosch; 2018	9	40-120	8	40-120	1.88	4740-6260
Hamad, Itani; 1998	8	12	8	12	1.50	7585-11,124
Hamad, Machaka; 1999	3	12	8	12	1.02	6772-13,459
Hamad, Mansour; 1996	1	13.8	6	18.4	1.05	2900
Hester, Salamizavaregh, Darwin, and McCabe; 1991, 1993	7	16.0-22.8	8	16.0-22.8	2.00	5240-6450
Pay and Frosch; 2005	1	12	8	12	1.50	4020
Rezansoff, Akanni, and Sparling; 1993	4	29.5-44.3	8, 9	29.5-39.3	1.60-1.80	3726-4031
Richter, Pujol, Sozen, and McCain; 2012	2	40	11	28.4	2.10	4940-4950
Seliem, Hosny, Rizkalla, Zia, Briggs, Miller, Darwin, Browning, Glass, Hoyt, Donnelly, and Jirsa; 2009	30	15-91	5, 8, 11	24.0-70.4	1.34-6.08	4060-10,200
Sim and Frosch; 2014	12	12-48	5, 6, 7, 8, 11	17-48	1.06-3.80	3990-5400
Thompson, Jirsa, Breen, and Meinheit; 1975	11	12-60	6, 8, 11, 14	16.0-35.4	1.18-2.84	2865-4710
Zekany, Neumann, Jirsa, and Breen; 1981	2	16-22	9, 11	14.2-15.6	1.42-1.77	3825-5650
Zuo and Darwin; 1998	27	17-40	8, 11	17-40	1.40-3.03	4250-15,650
Total	209					

^[1] Side cover data not recorded for two specimens in testing program

Table F.2: Summary of Confined Lap-Splice Specimen Database

Reference	No. of Tests	No. of Pairs within Tests	l_s (in.)	d_b (No.)	l_s/d_b	c_{so}/d_b	f_c' (psi)
Azizinamini, Pavel, Hatfield and Ghosh; 1997	25	16	15.0-57.5	8, 11	14.2-40.8	0.98-2.13	14,578-16,003
Darwin, Tholen, Idun, and Zuo; 1995	54	4	12-40	5, 8, 11	16-36	1.00-2.55	3810-5250
DeVries, Moehle, and Hester; 1991	8	0	12-22	9	10.6-19.5	1.22-1.72	7460-16,100
Ferguson and Breen; 1965	7	2	30.0-49.5	8, 11	30-36	3.25	2610-4170
Fleet and Frosch; 2019	6	3	40-50	8	40-50	1.50	6200-10,100
Glucksman and Frosch; 2018	6	5	40-60	8	40-60	1.50	6260-7360
Hamad, Machaka; 1999	6	6	12	8	12	1.02	9427-13,952
Hasan, Cleary, and Ramirez; 1996	1	0	12	7	13.7	5.29	3900
Hester, Salamizavaregh, Darwin, and McCabe; 1991, 1993	10	10	16.0-22.8	8	16.0-22.8	2.00	5240-6450
Kadoriku; 1994	34	0	14.9-37.4	6	19.9-49.9	1.52-4.72	3072-10,980
Rezansoff, Akanni, and Sparling; 1993	10	0	14.8-44.3	8, 9	14.8-39.3	1.61-1.83	3625-4089
Rezansoff, Konkankar and Fu; 1991	34	0	15.1-38.0	6, 8, 9, 11	13.4-29.5	1.00-1.77	3219-5742
Seliem, Hosny, Rizkalla, Zia, Briggs, Miller, Darwin, Browning, Glass, Hoyt, Donnelly, and Jirsa; 2009	38	38	27-91	8, 11	27.0-64.4	1.25-2.50	4060-10,200
Sim and Frosch; 2014	6	6	24-48	8	24-48	1.50	4400-5400
Thompson, Jirsa, Breen, and Meinheit; 1975	4	1	15-30	8, 11	14.2-21.3	1.42-2.00	3063-3507
Zekany, Neumann, Jirsa, and Breen; 1981	10	10	16-22	9, 11	14.2-15.6	1.42-1.77	3750-5700
Zuo and Darwin; 1998	63	0	16-40	8, 11	16-30	1.39-4.03	4250-15,650
Total	322	101					

VITA

Eric Taylor Fleet, the son of Robert Fleet and Lori Fleet, was born on November 9, 1993 in Oklahoma City, Oklahoma. Upon graduating from Edmond North High School in Edmond, Oklahoma in 2012, he chose to pursue his interests in mathematics, design, and Spanish at Oklahoma State University. In his time as an OSU Cowboy, Eric became a Tau Beta Pi scholar, a Centennial Leadership Fellow, and was named a Senior of Significance by the OSU Alumni Association. Through the School of Architecture and the College of Arts and Sciences at OSU, he graduated in 2017 with a Bachelor of Architectural Engineering degree with honors and a second major in Spanish Language. During the summer months of his undergraduate studies, Eric worked as a structural engineering intern for Kirkpatrick Forest Curtis PC in Oklahoma City, Oklahoma, and Magnusson Klemencic Associates in Seattle, Washington.

In 2017, Eric continued his education through the Burke Graduate Program at Purdue University, pursuing a Master of Science in Civil Engineering. He has worked as both a teaching assistant under Dr. Sukru Guzey and a research assistant under Dr. Robert Frosch in his time here. During his graduate studies in West Lafayette, Indiana, he conducted various experimental tests in the Bowen Laboratory for Large-Scale Civil Engineering Research at Purdue University. Eric has accepted a full-time position with Simpson Gumpertz & Heger (SGH) in Chicago, Illinois and is slated to begin upon completing his graduate studies in May 2019.